

ION IMPLANTATION INDUCED DEFECT FORMATION AND AMORPHIZATION IN
THE GROUP IV SEMICONDUCTORS: DIAMOND, SILICON AND GERMANIUM

By

DIANE P. HICKEY

A DISSERTATION PRESENTED TO THE GRADUATE SCHOOL
OF THE UNIVERSITY OF FLORIDA IN PARTIAL FULFILLMENT
OF THE REQUIREMENTS FOR THE DEGREE OF
DOCTOR OF PHILOSOPHY

UNIVERSITY OF FLORIDA

2007

© 2007 Diane P. Hickey

For my parents, Genevieve and Howard Hickey

ACKNOWLEDGMENTS

I acknowledge and thank the members of my dissertation committee. Dr. Kevin S. Jones, my advisor, has been an excellent guide throughout the graduate experience, and has provided many insightful thoughts into the workings of science outreach and the semiconductor industry. Dr. Mark Law, the Software Analysis of Materials Processing (SWAMP) Group co-advisor, has significantly helped in the organization of this dissertation, and also has put an indelible mark on my memory from the graduation ceremony for my Master's degree, when he said, "You're a Gator now." Dr. Paul Holloway has answered many questions about vacuum systems from my original project on silicon micro-electrical-mechanical systems, and was a wonderful advisor while I was chair of the student chapter of AVS Science and Technology Society. Dr. Stephen Pearton, an Australian from Tasmania, taught the first class that I took at the University of Florida, and through that class assured me that the decision to return to graduate school was the right decision. Finally, Dr. Scott Thompson has provided excellent industrial council and technical knowledge, and provided refreshing first-hand knowledge of the ways in research and industry interact.

Dr. Rob Elliman, of the Australian National University, provided the implants for this project, as well has been an excellent advisor who answered questions by email and was available for long discussions during MRS meetings. Dr. E.E. Haller, of Lawrence Berkley Laboratory and the Department of Materials Science and Engineering at the University of California – Berkeley, provided the high-purity germanium for this study, and co-authored the germanium papers that resulted from this work. Dr. Rob Chodelka was the original industrial science advisor for the diamond work presented here. The Gemesis Corporation graciously provided single-crystal diamond wafers for this study. Most of the analytical equipment used for this study is housed at the Major Analytical Instrumentation Center at the University of Florida.

Several members of its staff were instrumental in the completion of this work, including Dr. Jerry Bourne and Kerry Siebein. Ms. Siebein also co-authored one of the papers resulting from this study. Dr. Gerhard Fuchs and his group provided the furnace used for the high-temperature diamond anneals. Special thanks to Brandon Wilson for the operation and maintenance of the furnace, and especially his time during the anneals. Raman studies in this work were performed by Dr. David Hahn, of the University of Florida's Mechanical and Aerospace Engineering Department. Electron Energy Loss Spectroscopy was performed at the University of Central Florida.

Financial support for this work was partially provided by the Semiconductor Research Corporation contract #00057787. Special thanks are extended to the Applied Materials corporation, and Dr. Susan Felch, for the Graduate Student Fellowship. Smaller monetary fellowships were also provided by the University of Florida's Association of Academic Women and the Office of the President, as well as the AVS Manufacturing Science and Technology Group.

There are many other faculty at the University of Florida who have been instrumental to the papers and presentations I created during my tenure here. Dr. Simon Philpott provided insight during general defect discussions regarding germanium and diamond, as well as added insight into certain simulations. Dr. Susan Sinnott served as co-advisor to the AVS Science and Technology student chapter, and also provided letters of recommendation that assisted in landing various fellowships. Dr. Debbie Treise served as my advisor for the Science Communication Master's degree program in the College of Journalism. Dr. Rob Fox was always available to answer questions pertaining to technical electrical engineering or Auburn Football. Others at the University of Florida have made it a pleasure to spend time here. Ludie Harmon, Matthew

Walters and Teresa Stephens have been absolute joys to work with in the Materials Science and Engineering department.

The SWAMP Group has been an excellent group of people with whom to work. They include Dr. Mark Clark, Dr. Renata Camillo-Castillo, Dr. Erik Kuryliw, Dr. Robert Crosby, Dr. Russ Robison, Dr. Kevin Gable and Dr. Jennette Jaques. Current members of the SWAMP group continue to provide support and encouragement throughout the process, including Michelle Phen, Sam Moore, Leah Eldemen, Dan Gostovec, Sidan Jin, Saurabh Morarka, and Aijie Chen. Special thanks is given to Nick Rudawski who, in addition to being a current SWAMP group member, also kindly edited this document. Sherry Huo and David Kunderer are two undergraduates working with the group, and I wish them the best in their future endeavors. Thanks go to William 'Tre' Harrison who was my first research partner during the micro-electrical-mechanical systems project, as well as an excellent volleyball partner. Special thanks to Zachary Bryan, who has worked with me for two years in his research education for undergraduates position, and prepared most of the plan-views presented in this work, as well as co-authored two papers.

Many friends encouraged me in the pursuit of an engineering Ph.D. degree. Emmalyn Fuller-Garvett, Stephanie Bailey, Danielle Giglio-Danas, Jennifer Hussey-Kilgo, Hope Blass, Katie Allen, Amy Anderson-Whigham and Beth Miller all provided encouragement throughout the process. A couple of my good friends encouraged me to do well in life, but not go to grad school, presumably because they themselves were in the midst of their dissertation writing – Dr. V. Carol Chancey and Dr. Karla McInnis are specially acknowledged for support and insight. Anna Fuller, Stephen Tedeschi, Abby Queale, Dr. Carol Kem and Mike Davis, who have been a wealth of inspiration, fun and encouragement during this experience.

I have been blessed with the most wonderful family, who has encouraged and supported me throughout my life. Nothing that I have ever achieved or will achieve could have been done without them. For this, I would like to thank my all of my aunts, uncles, cousins, and closer family, Anthony Huffstetler, Brandon Huffstetler, Ryan Hickey, Karen Young, and especially my siblings who have always looked out for their baby sister – Lisa Hickey, Susan Huffstetler and Howard Hickey. And most of all, to my parents, Howard and Genevieve Hickey, without whose love and support none of this would be possible.

TABLE OF CONTENTS

	<u>page</u>
ACKNOWLEDGMENTS	4
LIST OF TABLES	11
LIST OF FIGURES	12
ABSTRACT.....	15
CHAPTER	
1 INTRODUCTION & MOTIVATION	17
Interest in Alternative Semiconductor Base Materials	17
The Cause and Problem of Extended Defects	18
Objective of Research.....	20
2 LITERATURE REVIEW	25
Introduction.....	25
General Concepts.....	25
Ion Implantation	25
Defects in the Crystalline Lattice	29
Amorphization.....	32
Solid Phase Epitaxial Regrowth	35
Simulation Process Tools	35
Relevant Literature for Ge, SiGe, SiC, and C.....	38
Germanium – Defects and Amorphization.....	38
Defects in Pure Ge.....	38
Amorphization, Regrowth and Lack of EOR Damage of Ge	40
SiGe Alloy – Defects and Amorphization.....	41
Silicon Carbide (SiC)- Ion Implantation and Amorphization	42
Diamond	43
Ion Implantation in Diamond	43
Controversies in Diamond Literature	47
Properties of the Elemental Crystal Systems.....	49
3 ANALYTICAL TECHNIQUES	51
Introduction.....	51
Sample Preparation for TEM.....	52
Transmission Electron Microscopy	58
Energy Dispersive X-Ray Spectroscopy	61
Electron Energy Loss Spectroscopy	62
Raman Spectroscopy	64

	Stopping and Range of Ions in Matter (SRIM)	66
4	RESULTS FROM NON-AMORPHIZING IMPLANTS INTO GERMANIUM	85
	Introduction.....	85
	Experimental Design	86
	Results.....	87
	Discussion.....	89
	Defect Density Analysis.....	89
	Defect Dissolution Rate.....	90
	Defect Location Analysis	91
	Conclusion.....	92
5	RESULTS FROM AMORPHIZING IMPLANTS INTO GERMANIUM.....	102
	Introduction.....	102
	Experimental Design	104
	Results.....	104
	High Energy Implant – 1 MeV	104
	Low Energy Implant – 40 keV	106
	Discussion.....	108
	Defects	108
	Trapped Interstitials and Activation Energy of 1 MeV EOR Defects in Ge	110
	Threshold Damage Density for Ge.....	111
	Conclusion	112
6	RESULTS FROM NON-AMORPHIZING MEV IMPLANTS INTO DIAMOND.....	125
	Introduction.....	126
	Experimental Design	127
	Preliminary Experiments	127
	Presented Experiment.....	127
	Results.....	129
	As-implanted Comparison: Orientation, Dose, Temperature.....	129
	Annealing: Low Dose.....	130
	Annealing: High Dose	130
	Annealing: Implant Temperature Effect.....	131
	Discussion.....	132
	Conclusion	134
7	RESULTS FROM AMORPHIZING MEV IMPLANTS INTO DIAMOND.....	145
	Introduction.....	145
	Experimental Design	146
	Results.....	147
	TRIM Results	147
	Swelling of Diamond Experiment	148

	Density of As-implanted Amorphous (α) C Layer	149
	Annealing Ion-implantation Induced Amorphous C	150
	Determination of the Graphitic Nature of Annealed Diamond	152
	EELS Results of the Amorphous Region	153
	Annealed Amorphous-Crystalline Interfaces	154
	Discussion.....	154
	Conclusion.....	157
8	SUMMARY AND FUTURE WORK.....	171
	Summary.....	171
	Non-amorphizing Si ⁺ Implants into Diamond and Ge, as Compared to Si.....	171
	Amorphizing Si ⁺ Implants into Diamond and Ge, as Compared to Si.....	172
	Future Work.....	173
APPENDIX		
A	SURFACE INITIATED DEFECTS OF ANNEALED DIAMOND.....	177
B	BORON IMPLANTATION INTO DIAMOND	182
	Introduction.....	182
	Experimental Design	184
	Results & Discussion.....	185
	LIST OF REFERENCES	187
	BIOGRAPHICAL SKETCH	197

LIST OF TABLES

<u>Table</u>		<u>page</u>
1-1	The mobility of carriers in semiconductors, as reported in the September 6, 2002 issue of Science.....	22
2-1	Relevant properties of the Group IV diamond-cubic semiconductors and graphite.....	50
3-1	Major Raman peaks from diamond, graphite and related materials. ⁷	80
5-1	Simulated damage values from current experiments.....	124
6-1	Implantation parameters.....	137
7-1	Simulated damage values from current experiments	170

LIST OF FIGURES

<u>Figure</u>	<u>page</u>
1-1	Cross-sectional TEM image of Intel Pentium transistors showing the appearance of dislocation loop defects. Courtesy of Intel and Scott Thompson.23
1-2	A comparison of the reported {311} defect in (a) Si and (b) Ge.....24
3-1	In-situ lift-out of diamond wedge, as viewed using the ion beam which is at a 52° angle to the stage.....69
3-2	The sample thickness before (a) and after (b) the thinning process.70
3-3	A TEM image of an as-implanted (110) single crystal diamond implanted with a 1 MeV 1×10^{14} Si ⁺ cm ⁻² at a temperature of 30° C.....71
3-4	XTEM of (100) oriented diamond after a 1 MeV 1×10^{15} cm ⁻² Si ⁺ implant (T _i = 30°C) annealed at 1050°C for 10 min: (a) XTEM image (labels denote platinum, carbon coating and surface) (b) SADP of top region (c) SADP of bulk.72
3-5	HRTEM image showing the middle of a damaged diamond layer from a (001)-oriented diamond implanted at 77 K with 1 MeV, 1×10^{15} Si ⁺ /cm ²73
3-6	Schematic diagram of the signals created during transmission of a high-energy electron beam through a thin solid sample.74
3-7	Single-crystal spot transmission electron diffraction patterns for the diamond structures (diamond, Si and Ge) for the (a) [001] and (b) [011] zone axis, and the hexagonal crystal structure for the (c) [2110] and (d) [0110] zone.75
3-8	De-excitation mechanisms for an atom that has undergone K-shell ionization: (a) emission of a characteristic K α X-ray and (b) emission of a KLM Auger electron.76
3-9	TEM and EDS characterization of sample.....77
3-10	The low-loss and K-ionization regions of the energy-loss spectra of three allotropes of carbon as detected using an EELS system.78
3-11	Screenshot of data displayed from the EELS system used for this study.....79
3-12	Raman spectra of diamond.....81
3-13	Raman spectra of carbon allotropes.....82
3-14	Comparison of simulation data to experimental images.....83
3-15	Comparison of simulation data to experimental images.....84

4-1	WBDF-XTEM images of (a) dot-like defects in Ge Si ⁺ implanted at 1 MeV with a dose of $1 \times 10^{14} \text{ cm}^{-2}$ following annealing at 450 °C for 10 min and (b) {311} defects in Si with the sample implantation following annealing at 850 °C for 10 min.	94
4-2	High resolution BF-TEM image of a dot-like defect seen in Ge Si ⁺ implanted at 1 MeV with a dose of $1 \times 10^{14} \text{ cm}^{-2}$ after annealing for 10 min at 450 °C.	95
4-3	WBDF-XTEM images of Ge and Si Si ⁺ implanted at 1 MeV with a dose of $1 \times 10^{14} \text{ cm}^{-2}$ after 10 min of annealing at various temperatures.	96
4-4	WBDF images of Si Si ⁺ implanted at 40 keV with a dose of $1 \times 10^{14} \text{ cm}^{-2}$ after annealing for 10 min at 750 °C:(a) XTEM and (b) PTEM.	97
4-5	WBDF-XTEM images of Ge Si ⁺ implanted at 40 keV with a dose of $1 \times 10^{14} \text{ cm}^{-2}$ (a) as implanted, and annealed for 10 min at (b) 350 (c) 450 (d)550 (e)650 (f)750 °C.	98
4-6	WBDF images of Ge Si ⁺ implanted at 40 keV with a dose of $1 \times 10^{14} \text{ cm}^{-2}$ and annealed for 10 min at 550 °C:(a) XTEM and (b) PTEM.	99
4-7	Microstructure evolution of Ge and Si after annealing for 10 min at various temperatures.	100
4-8	Plot of the logarithm of τ vs. $1/kT$ for 1 MeV Si ⁺ implantation into Ge after 10 min of annealing.	101
5-1	WBDF-XTEM images taken of Ge Si ⁺ implanted at 1 MeV to a dose of $1 \times 10^{15} \text{ cm}^{-2}$ (a) as-implanted and (b) after 10 min of annealing at 350 °C.	114
5-2	HRTEM images of Ge Si ⁺ implanted at 1 MeV to a dose of $1 \times 10^{15} \text{ cm}^{-2}$ as-implanted.	115
5-3	WBDF XTEM images of Ge Si ⁺ implanted at 1 MeV to a dose of $1 \times 10^{15} \text{ cm}^{-2}$ after annealing for 10 min at various temperatures.	116
5-4	XTEM images of Ge Si ⁺ implanted at 40 keV to a dose of $1 \times 10^{15} \text{ cm}^{-2}$ at 303 K(a) as-implanted and after annealing for 10 min at (b) 350 and (c) 380 °C for 10 min.	117
5-5	HR-XTEM images taken of Ge Si ⁺ implanted at 40 keV to a dose of $1 \times 10^{15} \text{ cm}^{-2}$	118
5-6	WBDF-XTEM images taken of Ge Si ⁺ implanted at 40 keV to a dose of $1 \times 10^{15} \text{ cm}^{-2}$ at 303 K and annealed for 10 min at (a) 450 (b) 550 (c) 650 and (d) 750 °C.	119
5-7	WBDF-XTEM images taken of Si Si ⁺ implanted at 40 keV to a dose of $1 \times 10^{15} \text{ cm}^{-2}$ at 303 K and annealed for 10 min at 750 °C (a) XTEM and (b) PTEM.	120
5-8	Graphical representations of the temperature dependence of the Ge EOR (a) defect density, (b) defect size, (c) dissolution rate and (d) trapped interstitials.	121

5-9	XTEM images of Ge Si ⁺ implanted at 1 MeV to a dose of $1 \times 10^{15} \text{ cm}^{-2}$ at 303 K.....	122
5-10	XTEM images of Ge Si ⁺ implanted at 40 keV to a dose of $1 \times 10^{15} \text{ cm}^{-2}$ at 303 K.....	123
6-1	WBDF-XTEM images of (001)-oriented single-crystal diamond Si ⁺ implanted at 1 MeV to a dose of $1 \times 10^{15} \text{ cm}^{-2}$ at (a) 77K and (b) 303K.	138
6-2	BF TEM images of (011)-oriented diamond Si ⁺ implanted at 1 MeV to a dose of $1 \times 10^{14} \text{ cm}^{-2}$ Si ⁺ at 303K.	139
6-3	WBDF-XTEM image of (001)-oriented diamond Si ⁺ implanted at 1 MeV to a dose of $1 \times 10^{14} \text{ cm}^{-2}$ at 303K after annealing at 1250 °C for 1 hr.	140
6-4	BF TEM image of (110)-oriented diamond Si ⁺ implanted at 1 MeV to a dose of $1 \times 10^{15} \text{ cm}^{-2}$ at 303K.	141
6-5	WBDF-XTEM images of (001)-oriented diamond Si ⁺ implanted at 1 MeV to a dose of $1 \times 10^{15} \text{ cm}^{-2}$ at 303K.	142
6-6	WBDF-XTEM images of (001)-oriented diamond Si ⁺ implanted at 1 MeV to a dose of $1 \times 10^{15} \text{ cm}^{-2}$ at 77K.	143
6-7	HRTEM image of damaged diamond layer in (001)-oriented diamond Si ⁺ implanted at 1 MeV to a dose of $1 \times 10^{15} \text{ cm}^{-2}$ after annealing at 1350 °C for 24 hrs.	144
A-1	WBDF XTEM images of single-crystal diamond Si ⁺ implanted at 1 MeV to a dose of $3 \times 10^{15} \text{ cm}^{-2}$ at 303 K after annealing for 24 hrs at 1350 °C.	178
A-2	WBDF XTEM images of single-crystal diamond Si ⁺ implanted at 1 MeV to a dose of $1 \times 10^{15} \text{ cm}^{-2}$ at 77 K after annealing for 24 hrs at 1350 °C	179
A-3	Images of single-crystal diamond Si ⁺ implanted at 1 MeV to a dose of $1 \times 10^{14} \text{ cm}^{-2}$ at 303 K after annealing for 2 hrs at 950 °C.	180
A-4	BF-XTEM images of single-crystal diamond un-implanted, after annealing for 2 hrs at 950 °C.....	181
B-1	WBDF-XTEM images of (001)-oriented diamond B ⁺ implanted at 2 MeV to a dose of $1 \times 10^{15} \text{ cm}^{-2}$ at 303K as implanted, and after annealing (a) in flowing N ₂ ambient at 1000 °C for 10 min and (b) in vacuum at 1350 °C for 24 hrs.....	186

Abstract of Dissertation Presented to the Graduate School
of the University of Florida in Partial Fulfillment of the
Requirements for the Degree of Doctor of Philosophy

ION IMPLANTATION INDUCED DEFECT FORMATION AND AMORPHIZATION IN
THE GROUP IV SEMICONDUCTORS: DIAMOND, SILICON AND GERMANIUM

By

Diane P. Hickey

August 2007

Chair: Kevin S. Jones

Major: Materials Science and Engineering

Silicon, which has been the workhorse of the semiconductor industry for the past several decades, is now being enhanced with other Group IV elements, such as carbon (silicon carbide) and germanium (silicon-germanium strained channels in transistors), to accentuate properties of silicon for various nanoelectronic devices. However, there is little understanding of the relationship between ion implantation and defect evolution in two of the three corners of the Group IV phase diagram. In particular, the rod-like {311} defect is theorized to be unique to the diamond crystal structure elements. Due to its ability to affect dopant diffusion, the {311} defect is well studied in silicon. However, few studies of germanium and none of diamond have analyzed extended defect formation and evolution using transmission electron spectroscopy. Using ion implantation to induce amorphization is a technological process step in Si devices and potentially for diamond nano-electronics. Defects associated with crystal regrowth in Ge and diamond are not well known. My research studies the formation conditions of extended defects and amorphization in carbon and germanium after ion implantation.

Ion implantation damage in diamond-cubic single-crystal silicon, germanium and diamond was produced by Si⁺ implantation at 1 MeV to a dose of $1 \times 10^{14} \text{ cm}^{-2}$ and $1 \times 10^{15} \text{ cm}^{-2}$. Damage in Si and Ge was produced by Si⁺ implantation at 40 keV to a dose of $1 \times 10^{14} \text{ cm}^{-2}$ and 1×10^{15}

cm^{-2} , and amorphizing damage in diamond was produced by Si^+ implantation at 1 MeV to a dose of 3 and $7 \times 10^{15} \text{ cm}^{-2}$. All implants were carried out at room temperature. For non-amorphizing implants ($10^{14} \text{ Si}^+ \text{ cm}^{-2}$) into Ge, dot-like defects formed immediately upon implantation and were stable up to temperatures of 650 °C. The activation energy of these defects was determined to be approximately $0.2 \pm 0.1 \text{ eV}$. For amorphizing implants ($10^{15} \text{ Si}^+ \text{ cm}^{-2}$) into Ge and upon solid-phase epitaxial regrowth, the same types of defects seen in Si were also seen in Ge. However, in Ge, the end-of-range defects were the least stable, dissolving at temperatures around 650 °C. The activation energy for the dissolution of end-of-range defects in Ge is approximately $0.4 \pm 0.1 \text{ eV}$. For diamond, non-amorphizing Si^+ implantation ($< 3 \times 10^{15} \text{ Si}^+ \text{ cm}^{-2}$) and subsequent annealing to temperatures as high as 1350 °C for 24 hours resulted in no implantation related defects. Amorphizing implants ($\geq 3 \times 10^{15} \text{ Si}^+ \text{ cm}^{-2}$) into diamond revealed a threshold for amorphization at approximately $6 \times 10^{22} \text{ vacancies cm}^{-3}$, higher than previously reported values. The diamond did not convert to graphite immediately after implantation, but instead resulted in an amorphous carbon layer, with a density of $1.3 \pm 0.1 \times 10^{23} \text{ atoms cm}^{-3}$, which is approximately 25% less dense than diamond and 15% more dense than graphite. After annealing at 1350 °C for 24 hours, the amorphous carbon converted to graphite. These results provide one of the first comparative studies of these Group IV semiconductor's defect evolution, thus potentially providing more accurate design of simulation programs and future electronic devices.

CHAPTER 1 INTRODUCTION & MOTIVATION

Interest in Alternative Semiconductor Base Materials

Silicon (Si) has been the main semiconductor base material for the past several decades. Although germanium (Ge) was the first transistor material,¹ Si's low cost and stable native oxide made it the more attractive material for microelectronic devices. Silicon's low cost and decades of research ensure its continued dominance over the next few years, but a theoretical limit to simple scaling does exist. In order to stay on track with Moore's Law,² many technologies are being explored, intended to both extend silicon's lifetime and, in some devices, to replace silicon. The 2005 International Technology Roadmap for Semiconductors³ highlights that research into new base materials is extremely important for the semiconductor industry.

Two attractive base materials are carbon (C), in the diamond form,⁴ and Ge.¹ Both have higher carrier mobilities than Si (Table 1-1). Both are elemental crystals, and do not suffer the complications ion-implantation into higher-electron mobility III-V semiconductors like gallium arsenide. Additionally, with the advent of high-k dielectric gate oxides, the need for a stable native oxide in these materials becomes less important. Ge and C are already being used as important semiconductor materials when alloyed with silicon. Silicon carbide (SiC) is one of the hardest materials known and produced today, and silicon-germanium (SiGe) has been used to increase performance in sub-100 nanometer (nm) transistors.

As the semiconductor industry explores other materials besides Si, leveraging decades of Si research could speed development time for new materials. Currently, in the pursuit for ultra-shallow junction devices, extended defects are a major concern in Si because defects can impact device performance.⁵ Figure 1-1 shows a transistor with dislocation loop defects apparent in the transmission electron microscope (TEM) image. The question remains as to whether these same

extended defects would form in alternate material devices, and, if so, would the defects be as detrimental to device performance as in Si.

The Cause and Problem of Extended Defects

Extended defects arise after ion implantation. Ion implantation is necessary to dope the base material to impart properties desirable in the electronic device. Extended defects are irregularities in the crystal that are large agglomerations of point defects, such as interstitial atoms or vacancies, or a combination of both. Common extended defects in Si, resulting from the agglomeration of interstitial atoms, are the {311} and dislocation loop defects. The {311} defect is the source of the dislocation loop.⁶ These defects have affected Si device performance for many years, inhibiting carrier mobility and therefore increasing leakage current.

The {311} defect is unique to semiconductors. This defect has never been observed in metals, and is theorized to be the stable interstitial defect in all diamond-structure crystals.⁷ However, it has only been reported in two elements – Si and Ge. In Si, the {311} defect has formed during electron irradiation^{7,8} and for a variety of ion implantation regimes at both high and low energies.⁹ However, the {311} defect has only been reported in Germanium in a handful of situations – electron irradiation and light element implantation.^{5,8,10-12} As yet, the defect in Ge has not been demonstrated using a typical dopant atom.

In addition, the direct comparison of a {311} defect in Si to a {311} defect in Ge raises questions. For example, Figure 1-2(a) shows an example of a high-resolution (HR) TEM image of a {311} defect in Si. It shows a well-organized defect structure. Figure 1-2(b), is a HRTEM image of a {311} defect in Ge on the same scale, created after a hydrogen (H) implant. Notice the jagged appearance of the Ge {311} as compared to the Si {311}.

Since these differences have been seen in pure Ge versus pure Si, Crosby et al. sought to understand the {311} defect formation in SiGe alloys. He found that the defect formation

changed as a function of alloy concentration. In $\text{Si}_x\text{Ge}_{1-x}$ alloys with a Ge concentration less than 25%, {311} defects continued to form; above 25% Ge content, {311} defects did not appear. Crosby concluded that the weaker bond strength of Ge prevented the formation of {311} defects.¹³ Additional differences in defect formation have been seen recently: an analysis of 10, 20 and 30% Ge concentrations in SiGe alloys revealed near surface vacancy nanocavities with increasing Ge concentration.¹⁴

Logically proceeding from Crosby's conclusion that the weaker bond strength of Ge prevents {311} formation, an element with a stronger bond strength, like C, should encourage {311} defect formation. However, it is well known that {311} formation in Si is actually inhibited by the presence of C. Rather than bond strength, this phenomena is attributed to the size difference of C to Si (C atoms are much smaller than Si), which allows interaction with {311} defect-forming interstitials and essentially 'traps' the interstitials preventing the atoms from migrating to agglomerate.¹⁵

However, if the entire crystal was C, rather than just an implant, the {311} defect is still theorized to be the stable interstitial defect.⁷ Advances in man-made single-crystal diamond development have progressed to a point in which, due to diamond's desirable qualities, diamond as a substrate for microelectronics is a growing possibility.⁴ Diamond may also form the {311} defect as an interstitial precipitate, but due to the difficulty of creating appropriate TEM samples this remains unconfirmed. Additionally, one scenario that creates extended defects in Si is the regrowth from an amorphous state. Using an amorphizing implant prior to a doping implant has become common practice in industry to prevent the diffusion of the dopant species away from the channel region and to increase dopant activation. Therefore, defect formation during this process is also of interest. However, past a certain damage point, diamond will not transition

back to a diamond cubic lattice but will instead undergo a phase transition to graphite upon annealing.¹⁶ Solid phase epitaxial regrowth, the direct transition to graphite, or extended defects have not been previously demonstrated in diamond using direct imaging techniques, like TEM. Therefore, there is no imaging evidence of extended defects in diamond.

Objective of Research

These differences highlight the fact that even though these are all Group IV semiconductors, behavior can vary greatly when processed using standard semiconductor techniques. The theory that the $\{311\}$ defect is the stable interstitial defect in all diamond-cubic structure elements, and the similarities inherent in being in the same column of the periodic table, allow a hypothesis that the same defects should occur in all three materials after the same implant conditions. However, the recent research discussed in the previous paragraphs indicates that this hypothesis may not be true in all situations.

My research studied the defect formation, evolution and amorphization occurring after ion implantation to determine whether the same defects occur in Ge and C as in Si under the same implant conditions. The expected result is that the same defects do form, and if so, leveraging the collected knowledge of Si's extended defects will save development time and research costs into devices based on C and Ge. If the expected result of similar defects is not found, the results of this research could be applied to adjust current simulation tools to save development time in potential future electronic devices.

The research documented in this publication is organized in the following manner. Chapter One provides the motivation and the objectives of this research, while Chapter Two reviews the current state of the literature. Chapter Three provides an overview of the characterization techniques used in this study, including a novel method for creating cross-sectional TEM samples from single crystal diamond substrates. Leveraging the research in non-amorphizing

implants into SiGe by Crosby, et al., Chapter Four presents the experimental results of non-amorphizing implants into pure Ge and Si, and discusses the differences in the formation and evolution of the extended defects. Extended defects are also known to occur in Si for amorphizing implants, therefore Chapter Five presents the experimental results of amorphizing implants into Ge, and discusses the Si similarities and differences in the results, in the frame of other current research. Knowing the similarities and differences presented in the previous results for Si and Ge, the results of the non-amorphizing implants in diamond are provided and discussed in Chapter Six. This covers implants below and to the verge of creating a continuous amorphous layer in diamond. Chapter Seven presents the results from amorphizing implants into single-crystal diamond, compares the results to those from Ge and Si, and presents the experimental results of amorphization thresholds. Chapter Eight summarizes the results based on the original hypothesis that the same defects that form in Si would also form in Ge and C. Since that hypothesis did not hold true for all scenarios, recommended future work is discussed.

Table 1-1. The mobility of carriers in semiconductors, as reported in the September 6, 2002 issue of Science. The diamond values were achieved using plasma-grown single crystal diamond.⁴

Semiconductor	Mobility, cm² V⁻¹ s⁻¹ (μ)	Maximum electric field, V cm⁻¹ (E_m)	Bandgap, eV (E_g)
Diamond (C)	4500 (electron) 3800 (hole)	10^7	5.5
Silicon carbide (SiC)	700 (electron)	3.0×10^6	3.26
Gallium nitride (GaN)	2000 (electron)	3.0×10^6	3.0
Gallium arsenide(GaAs)	8500 (electron)	4.0×10^5	1.42
Silicon (Si)	1500 (electron) 450 (hole)	3.7×10^5	1.12
Germanium (Ge)	3900 (electron) 1900 (hole)	2.0×10^5	0.66

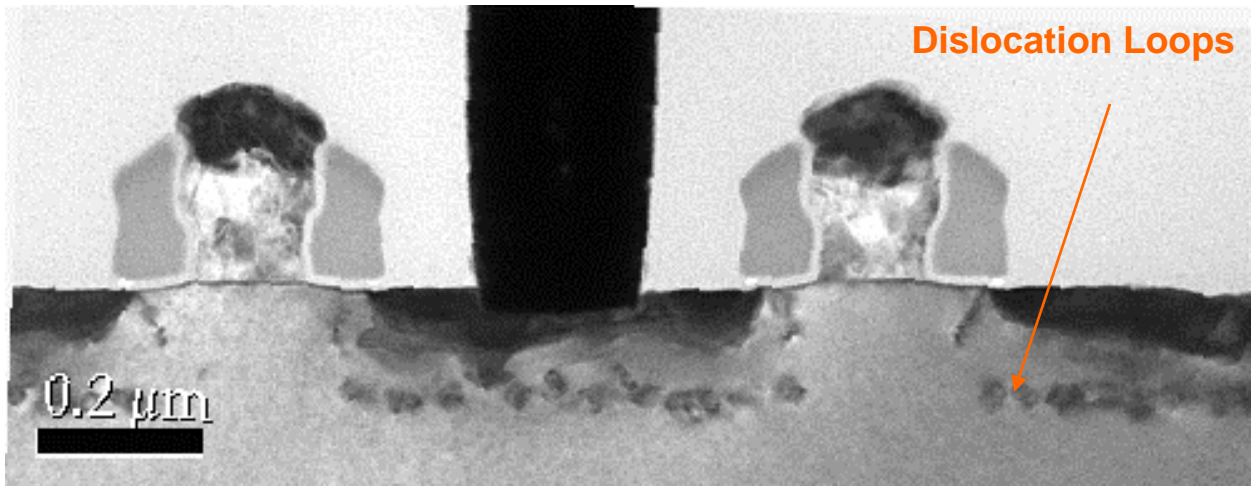


Figure 1-1. Cross-sectional TEM image of Intel Pentium transistors showing the appearance of dislocation loop defects. Courtesy of Intel and Scott Thompson.

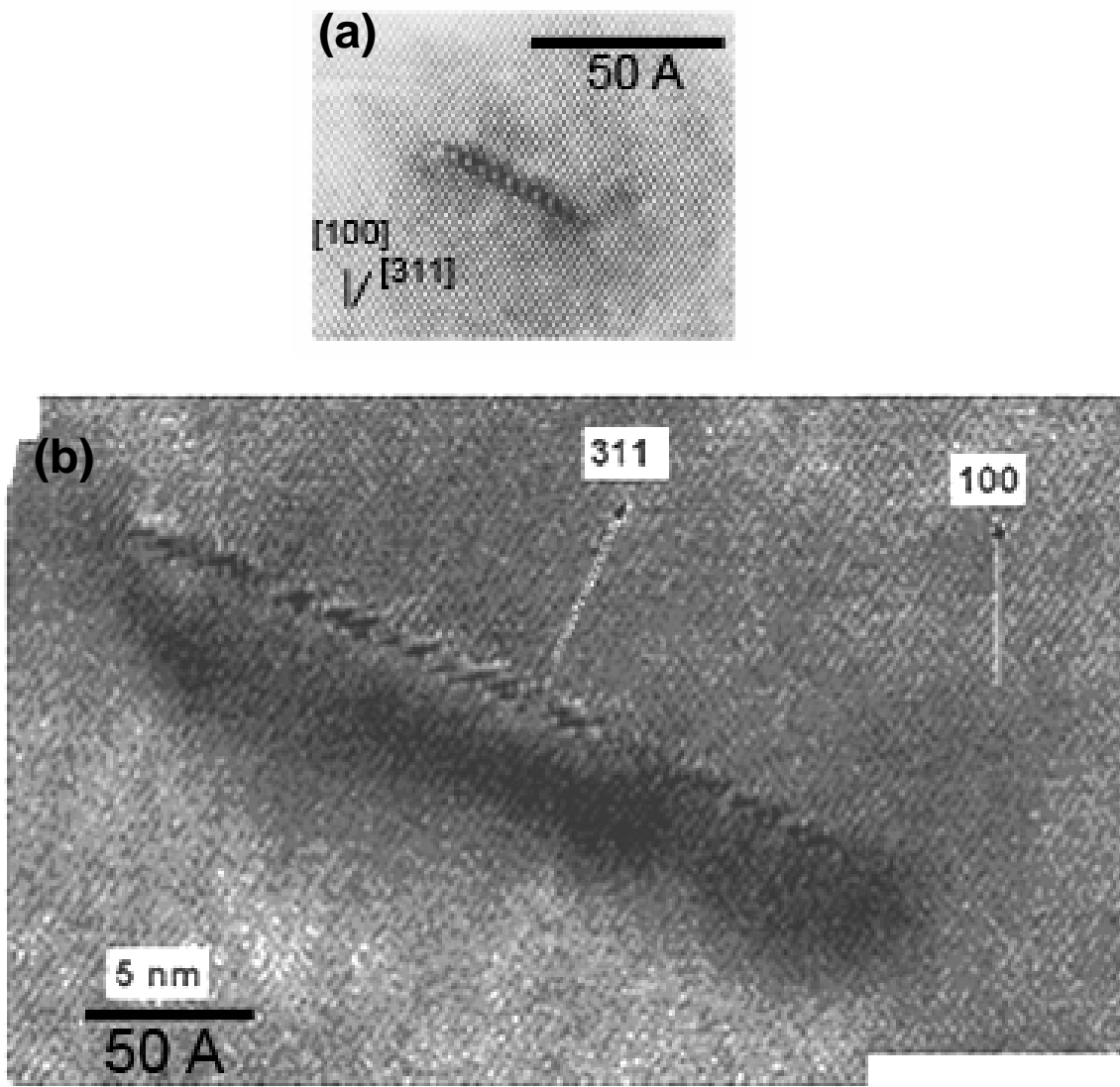


Figure 1-2. A comparison of the reported $\{311\}$ defect in (a) Si¹⁷ and (b) Ge.¹¹

CHAPTER 2 LITERATURE REVIEW

Introduction

Presented here are descriptions of general concepts associated with extended defects and amorphization in silicon (Si), and relevant literature reviews that describe the state of current knowledge in germanium (Ge), carbon (C) and their alloys with Si. If the reader is already familiar with the concepts of ion implantation damage in a crystal, annealing kinetics and the difficulty of modeling the crystalline-to-amorphous transition, then the first section of this chapter may be superfluous. The second part of the chapter will review relevant studies of extended defects, rising from both non-amorphizing and amorphizing implants, in Si, Ge, C and their alloys.

General Concepts

Ion Implantation

Ion implantation has been the preferred method of introducing dopants into semiconductor crystals for decades, due to its many advantages: reproducibility, accurate dose control, and tailored doping profiles. As such it is one of the most important tools in Si processing.¹⁸ Ion implantation is the forced entry of ions into a substrate through its surface. The ions travel through the lattice interacting with the lattice atoms through elastic collisions with electron clouds and inelastic electronic or nuclear collisions, which disrupts the lattice structure. If the energy transferred during the inelastic collision is greater than the displacement energy (E_d) of an atom, that atom will be dislodged from its lattice position. Stopping of the implanted ion is dominated by nuclear collisions at low energy implants, while electronic stopping is dominant for high energy implants.¹⁹

Nuclear collisions can be modeled using the following equation:

$$S_n(E) = 2.8 \times 10^{15} \cdot \frac{Z_1 Z_2}{(Z_1^{2/3} + Z_2^{2/3})^{1/2}} \cdot \frac{m_1}{m_1 + m_2} \quad (2-1)$$

where $S_n(E)$ is the nuclear stopping power as a function of energy, Z_1 the ion atomic number, Z_2 the substrate atomic number, m_1 the ion mass, and m_2 the substrate mass. Nuclear stopping contributes most of the damage after ion implantation. The second stopping mechanism, electronic stopping, can be modeled as:

$$S_e(E) = cv_{ion} = kE^{1/2} \quad (2-2)$$

where $S_e(E)$ is the electronic stopping power as a function of energy, E is the energy of the ion, v is the velocity of the ion, and c and k depend on the ion, substrate and the stopping mechanism. Nuclear stopping increases with increasing mass (m) and decreasing energy (E); electronic stopping increases with increasing implant energy (E), as shown in Equations 2-1 and 2-2. The rate at which an ion loses its energy is represented by the following differential equation, which takes into account both stopping mechanisms, and the atomic density of the substrate (N):

$$\frac{dE}{dx} = -N[S_n(E) + S_e(E)] \quad (2-3)$$

In this work, the projected range and damage peak of the implant will be an integral part of estimating damage in the crystal and also for determining threshold parameters for amorphization. To begin to determine the projected range of an implant, the range (R) of one ion, in some measure of distance, may be determined by rearranging the above differential equation and integrating over the distance:

$$R = \int_0^R dx = \frac{1}{N} \int_0^{E_0} \frac{dE}{S_n(E) + S_e(E)} \quad (2-4)$$

As the implantation process typically implants above 10^{10} , and even as high as 10^{20} ions cm^{-2} , the process of determining the projected range and straggle is of a statistical nature. The ion concentration as a function of depth is represented to the first order by:

$$C(x) = C_p \exp\left[\frac{-(x - R_p)^2}{2\Delta R_p^2}\right] \quad (2-5)$$

where C_p is the peak concentration at the center of the Gaussian distribution, R_p is the projected range of the ions into the substrate, and ΔR_p is the first standard deviation about R_p , also known as ion straggle. Dose (Q) is the total number of implanted ions, and can be expressed in terms of C_p and ΔR_p :

$$Q = \sqrt{2\pi}\Delta R_p C_p \quad (2-6)$$

The implant profile may not always be Gaussian in nature due to ion channeling. Channeling is the phenomena by which the ion trajectory is in line with atomic rows, and experiences a slower rate of energy loss. This results in a non-Gaussian distribution of ions and damage in the lattice. Channeling may be reduced or avoided by titling the substrate or amorphizing the crystal prior to implantation. Amorphization will be discussed in a future section. In this study, channeling was avoided by tilting the (011) and (001) crystals seven degrees from normal.

Four moments are used to fully describe the distribution of implanted dopants within a crystal: projected ion range (R_p), ion straggle (ΔR_p), skewness (γ) and kurtosis (β). Skewness describes the asymmetry of the profile about the Gaussian peak, and kurtosis describes the contribution of the profile tail on the flatness of the profile shape. All four moments can be mathematically represented in terms of dose and concentration as a function of depth:

$$R_p = \frac{1}{Q} \int_{-\infty}^{\infty} xC(x)dx \quad (2-7)$$

$$\Delta R_p = \sqrt{\frac{1}{Q} \int_{-\infty}^{\infty} (x - R_p)^2 C(x)dx} \quad (2-8)$$

$$\gamma = \frac{\int_{-\infty}^{\infty} (x - R_p)^3 C(x)dx}{Q\Delta R_p^3} \quad (2-9)$$

$$\beta = \frac{\int_{-\infty}^{\infty} (x - R_p)^4 C(x) dx}{Q\Delta R_p^4} \quad (2-10)$$

Thus far, the stopping of the ion by energy transfer has been described. If the energy per collision transferred to an atom equals or exceeds the atom's displacement energy (E_D), the lattice atom will be displaced from its lattice site. If the energy transferred exceeds the E_D , the displaced host atom then may continue to interact (by electronic or nuclear stopping) with other host atoms in the same manner as the incoming ions. This is called a collision cascade, and hundreds to thousands of these lattice atoms may be displaced per incoming ion depending on the ion's mass and energy. Each displacement leaves a vacancy, and each atom that does not come to rest on a lattice site is an interstitial atom. A vacancy and an interstitial are known as a Frenkel pair. For room temperature implants, it is assumed that all Frenkel pairs recombine during implantation, so only interstitials remain, in the amount of the original dose of the ion implant.²⁰

Both interstitials and vacancies naturally exist in any crystal above absolute zero according to the relation:

$$N_p = N \exp\left[\frac{-Q_p}{kT}\right] \quad (2-11)$$

where N_p is the concentration of point defects, N is the concentration of lattice sites, Q_p is the formation energy of the point defect, k is Boltzmann's constant, and T is temperature. For Si at room temperature, the formation energy for interstitials is 2 eV, and vacancies is 4.4 eV.²⁰

The simulation program commonly known as SRIM, the Stopping and Range of Ions in Matter,²¹ and its calculation program (commonly known as TRIM, for the Transport of Ions in Matter) is often used for simulating the damage caused by ion implantation. The TRIM program is a Monte-Carlo simulation which requires input parameters such as ion type, ion energy, target

substrate, target composition, density and E_d . The TRIM program does not take into account channeling effects, phase transformation of the material or the possibility that defects can be annihilated during the process, and therefore always overestimates the damage. Even with these drawbacks, it remains an excellent estimator for the damage created during ion implantation.¹⁹

Defects in the Crystalline Lattice

The dislodged atoms or the implanted ions may either come to rest on a vacant lattice position (fill a vacancy) or occupy a non-lattice position (become an interstitial). These types of defects are known as point defects. Other point defects which may exist after ion implantation and annealing are substitutional atoms (foreign atoms which sit on a host lattice site) and interstitial atoms (either self-interstitials or foreign interstitials). At a high enough density, the point defects can agglomerate into defect complexes, commonly known as extended defects. Defects that are interstitial in nature are referred to as ‘extrinsic’ defects; those that are created by vacancies are ‘intrinsic’ defects.¹⁹ To repair the defects created during ion implantation, annealing is used. The word ‘anneal’ comes from a Middle English word ‘analen’ which meant ‘to set on fire.’ Annealing is the process of heating the crystal to remove damage by adding energy into the system so that the defects become mobile. Upon annealing at moderate temperatures, point defects can interact to form extended defects. Extended annealing time or annealing at higher temperatures will result in the defects evolving so much that the atoms find lower-energy sites to occupy in the lattice and effectively ‘dissolve’ the defects, thereby restoring the crystal structure.¹⁹

These extended defects may include dislocation loops, stacking faults, rod-like interstitial defects, clusters and others. Jones et al. classified extended defects which occur in Si after ion-implantation and annealing into five types. These defect types are known as subthreshold, end-of-range (EOR), regrowth related, clamshell (or zipper), and solubility related defects.⁹

A visual representation of the principal damage features in Si as a function of dose and annealing temperatures, for MeV energy implants was presented by Libertino.²² No similar type representations seem to exist for Ge or C. For this study, the dose ranges into the crystals will be in the range of 10^{14} - 10^{15} cm⁻², and annealing temperatures will encompass and expand beyond those for defect formation in Si. This study focuses on the {311} and extended defects, occurring in the 10^{14} - 10^{15} cm⁻² dose range in Si, which have been industrially unfavorable for Si complementary metal oxide semiconductor (CMOS) processing.

{311} defect in the Si crystalline lattice. One particular defect that has been especially relevant to dopant motion in silicon is the rod-like {311} extended defect.¹⁷ Si and Ge have been the only elements to display this unique defect; it has never been seen in metals.⁵ This defect is the preferred interstitial precipitate in silicon, and Salisbury concluded that the {311} rather than the {111} is the normal plane for self-interstitial precipitation for all diamond structure crystals.⁷

The {311} defect is a planar defect that resides on the {311} habit plane and grows linearly in the <110> direction.²³ The {311} defect has three distinct stages of evolution: formation, growth and dissolution.²⁴ The defect is formed from an accumulation of point defects into clusters, known as sub-microscopic interstitial clusters (SMICs), since the clusters are not discernible by conventional TEM methods.^{25,26} Next, the clusters grow in the <110> direction and finally, at a high enough thermal budget, the {311} defects will dissolve in the matrix by ejecting interstitials.¹⁷ The exact mechanism of the {311} formation has been studied at length, and various models have been proposed in the literature.^{5,7} In silicon, the {311} defect is known to affect diffusion of dopants¹⁷ and are the source of the formation of another form of extended defects, dislocation loops.⁶ These dislocation loops are known to affect the electrical characteristics of silicon devices.⁵

Much is known about the {311} defect in silicon. A high resolution TEM image of a {311} defect was shown in Figure 1-2. The {311} defect is an average of 40 Å wide and varies in length. It grows in the <110> direction, and will trap 26 interstitials per nm. As annealing progresses, {311} defects will increase in size but decrease in density.¹⁷ There is no length dependence on the {311} defect evolution - the formation energy is constant. Unlike loops, the formation energy does not decrease as the size of the defect increases. The activation energy of a {311} has been estimated to be approximately 3.6 eV, which was derived from annealing curves.¹⁷ Various experimental conditions can create the {311} defect. According to Jones, Prussin and Weber, the {311} defect appears during various doping regimes. When the implant does not exceed the amorphization threshold, the {311} defects are the primary extended defect. When the damage exceeds the amorphization threshold, upon annealing, the {311} defect will develop in the region of the EOR.⁹ Using the activation energy of the {311} defect, the equivalent defect state for various times or temperatures can be determined.²⁷

The {311} defect occurs at both low and high energies. Defects created by Si ion implants into Si in the range of 20 keV to 150 keV (relatively low energies) have been mapped according to dose. The {311} defect was also seen after a Si⁺ implantation at 1.2 MeV implant of 5×10^{13} cm⁻² into Si and annealed at 680 °C for one hour,²⁶ and also 4 MeV implants of 1×10^{14} Si⁺ cm⁻² into Si annealed at 800°C for 15 min,²⁸ both of which are relatively high energies.

Besides ion implantation, the {311} defect has also been observed in unimplanted Si resulting from electron beam irradiation.^{7,8,29,30} Salisbury and Loretto's work with electron-irradiated silicon led to the determination that the (113) rather than the (111) is the normal plane for precipitation of self-interstitials in diamond-structure crystals.

Impact on Si doping. Control over dopant atom placement is one of the strongest benefits of ion implantation. However, dissolution of {311} defects during annealing gives rise to an unwanted side effect – transient enhanced diffusion (TED). During {311} dissolution, interstitials are emitted, and assist in the motion of dopant atoms away from the intended target depth in the bulk material.¹⁷ By moving atoms away from the targeted channel area, TED directly and negatively affects device performance.

{311} defects are also the precursors to extended defects which negatively impact device performance. Dislocation loops are two dimensional circular precipitates of interstitials inserted between two consecutive {111} planes. Robertson et al. showed that {311} defects are the preferential site for dislocation loop formation after an amorphizing implantation regime when the defects occur in the EOR.³¹

Additionally, the {311} defect formation has been known to be inhibited or enhanced by various dopants. The formation of the {311} is strongly enhanced by the presence of arsenic (As), but the dissolution remains unaffected.³² The density of interstitials in {311} defects decreases linearly with the increasing presence of C, which fully suppresses the TED nature of boron (B) in Si.¹⁵ The normal characterization method for {311} defect detection is TEM.

Amorphization

If the concentration of point defects exceeds a critical value during implantation, a phase transformation occurs, changing the crystalline solid into an amorphous solid. As mentioned before, light ions cause less damage than heavier ions. The damage tracks left in a material are called a displacement spikes, which are very linear with the track of the atom in light ions but consists of a volume of material with heavier ions. Morehead and Crowder assumed that, in crystalline Si, the displacements spikes relax to form amorphous carbon, and when these spikes overlap, a continuous amorphous layer is formed.³³ In Si, the amorphization process has been

modeled as a first-order phase transformation. Dose has a large effect on amorphization. For light ions, higher doses are needed to create a continuous amorphous layer, but for heavier ions, overlapping collision cascades allow for lower amorphization doses. Additionally, after ion implantation, three profiles may occur in Si:³⁴ the first is a profile that will not have an amorphous phase change upon implantation, the second is a buried amorphous layer and the third is a continuous amorphous layer.²⁷

Implantation temperature can have significant impact on whether amorphization will occur in Si. A room temperature implant of a Si⁺ implantation at 1.25 MeV to a dose of $1 \times 10^{16} \text{ cm}^{-2}$ into Si produced an amorphous layer approximately 400 nm thick, while a dose of $2.5 \times 10^{15} \text{ cm}^{-2}$ did not create any amorphous layer.³⁴ The same ion and energy implant at liquid nitrogen temperatures, 80 K, for a much lower dose of $5 \times 10^{14} \text{ Si}^+ \text{ cm}^{-2}$ into Si, resulted in a larger amorphous layer, nearly 1400 nm thick.³⁴ Low temperature implants are thought to ‘freeze in’ point defects, while room temperature implants assume that all Frenkel pairs recombine during implantation.²⁰ The ion dose rate, if too high, may heat up the sample during implantation, but this can be avoided by using a Waycool station.³⁵ Additionally, the morphology of the damage after amorphization at low temperatures is different than that at room temperature or higher. Pockets of crystalline material were shown to be trapped in the amorphous layer near the α -c interface of a liquid nitrogen temperature Si⁺ implant into Si. These crystallites were not seen in the same implant at room temperature.³⁴ At sufficiently high implant temperatures, amorphization can be avoided.²⁰

Amorphization changes the density of a material. By nature of disrupting the lattice, swelling occurs in the crystal. In Si, the density change is minimal, and difficult to observe by

XTEM. Using computational simulations, the amorphous phase of the Si material was determined to be approximately 1.76% less dense than crystalline Si.³⁶

Amorphization is a difficult phenomenon to model due to the fact that it is affected by ion dose, dose rate, energy, mass of the incoming ion, mass of the target ion, and temperature. Christel, Gibbons, and Sigmon suggested that displacing 10% of the Si lattice at low temperatures (14% at room temperature) would result in amorphization.³⁷ They used a transport equation, and in conjunction with other work, used it to determine the number of silicon recoils produced per unit volume at each depth. However, backscattering measurements were used to determine interface points, and not XTEM, which allows some room for error. Prior to Christel, energy-to-volume was put forth as a model to equalize the different factors that affect amorphization, with a general value of $6-10 \times 10^{20}$ keV/cm³ determined.³⁷ Since then, three parameters have been commonly used to describe amorphization in Si: critical damage, using either recoils or vacancies per volume (D_{crit} or D_C , respectively), threshold damage density (TDD), and displacements per atom (DPA). Threshold damage density is reported in terms of energy per volume, and has been identified for P⁺ implants into Si over a wide range of energies to a dose of 1×10^{15} cm⁻² as 1.0×10^{21} keV cm⁻³, which is slightly higher than the previous model.³⁵ The ion implantation community favors reporting the amount of damage needed to induce amorphization at liquid nitrogen temperature in displacements per atom (DPA), a unitless parameter. For Si, the DPA is 0.3.

For all the previous methods, a key point is the depth at which the measurement or calculation is performed. For a buried amorphous layer, there are two amorphous-crystalline (α -c) interfaces: one near the surface and one near the bulk. As the energy of the implant increases, the surface α -c interface becomes increasingly wider. For El-Ghor et al.'s 1.25 MeV Si⁺

implantation into Si, the authors used a range between 0.3 - 0.9 μm depth to define the α -c interface.³⁴ The bulk interface is normally quite abrupt, due to the sharp decrease of implant damage in the EOR region. Christel and Prussin both used the bulk interfacial measurement to determine the amorphization thresholds in Si, though both used different methods to determine the position of the interface.^{35,37}

Solid Phase Epitaxial Regrowth

Annealing at sufficient temperatures will cause the reorganization back into the crystalline structure, starting at the interface between the amorphous region and the crystalline bulk substrate. This is called solid phase epitaxial regrowth (SPER). Three kinds of defects may occur in the lattice during SPER: end-of-range (EOR), clamshell, and regrowth-related defects. Regrowth-related defects look like hairpins, clamshell defects are a line of defects extended horizontally across the sample and are created when the two advancing fronts meet, while the EOR defects are furthest from the surface, and consist of rod-like $\{311\}$ and dislocation loop defects.³⁴ The EOR defects have been well studied.^{36,38} Defect evolution both before and after SPER is important because defects can influence dopant motion and mobility within the crystal.¹⁷ These defects directly affect dopant electrical activation, without which the semiconductor could not be used as an electrical device.

Simulation Process Tools

Many computation methods have been used to model aspects of defects in Si. This is important because the cost of creating and testing devices for Si is expensive, and would be more so for devices made from Ge or C. Additionally, the development of physics-based models that accurately describe defect evolution can be assimilated into process simulators, which have become an essential step for device optimization.^{39,40} The computational methods that have been

used to model defects are ab initio, molecular dynamics, kinetic Monte Carlo simulations and continuum models.

Continuum process simulators. By far, the physical based continuum process models are the most useful to industry due to the fact that the models are computationally less expensive than other techniques.³⁹ In continuum process simulators, the physics of the system is calculated as a series of differential equations for each particle type. Typically these equations are continuity equations, where each particle gain or loss is formulation in terms of its generation and recombination rates and the diffusion flux.^{40,41} The benefits of this system are that it is fast, it can model a wide range of size implants and temperature ranges and times and is able to be compared to experimental evidence.^{39,42}

The {311} continuum model solves for the total number of interstitials in the {311} defects and the total number of the {311} defects. The evolution of {311} defects unfauling into loops at the EOR damage was modeled by Avci et al.⁴³ using the Florida Object Oriented Process Simulator (FLOOPS).³⁹ Recently, Zechner et al.⁴⁴ proposed a physics based model using five reaction equations to model the formation and growth of the {311} defect over a wide range of implantations, doses and annealing temperatures. This simulation matched experimental evidence. The {311} defect is now well-modeled for a wide range of implantation regimes for silicon using the continuum process simulators.

The continuum methods are the best for industrial applications. However, these simulations are based on what can be ascertained from experimental evidence. In the case of Ge and C, little or no experimental evidence exists to be able to create a continuum model. In order to compare Si to Ge and C, a more basic model, albeit requiring a slower method with more computational power, might be needed.

Other simulation tools. For silicon, the actual mechanisms that control formation of the {311} have been attempted to be modeled at the atomic level, and these simulations might prove useful in comparing the three elements of C, Si and Ge. The {311} defect has been modeled using first principals calculations (ab initio). From these calculations, the formation energy for the {311} defect was determined to be 0.7 eV, and additionally, growth in the [011] direction was predicted from the model.⁴⁵ This is much lower than the experimentally determined value of 3.6 eV. The ab initio authors estimated the smallest stable planar {311} defect contained approximately 40 interstitials with a width of 19 Å and a length of 27 Å.⁴⁵ Although these simulations can give insight into the atomic interactions of defects, the simulations are not practical for use either for industrial applications or for comparing to experimental results.

The structure and mechanism of the {311} defect has also been studied using the tight-binding (TB) method. These calculations determined that the {311} defect could be calculated as stable with small bond distortions and with smaller energies per interstitial atom than a self-interstitial in bulk Si.⁴⁶ However, due to the computational power required, TB studies only analyze approximately 10^3 - 10^4 atoms and are not comparable to experimental results.

These methods provide insight for making simulations of larger atom counts more accurate. Physical parameters determined from AB and TB studies can be fed into continuum and kinetic Monte Carlo simulations. Kinetic Monte Carlo (KMC) computer codes take the dynamics of defects (such as diffusion, emission from cluster, and recombination) into account. These types of simulations have also been called atomistic simulations and take into account rate theory and atomic diffusion. The amorphization and recrystallization processes in silicon have been modeled at the atomic level. KMC codes differ from continuum models in that they keep track of the location of every frenkel pair provided by binary collision approximation simulations

(such as SRIM)²¹ or molecular dynamics calculations. Parameters that define the atomic interactions (such as diffusivities, binding energies, capture radius) are all derived from ab initio or MD calculations. However, as KMC simulations can only model up to a million atoms at approximately 10^{-3} seconds,⁴⁷ these are not appropriate for industrial use. However, since atomistic simulations rely on physical parameters such as bond energy, and simulations in silicon and carbon have already been used in atomistic simulations of grain boundaries,⁴⁸ it is theoretically possible to simulate the formation of a {311} defect in a lattice of either Si, Ge or C with an atomistic simulation.

Relevant Literature for Ge, SiGe, SiC, and C

Germanium – Defects and Amorphization

Germanium was the original base material in the first transistors, and was the dominant material for semiconductors in the 1960s. Due to its inability to form a stable native gate oxide, Ge was surpassed by Si as the semiconductor material of choice. Ge's native gate oxide dissolves in waters, and its growth is non-uniform and sensitive to humidity. However, due to the development of high-k dielectrics instead of native oxides for use as a gate material, Ge is being seriously considered as an alternative channel material for mainstream CMOS devices. Although defects in Ge have not been as thoroughly studied as in Si, Ge is currently being used in the SiGe alloy to strain the channel (which increases carrier mobility) in current generation transistors. Of the group IV elements, Si and Ge are the only two which are fully miscible in each other, and form a solid solution across all compositional percentages. Research so far indicates that ion implantation and dopant interaction in Ge seems to be fundamentally different than Si.¹

Defects in Pure Ge

Defects have been viewed in Ge for as long as Si, but due to its comparative lack of interest, the study has not been as intense. The {311} defect has nevertheless been seen in pure

Ge for decades. Early studies focused on electron irradiation in Si and Ge, while later studies have focused on light ions. An example of a recent {311} defect created in pure Ge was shown in Figure 1-2. In that example, the Ge was implanted with H⁺ (15-80 keV, 5×10^{15} - 7×10^{16} cm⁻¹) and annealed at temperature between 280-400°C for 30-60 minutes.¹¹

Electron irradiation. Electron irradiation has produced the {311} extended defect in Ge.^{10,29} Electron irradiated Ge showed small interstitial loops on {311} planes, which grew in the <110> direction upon annealing. At 450 °C for ten minutes, the defects began to transform, and became perfect dislocation loops when the ten minute anneals reached 500 and 600 °C.¹⁰ In a separate study, rod-like defects along the {111} and {311} planes were also seen in Ge electron irradiated at temperatures between 400-500 °C along with defects found in Si irradiated at 650-700 °C.⁸

Hydrogen (H) and helium (He) ion implantation. Ion implantation of H⁺ has also produced the {311} extended defect in Ge. In 2005, Akatsu et al. studied the extended defects after H⁺ implantation into pure Si and Ge (5×10^{15} H⁺cm⁻² and 7×10^{16} H⁺cm⁻² at 50 and 80 keV).¹¹ After annealing at temperatures ranging from 280 – 400 °C and times between 30-60 minutes, a large density of {311} defects were observed in Ge but not in Si. The Ge formed spherical nano-cavities as well as the {311} defect, but these nanocavities were not observed in Si either. This was attributed to the differences in chemical and physical interactions between the hydrogen ions and the respective crystal.¹¹ However, previous knowledge of Si defect evolution shows that microstructural evolution in Si is unusual at temperatures lower than 400 °C; therefore, a direct comparison at these temperatures, as compared to the melting point of each material, is a poor comparison.

In addition to H, ion implantation of He has produced the {311} defect in pure Ge. Hutchinson et al. implanted Ge with 1.23 MeV He ions (1×10^{16} He⁺/cm²) at room temperature, performed no anneal, and observed voids (probably He bubbles) and {311} defects. A model was suggested explaining the development of the {311} defects incorporating hexagonal Ge, 5, 7 and 8-member rings.¹²

Additionally, rod shaped defects and {311} defects were also observed when implanting He⁺ into Ge at a dose of 1×10^{16} cm⁻² at an implant temperature of 20 °C and at 600 keV, after a 12 minute anneal at 640 °C. These defects lack the rigid zigzag pattern normally seen in Si. These defects were observed for all annealing temperatures between 450 °C and 650°C; however, above 550 °C the rod-shaped defects began to turn into dislocation loops.^{49,50} Supposedly, rod like defects, along the {111} and {311} planes, were also seen in Ge implanted with He ions at a dose of 1×10^{16} at 500 keV with no anneal, however, no micrograph was provided. The {111} rod like defects were attributed to the split <100> interstitial configuration.⁸

Amorphization, Regrowth and Lack of EOR Damage of Ge

All of the above implantation experiments in Ge were below the amorphization threshold. Ge will amorphize, as does Si, and will fully regrow at temperatures around 400°C. The regrowth rate of Ge is approximately 2 Å min⁻¹ at 350°C and 13 Å min⁻¹ at 380°C.⁵¹ Unlike Si, {311} defects resulting from EOR damage for amorphizing implants has not been reported. In 2005, Chao reported amorphizing Ge with a 45 keV, 1×10^{15} Ge⁺cm⁻² ion implant into pure Ge, resulting in an amorphous layer 1700 Å deep. No EOR defects were reported upon regrowth.⁵² Satta et al. did not observe any EOR damage in Ge after a 40 keV implant and SPER, either.⁵³⁻⁵⁵

Swelling of the crystal is associated with amorphization due to a decrease in density in the amorphous layer. The swelling in Ge was measured by step height versus implant temperature during 1 MeV Ge⁺ implants into Ge.⁵⁶ For doses of 1×10^{15} Ge⁺ cm⁻², and room temperature

implants, the crystal swells approximately 2%.⁵⁶ Non-intuitively, ion-implantation can also assist with crystalline regrowth after amorphization in Si and Ge, due to dynamic annealing.⁵⁷ With extremely high energy and heavy ions, a void-filled phase is also formed alongside the amorphous phase in Ge. For fluences exceeding 1×10^{17} atoms/cm² into pure Ge, a 30% decrease in density has been reported.^{56,58}

SiGe Alloy – Defects and Amorphization

Crosby et al. studied the {311} defect formation in Si_{1-x}Ge_x from Ge concentrations ranging from 0 to 50%. He noted that although the {311} defect was formed in SiGe alloys up to 5% Ge, it was not formed when the alloy surpassed a 25% Ge content.¹³ The decreased binding energy and the number of Si interstitials effectively increased the activation energy for {311} formation.^{41,59} Tan has suggested that a 15% or above distortion of the Si lattice would result in the destabilization of the {311} defect configuration.⁵ This would mean that a 16-20% Ge content would be required to destabilize the {311} defect.⁶⁰ Recently, vacancy nanoclusters have been detected in ion-implanted SiGe. These clusters have been found using Copper (Cu) gettering and positron analysis techniques. The vacancy clusters are located near the surface in SiGe with Ge percentages of 10-30%.¹⁴

Amorphization is a phenomenon by which the crystal lattice loses long range order after ion-implantation past a critical damage point. It is associated with a reduction in material density, approximately 1.5-2.1% in SiGe alloys, which causes the crystal to swell.⁶¹ Many factors influence whether amorphization will occur, including implant temperature, dose weight, mass of the ion, mass of the target atoms, energy of the ion and dose rate. In SiGe alloys, the threshold for amorphization is noted to decrease with increasing Ge content.¹⁴

Ge & SiGe summary. The {311} defect has been observed in SiGe alloys under 25% Ge, and in electron-irradiated and light-element implanted pure Ge. Annealing temperatures

necessary to produce this defect are significantly lower than Si, in the 350-650 °C range. No reports of {311} defects or dislocation loops resulting from EOR damage in amorphizing implants have been reported.

Silicon Carbide (SiC)- Ion Implantation and Amorphization

Silicon carbide is a wide band-gap semiconductor, extremely hard and is being considered as an ideal material for use in high-temperature, high-power, and high-frequency applications.⁶² SiC has a relatively low electron carrier mobility ($700 \text{ cm}^2 / \text{V s}$) as compared to Si ($1500 \text{ cm}^2 / \text{V s}$) and single crystal plasma deposited diamond ($4500 \text{ cm}^2 / \text{V s}$).⁴ SiC has been used as a base material for growing CVD diamond. However, the grown diamond is not of device quality due to its polycrystalline nature. SiC has also been simulated by implanting high doses of Si into diamond.¹⁹ SiC, while a fascinating technological material, will only be briefly discussed here as it relates to the present study.

Ion implantation in SiC has been studied by experimental and computation techniques. The displacement energy (E_d) for SiC is slightly more complicated than for single-element crystals. The E_d in SiC for a carbon atom is approximately 20 eV, and for a silicon atom, 25-40 eV.⁶² Ion implantation of Si into diamond in high fluences (10^{17} - 10^{18} ions/cm²) at elevated temperatures (900 °C) have produced large grains of SiC. The low dose results in layers of epitaxial SiC stripes, while the higher dose produces large grains of SiC; however, the diamond bulk material next to the grains becomes amorphous in the process.⁶³ Others have used high-fluence Si⁺ implanted into diamond to create SiC.⁶⁴ Devanathan et al. studied the amorphization of SiC by ion implantation. It was determined that amorphization is onset after 0.2 displacements per atom (DPA) is achieved. The decrease in density accompanying amorphization is about 15%, while previous studies put the decrease at approximately $12 \pm 4\%$.⁶² Ishimaru reported the DPA for SiC was 0.5 for an elevated temperature of 350 K.^{65,66}

Diamond

Diamond, in many crystallographic forms but especially single-crystal diamond, is gaining academic and industrial interest.^{67,68} The creation of synthetic diamond was first reported in 1955,^{69,70} and like SiC, is expected to be an important semiconductor for high power and high frequency electronic applications.⁷¹ An attractive diamond quality for electronic devices is the high carrier mobilities demonstrated in single crystal plasma deposited diamond.⁷² The popularity of diamond for electronic applications became evident in the mid-to-late 1990s through the assembly of a number of symposiums in the materials research community.⁷³ Most current interest in diamond is focused on diamond films, which are a CVD-grown combination of sp^2 and sp^3 bonded C, with the possibility of H as well. Diamond is being used in MEMS devices,^{74,75} AFM tips,⁷⁶ FETs,^{71,77} Diodes,⁶⁸ pn junctions,⁷⁸ and there is also development of metal contacts to diamonds for electronic applications.⁷⁹ Currently, ion implantation of single-crystal diamond is of great interest to the MEMS community for creating single crystal diamond microstructures.

Ion Implantation in Diamond

Although TEM experiments are sparse, much is already known about ion implantation in diamond. Both natural diamonds and synthetic diamonds (created by both high temperature high pressure (HTHP) and chemical vapor deposition (CVD) methods) have been used in experiments. Since the HPHT diamonds have the same structure and defects as natural diamond,¹⁹ studies of both kinds of diamonds will be presented. In general, ion implantation into diamond behaves in a similar fashion to silicon. A few key points of interest in the literature include a debatable E_d for SRIM²¹ simulations, implant temperature considerations, and the possibility of a direct graphitization transformation after implantation over the threshold limit.

Sub-graphitizing implants and repairing anneals. The literature has reported that implant conditions that create less than approximately 10^{22} vac/cm³ will not graphitize the single crystal diamond (not film) upon annealing,¹⁶ though a recent study puts the number at 9×10^{22} vac/cm³.⁷⁵ According to Hall measurements, furnace annealing at a temperature up to 900°C appears to repair the implantation damage to the crystal⁸⁰. Kalish agreed that below the critical dose, the material will gradually anneal back to diamond, starting at annealing temperatures as low as 330 °C. The defects dissolve at higher temperatures, and for annealing above 1000 °C, the diamond crystal structure will be fully restored.⁸¹ This temperature was determined by density measurements at the temperature at which the crystal restores its original density after annealing.⁸¹ Additionally, it is reported that damage to the lattice can be repaired almost immediately by modulating the implantation temperature. Below a 50°C implantation temperature, vacancy and interstitial movement is inhibited. Above 50°C, interstitial diffusion begins to annihilate vacancies, and above 500°C, vacancies diffuse and begin to form extended defects.⁸² Even a perfect crystal of diamond reverts to graphite when annealed at over 1800 °C in an excellent vacuum.⁸³

Activation energy and mobility of interstitials in diamond. As just reported, below an implant temperature of 320 K, both interstitials and vacancies are “frozen in.” Above 320 K but below 800 K, interstitials are mobile but vacancies are not. Above 800 K, both interstitials and vacancies are mobile.⁸⁴ That is why the critical dose in diamond also relies on the implant temperature.⁸⁵ It has been determined, using the work by Moorehead and Crowder as a basis then adding data from Kalish, Prawer and Prins, that the activation energy for the diffusion of an interstitial in diamond is 0.2 eV, up to temperatures of 700 K.⁸⁵ For more information of self-interstitial energy levels in diamond, see the work by Davis and Smith.⁸⁶

Doping of diamond. Vavilov implanted B⁺ into diamond in the 1970s, and (after etching off the ‘graphitized’ layer) measured the p-type conduction. Braunstein and Kalish repeated similar experiments.⁸³ Two methods proven successful when doping B⁺ are the Prins-suggested cold implantation rapid annealing (CIRA)¹⁹ and low dose drive in (LODDI).⁸⁷ The CIRA method has been used to dope diamond with B⁺, C⁺ N⁺ and O⁺.⁸⁸ Optimization of the B⁺ CIRA process led to good quality diamond and hole mobilities in excess of 1000 cm² /V s.⁸⁹

p-type doping of diamond. MeV-ion implantation has shown to be a promising method for doping of diamond. Lower energies (<640 keV) and low doses (~10¹³ cm⁻²) of implanting boron has been tried using the CIRA method, followed by hour-long anneals at 1100 °C then 10 min at 1450 °C.⁹⁰ The implantation of 2 MeV B⁺, followed by furnace annealing at 1450 °C, was used as a justification of the high pressure theory.⁸³ An activation energy of the boron acceptors was determined to be 0.372 eV.⁹¹ Uzan-Saguy later published a doping efficiency of 2% for 2 MeV B⁺ atoms at a dose of 1 × 10¹⁵ cm⁻² implanted at 77 K. No diffusion of B⁺ was observed in that study.⁸⁹ In 2004, Vogel et. al implanted mimicked the experiment, but at room temperature, implanting 2 MeV B⁺ atoms into natural diamond samples and achieved 30% activation of the implanted boron atoms for a dose of 1 × 10¹⁴ cm⁻² and 15% for a 1 × 10¹⁵ cm⁻² dose, and claimed it to be the highest at that time for ion-implanted diamond.⁹² That experiment used annealing temperatures up to 1650 °C in a furnace under vacuum. It was determined that annealing at temperatures above 1500 °C for 15 min did not improve the quality of the implanted layer, but instead decreased it. Low residual defects after the 1500 °C anneal were determined by sheet conductivity and mobility measurements.⁹² The present research performed an XTEM study of this implant regime, and the results are reported in Appendix B.

n-type doping of diamond. While boron doping has been met with some success in diamond, n-type doping of diamond is proving to be more difficult than p-type doping. Nitrogen is a n-type dopant in diamond, but lies approximately 1.7eV below the conduction band, making it a deep donor. Phosphorus, a common n-type dopant in Si, imparts four times as much damage when implanted into diamond as does boron, and this is a major problem in doping diamond. Co-doping with hydrogen has been able to increase the conductivity slightly.⁸³ Damage also has an effect; n-type conductivity has been reported in high-fluence Si⁺-implanted diamond.⁹³ The presence of defects does not seem to enhance diffusion of light dopants in diamond like it does in Si, up to temperatures of 1300 K. However, slight diffusion of boron has been reported above 1300 K.⁹⁴ Additionally, p- and n-type doping of diamond has also been performed by growing doped diamond by CVD processes.⁹⁵

Defects in diamond. The {311} defect has never been reported in diamond, even though Salisbury concluded that the {311} rather than the {111} is the normal plane for self-interstitial precipitation for all diamond structure crystals.⁷ Additionally, ion implantation has been studied in diamonds for over three decades,⁸² but reports of any kind of defect are sparse. This is because, in the past, creating a TEM sample of single crystal diamond has been very difficult, due to diamond's high bond strength.⁹⁶ TEM is the best method to pursue a number of current research questions in diamond, especially defect formation and evolution as the result of ion implantation and annealing.¹⁹ Recently, use of the focused ion beam (FIB) has led to the ability to create TEM cross sections of diamonds in a more timely fashion, and that method will be presented later in this paper.

The (100) split interstitial has been calculated to be the stable defect in diamond after ion implantation.^{81,97} Additionally, after ion implantation, intrinsic defects can be electronically active.⁸³ Electrical conduction in diamond is impeded by the high density of residual defects.⁸³

Amorphization vs graphitization of diamond. It is well known that past a critical damage value, the diamond lattice is too damaged to repair itself.⁸³ Above this critical dose, the diamond converts to a form of amorphous carbon, supposedly stable up to an annealing temperature of approximately 430°C. When the annealing temperature exceeds this temperature, the crystal begins to graphitize by forming sp² bonded nanoclusters.⁸¹ However, Prins theorized that the amorphous region was not truly amorphous, but is actually a vacancy rich diamond crystal lattice.⁹⁸ In a later paper, Prins stated that relaxation to the graphite state might occur before a real amorphization (such as in silicon) takes place.⁹⁹

In 1999, Kalish et al. reported that complete “graphitization” is reached at 600 °C (after a 20 min anneal) when conductivity becomes metallic, due to an overlapping of the localized states.⁸¹ However, the density of the amorphous layer does not equal to that of graphite until approximately 800 °C with a sharp drop in density occurring near 500 °C.⁸¹ “Graphitization” in the literature is a term that sometimes means that the electrical properties of the damaged diamond are metallic, and not that a true graphite material has formed. This process has been simulated by computational methods; molecular dynamic images of the evolution from damaged diamond to graphitic planes were demonstrated by Kalish et al.^{81,100}

Controversies in Diamond Literature

Critical dose threshold for amorphization. The critical implantation dose to effect graphitization upon annealing was originally determined to be 1×10^{22} vacancies (vac) cm⁻³ by Uzan-Saguy et al. in 1995.¹⁶ This threshold has been widely referenced in the literature. The method of determination was to implant an amorphizing dose into the crystal, and after

annealing, etch in boiling acids. The depth of etchable material, assumed to be graphite, was determined by using a buried marker layer. In 2005, Brunetto et al. theorized the threshold to be just slightly higher, at approximately 2×10^{22} vac cm⁻³.¹⁰¹ In 2006, Olivero et al. estimated the damage threshold to be approximately 9×10^{22} vac cm⁻³.⁷⁵ And Prawer noted that the threshold is extremely dependent on implantation temperature, and states that graphitization can be completely avoided for high enough implantation temperatures.¹⁰²

Displacement energy. In the original study of diamond that set the ‘graphitization threshold’ at 10^{22} vac cm⁻³, the E_d of one carbon atom was determined to be 45 eV.¹⁶ However, other values have been determined in the literature, ranging from 52 eV⁸¹ using molecular dynamics to 55 eV⁹⁸ by volume expansion methods. Using these various E_d values in SRIM²¹ simulations results in little difference in terms of projected damage range (R_d) and peak damage depth (R_p) in diamond.

Displacement spikes. Displacement spikes in diamond have been a controversy in the literature.^{83,102} Some argue that displacement spikes from the ion trajectory relax to form ‘graphite-like’ material.¹⁰² However, it has been theorized that by using MeV ions, the cap of undamaged diamond keeps the damaged layer under enough pressure so that this prevents the buried damage layer from relaxing to the graphitic structure.^{89,103} Raman studies have been used to provide justification.

Transmission electron microscopy studies of single crystal diamond. The few TEM studies that do exist have been either plan-view or diamonds thinned by oxidation thinning, and have been used to study the defects in HPHT crystals. In 2001, plan view TEM studies were done on ion-implanted natural diamond.¹⁰⁴ Yin has reported on the defects in a lab-grown high pressure high temperature (HPHT) diamond crystal studied using plan view TEM as one method.

^{96,105,106} Additional TEM studies of HTHP single crystal diamond whiskers ¹⁰⁷ and particles ¹⁰⁸ have been conducted. However, these sample preparation methods were not area selective in nature. Additionally, none of these studies looked at defect creation or evolution. Planar defects have been seen in polycrystalline diamond films, and studied by HRTEM and scanning TEM; these defects consisted mostly of microtwins.¹⁰⁹ The only reported cross-sectional TEM study of diamond seems to be by Adams et al.,¹¹⁰ who studied ion beam sputtering and damage in a single crystal diamond.

Properties of the Elemental Crystal Systems

As a comparative study between three elemental crystal systems, the current work used many published properties of three elements involved: C, Si and Ge. Some of these constants and properties are summarized in Table 2-1 for convenience and reference. Si, the most widely studied of the three systems, is listed first. In general, Si's property values are in between those of C and Ge, which makes sense as it is between the two in the fourth Group of the periodic table. It is interesting to note, though, that both carrier mobilities are actually lower in Si than in Ge and Diamond. Also listed are some references for graphite, as also being a C crystal system, and these values are used in Chapters 6 and 7 when studying the evolution of damaged crystalline diamond.

Table 2-1. Relevant properties of the Group IV diamond-cubic semiconductors and graphite.

Property	Si	Ge	Diamond	Graphite	Reference
Atomic Weight	28.09	72.61	12.01	12.01	111
Melting Point, °C	1414	938.25	4440-4773 (melting point, 12.4 GPa)	4473- 4489 (triple point, 10.3 MPa)	111 19
Lattice parameter (a), Å	5.4282	5.6580	3.567	a=2.461 c = 6.708	112, 19
Tetrahedral Covalent Radius, Å	1.17	1.22	0.77	n/a	111
Atomic Radius, pm	118	123	77	77	111
Space group	<i>Fd3m</i>	<i>Fd3m</i>	<i>Fd3m</i>	<i>P6₃/mmc</i>	19,113
Bond Dissociation Energy, D° ₂₉₈ / kJ mol	Si-Si 310	Ge-Ge 264.4 ± 6.8 Ge-Si 297	C-C 595.63 C-Si 447 C-Ge 455.7 ± 11		114
Atomic concentration, atoms/cm ³	5.00e22	4.42e22	1.76e23	1.14e23	19,113
Packing fraction for diamond crystal structure	34%	34%	34%	n/a	113
Minimum Room Temp. Energy (Band) Gap (eV)	1.12	0.67	5.4	-0.04	115 19
Hole Mobility (room temp), cm ² /V s (CRC, pg 12-82	500	1820	1400	n/a	115
Electron Mobility (room temp), cm ² /V s	1900	3800	1800	n/a	115
Displacement Energy (E _D), eV	15	15	50, 52 SiC: 20 (C) 25-40 (Si)	28	21 101,116 62

CHAPTER 3 ANALYTICAL TECHNIQUES

Introduction

Transmission electron spectroscopy is one of the best analytical techniques for comparing the defect formation and amorphization phenomena of ion-implanted carbon (C) and germanium (Ge) to that of silicon (Si), because direct imaging of the crystal is possible. The most challenging aspect of TEM analysis is the sample preparation, and therefore it shall be treated first in this chapter. Few TEM studies of C in its diamond cubic form exist, due to the historically difficult preparation technique.⁹⁶ In order to study ion-implanted diamond, the author created a technique to make relatively quick cross-sectional (XTEM) samples of diamond using a focused-ion beam (FIB). This technique was published in the *Journal of Vacuum Science Technology-A*,¹¹⁷ and its presentation won the AVS Manufacturing Science and Technology Group Fellowship Grant at the 2005 AVS International Symposium for best paper as well as Grand Prize in the Materials Characterization Poster Division at the 2006 Joint Symposium of the FLAVS and Florida Society for Microscopy.

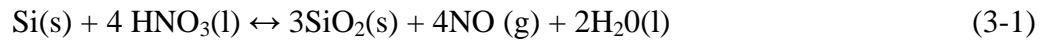
After sample preparation of all three materials has been discussed, TEM, as well as the in-situ tools of EDS and EELS, will be described. Raman optical scattering was also used to confirm the results of damage to the diamond crystal, attempting to determine amorphization or graphitization. The simulation tool, SRIM-2006 (The Stopping and Range of Ions in Matter)²¹ has been used extensively in this work to simulate the damage in each crystal created by the incoming ion implantation process. A short description of the benefits and limitations of each of these analytical techniques will be presented.

Sample Preparation for TEM

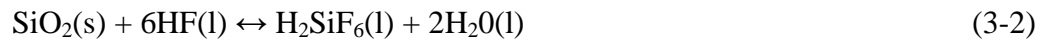
Transmission electron microscopy imaging requires samples normally less than 200 nm in thickness, and approximately 50 nm or less for high-resolution imaging. The physics of imaging, and why a thin material is required, is discussed in the next section. There are many different sample preparation techniques for different materials.¹¹² Only two will be discussed here, which are appropriate for the semiconductors Si and Ge: cross-sectional (X) TEM sample preparation by automated focused ion beam milling (FIB) scripts and plan-view (P) TEM sample preparation using chemical and mechanical polishing techniques. Then a novel method of creating XTEM samples for single-crystal diamond will be presented.

Silicon & Ge XTEM sample preparation. Using an FEI dual beam FIB, and the provided automated script for creating XTEM samples of Si, XTEM samples of both Si and Ge were produced.¹¹⁸ This is essentially a milling technique in which a source, usually gallium (Ga), ions are accelerated towards a target and sputter target ions from the sample. Mill rates can be adjusted through adjustment of the dose rate of the ion. Since the Ga ion beam also creates damage of the sample, the bulk material is first coated with carbon to protect the surface from initial views using the ion beam. Approximately 150 nm of carbon is sufficient. Once the sample is in the FIB chamber (which is under vacuum), the sample is oriented along the (111) cleave planes (in the $\langle 110 \rangle$ direction) so that the final XTEM sample will be viewed in the $\langle 110 \rangle$ direction. Platinum (Pt) is then deposited over the surface area of choice, to protect the surface from future milling steps. The carbon and Pt layers will be visible in the XTEMs presented in this work. Milling continues until a material sample approximately $15 \mu\text{m} \times 2 \mu\text{m} \times 0.1 \mu\text{m}$ is freed from the bulk. The sample is removed ex-situ and placed on a copper-supported carbon-film backed grid.

Silicon & Ge PTEM sample preparation. To view a sample from the top-down in the near surface region, rather than a cross-section, a PTEM method is used. First, a 3-mm section is milled from the bulk, and the surface is crystal-bonded to a metal chuck. The material is then mechanically polished using alumina slurry to approximately 0.2-0.4 μm thick. At that point, appropriate etch chemistries are used per each material to create an electron transparent region in the center of the 3-mm disk: for Si, a 25:75 buffered hydrofluoric acid (49% HF): nitric acid (HNO_3) solution is used, and for Ge, a 15:85 48% HF: HNO_3 mixture is appropriate.¹¹² The HNO_3 oxidizes the semiconductor, as shown here with Si:



Then, the HF etches the oxide, as shown again with Si:



This is the same mechanism responsible for HF etching glass (as it is also SiO_x), therefore, HF is always stored in polyethylene or Teflon containers. Great care should be taken with both chemicals as both are highly corrosive. After acid etching, the samples are briefly rinsed in water, air or nitrogen dried, and are ready for imaging in the TEM.¹¹²

Single crystal diamond XTEM sample preparation. Due to the difficulty in creating TEM samples from single crystal diamond, few studies have been reported.⁹⁶ In the 1960s, TEM samples were prepared from natural diamond by oxidation thinning, which is flowing oxygen at 750°C or carbon dioxide at 1350°C over the diamond substrate, thereby gas etching the crystal.¹¹⁹ However, this process does not protect the surface and is not selective of the area. Other disadvantages of this method are that the sample must be boiled in an acid mixture to remove the surface layer of carbon that forms and such high temperatures may anneal out defects present in the sample.¹²⁰ In 2001, plan view TEM studies were performed on ion-implanted natural

diamond.¹⁰⁴ Yin has reported on the defects in a lab-grown high pressure high temperature (HPHT) diamond crystal studied using TEM as one method.^{96,105,106} Additional TEM studies of HTHP single crystal diamond whiskers¹⁰⁷ and particles¹⁰⁸ have been conducted. However, these sample preparation methods were not area selective in nature. Recently, Adams¹¹⁰ et al studied ion beam sputtering and damage in a single crystal diamond.

The focused ion-beam has been used to create TEM samples in single crystal silicon and other materials faster than traditional methods.¹¹⁸ Following FIB sample preparation, ex-situ liftout is common using micromanipulation tools, but in-situ liftout is also possible and preferable for the study of ion-implanted diamond. Ex-situ liftout of diamond specimens is not preferable for two reasons: (1) the film commonly on the back of TEM grids is carbon, thus potentially compromising any EELs spectrum analysis of the ion-implanted diamond and (2) if the sample is not thin enough for high resolution work, it can not be thinned further in the future. This may become an issue if the source material has been processed further. In addition, the diamond surface must be protected prior to creating the FIB cross-section, otherwise the gallium ion beam could produce unrelated crystal damage as deep as 30 nm.¹¹⁸

This method was developed to create XTEM samples from HPHT single crystal diamonds, approximately 5 x 5 x 1 mm³, provided by The Gemesis Corporation. The diamonds in this study were ion-implanted, and after implantation, a 1000Å layer of SiO₂ was either PECVD or sputter deposited on the implanted surface, with the thermal exposure of the diamond being 310° C for one minute during PECVD deposition. The purpose of the SiO₂ layer was to compositionally separate the carbon of the crystalline diamond from the conductive carbon coating applied next. Approximately 150 nm of carbon was evaporated onto the sample, for conductivity and protection of the sample surface.

Process steps. Using a FEI Strata DB235 dual beam scanning electron microscope (SEM) and focused ion beam (FIB), a sample area was selected. A $20\ \mu\text{m} \times 2\ \mu\text{m} \times 1.2\ \mu\text{m}$ platinum box was deposited onto the chosen area. Using a 5000pA ion beam sourced by gallium, a trench six microns deep was milled away on three sides of the platinum box. Tilting 45° , an undercut using a 3000pA ion beam released the sample wedge from the substrate bulk. The Omniprobe Autoprobe 200TM in-situ lift-out system was then inserted along with the platinum gas injection needle, and placed on the corner of the sample. Platinum was deposited to attach the sample to the needle tip. The sample was then lifted out and retracted with the Omniprobe needle, as shown in Figure 3-1. The bulk sample was then removed from the chamber. An Omniprobe copper grid was inserted and adjusted in the FIB. The platinum needle and the Omniprobe needle, with sample still attached, were reinserted into the FIB, maneuvered to the copper grid, and attached to the grid with platinum, using a 300 pA ion beam. Once attached, the Omniprobe needle was cut away from the sample using a 5000 pA focused ion beam. Both the platinum needle and the Omniprobe needle were then retracted. At this point, the sample was approximately $15\ \mu\text{m} \times 2\ \mu\text{m} \times 2\ \mu\text{m}$; the thickness of the sample is shown in Figure 3-2(a). Tilting the stage normal to the ion column, the sample was thinned, first using a 300 pA focused ion beam, then 100 pA and final thinning was completed with a 50 pA beam. All ion beam energies described here were 30 keV. The sample was thinned from a $+1^\circ$ and -1° to normal, and alternating scan rotation setting of $+1^\circ$ and -1° , so that the end of the sample would be thin moving to a thicker (approximately 200 nm) region at the base section attached to the grid. Figure 3-2(b) shows the thickness of the sample after the thinning process, approximately 50 nm toward the end, and approximately 200 nm near the base (area attached to grid). The sample can then be viewed in the TEM without further processing.

Results of the method. The single crystal diamond TEM samples produced by this method have been imaged in both regular resolution TEM and high resolution TEM (HRTEM) with good results. Figure 3-3 shows an image obtained on a JEOL TEM 200 CX clearly showing the layers of platinum, carbon, and silicon oxide above the diamond crystal, and also shows the implant damage from the 1×10^{14} Si/cm² dose as it was implanted (without any anneal). Figure 3-4 (a) shows an XTEM image from a damaged diamond implanted with 1MeV, 1×10^{14} Si⁺/cm², and annealed for 10 minutes at 1050 °C. Selected area diffraction imaging is shown to be possible from the heavily damaged region [Fig. 3-4(b)] as well as the bulk undamaged region [Fig. 3-4(c)]; both SADP show the characteristic pattern of a diamond-crystal structure as viewed in the <011> beam direction. The method also produces good results when imaged under HRTEM conditions, as shown in Figure 3-5. As carbon is a less massive ion than Si or Ge, a clear on-axis HRTEM image is more difficult to obtain due to its smaller atomic size. However, individual rows of atoms are able to be imaged even in a heavily damaged region of a diamond implanted at 77 K with 1 MeV, 1×10^{15} Si⁺/cm². This process does indeed allow all TEM analysis as in traditional cross-section techniques.

Advantages of method. In creating these TEM samples, the total time per sample was less than three hours, a significant reduction compared to traditional sample preparation techniques. In addition to the time savings, another advantage over traditional sample preparation methods that is particularly good for rare substrate material like single crystal diamond is that very little material is needed, and the source of the sample can be reprocessed, increasing research efficiently and controlling costs at the same time. This method differs from other FIB methods by accounting for the nuances of analyzing single crystal diamond. Carbon coating is often used to make insulating and semi-conducting samples conductive for use in the FIB. However, as the

point of this research will be, in part, to study the phase transformation of crystalline diamond, having a carbon layer deposited directly onto the diamond (carbon) substrate could compromise characterization methods such as electron energy loss spectroscopy (EELS). To avoid this compromise, a layer of SiO₂ was deposited to differentiate the two layers. The top layer, in black [Fig. 3-3], shows the platinum deposited to protect the surface from the Ga ion beam milling currents. The three layers of carbon coating, which protect the surface from the Ga ion beam damage, are clearly visible beneath the platinum. The next layer is silicon oxide, deposited to separate the carbon deposition from the carbon sample. Finally, the HPHT single crystal diamond is visible with the implant damage appearing as a dark band. Other FIB sample preparation methods choose not to use in-situ lift out, but instead use an ex-situ micromanipulation technique. This method involves removing the sample from the FIB after it has been released from the bulk, and then transferring the sample from the substrate to a grid by static forces. However, the grid is often backed by a carbon film. If this method were used for the single crystal diamond, characterization methods such as EELS could again be compromised due to the presence of carbon film behind the carbon sample. In addition, the precision of this method allows accuracy and easy variation in the orientation of the cross-section fabricated. This can be an issue since the traditional orientation of a silicon substrate, i.e. (100), is not always known for single crystal diamonds produced via the HTHP method. Site specific plan view samples are possible but require a different technique, and will not be discussed here.

Possible improvements to method. Although this method has proved sufficient, it can be improved. HRTEM lattice images do show that the diamond lattice can be observed; however image resolution can be improved by using lower ion beam energy on the final thinning cuts to impart less damage from the Ga ion beam. This method used a 30 keV beam during the entire

thinning process. A direct 30 keV beam, according to SRIM (using a displacement energy of 45 eV per carbon atom¹⁶) created a damage peak at approximately 15 nm. However, the thinning beam was not direct on, but only at a glancing angle, so the damage can be assumed to be less. Two characterization techniques were additionally used to determine that FIB damage was kept to a minimum. HRTEM showed that, even on the $1 \times 10^{15} \text{ Si}^+/\text{cm}^2$ implant, the sample stayed crystalline throughout its entire damaged region. Additionally, electron dispersive x-ray spectrometry (EDS) showed Ga (the ion used in this FIB process) was highly present in the platinum deposition layer (as is to be expected) but only in background amounts in the rest of the sample. Although these methods show that the Ga ion beam did not do extreme damage, even less damage could be achieved by switching to a lower energy ion beam for the final thinning cuts. For example, a direct 5 keV Ga ion beam would have a damage peak only 5 nm into the diamond lattice (according to SRIM²¹) as compared to 15 nm caused by a direct 30 keV beam. Additionally, oxygen gas FIB accessories, available from FEI, would allow for faster mill rates.

Transmission Electron Microscopy

The sample preparation process for transmission electron microscopy (TEM) is challenging (as discussed in the last section). TEM provides high lateral spatial resolution, as high as 0.2 nm point-to-point for some instruments. Image and diffraction patterns may be obtained from the same sample. The signals used in image and diffraction modes are also used in other TEM in-situ characterization tools such as EDS and EELS. The TEM has an incredible range of magnifications, from 50 to 10^6 increase in magnification, made possible by the small wavelength of highly-energetic electrons. Thin samples insure few scattering events to the probe electrons, making signal resolution quite accurate.^{112,121}

Electrons, normally in the energy range of 100-400 keV, are generated by either a field emission gun or a tungsten filament. Using electro-magnetic focusing lenses, a beam of coherent

and ideally monochromatic electrons is focused to a thin foil sample.¹²¹ Upon passing through a solid sample, the electrons interact with the foil in a number of ways, as shown in Figure 3-6.¹²² For TEM, the elastically scattered electrons (Bragg scattering) generates the bulk of the signal used for imaging and diffraction pattern generation. The principles of image and diffraction pattern creation in the TEM are based on Bragg's law of diffraction:

$$2d \sin \theta = n\lambda \quad (3-3)$$

where d is the inter-planar spacing (listed in Table 2-1 for the crystal systems used in this study), θ is the diffraction angle, n is an interger and λ is the wavelength of the incident electron.¹²² For diffraction patterns, the intensity and distribution of the diffracted spots provides information such as lattice type, the lattice constant (listed in Table 2-1 for the crystal system used in this study) and crystallographic orientation.¹²⁰ The planar spacing (d) can be determined for a particular crystal system by using the lattice constant (a) and Miller indices (h,k,l) as shown:

$$d = \frac{a}{\sqrt{h^2 + k^2 + l^2}} \quad (3-4)$$

The diffraction patterns for the diamond crystal systems, like Si, Ge and carbon in the diamond crystal structure, are shown in Figure 3-7; the pattern arising from looking at a (001)-surface oriented plan view is shown in Figure 3-7(a), and from a (011)-oriented cross section is shown in Figure 3-7(b). The diffraction pattern for hexagonal crystal structures is shown in Figure 3-7(c) and (d), which both contain the most intensely diffracted plane in the graphite crystal system, the (0002) plane.^{112,123,124} For diamond-like carbon films, TEM is a widely-used tool for differentiating between the different crystalline phases of carbon.¹²⁰ Crystalline materials will produce a spot pattern, as already shown; polycrystalline materials display a distinct ring pattern, and amorphous materials produce a hazy ring pattern.¹²¹ Normally, selected area diffraction patterns (SADP) are imaged directly from the interaction with the foil. However, in this study,

two TEM instruments were used. For imaging in the FEI 2010 TEM, HRTEM images were used to generate Fast Fourier Transform (FFT) patterns, which look like SADP and provide the same crystallographic information, but are not generated directly from electron-foil interaction. The method of generation, either direct SADP or FFT, will be designated on provided figures in this study.

In imaging mode, the TEM operator may select to view the transmitted electrons or the diffracted electrons. Using centered bright field (BF) mode, only the transmitted electrons will be viewed on phosphorus screen. Therefore, areas of the crystal that have scattered electrons due to irregularities in the plane will appear dark, such as damaged crystalline regions or defects. BF TEM is useful for measurements (because the sample is not tilted). In weak-beam dark field (WBDF) mode, the sample is brought to a two-beam condition, so that only a certain plane is aligned to the transmitted beam. WBDF TEM microscopy is most useful for imaging defects in the lattice.¹¹²

One of the benefits of TEM is that small sample sizes may be used, which is extremely beneficial when working with rare HPHT diamond crystals. Additionally, crystallographic information may be obtained and correlated with the imaged samples, as will be shown not only with SADP but also EELS analysis. The major drawback to TEM analysis has already been discussed in detail: the intense effort involved in making a sufficiently thin (less than 200 nm) sample. Another drawback of TEM imaging is that three-dimensional data provided by scattered electrons is projected onto a two-dimensional phosphorus screen, giving TEM little field of view. Three dimensional data must be derived from tilting the sample or adjusting the focal point to different depths in the thin foil.¹¹² Additionally, diffraction techniques are not sensitive to small

amounts of amorphous material, and therefore other techniques such as Raman and EELS must be used to confirm the presence of amorphous carbon.¹²⁰

Energy Dispersive X-Ray Spectroscopy

Energy-Dispersive X-Ray Spectroscopy (EDS) systems can detect X-rays from all the elements in the periodic table above beryllium if sufficient quantities are present, approximately 1-2% by weight. Therefore, it is an excellent tool for detecting chemical species. The main advantages of an EDS system are its speed of data collection and ease of use.¹²⁵ The main disadvantage for this study is the weight percent detection limit: dopant atoms and background nitrogen (in the diamond samples) were present below the resolution of the EDS system. EDS systems are present in many electron column instruments; for this study, an EDS system attached to an FEI 2010 TEM was used.

EDS uses the X-ray signals produced from high-energy electron interaction with a solid, as shown in Figure 3-6. X-rays are produced as a result of ionization of an atom where an inner-shell electron is removed during the interaction with the electron. In order to return the ionized atom to its ground state, an electron from an outer shell fills the inner-shell spot, and in the process, must release energy equal to the difference in potential energy between the two shells. As shown in Figure 3-8, the excess energy (which is unique to each atomic transition) is released in the form of a characteristic X-ray [Fig. 3-8(a)] or an Auger electron [Fig. 3-8(b)].¹²² In the case of electrons with many filled shells, the ejection of one electron from an inner shell may begin a cascade which produces many signals from a single electron-atom interaction.¹²⁵

For this research, EDS was used to confirm two experimental parameters: first, that a deposited oxide layer did indeed separate the carbon sample from the conductive carbon layer applied to protect the surface from the Ga ion beam during sample preparation, and second to confirm that the Ga ion beam did not deposit Ga ions in the surface layer of interest.

The layer of silicon dioxide (SiO_2) was deposited on the surface of the crystal, either by plasma enhanced chemical vapor deposition (PECVD) or e-beam sputtering. The PECVD SiO_2 adhered better to the crystal surface than the sputter deposited layer; however, at high temperature annealing cycles, the PECVD layer would flake off. The main drawback of the PECVD layer was that it exposed the sample to a thermal budget of 310 °C for 3 minutes. For diamond and Si, this is a relatively low thermal budget as compared to their melting (and in the case of silicon) regrowth temperatures. However, this was an issue for the Ge samples which show some defect evolution and regrowth in the 300-400 °C range. Sputter deposition was performed at room temperature in the Benton Clean Room Laboratory at the University of Florida. However, it flaked off the sample after even initial annealing sequences. In order to characterize the existence of the SiO_2 layer, and to verify the aforementioned lack of Ga ion damage to the diamond crystal surface during sample preparation, energy dispersive X-Ray Spectroscopy (EDS) was employed. Figure 3-9 shows the path of the line scan across an ion-implanted diamond XTEM created using the aforementioned sample technique and the equivalent EDS spectrum. As shown, no Ga ion damage is present in the sample, and the SiO_2 layer does provide a sufficient separation distance between the carbon coating and carbon sample. The implanted Si ions or the as-grown HPHT nitrogen contaminant atoms were not detectable using EDS, due to its low concentration in the crystal.

Electron Energy Loss Spectroscopy

In this study, electron energy loss spectroscopy (EELS) was used to determine the bonding in the amorphous and crystalline regions of the ion-implantation damaged diamond. In EELS, high-energy electrons are used to probe the electronic structure of the solid through columbic interactions. EELS obtains information from either the inner-shell electrons (K-shell) or from those in outer shells (L, M, N). Electrons (normally of energies of ~5 to 2000eV) traveling

through a solid can lose energy in many ways, as shown by Figure 3-6.^{120,122} For EELS, the main losses used are plasmon scattering, single-particle electron excitations (signals from valence electrons) and ionization of atoms (signals from core electrons). For carbon, EELS can determine the changes in three bonding configurations: diamond, graphite and amorphous carbon. For very thin samples, such as CVD grown films, both low loss (signals from valence electrons) and high loss (signals from core electrons) can be used to characterize the bonding of the solid.¹²⁰ For slightly thicker samples (greater than 50 nm), low loss signal is obscured by the contribution from plasmon scattering.¹²⁶

Identification of each carbon phase comes from the high energy electron losses due to excitation of core electrons, also known as K-shell electrons, as shown in Figure 3-8.¹²² These loss peaks are observed as specifically-shaped structures in the K-shell ionization loss spectra. These appear at higher energies than the threshold energy for K-shell excitation due to plasmon creation and interband transitions. The position and shape of this region of the loss spectra is very dependant on the density of states in the conduction band (for diamond) or above the Fermi level (for graphite). These finely defined spectra can be used to distinguish between diamond, graphite and amorphous carbon, as shown in Fig. 3-10.¹²⁶ The diamond spectrum consists of three peaks, at approximately 294, 299 and 306 eV (after aligning the zero loss peak at zero). The graphite spectra has two almost identically intense peaks at 286 and 294 eV (again, dependent on the location of the zero-loss peak). Finally, the amorphous peaks occur at the same energy levels as graphite, 286 and 294 eV, however, the first peak is almost half the intensity of the second peak, as shown in Fig.3-10.¹²⁶

Reported literature says that the percentages of sp^2/sp^3 bonding can be determined by EELS, and is used extensively to characterize chemical vapor deposition (CVD)-grown diamond

films;¹²⁷ however this requires extremely thin samples on the order of 10-20 nm.¹²⁶ A drawback of the FIB method of sample preparation leaves the diamond too thick or, in the extremely thin regions, too damaged. Even though final thinning of the sample is performed using a glancing angle of the Ga ion beam to thin the sides of the XTEM sample, some lateral damage (~5 nm) can occur. Therefore, for a sample approximately 100 nm thick, as little as 90 nm may be crystalline. To confirm that the amorphous spectrum, a FIB damaged region near the tip of the diamond sample was probed. EELS analysis was performed on a FEI Technai TEM at the University of Central Florida. Figure 3-11 shows the screen-shot from the EELS software package on the Technai system. On the upper left, a BF TEM image is shown, with the line scan shown. The point at which the EELS spectrum is taken is designated by a red cross (in the FIB damaged region), and the spectrum is shown. Note the characteristic amorphous K-loss peaks (compare to the standard spectrum in Fig. 3-10). EELS data is presented in Chapter 7 to determine the bonding in damaged diamond after amorphization and before and after annealing.

Raman Spectroscopy

Raman spectroscopy has been the most widely used tool for the examination of the types of bonding present in carbon films,¹²⁰ because it is sensitive to the details of atomic arrangement and chemical bonding. Raman is able to distinguish various types of carbon: diamond, graphite, amorphous carbon and hydrogenated carbon, as well as stressed diamond (as grown on a substrate) and defect structures.¹²⁸ Raman is extremely sensitive to graphitic phases of carbon due to its high scattering centers.

Raman spectroscopy is able to detect different bonding in materials due to the relationship that each bond vibrates with only one fundamental vibrational frequency.¹²⁹ An intense monochromatic light beam, normally created by a laser, impinges on a sample. The chemical bonds are distorted by the electric field of the incident radiation. When the radiation passes, the

bonds relax and most of the stored energy is reradiated at the same frequency as the incident light. A small portion of the stored energy is transferred to the sample, which excites the vibrational modes of the chemical bonds. These vibrational energies are subtracted from the energy of the incident beam and appear as Raman lines. The separation of the Raman lines from the frequency of the incident light is a direct measure of the vibrational frequencies of the bonds in the sample.¹²⁹

Both the position and the width of the Raman peaks provide information on the type of carbon present, the structural perfection and the internal stress state, as shown in Table 3-1 which lists the various peaks and widths of Raman peaks produced by various forms of carbon.¹²⁰ The standard spectrum for natural single-crystal diamond is shown in Figure 3-12(a). The parameter of full width at half-maximum (FWHM) is a measure of the peak's width (in cm^{-1}) taken at half of the maximum intensity of the peak, and varies with the type of bonding detected. Raman spectrum taken from an unimplanted HPHT diamond used in this study is shown in Figure 3-12(b). This spectrum has the characteristic tall, skinny peak (a low FWHM of 6 cm^{-1}); however, it is shifted slightly by 2.5 cm^{-1} from the standard diamond peak. Peak shifting may be caused by a number of stresses to the crystal: foreign atoms, stress or defects.¹²⁸ For the diamonds used in this study, the shift may be due to the nitrogen impurity present in the HPHT samples, obvious due to the yellow-orange color of the diamond wafers.

In this study, the Raman system used a He-Ne Laser at 632.81 nm with a spot size of approximately $5 \mu\text{m}$, located in Dr. David Hahn's lab in the Department of Mechanical Engineering at the University of Florida. Spectra of various carbons are shown in Figure 3-13 (a),¹²⁷ and can be compared to a spectrum from a graphite standard using this system, shown in Figure 3-13(b). The spectrum contains the two characteristic peaks of graphite, as listed in Table

3-1. Note the low intensity of the signal (the y-axis) due to the opaqueness of the graphite. All Raman spectra used in this study were taken from samples being placed on a glass slide. In order to confirm that the glass slide did not contribute to the signal, the spectrum from the glass slide (unfocused) is presented in Figure 3-13(c). The low intensity and consistent background signal confirm that the glass slide did not detrimentally affect the spectra used in this study.

The main drawback of the Raman method is the spot size, especially for this study. The 5 μm spot size was larger than the band of amorphous carbon material in the diamond XTEM samples, so although cross-section analysis was performed, it must be noted that both the crystalline and amorphous regions were represented in a single spectrum. Bulk measurements of the implanted diamonds were also used to determine the crystalline or amorphous nature of the material. A smaller spot size would be ideal for analysis of the current experiment. However, nano-Raman systems are extremely new, and have only recently begun use as a characterization tool in the research arena, and may become a future tool for study of XTEM ion-implanted diamond.¹²⁷

Stopping and Range of Ions in Matter (SRIM)

The Stopping and Range of Ions in Matter (SRIM)²¹ is a widely used tool to simulate ion-implantation damage in crystals. Introduced in 1989, SRIM has been upgraded approximately every five years. The version of SRIM used for this study was the 2003 version for experiments performed before 2006, and the 2006 version for experiments since. However, no significant changes were made to the 2006 version of SRIM concerning the elements or stopping powers involved in this study.

SRIM is known to be very accurate for simulating the ion-implantation damage in crystals.¹⁹ It has been used to study the threshold damage in Si,³⁵ the threshold damage in diamond,¹⁶ and countless other studies into the phenomena arising in semiconductors after ion-

implantation. Advantages of SRIM is that it is easy to use and widely adopted in the community for estimation of ion-implanted damage. However, the limitations of SRIM may be significant, depending upon the experiment. First of all, SRIM only simulates damage into crystalline systems. SRIM does not simulate damage into an amorphous material. Also, it does not estimate when a material becomes amorphous. SRIM does not take into account dynamic annealing, which is the heating of the lattice that takes place during implantation, either due to implant temperature or heating by a high dose rate. Therefore, SRIM simulates low temperature (liquid N₂) temperature implants better than higher temperature (room and above) implants.

As few to no XTEM studies of ion-implanted diamond are reported, it was important in this study to confirm that SRIM does simulate the damage into diamond after non-amorphizing ion-implantation well, before beginning any serious experiments that used SRIM results to hypothesize about defect formation or amorphization in diamond. XTEM diamond samples would be used to compare SRIM results to the experimental results. First of all, alterations to the SRIM defaults of carbon as a target material were necessary, since the default is for the graphite form of the carbon crystal. The parameters adjusted were density (2.253 g/cm³ to 3.5 g/cm³, graphite to diamond respectively) and displacement energy, Ed (28 to 50 eV, graphite to diamond respectively). All simulations were run using the 'Full Cascade' mode. For a detailed explanation for the choice of displacement energy, see Chapter 2.

All as-implanted TEM images of the non-amorphizing implants matched well to the TRIM simulations. Figure 3-14(a) shows the plotted SRIM results of a 1 MeV Si⁺ implant into diamond, plotting vacancies, interstitials and final ion depths. Figure 4-14(b) is a bright-field (BF) TEM image of (011)-oriented diamond implanted with 1×10^{14} Si⁺/cm² at 303 K. BF TEM imaging conditions were used as to not introduce tilt into the image. The ion-implantation

induced damage band matches well with the simulation's prediction. The damage for this dose and energy seems to be centered on the projected range, rather than the damage peak. The (100)-oriented diamond with the same dose had similar results. A higher dose, $1 \times 10^{15} \text{ Si}^+/\text{cm}^2$, and its simulation results are shown in Figure 3-15(a) for a (001)-oriented diamond. The SRIM simulation is the same as it was for the lower dose, since dose is not taken into account in the implantation dose (only energy and species). However, with the order-of-magnitude higher dose, the damage band is much clearer in the on-axis (011) BF TEM image (Fig. 3-15(b)). The damage band is centered equally between the damage peak and the projected range. Although the damage is quite clear, the crystal did not create a continuous buried amorphous region. This was confirmed by HRTEM imaging (Fig. 3-15(c)), which revealed a crystalline lattice image even in the middle of the damage band. Further confirming the imaging results is the fast Fourier transform (FFT) selected-area diffraction pattern of the Figure 3-15(d) image showing a perfect diamond pattern. These results confirm that SRIM is an accurate simulation tool for non-amorphizing ion-implants into diamond, and has been used extensively in this study.

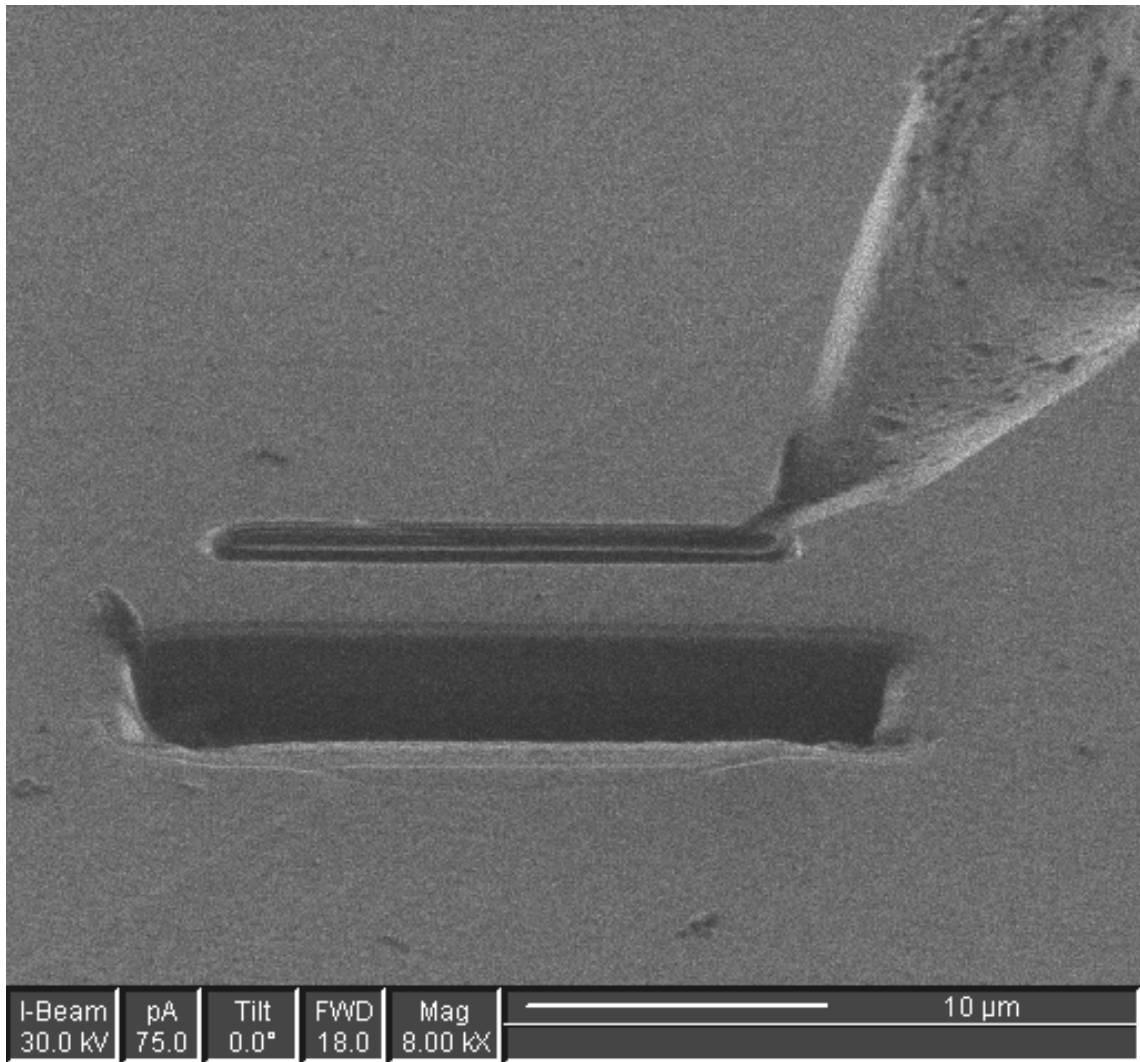
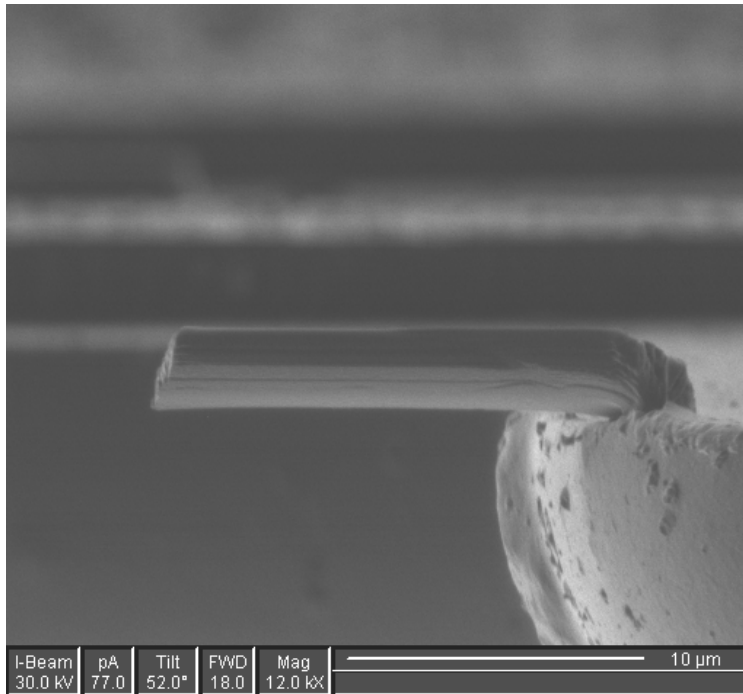
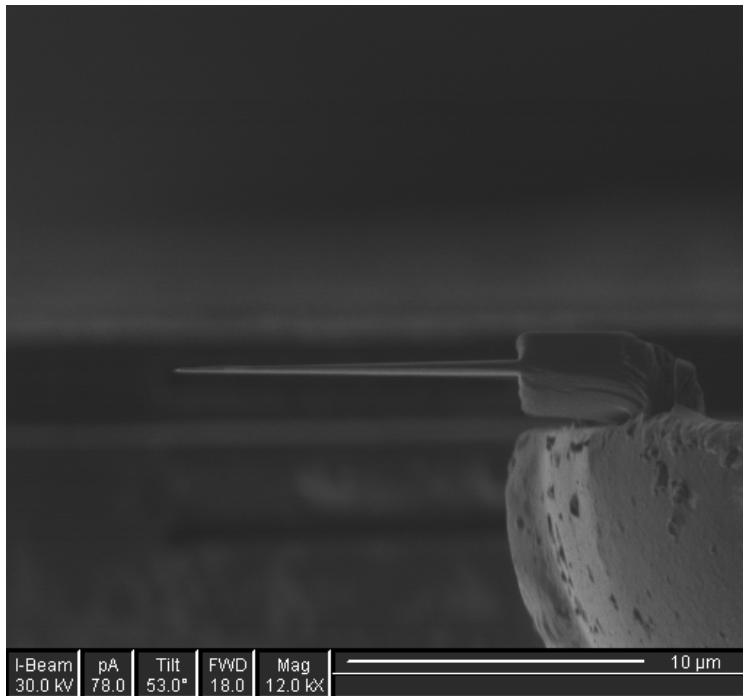


Figure 3-1. In-situ lift-out of diamond wedge, as viewed using the ion beam which is at a 52° angle to the stage. The diamond sample is approximately 3 μm deep on the far side, and the surface of the sample has been protected by a layer of platinum.



(a)



(b)

Figure 3-2. The sample thickness before (a) and after (b) the thinning process.

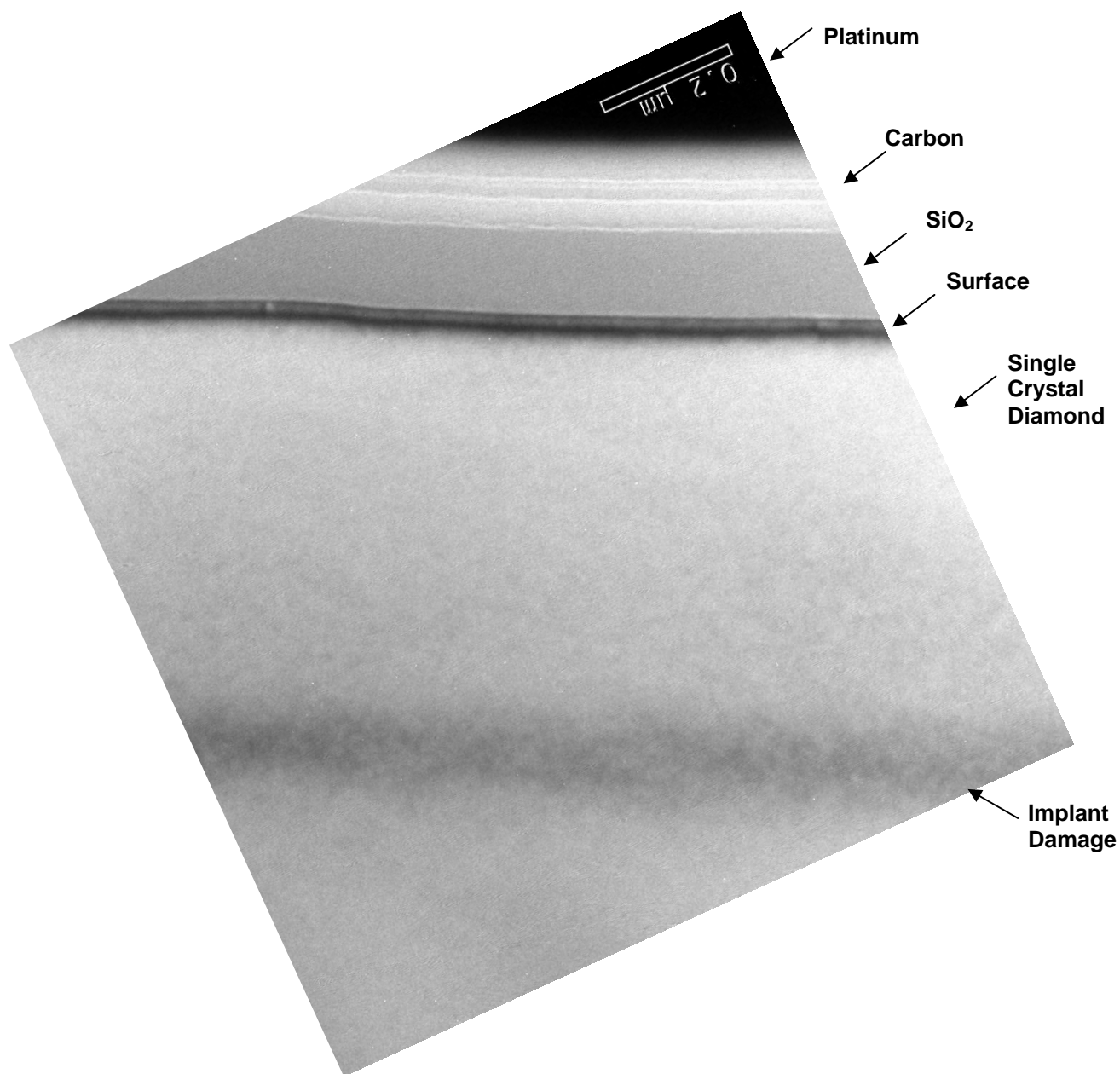


Figure 3-3. A TEM image of an as-implanted (110) single crystal diamond implanted with a 1 MeV 1×10^{14} Si⁺ cm⁻² at a temperature of 30° C.

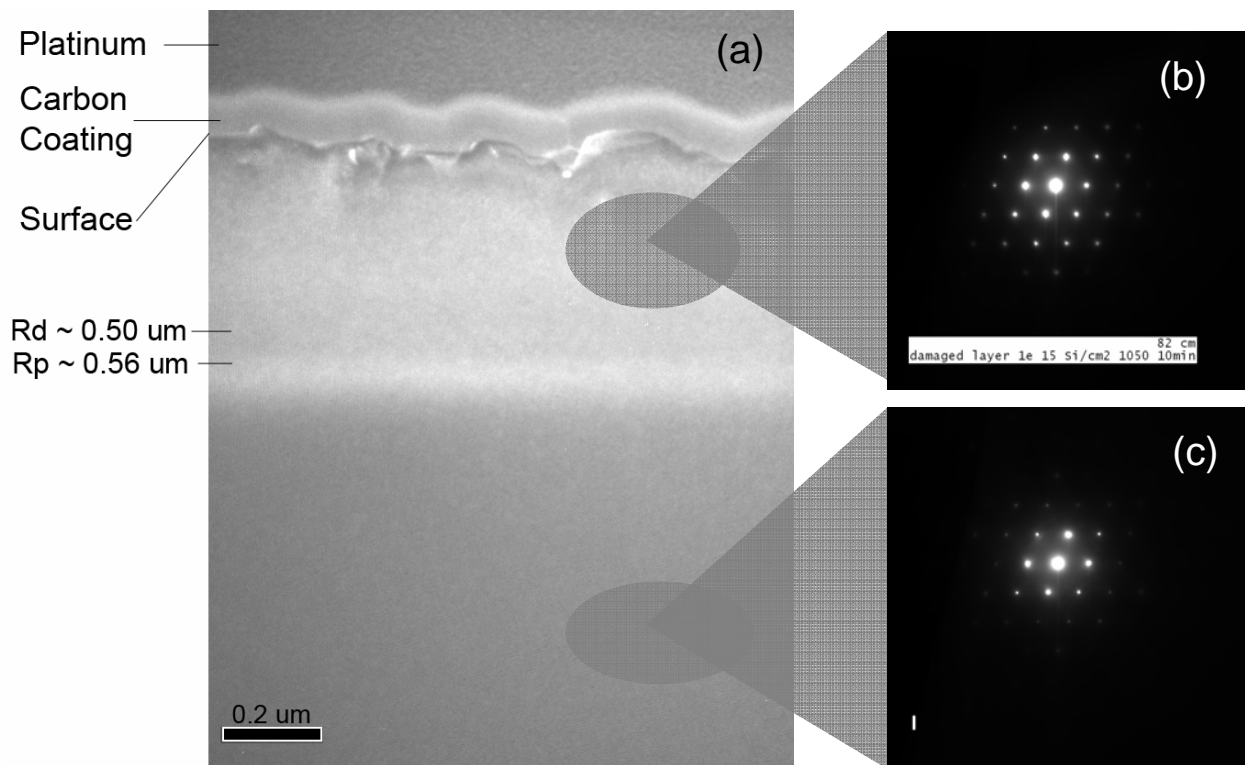


Figure 3-4. XTEM of (100) oriented diamond after a 1 MeV $1 \times 10^{15} \text{ cm}^{-2} \text{ Si}^+$ implant ($T_i = 30^\circ\text{C}$) annealed at 1050°C for 10 min: (a) XTEM image (labels denote platinum, carbon coating and surface) (b) SADP of top region (c) SADP of bulk.

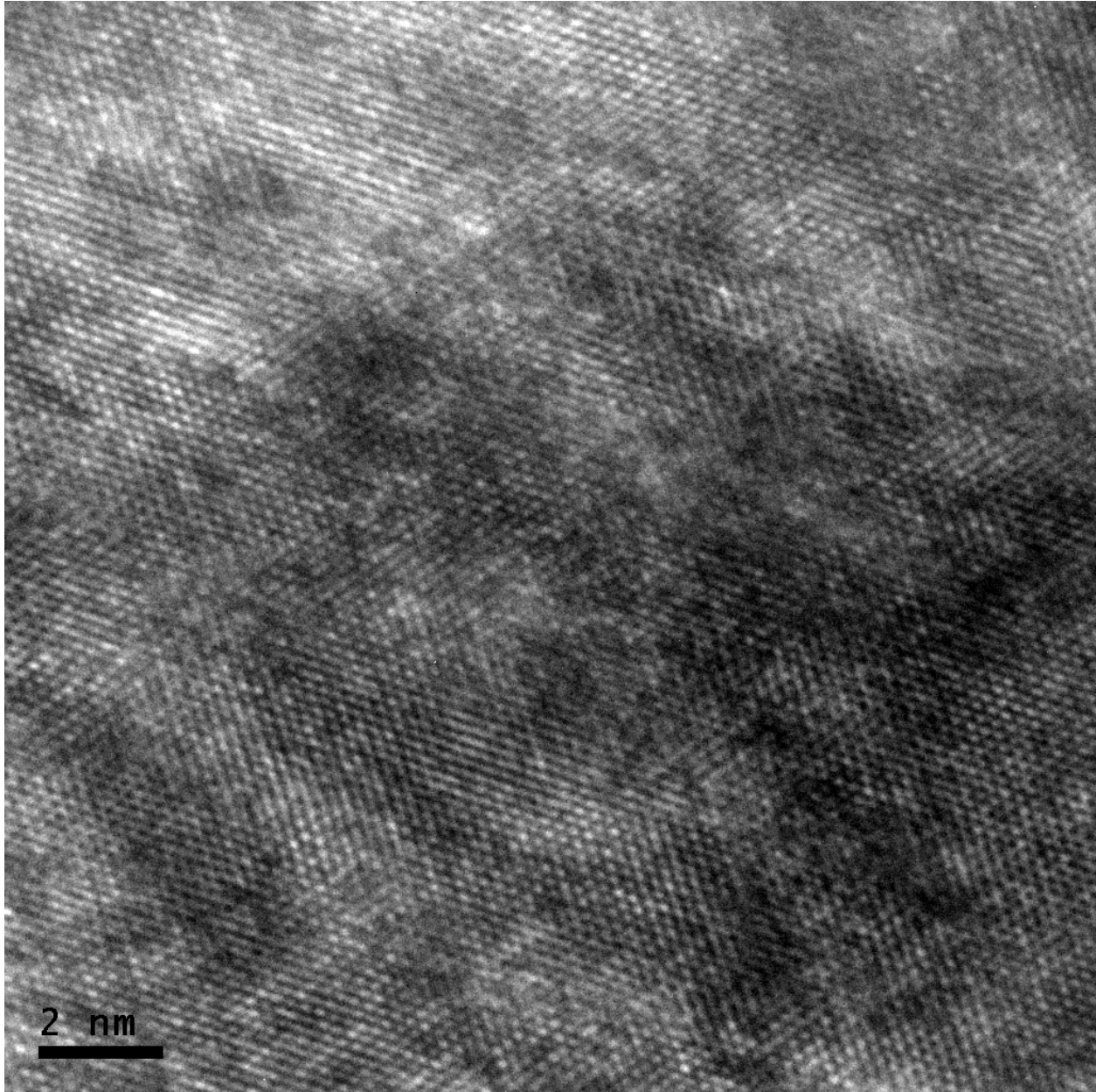


Figure 3-5. HRTEM image showing the middle of a damaged diamond layer from a (001)-oriented diamond implanted at 77 K with 1 MeV, 1×10^{15} Si^+/cm^2 . No continuous amorphous layer exists; pockets of amorphous material reside in a crystalline matrix.

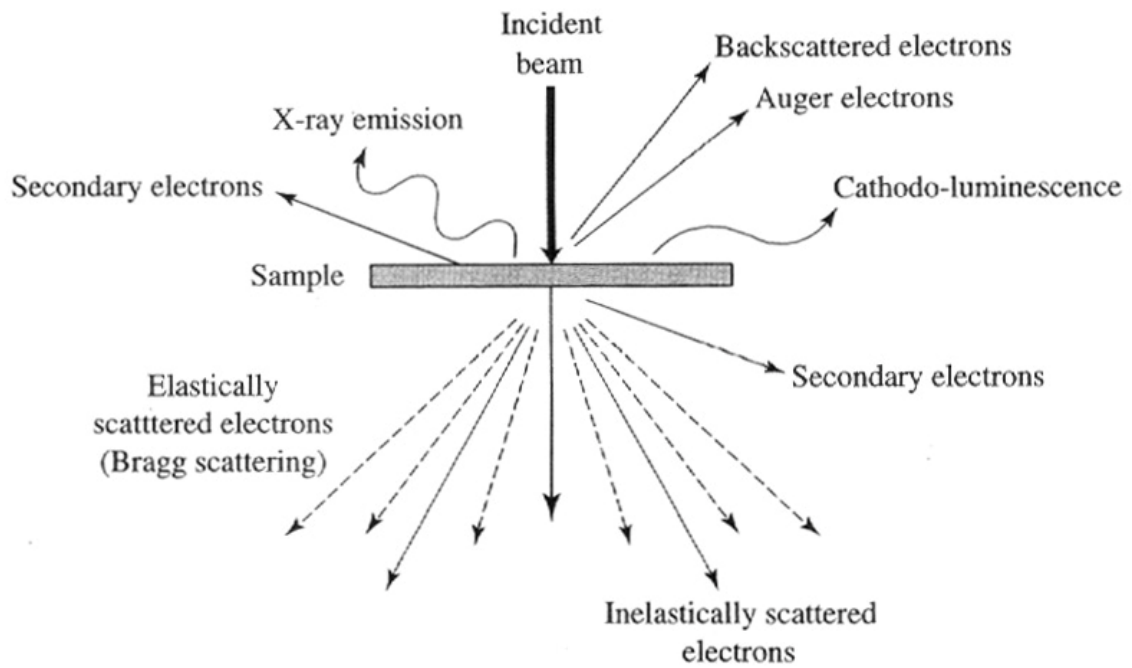


Figure 3-6. Schematic diagram of the signals created during transmission of a high-energy electron beam through a thin solid sample.¹²²

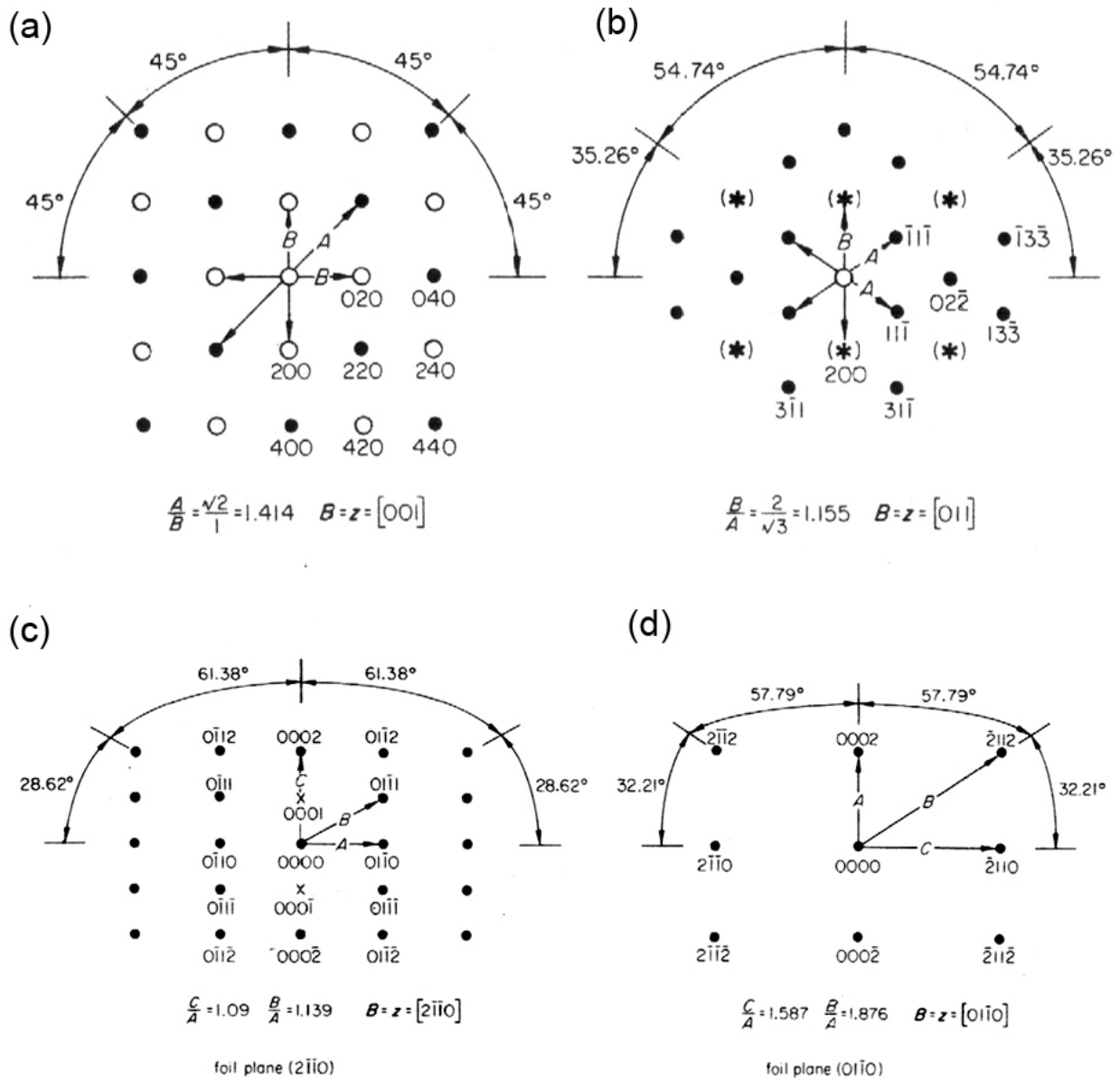


Figure 3-7. Single-crystal spot transmission electron diffraction patterns for the diamond structures (diamond, Si and Ge) for the (a) [001] and (b) [011] zone axis, and the hexagonal crystal structure for the (c) [2110] and (d) [0110] zone . Asterisks (*) indicate spots occurring in the pattern from double diffraction, crosses (×) indicate the positions of forbidden reflections, but occurring in the pattern by double diffraction, open circles (○) indicate additional weaker spots; z is the zone axis and **B** is the beam direction.¹¹²

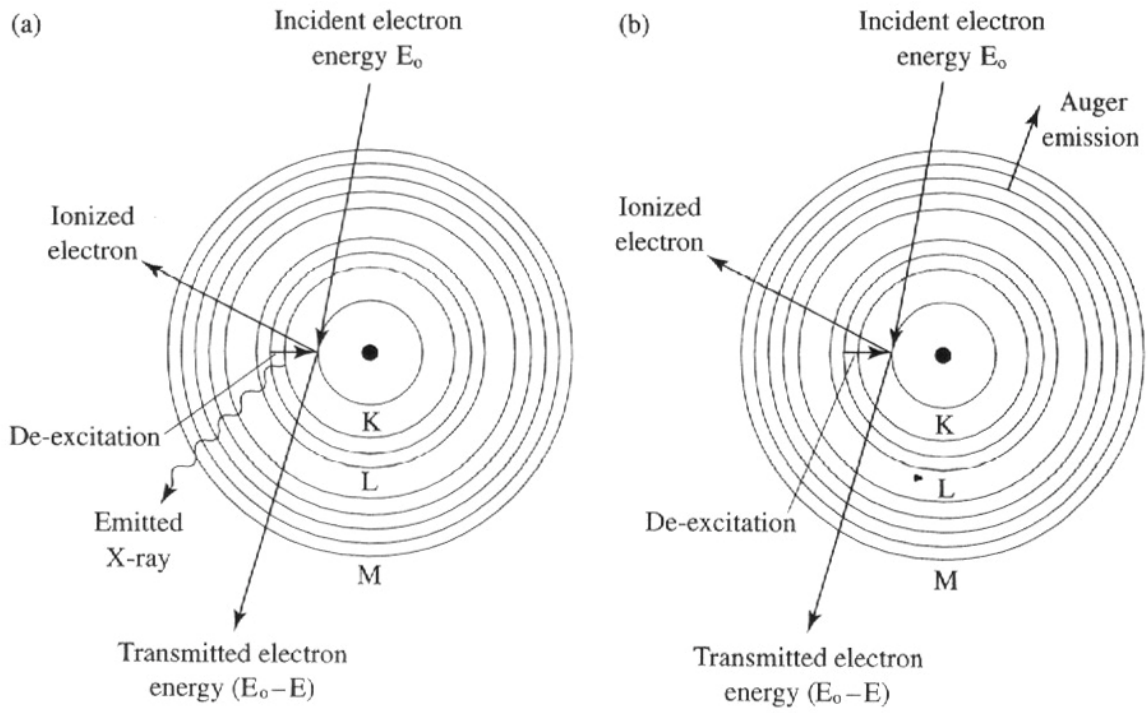


Figure 3-8. De-excitation mechanisms for an atom that has undergone K-shell ionization: (a) emission of a characteristic $K\alpha$ X-ray and (b) emission of a KLM Auger electron. ¹²²

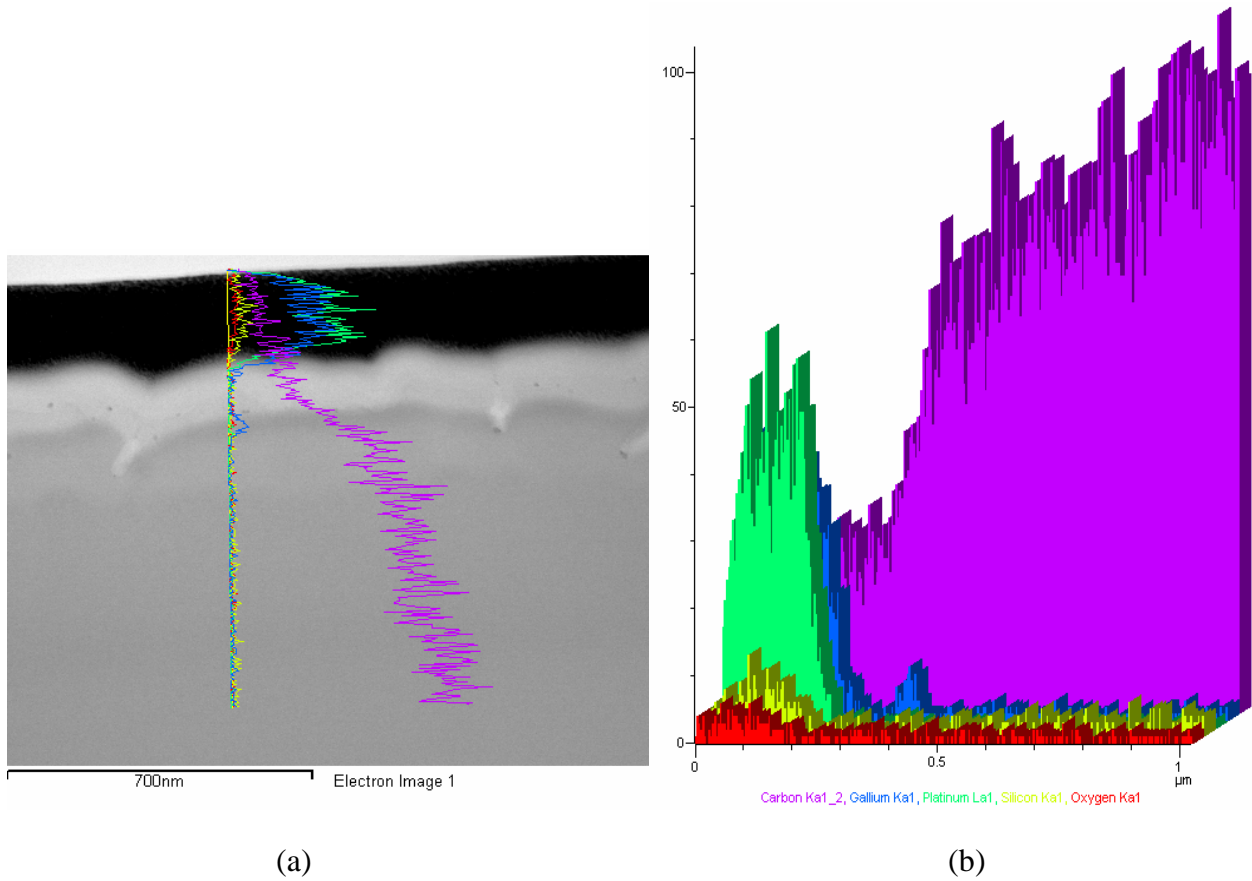


Figure 3-9. TEM and EDS characterization of sample. (a) TEM image of a (001)-oriented diamond implanted with 1 MeV, $1 \times 10^{15} \text{ Si}^+ \text{ cm}^{-2}$ at room temperature, and annealed at 1050 °C for 10 minutes, with the EDS line scan data overlaid. (b) EDS spectra of the line scan of the TEM sample showing relative counts of elemental species.

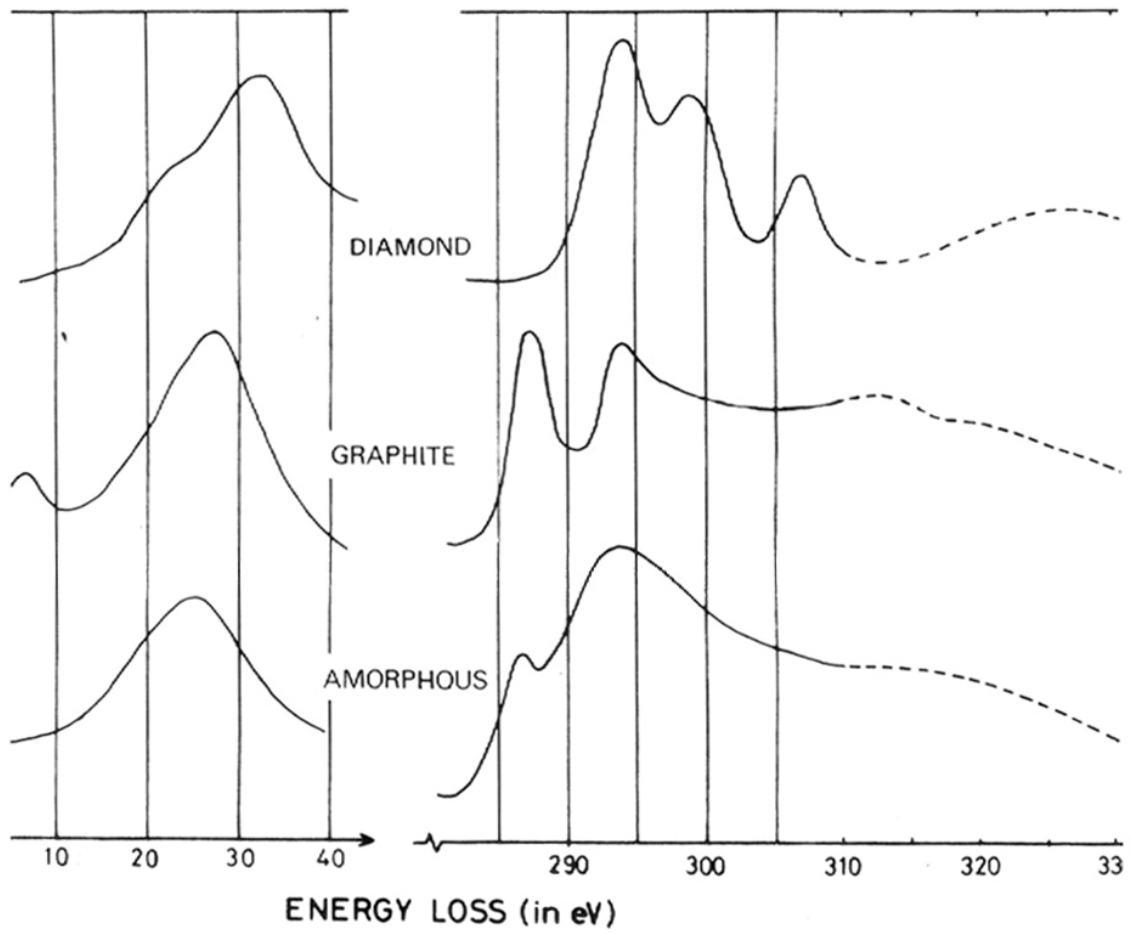


Figure 3-10. The low-loss and K-ionization regions of the energy-loss spectra of three allotropes of carbon as detected using an EELS system.¹²⁶

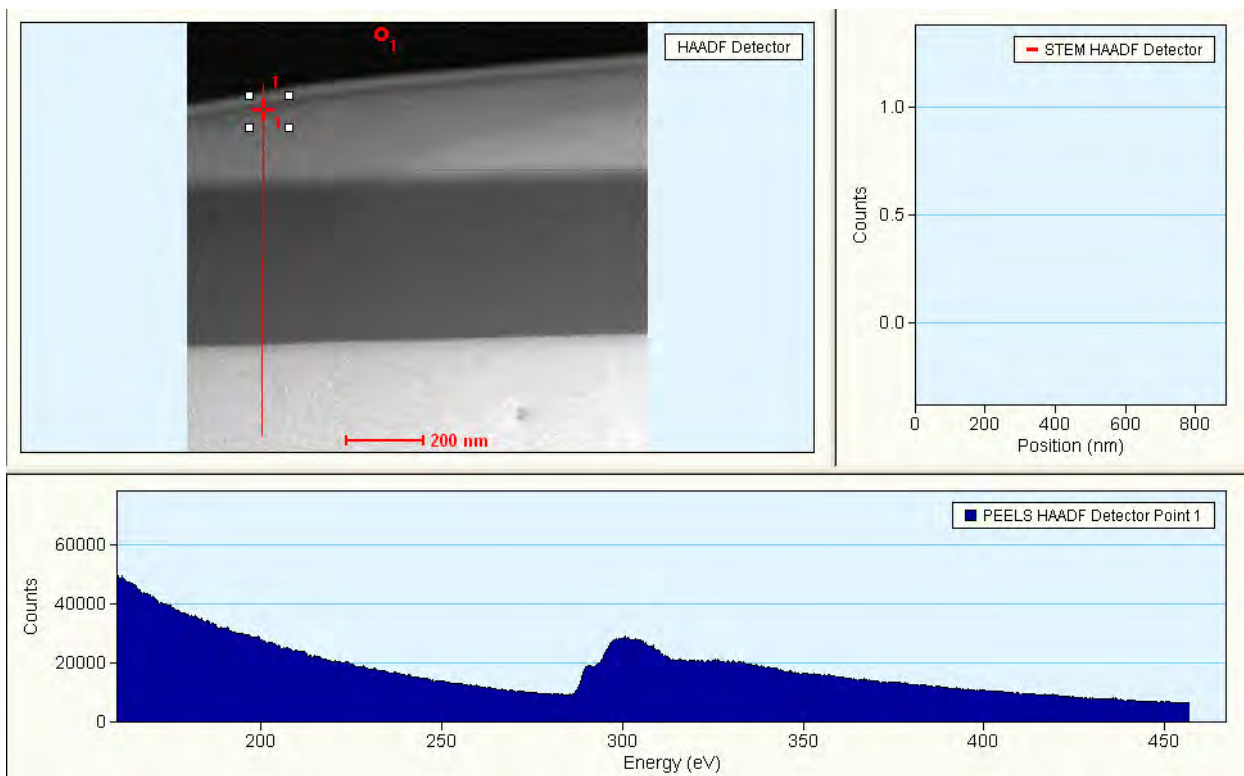
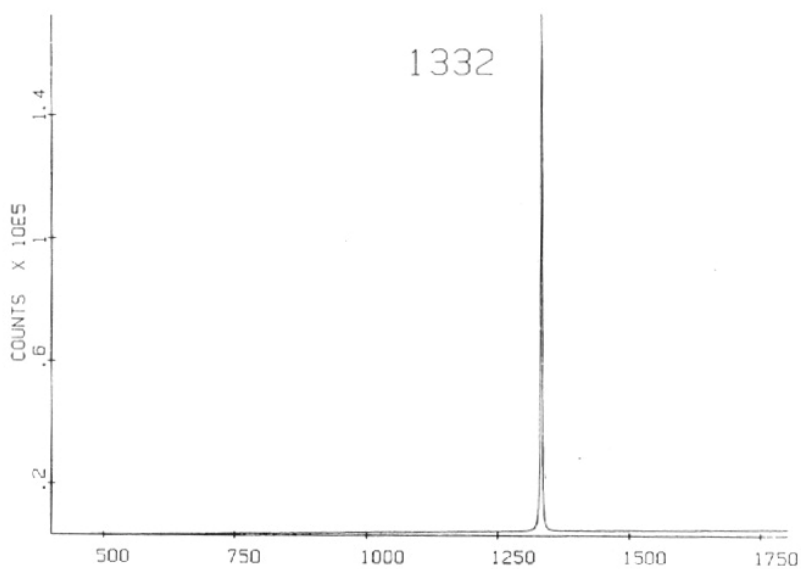


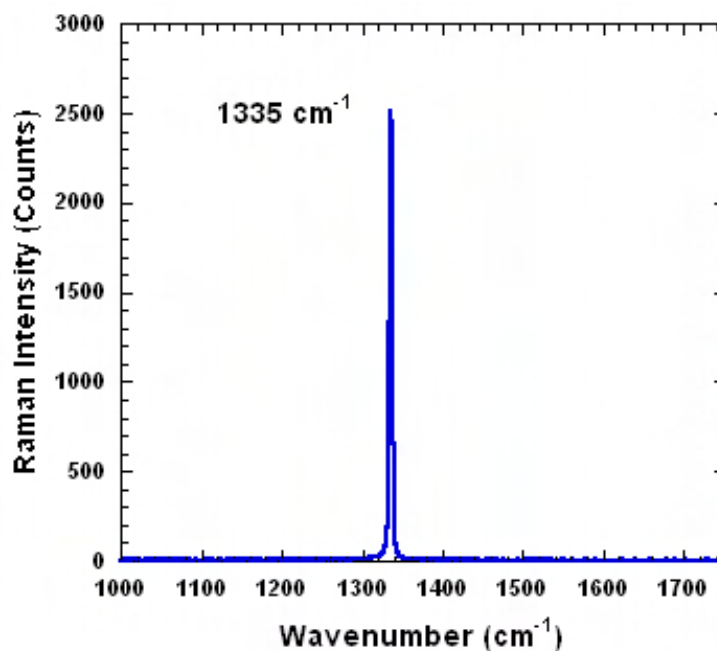
Figure 3-11. Screenshot of data displayed from the EELS system used for this study.

Table 3-1. Major Raman peaks from diamond, graphite and related materials. ¹²⁰

Peak Position	Type of Carbon	Description
$\sim 1140 \text{ cm}^{-1}$	Small size ($< 0.1 \text{ }\mu\text{m}$) cubic diamond	Occasionally observed in diamond films with very small grain sizes ($< 0.1 \text{ }\mu\text{m}$)
$1315\text{-}1326 \text{ cm}^{-1}$	Hexagonal diamond	Broad band, observed in shock wave produced diamond
1332 cm^{-1}	Cubic diamond	First order peak with full width at half maximum of 1.9 cm^{-1} for natural diamond
1345 cm^{-1}	Amorphous carbon	Broad band. It becomes a shoulder of the 1550 cm^{-1} band when the material is hydrogenated
1355 cm^{-1}	Microcrystalline graphite	Observed in materials with small grain sizes
1550 cm^{-1}	Amorphous or diamond-like carbon	Broad band
1580 cm^{-1}	Graphite	First order peak
2458 cm^{-1}	Cubic diamond	Second order peak
2710 cm^{-1}	Microcrystalline graphite	Second order peak
3240 cm^{-1}	Graphite	Second order peak



(a)



(b)

Figure 3-12. Raman spectra of diamond. (a) Raman spectrum of natural diamond¹²⁸ (b) Peak from bulk un-implanted diamond used in our study. Peak is at 1335 cm^{-1} with a FWHM of 6 cm^{-1} , which is a 2.5 cm^{-1} shift from the reported diamond peak. The shift may be due to the nitrogen impurity (giving rise to the yellow-orange color of the diamond).

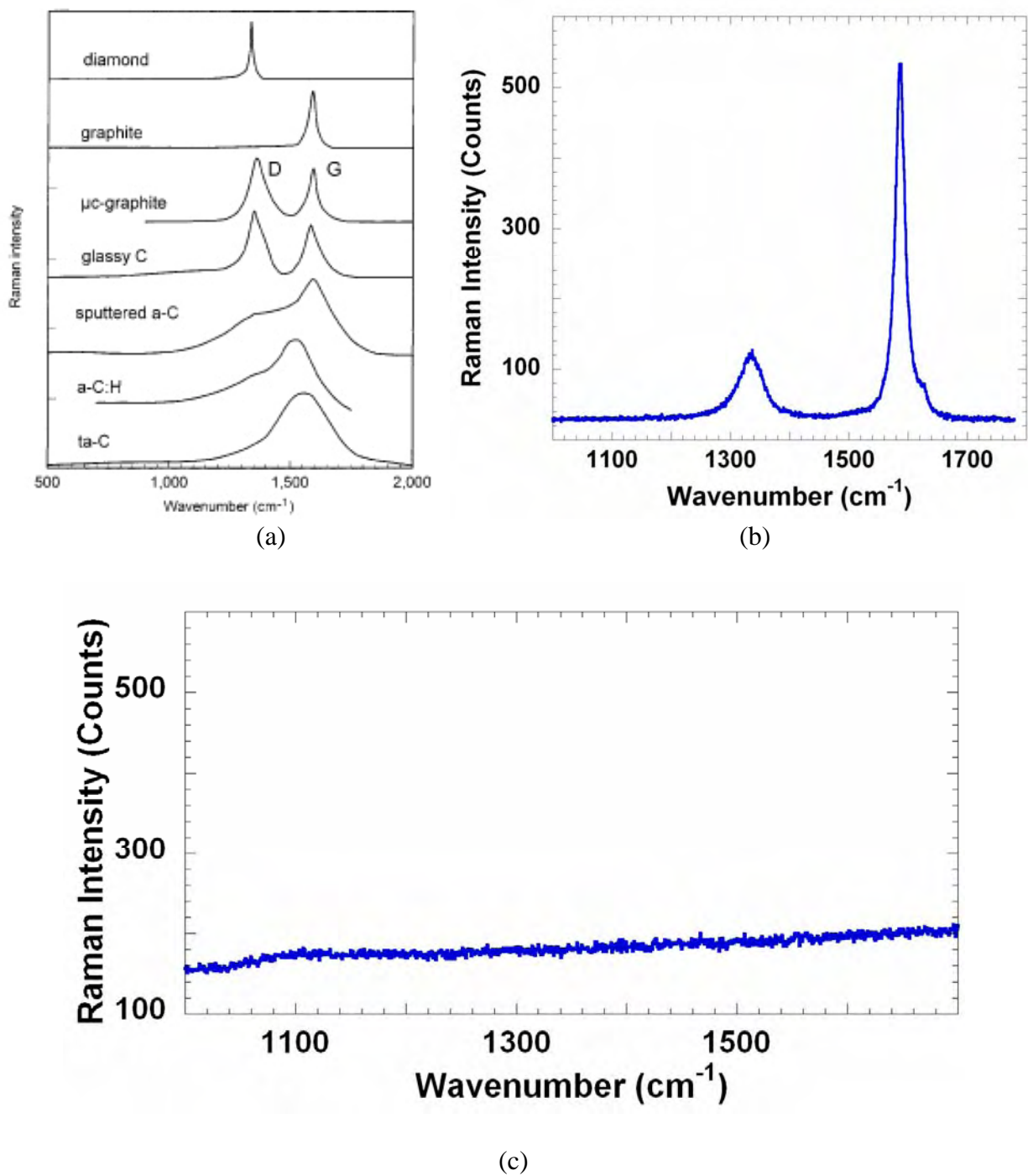


Figure 3-13. Raman spectra of carbon allotropes. (a) Comparison of typical Raman spectra in carbons.¹²⁷ (b) Graphite standard. There are peaks at 1335 cm⁻¹ (FWHM= 49cm⁻¹) and 1587 cm⁻¹ (FWHM= 23 cm⁻¹). (c) Glass slide background spectra.

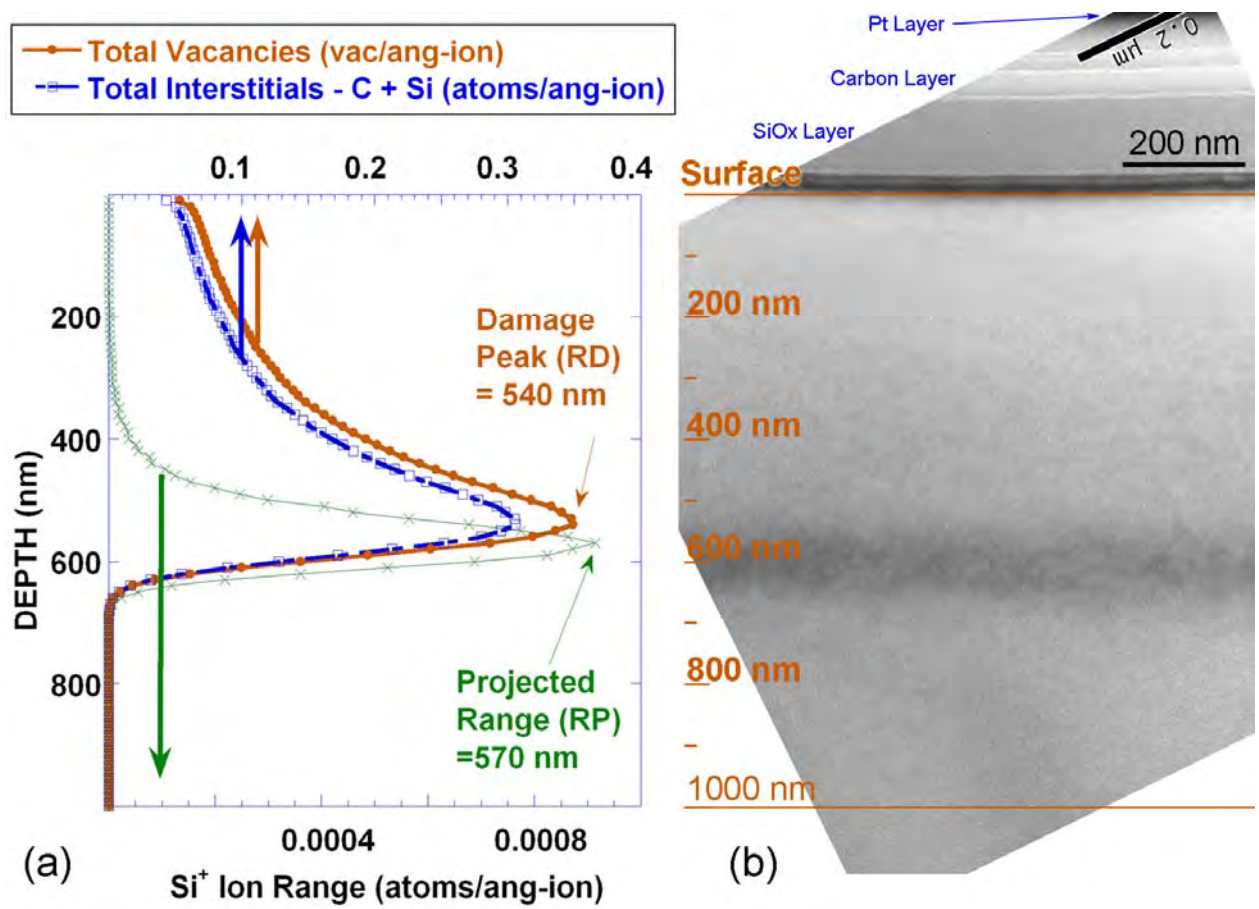


Figure 3-14. Comparison of simulation data to experimental images. (a) SRIM plotted data of damage created by Si^+ implantation at 1 MeV into diamond, showing total vacancies, interstitials and ion range. (b) BF XTEM image of (011)-oriented diamond Si^+ implanted at 1 MeV to a dose of $1 \times 10^{14} \text{ cm}^{-2}$.

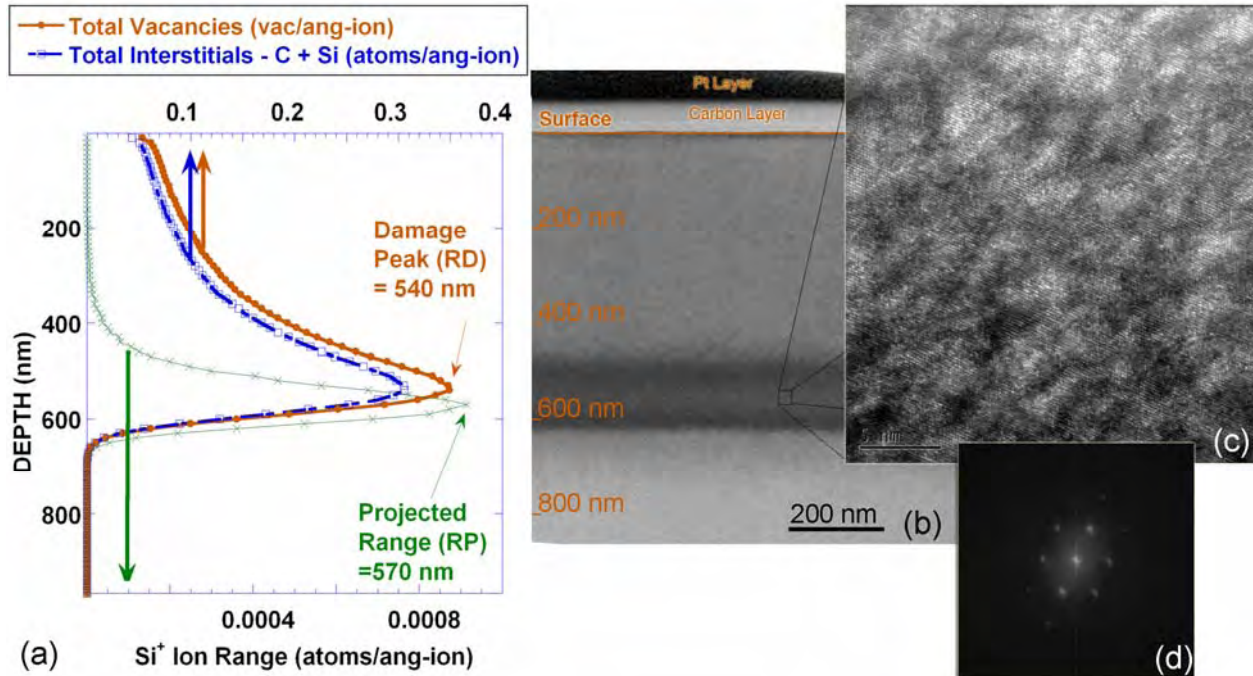


Figure 3-15. Comparison of simulation data to experimental images. (a) SRIM plotted data of damage created by Si⁺ implantation at 1 MeV into diamond, showing total vacancies, interstitials and ion range. (b) BF-XTEM image of Si⁺ implantation at 1 MeV to a dose of $1 \times 10^{15} \text{ cm}^{-2}$ into (001)-oriented diamond. (c) HRTEM of damaged area. (d) FFT of damaged diamond HRTEM image.

CHAPTER 4

RESULTS FROM NON-AMORPHIZING IMPLANTS INTO GERMANIUM

The literature review in Chapter 2 presented current controversies in the differences between defect formation in germanium (Ge) and silicon (Si). Both crystals have been reported to form the interstitial {311} defect for non-amorphizing implants, but only in light ion or electron irradiation in Ge.^{10-12,29,49} Additionally, recent research into SiGe alloys have resulted in results that showed that with increasing Ge content, {311} defects do not form¹³ and that possible vacancy defects are created in the near surface region.¹⁴

To explore the Ge {311} controversy, cross-sectional transmission electron microscopy (XTEM) was used to study defect formation and evolution in (001) Ge and Si wafers Si⁺ implanted at 40 keV and 1 MeV with doses of $1 \times 10^{14} \text{ cm}^{-2}$. As expected, upon annealing, {311} extended defects form and subsequently dissolve at the projected range for non-amorphizing implants into Si. In Ge, however, no {311} defect formation is observed for the 1 MeV non-amorphizing Si⁺ implant after annealing at temperatures between 350 - 850 °C. Instead, small dot-like defects are observed after 1 MeV Si⁺ implantation into Ge, which dissolve upon annealing between 650 - 750 °C for 10 minutes. Some evidence of dot-like defects is also observed in the lower energy implant regime, however these defects seem to be just at the level of detection for XTEM.

Introduction

There is interest in replacing the channel material of transistors with Ge instead of Si because of its significantly higher carrier mobilities.¹¹⁵ Recent advances in the use of high-k dielectrics have assisted in this regard by reducing the need for a stable Ge-based gate oxide. Additionally, SiGe alloys are being used in the current generation of devices to induce strain in the transistor channel, which in turn increases carrier mobility.¹³⁰ Ion-implantation remains the

preferred method of introducing dopants into the extension region of transistors next to the gate.¹³¹ However relatively little knowledge of the formation and evolution of ion-implantation related defects in Ge exists. Early studies of electron^{10,29} or light ion (hydrogen (H^+) and helium (He^+))^{11,12,49} implants into Ge reported {311} defect formation. As recently as 2005, Akatsu et al. reported observing {311} defects in bulk Ge implanted with He^+ at doses between 5×10^{15} and $7 \times 10^{16} \text{ cm}^{-2}$, at energies between 15 and 80 keV, and annealed at temperatures between 280 °C and 400 °C for 30 to 60 min.¹¹ The {311} defect, however, has not been reported in Ge for any ion species heavier than He^+ . Recent studies of amorphizing implants into Ge have not reported any rod-like extended defects for low energy implants.⁵⁴ To summarize, extended defects have been reported for light ion and electron irradiation but have not been seen for low energy implants using typical dopant atoms. It is well known that in Si, extended defect formation occurs for a wide range of implant and annealing conditions.⁹ Recent studies in SiGe alloys suggest that above 25% Ge, no {311} defects are observed, though only alloys were studied.¹³ Hence, the purpose of this chapter is to understand extended defect formation and evolution in bulk Ge after non-amorphizing Si^+ -implantation at high energy.

Experimental Design

Undoped (001) Czochralski grown high-purity Ge wafers and undoped (001) Czochralski grown Si wafers were Si^+ implanted at 1 MeV and 40 keV with doses of $1 \times 10^{14} \text{ cm}^{-2}$. Samples were held at 30 °C during implantation and tilted 7° relative to the incident ions to avoid ion channeling. In Si, this implant regime is known to produce easily visible {311} extended defects after annealing. The 1 MeV Si^+ implanted wafers were capped with 100 nm of silicon dioxide (SiO_2) via plasma-enhanced chemical vapor deposition (PECVD) at 300 °C for 3 min to prevent possible oxidation during furnace annealing. Subsequent annealing was conducted in a Lindberg tube furnace for 10 minutes in a flowing nitrogen (N_2) environment at temperatures ranging from

350 °C to 850 °C for Ge, and 650 °C to 950 °C for Si. This broad range of temperature for Ge encompasses those below the amorphous regrowth temperature of 400 °C¹³² and near the melting point of 938 °C¹¹¹. An FEI focused-ion beam and ex-situ lift-out system was used to prepare the Si and Ge XTEM samples, while traditional polishing methods and etch chemistry appropriate to each material was used to prepare plan-view TEM (PTEM) samples.¹³³ Transmission electron microscopy analysis was performed on a JEOL 200CX microscope using g₂₂₀ weak-beam dark-field (WBDF) imaging conditions and a JEOL 2010 microscope using on-axis bright-field (BF) imaging conditions for high-resolution imaging.

Results

Upon Si⁺ implantation at 1 MeV, and without any annealing, WBDF XTEM imaging revealed small dot-like defects in Ge extending from the surface to 1.1 μm below the surface. In Si, however, no discernable defects were observed prior to annealing. Upon annealing, Ge defects and Si defects display radically different morphology, as seen on the same scale using WBDF-XTEM imaging. In Ge, defects appear as dot-like defects as presented in Figure 4-1(a). These defects are too small to produce a clear phase contrast image when imaged using BF-HRTEM imaging, shown in Figure 4-2. The defects are an average size of approximately 12 nm in diameter over all annealing conditions. However, the defects in Si appear as rod-like defects, elongated along <110> directions, and in this study were at their coarsest after annealing for 10 min at 850 °C (60% of the melting point of Si (T_{MP Si})), as shown in Figure 4-1(b). These rod-like defects are commonly referred to as {311} defects as the defects have {311}-type habit planes.¹³

Microstructural evolution for 1 MeV Si⁺ implantation into Ge and Si is shown in Figure 4-3. The projected range (R_p) of the damage in Ge is predicted to be approximately 0.91 μm below the surface, while the damage peak (R_d) should occur at approximately 0.72 μm, according to

simulations.²¹ This is in good agreement with TEM analysis, as the density of defects was greatest between R_d and R_p . The simulation also agrees with the experiment for the implant into Si, with R_p and R_d of approximately 1.19 μm and 1.04 μm , respectively.

In Ge, the dot-like defects which appear immediately after implantation are shown after a 350 °C anneal for 10 min in Figure 4-3 (a). The defects decrease in density after the 450 and 550 °C anneals for 10 min and remain until finally dissolving at temperatures between 650 and 750 °C, as shown in g Figures 4-3 (b)- (d). The defects decrease in density but their average diameter remains at approximately 12 nm. However, in Si, after annealing for 10 min at 750 °C, extremely small rod-like defects begin to appear in densities right at the limit of detection, but are visible in the micrograph presented in Figure 4-3(e). After 10 min at 800 °C, the defects have reduced in number but increased in size, as shown in Figure 4-3(f). This trend continues at 850 °C, where the defects have grown into large, easily visible $\{311\}$ extrinsic defects, averaging approximately 170 nm in size with some as large as 300nm, as evident by the micrographi in Figure 4-3(g). Presented in Figure 4-3(h), after 10 min at 950 °C, the defects in Si have dissolved.

For the lower energy implants, neither Si nor Ge shows any defects after initial implantation as observed using WBDF XTEM and PTEM methods. Upon annealing, Si forms the characteristic $\{311\}$ defects, visible both in WBDF-XTEM and PTEM imaging conditions, as shown in Figure 4-4 (a) and (b), respectively. The majority of the defects lie in the region between R_D (~ 36nm) and R_P (~ 68nm), though some defects extend to the end-of-range (EOR) of the implant, as observed in Figure 4-4(a). In contrast, the Ge implanted with Si^+ at 40 keV, shown in Figure 4-5, shows no defects in WBDF-XTEM for any annealing temperature, though for some annealing temperatures 450 and 550 °C, dot-like defects are visible in PTEM, presented in Figure 4-6(b). The fact that the defects are observed in the PTEM micrographs and not in the

XTEM micrographs, presented in Figure 4-6(a), coupled with the lack of repeatability in viewing these dot-like defects at various anneal temperatures, may indicate that these dot-like defects seen in the Si⁺ implanted at 40 keV Ge samples are artifacts of the PTEM sample preparation process.

Discussion

Si defects have been well documented to follow a specific process. Theoretical sub-microscopic interstitial clusters (SMICs) evolve into small {311} defects, and with increasing thermal budgets, larger defects grow at the expense of smaller defects.¹⁷ In low dose Si⁺ implantation regimes, like $1 \times 10^{14} \text{ cm}^{-2}$, and with a high enough thermal budget, like 950 °C, the large defects become unstable and dissolve.¹⁷ However, the evolution of the defects in Ge, under this same implant energy and dose regime, is quite different, as shown in Figure 4-7. Though the density of the defects decline with increasing anneal temperature (similar to Si, Fig. 4-7(a)), the size of the defects stays constant, in sharp contrast to the increasing size of the defects in Si.

Defect Density Analysis

Plan-view quantification of Si⁺ implantation at 1 MeV is not possible because the defects are deeper than the Ge extinction distance for TEM analysis.¹¹² However, defect count analysis is possible in the XTEM samples because these samples were prepared using a standard automatic FIB process, so all samples are approximately the same thickness of approximately 100 nm. The density of defects can be derived from these XTEM images by the following method: each sample was made using the same automated XTEM procedure on a dual beam FEI Focused Ion Beam instrument, which resulted in samples uniformly thick, approximately 100nm. Images of defects were then taken at various magnifications, always using the WBDF g_{220} imaging condition. Two different scientists independently counted and measured the defects, with no significant discrepancy between the two scientists. Using this method, the resolution

limit for the detection of small defects (10 nm in diameter) is approximately 10^{10} defects/cm³. Ge defect counts after anneals of 750 °C and 850 °C for 10 minutes are right at this detection limit, while Si defects after anneals of 650 °C and 950 °C were below this resolution (no defects were observed).

Using the above method, defect densities in both Ge and Si were determined. In Ge, after annealing at 350 °C for 10 minutes, a defect density of 2×10^{12} cm⁻³ was observed. At 450 °C, the density of defects declined to approximately 5×10^{11} cm⁻³, and then leveled off at approximately 2×10^{11} cm⁻³ after anneals at 550 and 650 °C. Defects in Ge dissolved completely at 750 and 850 °C, and the defect counts in these images were right at the detection limit of this method. This is graphically represented in Figure 4-7(a). Interestingly, the average size of the defect remains the same, approximately 10 - 15 nm throughout the microstructural evolution, as evidenced by Figure 4-7(b). The Ge defects after 10 min at 450 °C may be small loops. However, either the small size or the off-axis habit plane prevented obvious identification using on-axis high-resolution phase contrast imaging. No {311} defects were observed in the high-resolution images.

Defect Dissolution Rate

Assuming an Arrhenius relationship between temperature and the dissolution rate of the Ge defects, an activation energy and time constant were derived. Beginning with the following two formulas, where D is the dissolution rate of the dot-like defects and is a function of time and temperature, D_0 is the number of defects at time zero, t is time and τ is the time constant:

$$D(t, T) = D_0 e^{-t/\tau} \quad (4-1)$$

τ is more explicitly given as:

$$\tau = \tau_0 e^{E_a/kT} \quad (4-2)$$

where τ_0 is a pre-exponential factor, E_a is the activation energy, k is Boltzmann's constant and T is the absolute temperature. From the defect analysis, the number of defects after implantation, but before annealing was approximately $1.18 \times 10^{12} \text{ cm}^{-2}$. However, this makes the activation energy calculation difficult, as the first value after annealing is approximately $1.92 \times 10^{12} \text{ cm}^{-2}$, larger than the initial count. For the sake of calculation, D_0 is estimated to be slightly larger than the 350 °C quantity. Interesting, the increase, and then decrease, in visible defects between the as-implanted state and subsequent anneals may indicate that more than one mechanism is contributing to the defect evolution. Thus, τ at a given temperature may be estimated using equation (4-1). The value of E_a is obtained by plotting the logarithm of τ versus $1/kT$ and determining the slope, as presented in Figure 4-8. Doing this, E_a is approximately $0.2 \pm 0.1 \text{ eV}$.

Defect Location Analysis

Defect location within each material differs between Ge and Si. In the 1 MeV Si^+ implant into Ge, defects are seen immediately after implantation and stretch from the surface to the predicted projected range of 0.91 μm . Defects in the same implant into Si are not seen until after annealing for 10 min at 750 °C, and are concentrated around and below the predicted R_p of 1.19 μm . In Ge, the defect density peaks at depths shallower than the projected range, whereas in Si where the majority of defects reside below the projected range. Additionally, defects in Ge seem to dissolve more rapidly near the surface, whereas in Si, the ripening process of each defect is not affected by its proximity to the surface, as shown in Figure 4-3. This phenomenon may be due to a difference in the stability of the vacancy population in the near surface region of Ge versus Si.¹³⁴ This hypothesis gains merit in light of a recent report that in SiGe, MeV implants into 30 atomic % Ge concentration SiGe alloys showed near-surface vacancy nanocavities,

confirmed by positron analysis.¹⁴ Crosby et al. also noted differences in defect formation for increasing concentrations in SiGe alloys. The experiment used SiGe, with 0, 2, 5, 25, 35, and 50 atomic % Ge, with Si⁺ implantation at 40 keV, with a dose of 1×10^{14} cm⁻² and annealed at 750 °C for various times. They noted {311} defect formation, similar to Fig.4-4 (b) for low concentrations of Ge. At 25 atomic % Ge and subsequent higher concentrations, no {311} defects were observed, but instead dislocation loops formed immediately. No XTEM analysis was reported in the previous study to compare to the current results. The results of this study agrees with Crosby's presented trend as no {311} defects were visible in Si⁺ implanted pure Ge. Future work focusing on the defect formation in lower energy implants into pure Ge is necessary to confirm the lack of defects shown in this study.

Conclusion

Unlike the original hypothesis proposed in the introduction, Ge does not display the characteristic behavior of Si for non-amorphizing implants. Although {311} defects were reported for H⁺ implantation in Ge¹¹ and for other electron or light ion implants,^{10,12} no {311} defects, platelets, or any type of planar defects were observed for heavier ion implants. This is consistent with Crosby et al.'s observations of decreasing density of {311} defects in SiGe alloys with increasing Ge content.¹³ Crosby suggested that the bond strength¹¹¹ differences between Si and Ge may cause the {311} defect to become thermodynamically unfavorable at high Ge content. Unlike Si, the location of the defects in Ge is closer to the surface implying some of the defects may be intrinsic. In addition, the size distribution of the defects in Ge remains relatively constant throughout the annealing process. These results suggest that {311} defect formation may be unique to Si.

Future work regarding extended defects in Ge could focus on characterizing the dot-like defects and clarifying the formation mechanism. Chronological studies could be used to better

quantify the activation energy of the dot-like defects. Additionally, positron analysis could be used to confirm a vacancy mechanism at work for potential intrinsic near-surface defects as opposed to extrinsic defects towards and beyond the projected range.

The results of this chapter show that, for non-amorphizing implants, defects do form in Ge but are fundamentally different than those seen in Si. Amorphization of Si is a processing step that has gained importance, but also results in stable defects that may be detrimental for device performance. The next chapter, then, will focus on whether these detrimental defects also form after amorphizing implants into Ge, and whether the stability of the defects differs from that of Si.

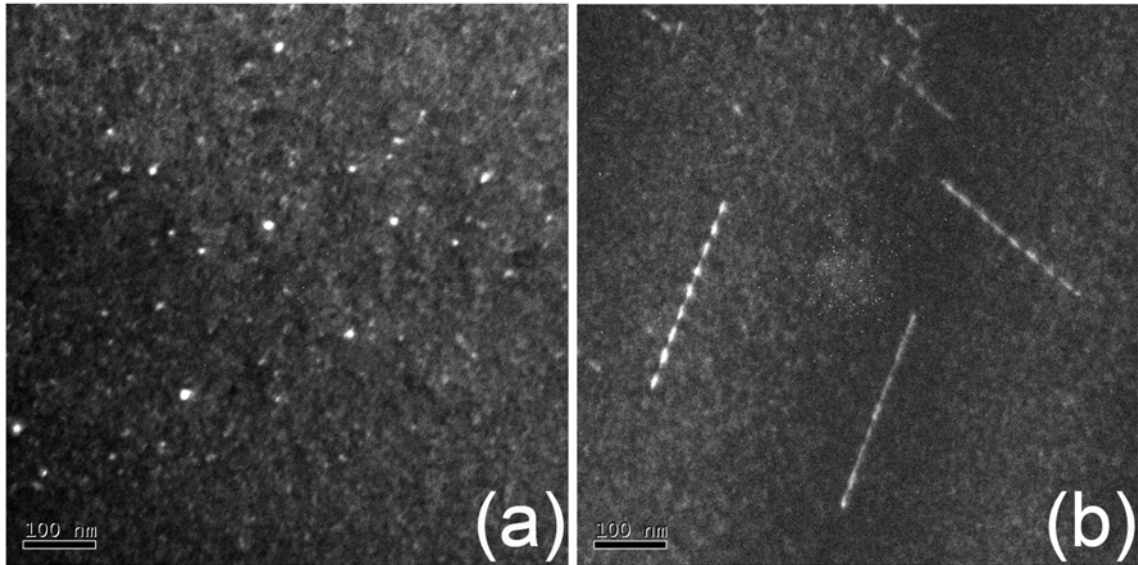


Figure 4-1. WBDf-XTEM images of (a) dot-like defects in Ge Si⁺ implanted at 1 MeV with a dose of $1 \times 10^{14} \text{ cm}^{-2}$ following annealing at 450 °C for 10 min and (b) {311} defects in Si with the sample implantation following annealing at 850 °C for 10 min.

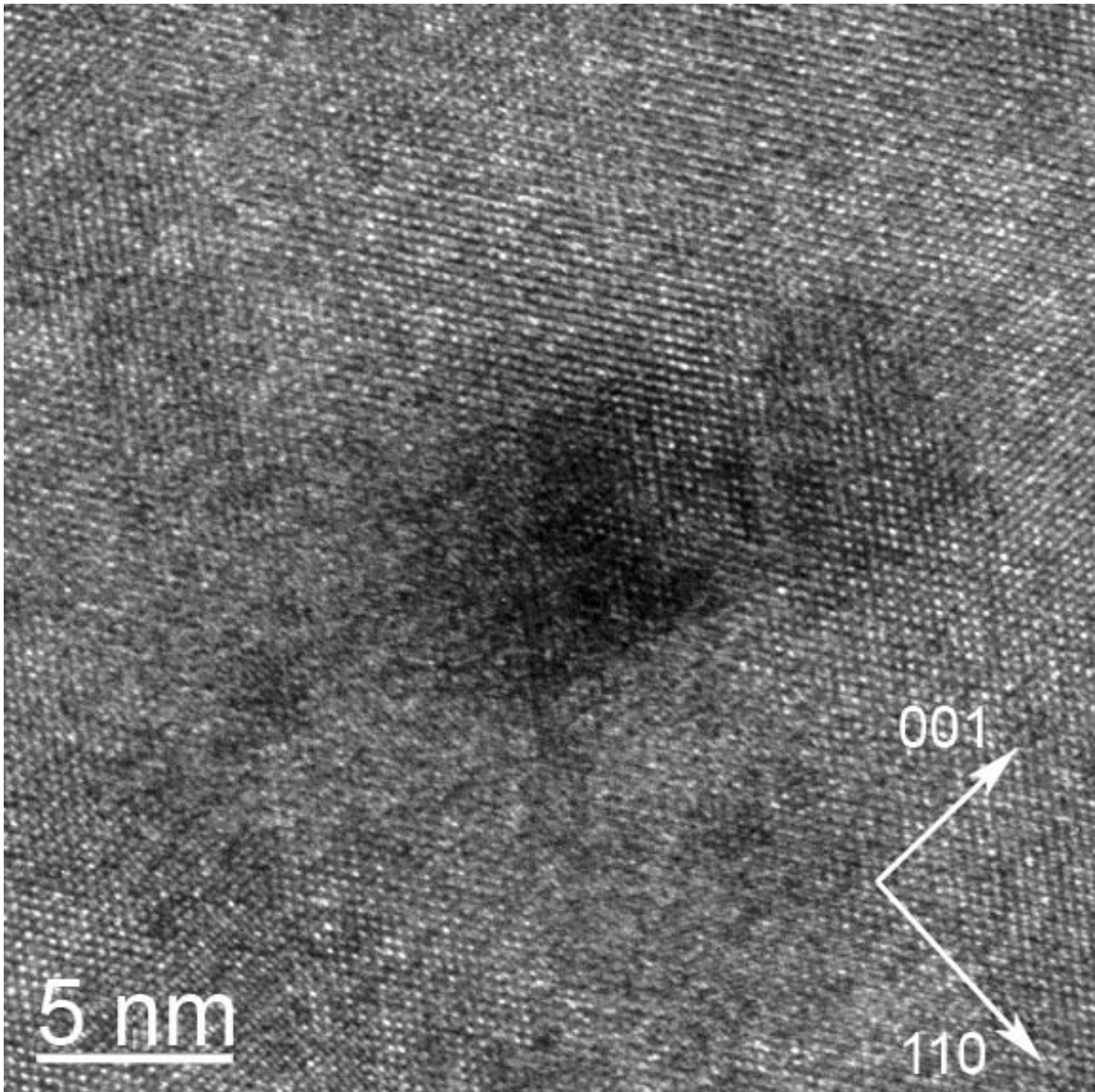


Figure 4-2. High resolution BF-TEM image of a dot-like defect seen in Ge Si⁺ implanted at 1 MeV with a dose of $1 \times 10^{14} \text{ cm}^{-2}$ after annealing for 10 min at 450 °C.

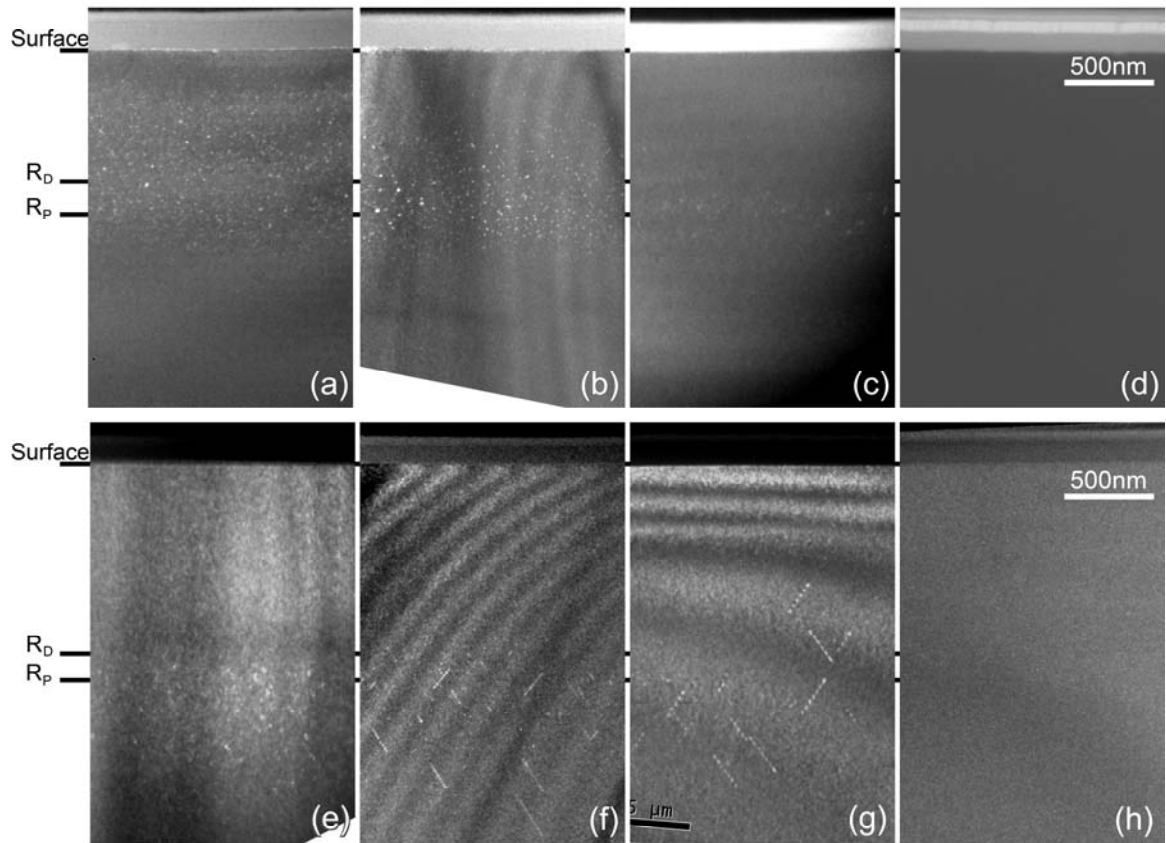


Figure 4-3. WBDF-XTEM images of Ge Si⁺ implanted at 1 MeV with a dose of $1 \times 10^{14} \text{ cm}^{-2}$ after 10 min of annealing at (a) 350 (b) 450 (c) 650 (d) 750 °C and Si with the same implantation after 10 min of annealing at (e) 750 (f) 800 (g) 850 and (h) 950 °C.

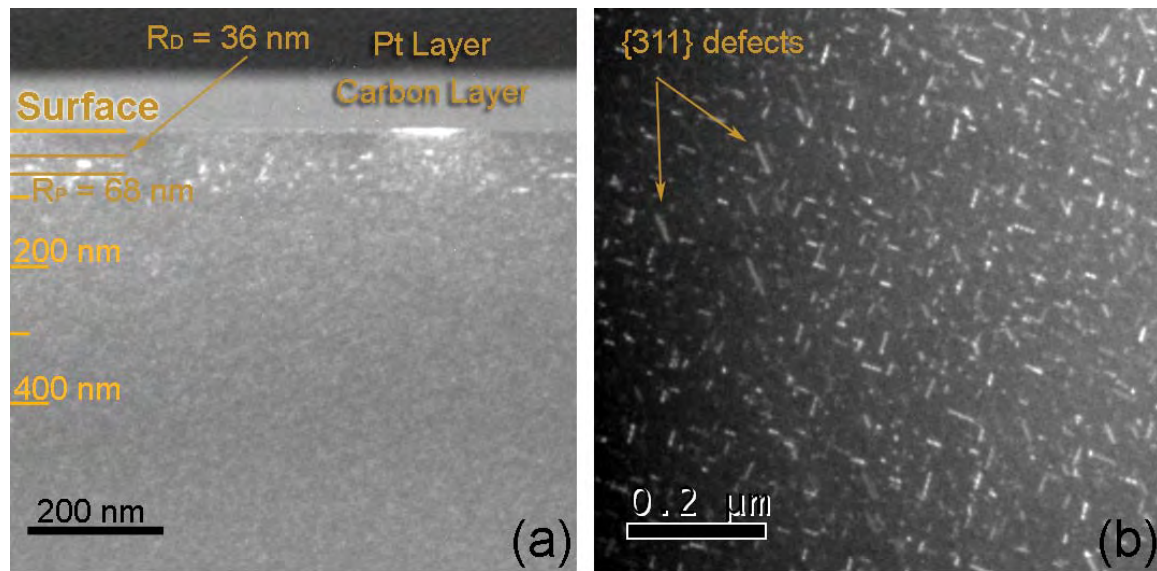


Figure 4-4. WBDF images of Si Si⁺ implanted at 40 keV with a dose of $1 \times 10^{14} \text{ cm}^{-2}$ after annealing for 10 min at 750 °C:(a) XTEM and (b) PTEM.

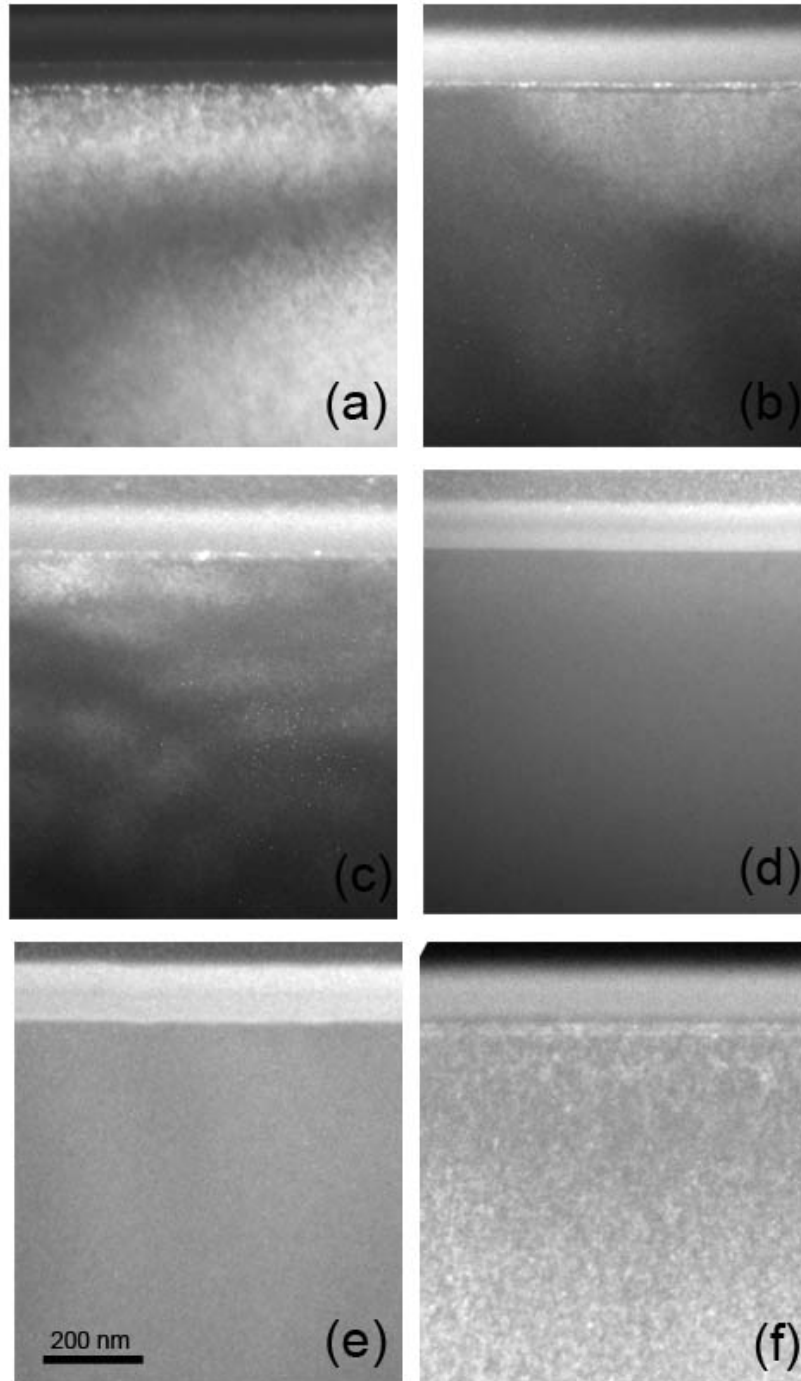


Figure 4-5. WBDF-XTEM images of Ge Si⁺ implanted at 40 keV with a dose of $1 \times 10^{14} \text{ cm}^{-2}$ (a) as implanted, and annealed for 10 min at (b) 350 (c) 450 (d) 550 (e) 650 (f) 750 °C

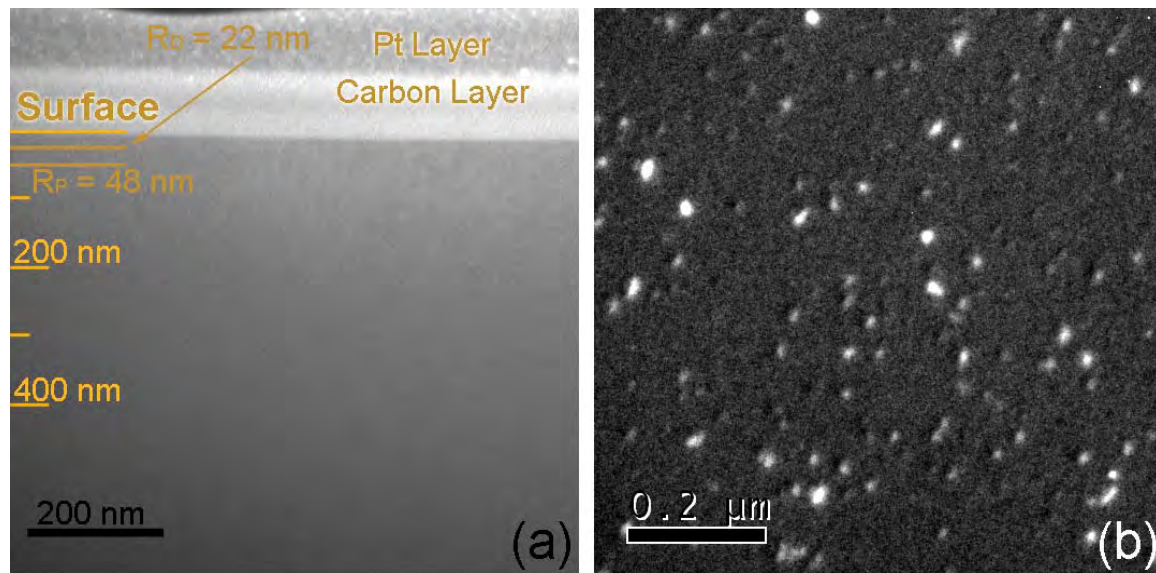


Figure 4-6. WBDF images of Ge Si^+ implanted at 40 keV with a dose of $1 \times 10^{14} \text{ cm}^{-2}$ and annealed for 10 min at 550 °C:(a) XTEM and (b) PTEM.

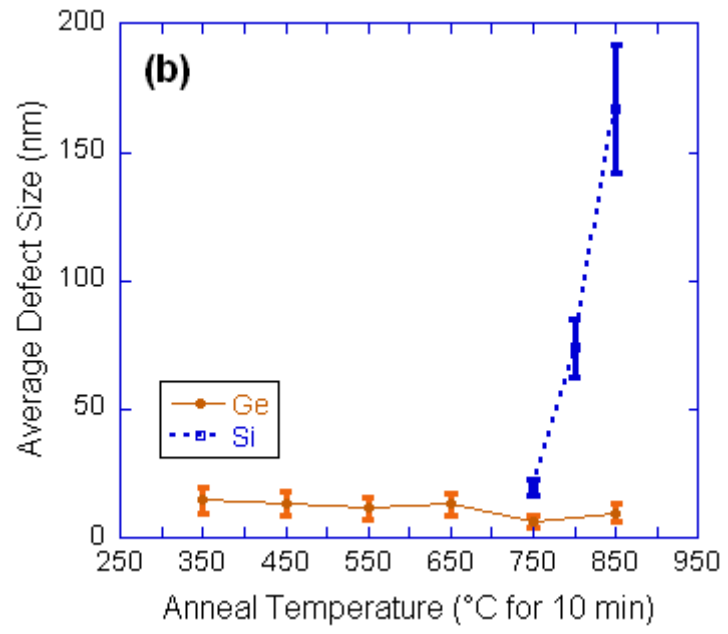
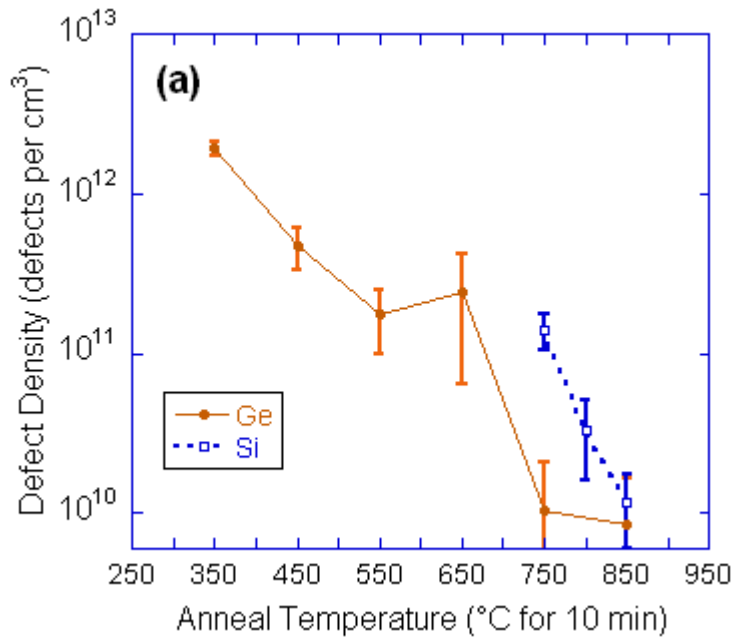


Figure 4-7. Microstructure evolution of Ge and Si after annealing for 10 min at various temperatures: (a) defect density versus temperature and (b) average defect size versus temperature. The TEM detection limit in (a) is approximately 10^{10} cm^{-3} .

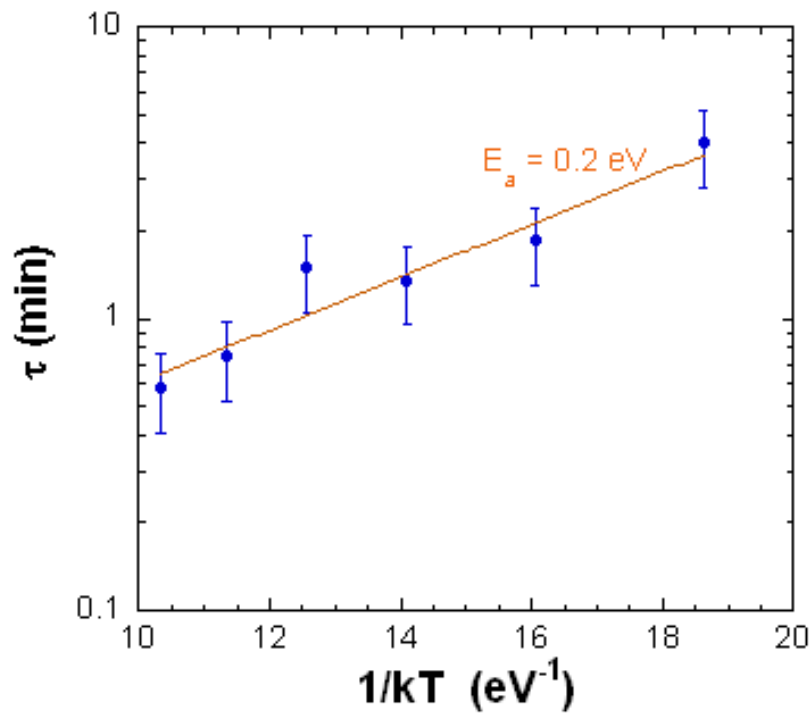


Figure 4-8. Plot of the logarithm of τ vs. $1/kT$ for 1 MeV Si^+ implantation into Ge after 10 min of annealing. The value of E_a is approximately $0.2 \text{ eV} \pm 0.1 \text{ eV}$.

CHAPTER 5 RESULTS FROM AMORPHIZING IMPLANTS INTO GERMANIUM

The previous chapter showed that Germanium (Ge) does not form {311} defects in either the low or high energy Si⁺ implantation regime in which these defects form in Si. The plus-one model, which states for every ion implanted there should be an interstitial remaining after initial implantation, only holds for a sub-amorphizing implant, and not an amorphizing implant.

However, extended defects, such as {311} defects and dislocation loops, are seen in Si for amorphizing implants after annealing. In addition, for buried amorphous layers, Si has shown other defects as well, including regrowth-related, clamshell and end-of-range (EOR) defects.⁹

This chapter presents the results from amorphizing implant experiments. Ge which is Si⁺ implanted at 1 MeV at a dose of $1 \times 10^{15} \text{ cm}^{-2}$ creates a buried amorphous layer that, upon regrowth, exhibits EOR, regrowth-related, and clamshell defects. Unlike Si, no planar {311} defects are observed. The minimal EOR defects are small dot-like defects and are very unstable, dissolving between 450 and 550 °C. This is in contrast to Si, where the EOR defects are very stable. The amorphous layer results in both regrowth-related defects and clamshell defects, which were more stable than the EOR damage. Ge implanted with Si⁺ at 40 keV at the same dose creates an amorphous layer that extends from the surface to approximately 70 nm deep. No defects were seen upon regrowth in Ge, while {311} defects and loops are observed in Si.

Introduction

The potential benefits of using Ge as a channel material we presented in Chapter 4, and need not be repeated. Despite the renewed interest in Ge, relatively little knowledge of the formation and evolution of ion-implantation related defects in Ge exists. Amorphization is a process step that, in Si, assists in the activation and (non)diffusion of dopants. However, the stable EOR defects that form during SPER in Si can be detrimental to device performance and

affect production yield. Therefore, it is an important phenomena to study when looking at alternate channel materials.

Amorphization is a phenomenon by which the crystal lattice loses long range order after ion-implantation past a critical damage point. It is associated with a reduction in material density, approximately 1-2% in Si, Ge and SiGe alloys, which causes the crystal to swell.^{56,58,61,66} Many factors influence whether amorphization will occur, including implant temperature, dose weight, mass of the ion, mass of the target atoms, energy of the ion and dose rate. Normally, adding energy to the crystal in the form of heat recrystallizes the damaged material, and the crystal regrows from the bulk seed base and eventually repairs the entire lattice. Non-intuitively, ion-implantation can also assist with crystalline regrowth after amorphization in Si and Ge, due to heating from the ion-beam.⁵⁷ With extremely high energy and heavy ions, a void-filled phase is also formed alongside the amorphous phase in Ge.⁵⁸

In Si, amorphization results in EOR defects that are initially observed as planar {311} defects and evolve into stable dislocation loops upon annealing.⁶ End-of-range defects can dominate dopant diffusion and leakage in junctions formed using amorphizing implants. In addition, a buried amorphous layer has been shown to produce regrowth-related defects as well as clamshell defects in Si.⁹

Recent transmission electron microscopy (TEM) studies of dopant implants into Ge reported no EOR damage formation for amorphizing implants.^{52-55,135} However these were lower energy implants and the EOR defect density is known to increase with increasing implant energy.¹³⁶ Extended defects in Ge, reported as {311} defects, have been observed after non-amorphizing light ion implantation¹¹ and electron-irradiation,¹⁰ though no published reports exist on the formation of stable regrowth related defects or clamshell defects in implanted Ge.

Experimental Design

Undoped (001) Czochralski grown high-purity Ge wafers were Si⁺ implanted in a tandem accelerator at 1 MeV and 40 keV at 30°C to a dose of $1 \times 10^{15} \text{ cm}^{-2}$ with 7° of tilt. The wafer implanted at 1 MeV was capped with 100 nm silicon dioxide (SiO₂) via plasma-enhanced chemical vapor deposition at 300 °C for 3 min to prevent possible oxidation during furnace annealing. Subsequent annealing was conducted for 10 min in a nitrogen (N₂) ambient at temperatures between 350 – 850 °C in a Lindberg tube furnace. Solid phase epitaxial recrystallization (SPER) of ion-implantation induced amorphous layers in Ge is known to occur at approximately 400 °C.^{51,132} After annealing, cross-section TEM samples (XTEM) were prepared using a FEI Dual Beam Focused Ion Beam and Omniprobe lift-out system. Plan-view TEM (PTEM) samples were prepared of the samples implated at 40 keV using traditional techniques and appropriate etch chemistries.¹³³ Plan-view TEM samples of the samples implanted at 1 MeV were not performed because the projected range of the implant is 9400 Å (940nm), and the extinction distance in Ge for the 220 reflection is 452Å (45nm); therefore, defects seen at or beyond the projected range of the implant could not be imaged via PTEM^{21,112} Transmission electron microscopy analysis was performed on a JEOL 200CX microscope using g_{220} weak beam dark field (WBDF) imaging conditions and a JEOL 2010 microscope using on-axis bright-field (BF) high-resolution imaging.

Results

High Energy Implant – 1 MeV

The implant conditions created a buried amorphous layer starting approximately 0.1 μm below the surface and extending to a depth of 1.2 μm as shown in Fig. 5-1(a). The WBDF image shows that the upper and lower amorphous-crystalline (α -c) interfaces are rough. This agrees well with the rough α -c Ge interface previously reported after an amorphizing implant.^{53,54}

Transmission electron microscopy analysis shows that the near surface region is not completely crystalline but rather contains pockets of crystalline material embedded in the amorphous Ge as shown in Figure 5-2(a). High resolution TEM lattice imaging confirmed the crystalline nature of the pockets of embedded Ge in the near surface region. Transmission electron microscopy of the as-implanted lower α -c interface also shows pockets of crystalline Ge embedded in the amorphous phase along the rough interface region, shown in Fig.5- 2(b). The transition region for the upper interface is approximately 140 nm, while the lower interface is much more abrupt at 65 nm.

After annealing the sample at 350 °C for 10 min, approximately 100 nm of regrowth was observed, as shown in Figure 5-1(b). This agrees well with Csepregi et al.'s reported 350°C regrowth rate of (001) Ge of 9 nm/min.¹³² This regrowth created a significantly smoother α -c interface. End-of-range damage is observed after and consists of small dot-like defects that extend beyond the α -c interface. End-of-range dislocation loops in implanted Ge have not been previously reported. Planarization of the bulk interface occurred, while no well-defined crystalline advancing front developed in the near-surface region. Figure 5-3(a) shows that after annealing at 450 °C for 10 min, the Ge has completely recrystallized. Regrowth-related defects, clamshell (or zipper) defects, and EOR defects are observed. Regrowth-related defects, which appear as threading dislocations with a primarily vertical line direction in the image, are the result of imperfect solid phase epitaxial recrystallization. These defects are known to nucleate at either a rough interface or when the solid phase epitaxial growth process proceeds around an embedded crystalline region.¹³⁷ The density of regrowth-related defects appears greater in the layer that nucleated at the surface. This may be the result of the wider transition region near the surface.

Clamshell defects occur when the two advancing crystalline growth planes meet and are approximately parallel to the surface.⁹ Previous studies have suggested these defects in Si have a Burgers vector parallel to the surface and thus have a pure shear character. Transmission electron microscopy $g \cdot b$ analysis using many two-beam conditions indicated these dislocations in Ge do not display shear nature. Instead the dislocation appears to be a mixture of 60° and 90° perfect dislocations. The EOR defects are approximately 1.1 μm below the surface and appear to be loops similar to what is seen in Si.⁹ These dislocation loops appear to evolve from small loops. No {311} defects are ever observed in the defect evolution process. This suggests that, unlike in Si where it has been shown that {311} defects unfault into dislocation loops, in Ge the loops appear to skip this step and evolve directly from submicroscopic clusters to dislocation loops.⁶ If {311} defects do form in the EOR region and unfault into loops, the defects must do this before becoming visible in WBDF imaging conditions.

Regrowth-related damage is still apparent after 10 min at 550 °C, as shown in Figure 5-3(b), though a reduction in EOR damage density occurred from the 450°C anneal, indicating that the EOR defects are relatively unstable in Ge. After the 650 °C anneal, no EOR and virtually no clamshell defects remain, as displayed in Figure 5-3(c). Only the regrowth-related defects are still visible in the XTEM image. Therefore, it can be concluded that regrowth-related defects are the most stable in high-energy implants into Ge. Very few regrowth-related defects remain after anneals at 750 °C as presented in Figure 5-3(d), and at 850 °C (not presented) no defects are detected (defect density $< 10^8 \text{ cm}^{-2}$).

Low Energy Implant – 40 keV

The low energy implant conditions formed an amorphous layer that extends from the surface to approximately 70 nm below the surface, as shown in Figure 5-4(a). Similar to the high energy implant, the amorphous-crystalline interface is rough. Annealing for 10 min at 350 °C

initiated SPER, with approximately 15 - 20 nm of regrowth, shown in Figure 5-4(b). This results in a regrowth rate of approximately 1.5 -2.0 nm/min. This is significantly higher than Zellama's reported rate of 0.2 nm/min⁵¹ at 350 °C and but only slightly higher than Csepregi's reported SPER rate of 1.0 nm/min¹³² in (001) orientation at 350 °C. Additionally, the interface has planarized during regrowth. Compared to the rough as-implanted interface, which has a range of approximately 10 nm, as shown in Figure 5-5(a), the regrown interface has planarized to less than 3 nm in the interface region, as shown in Figure 5-5(b).

Annealing for 10 min at 380 °C, shown in Figure 5-4 (c), fully recrystallizes the amorphous region. The minimum regrowth rate possible for this time and temperature is 70 Å/min, which is still higher than Zellama's 1979 reported 13.2 Å/min. However, it is possible that the regrowth rate is higher than the 70 Å/min, as full recrystallization was achieved and no final interface exists. The HRTEM image also shows a Ge oxide (GeOx) layer has formed on the surface during annealing, as noted on Figure 5-4(c). GeOx is known to vary in thickness, due to its formation being highly dependent on humidity. Though the samples were annealed in a flowing high-purity N₂ atmosphere, trace amounts of water vapor and oxygen are known to exist in the system, and may have contributed to the GeOx formation.

The resulting regrown crystalline layer is defect-free. No EOR defects or regrowth related defects, as seen in the MeV implant, are seen in HR imaging, shown in Figure 5-4. Subsequent 10 min anneals, at 450, 550, 650 and 750 °C, shown in Figure 5-6 (a) - (d) respectively, show no defects in the regrown region, though all show the GeOx layer. The 450 – 650 °C oxide layers appear to be a consistent thickness, which indicates a limiting mechanism in the diffusion of oxygen from the ambient to the bulk Ge. After the 750 °C anneal for 10 min, the surface of the Ge wafer, which originally was highly reflective, became visibly clouded, possibly indicating the

presence of a significant oxide layer. GeO_x is known to be water soluble, and the presence of a surface oxide layer on the 750 °C sample was confirmed when a water-based solvent was applied to the surface of the sample, removing the dull surface layer and revealing reflective Ge underneath. Transmission electron microscopy of this sample confirms that the sample was preferentially etched, as indicated by etch pits visible in Fig. 5-6(d). The pit wall normals are at an approximate 54° angle to the wafer normal, indicating the pit normals are {111} planes. surface, indicating etching along the (111) plane in the <110> direction. Pyramidal etch pits are common in diamond-cubic systems. The etch pits were created during annealing, because the carbon-coating prior sample preparation filled in the pit, as evidenced in Figure 5-6(d).

TEM of Ge, Si⁺ implanted at 40 keV, revealed no defects. However, Si wafers implanted similarly to the Ge, displayed the characteristic {311} extended defect formation and loop evolution during annealing. Figures 5-7 (a) and (b) show TEM images of Si⁺ implanted Si annealed at 750 °C for 10 min, showing defects in both cross-section [Fig. 5-7(a)] and plan view, respectively. The defects are concentrated in the EOR region, approximately 60-100nm below the surface.

Discussion

Defects

The type and stability of defects found in Ge differ from what has been previously reported in Si. The type of defects in the high energy case mimic Si defects resulting from the recrystallization of a buried amorphous layer, but the stability of these defects is quite unlike Si. Additionally, few EOR defects were observed during the Ge regrowth process in the high energy implant. Finally, none were seen in the lower energy implant.

In the 1 MeV implant, the existing Ge EOR defects were the first defects to dissolve between 450 and 550 °C. The clamshell defects annealed out between 550 and 650 °C. The

regrowth-related defects, also known as hairpin dislocations, were clearly visible after 10 min at 450 °C and did not dissolve below 750 °C, while the defects lack the morphology of the hairpin dislocation seen in Si.¹³⁷ The line direction of the regrowth defects in Si is observed to be very similar to what is observed in these samples. In Ge, the line direction appears to move but this may be related to the increased density of dislocation in the upper regrowth layer. A $g \cdot b$ analysis of the Ge regrowth defects confirmed that the Burgers vectors are perfect with $\vec{b} = \frac{a}{2} \langle 110 \rangle$. Jones et al reported that in Si, hairpin dislocations were less stable than clamshell defects, which were in turn less stable than EOR defects.⁹ In Si, EOR defects are the most stable defect, while we find that in Ge, EOR defects are the least stable of the three types of defects. It has been shown in Si that reducing the threshold damage density (TDD) for amorphization either by increasing the implant temperature or increasing the dose rate results in fewer EOR defects.¹³⁶ The decrease in EOR defect density and stability in Ge, as compared to Si, may be a result of fewer interstitials in the EOR available to form extended defects. As previously noted, the TDD in Ge is less than in Si, making it easier to amorphize Ge than Si using the same implant. Therefore, for the same damage profile, more of the total damage profile is within the amorphous range for Ge, leaving less interstitials in the EOR region available for defect formation.

No defects were seen in the low energy as-implanted or annealed TEM images. This agrees with previous low energy amorphization studies of a 6 keV amorphization investigation by Satta et al. in 2005.⁵⁴ The absence of EOR defects may be the result of (1) lower energy implants leaving less interstitials past the a-c interface to participate in extended defect formation, (2) the bond-strength differences between Si and Ge making EOR defects less stable, and/or (3) the defects are below the resolution of TEM. The first explanation, lower energy implants leave less

interstitials in the EOR region to participate in defect formation, is a phenomenon seen in Si. As the energy of the implant is lowered, less EOR defects are observed.³⁶ Extremely low energy implants can avoid EOR defects entirely. The second explanation regarding bond strength was postulated by Crosby et al. to explain the decrease in {311} formation with increasing Ge content in SiGe alloys.¹³ The third explanation, that any extended defects which may occur are below the resolution of the TEM, is unlikely as the a-c interface region was thoroughly examined using HRTEM imaging in the search for EOR defects.

Trapped Interstitials and Activation Energy of 1 MeV EOR Defects in Ge

Using data from the XTEM images, an activation energy for the dissolution rate of the EOR defects was determined. It should be noted that there are many assumptions in this calculation as well as an extremely small sample size. The initial assumption made in order to perform the calculation is that the EOR defects seen in Ge are faulted Frank loops that are circular in nature and reside on the (111) plane. The defects appear to behave like the Si EOR loops, in the fact that the defects decrease in density, as shown in Figure 5-8(a), but increase in size, as shown in Figure 5-8(b) with each higher temperature annealing step, a phenomenon known as Ostwald Ripening. Using this data, and analogous calculations as shown in the previous chapter, the activation energy (E_a) is determined to be approximately 0.4 ± 0.1 eV, as determined using Figure 5-8(c). However, it should be noted that this is an extremely low number of data points, and further study should be conducted to refine the result. The number of trapped interstitials in the defects appears to stay almost constant, at approximately 1×10^{14} cm⁻², as shown in Figure 5-8(d). This is also consistent with Ostwald ripening, where the large defects grow at the expense of small defects.

Threshold Damage Density for Ge

An approximate 2% decrease in density accompanies amorphization in Si, Ge and SiGe alloys in this dose regime.^{56,58,61,66} Using XTEM, the thickness of the amorphous layer (t_a) can be determined, giving a thicknesses of approximately 1050 nm and 73nm for the 1 MeV and 40 keV Si^+ implantation, as shown in Figures 7-8 (a) and 7-9(a), respectively. Performing a mass balance calculation using the densities of both the amorphous (ρ_a) and crystalline (ρ_c) layers, and the known amorphous layer thickness (t_a), the thickness of the crystalline layer (t_c) that was converted to amorphous material can be obtained, using

$$\rho_a \cdot t_a = \rho_c \cdot t_c \quad (5-1)$$

$$t_c = (\rho_a / \rho_c) \cdot t_a = .98 t_a \quad (5-2)$$

This simple calculation results in a converted crystalline layer (c-layer) thickness of approximately 1030 nm and 72 nm for 1 MeV and 40 keV Si^+ implantation, respectively. At first this does not seem like a significant change. However, the significance of the reduction is important to determine threshold damage densities. By comparing the depths of the converted c-layer, and using simulated damage profiles, the damage necessary to amorphize Ge can be determined. Figures 5-9(b) and 5-10(b) both show the simulated vacancy profile determined superimposed on the XTEM image.²¹ The damage matches well with the amorphous layer depth. Then, the calculated c-layer thickness is used to determine the damage thresholds, as shown in Fig. 5-9(c) and 5-10(c), plotting TDD and critical damage (D_C) in Ge versus depth for 1 MeV and 40 keV Si^+ implantation. It is important to use the converted c-layer thickness, rather than the amorphous layer thickness, to determine the correct value, as simulations do not take into account amorphization or the swelling caused by it. The literature has reported the damage necessary to amorphize a semiconductor by TDD (favored by the semiconductor community), D_C

(favored by the diamond community) and displacements per atom (DPA) (favored by the ion implantation community). All three can be derived from simulations, and all three are reported here. Additionally, the values for amorphization from 40 keV Si⁺ implantation into Si are also provided. It should be noted that no 1 MeV amorphizing implant into Si was performed in this study. Table 5-1 summarizes the results. The D_C necessary to amorphize Si is analogous to displacing every atom off its lattice site.²⁰ That agrees with the determination here that the D_C for Si is approximately 5×10^{22} vacancies/cm³. The D_C determined for Ge is roughly $4 \pm 2 \times 10^{22}$ vacancies/cm³, which is approximately the atomic density of Ge, 4.42×10^{22} cm⁻³. In fact, all three Ge values are slightly lower than those calculated for Si. These results indicate that Ge is easier to amorphize than Si. This is logical, as Ge is known to have weaker bond strength than Si.¹¹⁴

Conclusion

Transmission electron microscopy was used to characterize the extended defects arising from annealing Si⁺ implantation induced amorphized Ge. Although {311} defects have been previously reported in Ge after light ion implantation and electron-irradiation no {311} defects were observed over a wide range of annealing temperatures. In this study, end-of-range dislocation loops were observed, possibly due to the high implant energy, as these defects have not been seen in previous lower-energy studies. In addition, regrowth-related defects and clamshell defects were also observed, with regrowth-related defects exhibiting the greatest stability. Amorphization thresholds were determined for Ge, confirming that Ge is easier to amorphize than Si. The threshold defect density of Ge determined from these experiments is approximately $6 \pm 3 \times 10^{20}$ keV/cm³.

The defects shown during solid phase epitaxial regrowth in Ge agree well with what is seen in Si, which is different than the previous chapter. It would seem that the hypothesis

presented previously, that the same defects would appear in Ge that do in Si, is correct. However, there is some difference in behavior. In Si, the end-of-range dislocation loops are very stable; while in Ge, the end-of-range defects are the least stable defects, annealing out at 650 °C for 10 min. In Si, {311} defects are seen in the end-of-range, while these defects have not been seen in Ge. Future work should focus on computation simulation to see if bond strength really is the deciding factor in the stabilization of the {311} defect.

Thus far, the defects arising after ion-implantation in Ge have been compared to the defects in Si. For amorphizing implants, similar type defects occurred in both semiconductors, though the stability of these defects differ. In non-amorphizing implants, Si⁺ implantation into Ge results in dot-like defects as compared to the {311} defects in Si. The next experiment will focus on non-amorphizing implants into another potential alternate channel material: single crystal diamond.

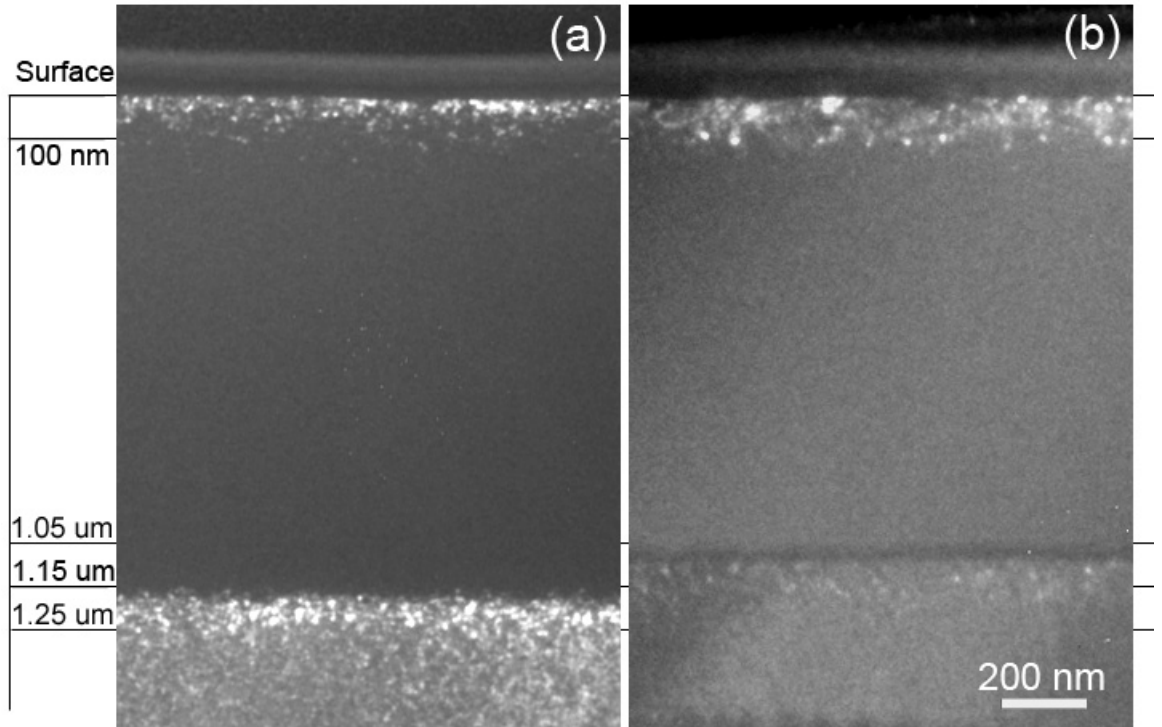


Figure 5-1. WBDF-XTEM images taken of Ge Si⁺ implanted at 1 MeV to a dose of $1 \times 10^{15} \text{ cm}^{-2}$ (a) as-implanted and (b) after 10 min of annealing at 350 °C.

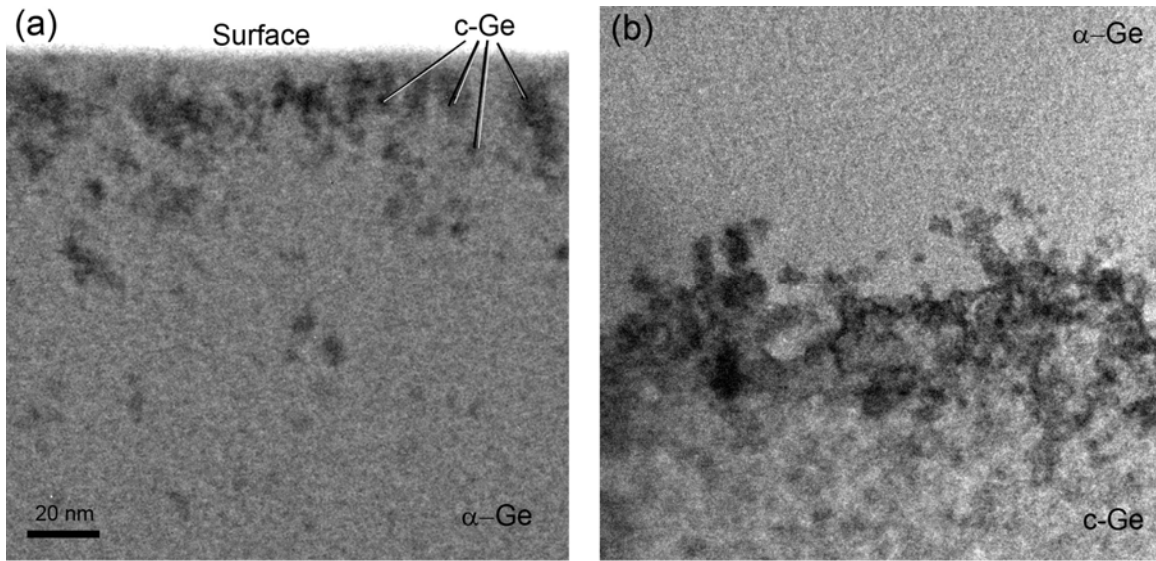


Figure 5-2. HRTEM images of Ge Si⁺ implanted at 1 MeV to a dose of $1 \times 10^{15} \text{ cm}^{-2}$ as-implanted (a) surface crystalline-to-amorphous transition region and (b) EOR amorphous-to-crystalline transition region.

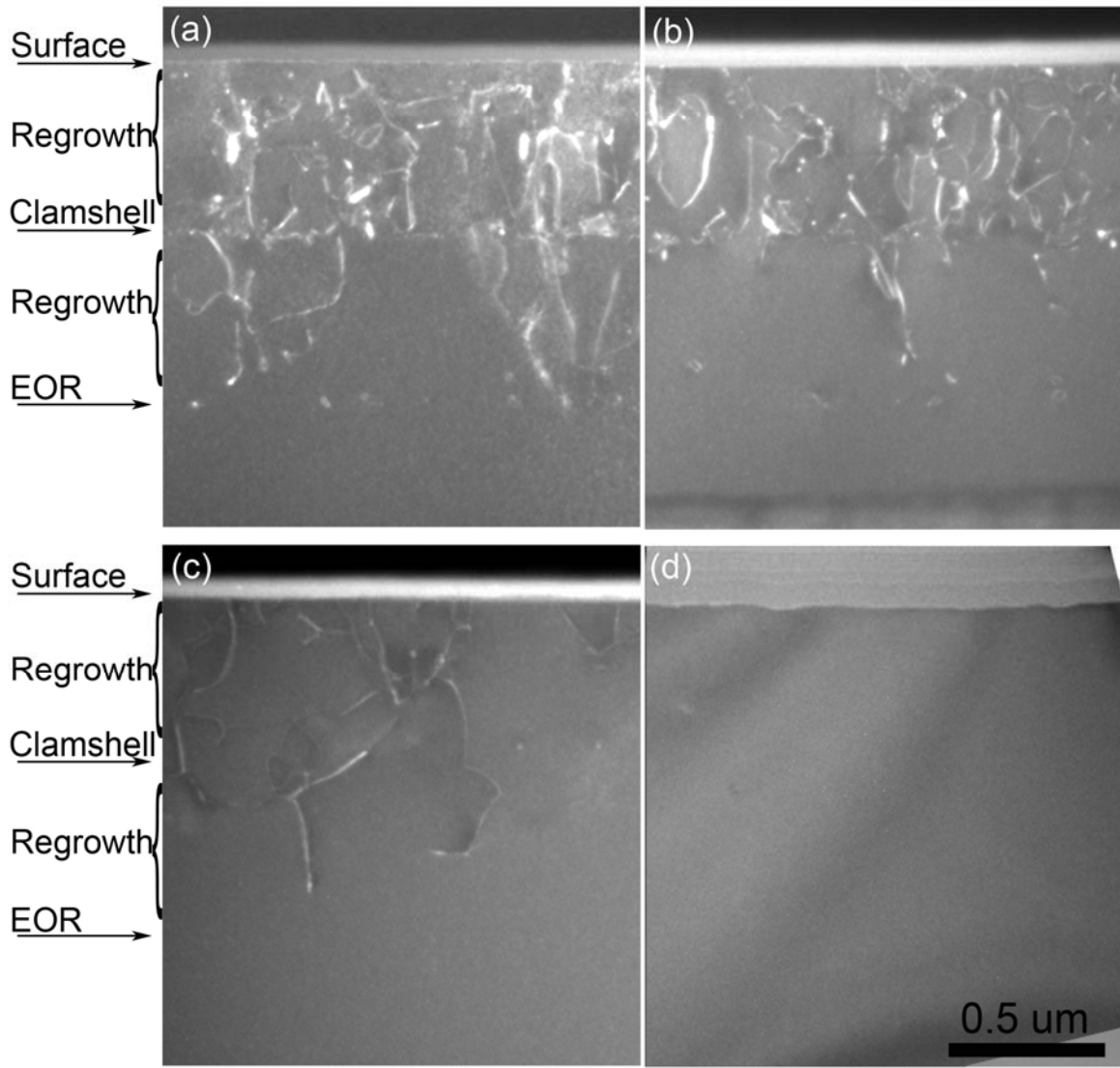


Figure 5-3. WBDF XTEM images of Ge Si⁺ implanted at 1 MeV to a dose of $1 \times 10^{15} \text{ cm}^{-2}$ after annealing for 10 min at (a) 450 (b) 550 (c) 650 and (d) 750 °C. Types of defects are labeled next to the images.

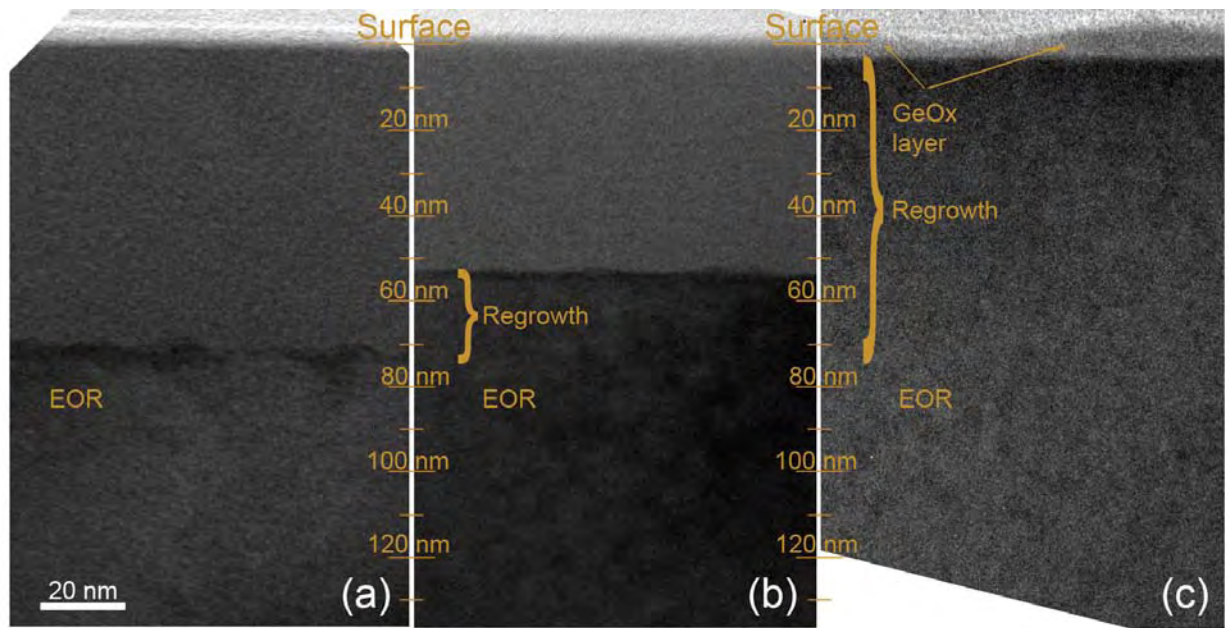


Figure 5-4. XTEM images of Ge Si⁺ implanted at 40 keV to a dose of $1 \times 10^{15} \text{ cm}^{-2}$ at 303 K (a) as-implanted and after annealing for 10 min at (b) 350 and (c) 380 °C for 10 min.

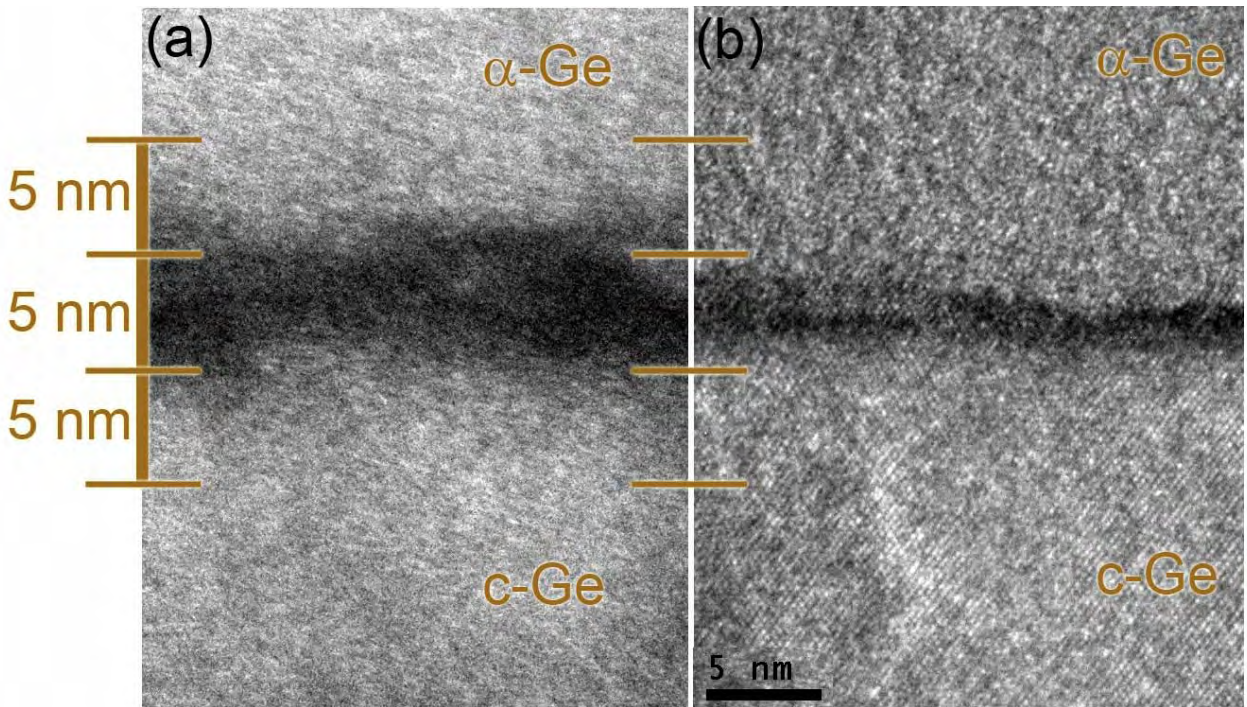


Figure 5-5. HR-XTEM images taken of Ge Si^+ implanted at 40 keV to a dose of $1 \times 10^{15} \text{ cm}^{-2}$ (a) as implanted, with a rough a-c interface approximately 10 nm thick and (b) after annealing at 350 °C for 10 min.

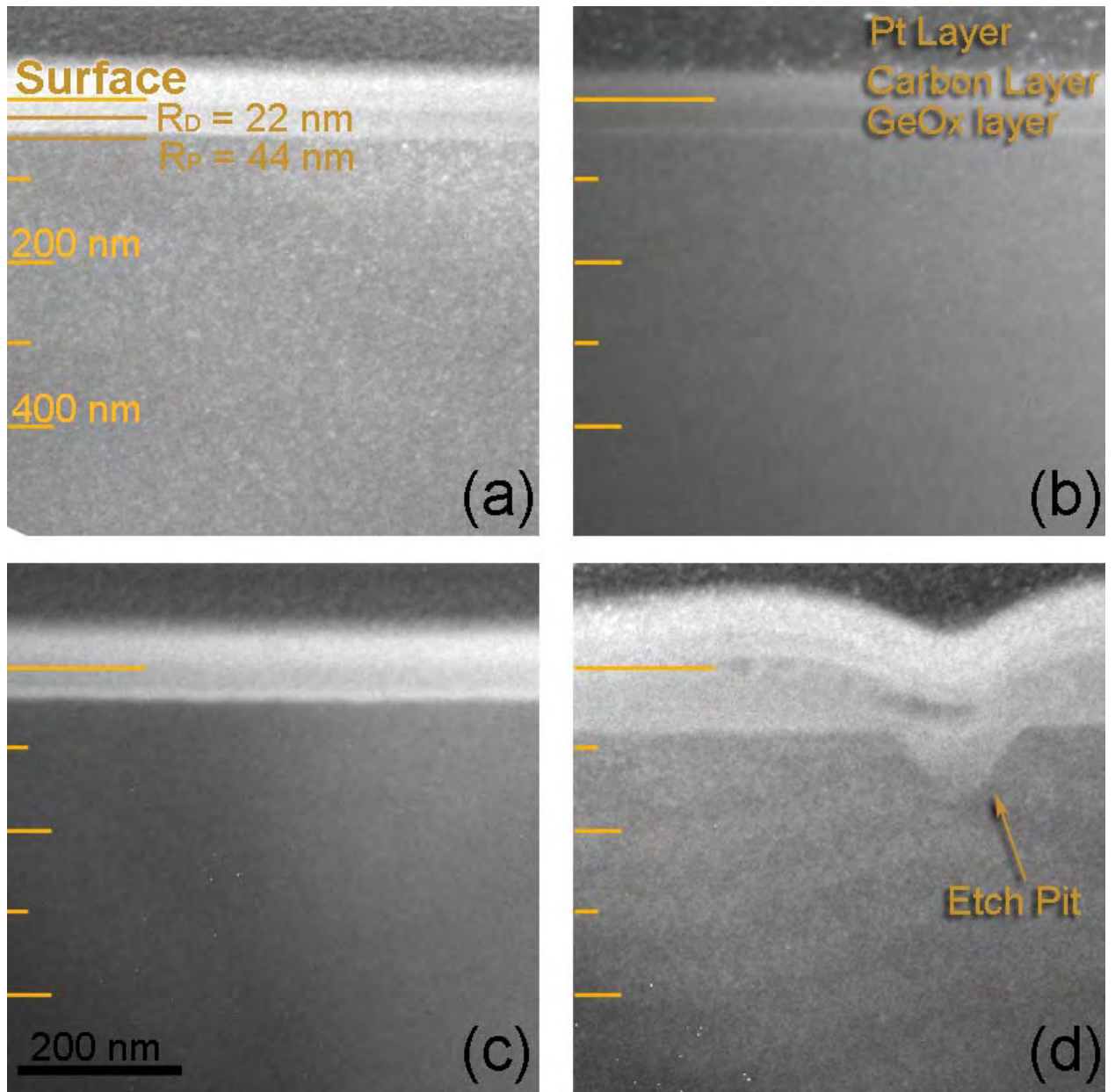


Figure 5-6. WBDf-XTEM images taken of Ge Si⁺ implanted at 40 keV to a dose of $1 \times 10^{15} \text{ cm}^{-2}$ at 303 K and annealed for 10 min at (a) 450 (b) 550 (c) 650 and (d) 750 °C.

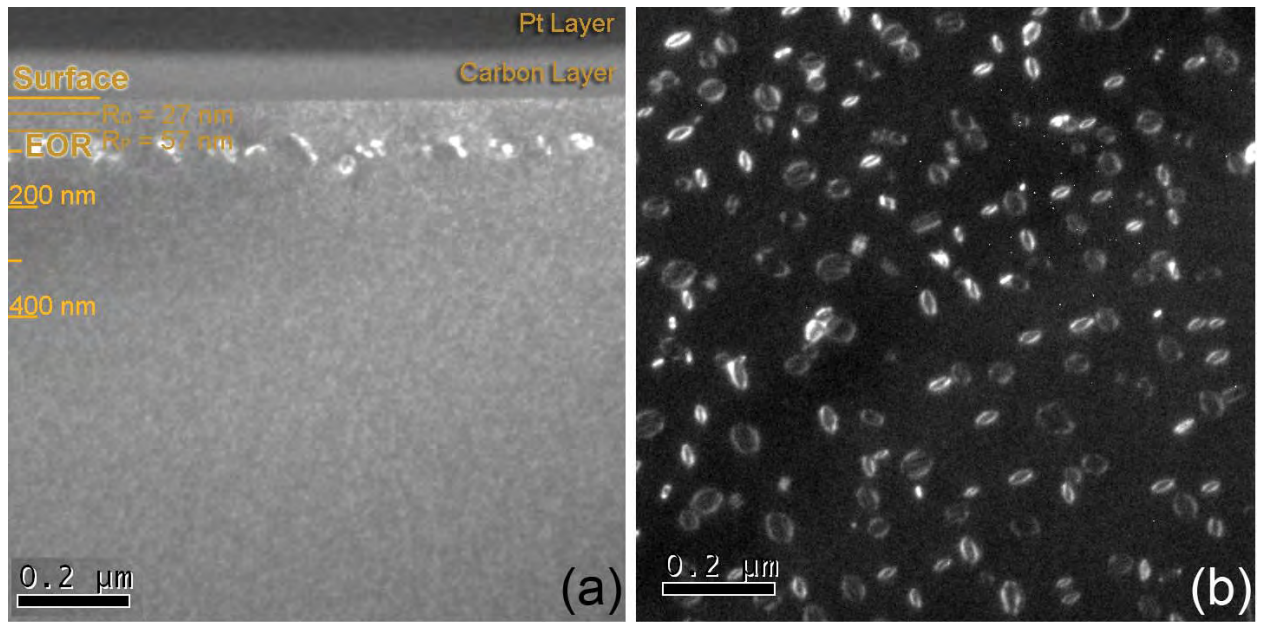


Figure 5-7. WBDF-XTEM images taken of Si Si⁺ implanted at 40 keV to a dose of $1 \times 10^{15} \text{ cm}^{-2}$ at 303 K and annealed for 10 min at 750 °C (a) XTEM and (b) PTEM.

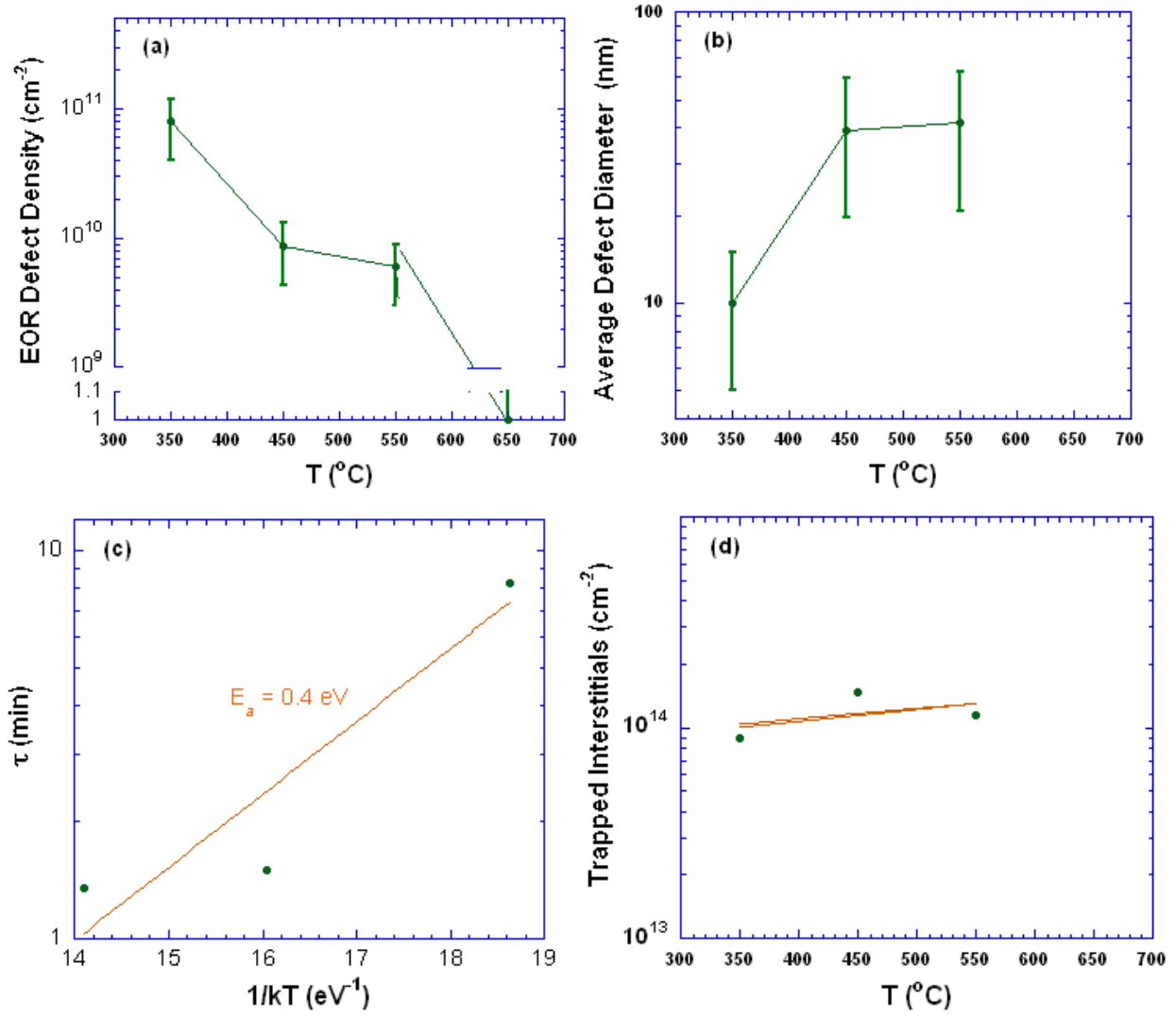


Figure 5-8. Graphical representations of the temperature dependence of the Ge EOR (a) defect density, (b) defect size, (c) dissolution rate and (d) trapped interstitials.

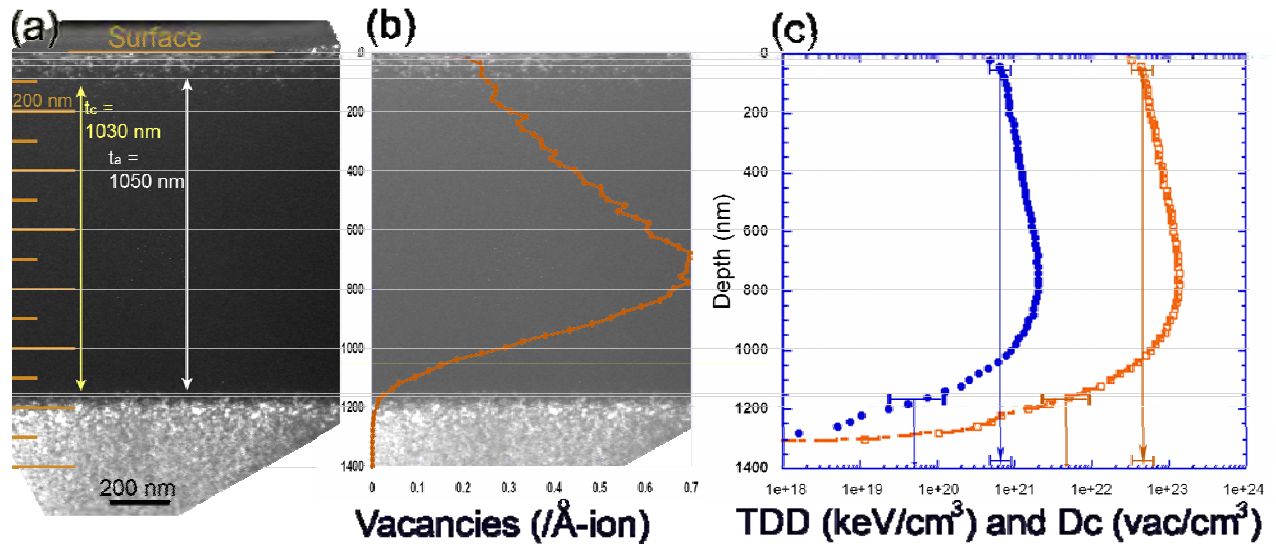


Figure 5-9. XTEM images of Ge Si⁺ implanted at 1 MeV to a dose of $1 \times 10^{15} \text{ cm}^{-2}$ at 303 K (a) as-implanted and (b) as-implanted with simulated total vacancies. (c) Plot of TDD (●) and D_c (□) versus depth as predicted by simulations.

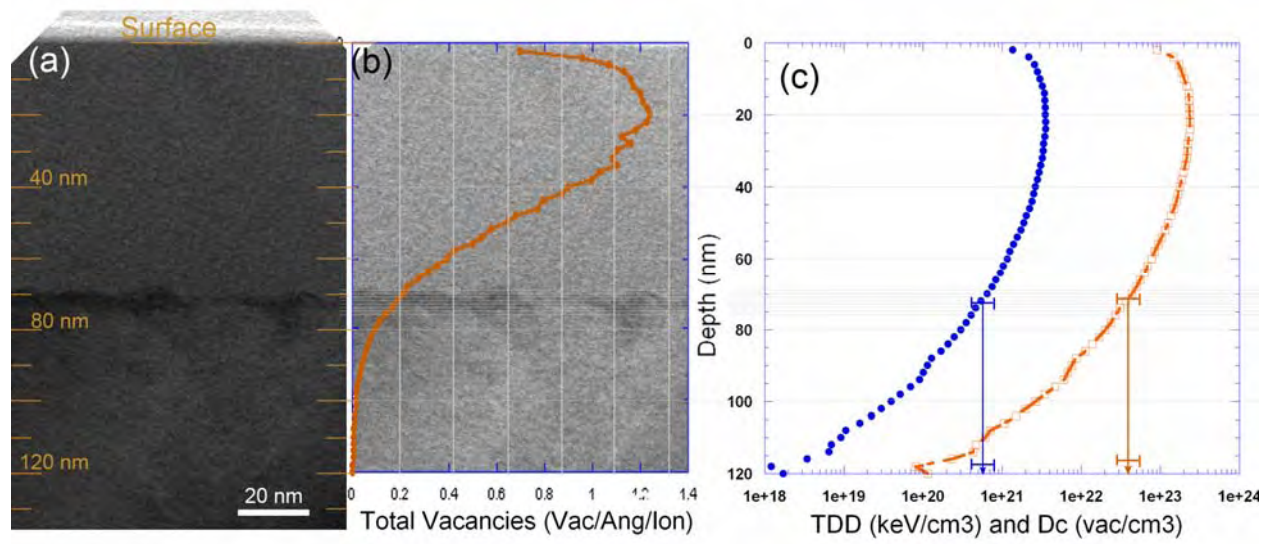


Figure 5-10. XTEM images of Ge Si⁺ implanted at 40 keV to a dose of $1 \times 10^{15} \text{ cm}^{-2}$ at 303 K (a) as-implanted and (b) as-implanted with simulated total vacancies. (c) Plot of TDD (●) and D_c (□) versus depth as predicted by simulations.

Table 5-1. Simulated damage values from current experiments.

Material, Implant Energy, Temperature & Dose	Threshold Damage Density (keV/cm ³)	Critical Damage (vacancies/cm ³)	DPA (unitless)
Ge 1000 keV, 303 K, 1×10^{15} Si ⁺ cm ⁻²	$7.0 \pm 2 \times 10^{20}$	$4.5 \pm 1.5 \times 10^{22}$	0.8 ± 0.2
Ge 40 keV, 303 K, 1×10^{15} Si ⁺ cm ⁻² <i>Bulk Interface Measurement</i>	$5.5 \pm 1.5 \times 10^{20}$	$3.5 \pm 1 \times 10^{22}$	0.9 ± 0.1
Si 40 keV, 303 K, 1×10^{15} Si ⁺ cm ⁻² <i>Bulk Interface Measurement</i>	$7.5 \pm 1.5 \times 10^{20}$	$5.0 \pm 1 \times 10^{22}$	1.0 ± 0.2

CHAPTER 6 RESULTS FROM NON-AMORPHIZING MEV IMPLANTS INTO DIAMOND

Thus far, the defects created from ion-implantation in silicon (Si) have been compared to those in germanium (Ge). However, carbon (C) was also presented in Chapter 1 as a potential base material, though little direct transmission electron microscopy (TEM) research has been performed on single-crystal diamond. Additionally, there has been a growing interest in utilizing synthetic diamond for engineering applications since diamond was first synthesized by Bundy.⁷⁰ The development over the past few years of increased production of both chemical vapor deposition (CVD) grown and high-pressure-high-temperature (HPHT) man-made diamonds, along with reported high carrier mobilities⁷² and the demonstration of diamond transistors⁸⁰ have all driven this increasing interest.⁴ In order to be an effective semiconductor, single-crystal diamond must be precisely doped to increase conductivity without graphitizing the diamond. Ion implantation has been used for decades to dope silicon for use in microelectronics. Similarly, ion implantation has been studied for over 30 years in diamond.^{82,138} However, with the small amount of TEM analysis, repair of the crystal after ion implantation and the identification of associated defects has been derived from electrical measurements and spectrometry analysis techniques. Direct imaging of the transformation has not been captured.

This chapter presents the results of non-amorphizing Si^+ implantation into single crystal diamond, and the evolution of the damage upon annealing. Unlike Si, no {311} defects are observed. Unlike Ge, no dot-like defects are observed. Only a slight contrast in the damaged crystal is apparent in the TEM images after implantation. After annealing, the contrast is reduced, but no extended defects are observed to form. An implant temperature comparison of a Si^+ implantation at 1 MeV with a dose of $1 \times 10^{15} \text{ Si}^+ \text{ cm}^{-2}$ revealed that, upon annealing, implantation at 77 K creates buried discontinuous amorphous regions but implantation at 303 K

anneals to a perfect crystal. This indicates that this implant is right at the verge of the amorphization threshold.

Introduction

In Si, evolution of defects related to ion-implantation has been studied by TEM. Transmission electron microscopy would be an excellent method to further pursue a number of research questions in C, especially defect formation and evolution as the result of ion implantation and annealing, and the phase transformation from crystalline C to amorphous C. Transmission electron microscopy samples require a thickness between 50 - 300 nm to be electron transparent. Creating these samples is typically a very time-consuming process because of the properties of diamond. {Yin, 2000 #36} Mechanical polishing and ion milling methods are typically used to create samples from CVD-grown diamond films, and high resolution TEM (HRTEM) has been used to image CVD-grown diamond film defects.¹²⁰ Due to the difficulty in creating TEM samples from single crystal diamond, few studies have been reported.⁹⁶ In the 1960s, TEM samples were prepared by oxidation thinning, by flowing oxygen at 750 °C or carbon dioxide at 1350 °C over the diamond substrate, thereby gas etching the crystal.¹¹⁹ However, this process does not protect the surface and is not selective of the area. Other disadvantages of this method are that the sample must be boiled in an acid mixture to remove the surface layer of carbon that forms and such high temperatures may anneal out defects present in the sample.⁹⁶ In 2001, plan view TEM (PTEM) studies were performed on ion-implanted natural diamond.¹⁰⁴ Yin has reported on the defects in a lab-grown HPHT diamond crystal studied using TEM as one method.^{96,106} Additional TEM studies of HTHP single crystal diamond whiskers¹⁰⁷ and particles¹⁰⁸ have been conducted. However, these sample preparation methods were not area selective in nature.

Experimental Design

Preliminary Experiments

Preliminary experiments on plasma-doped single crystal diamonds were performed to determine appropriate annealing conditions to study the elimination of damage from diamond after ion implantation. As the literature reports anneal temperatures from 300 °C¹⁹ to 1600 °C⁹², and Si is known to only produce defects in certain doses and temperature regimes, preliminary experiments were necessary to determine appropriate temperatures. The samples were annealed at 300, 400, 500, 700, and 900 °C, with the results from these experiments and recent literature results indicating that temperatures above 900 °C are necessary for damage elimination,⁹² though some recent literature still contradicts this conclusion.⁷⁵

Presented Experiment

Gem-quality HPHT single-crystal diamond samples, approximately $5 \times 5 \times 1 \text{ mm}^3$, were Si⁺ implanted according to Table 1. This ion species was chosen to reduce variables between comparing this experiment with the Ge and Si experiments, and to keep from introducing dopant interaction effects due to the electrical differences between group elements. It is well known that Group III and IV dopants can affect the formation and dissolution of defects in Si, and this additional effect was not desired for these experiments.^{27,32,139} The implantation of Si⁺ into the diamonds was performed in a tandem accelerator ion implanter, with a dose rate of $0.44 \mu\text{A}/\text{cm}^2$ for all experiments. Samples were tilted 7° relative to the incident ions to minimize ion channeling. The original nitrogen (N₂) impurity concentration of the diamonds, obvious from the visible light-orange color, is on the order of $10^{18} - 10^{20} \text{ cm}^{-3}$,¹⁴⁰ and was uniform throughout the crystals.

According to simulations,²¹ the damage should peak (R_d) at approximately 540 nm and the projected range (R_p) of the damage should be approximately 570 nm below the surface of the

diamond for 1 MeV Si⁺ implantation, and 840 nm and 900 nm for 2 MeV Si⁺ implantation. After implantation, a 1000Å layer of silicon dioxide (SiO₂) was plasma-enhanced chemical vapor deposition (PECVD) deposited on the (011)-oriented sample surfaces, Si⁺ implanted at 1×10^{14} Si/cm², with the thermal exposure of the diamond being 310 °C for approximately one minute. A separate 1000Å layer of SiO₂ was sputter-deposited onto the (011)-oriented sample surfaces, Si⁺ implanted at 1×10^{15} Si/cm², with the thermal exposure of the diamond being less than 100 °C. The original purpose of the SiO₂ layer was to compositionally separate the C of the crystalline diamond from the conductive carbon coating applied during sample preparation. However, surface etching occurred after initial anneals as C is highly reactive with oxygen (O₂) at higher temperatures¹⁴¹ and this practice of placing an O₂ compound next to a reactive C layer was eliminated for further samples. It should be noted that the SiO₂ PECVD layer remained on after annealing at 950 °C; however, the sputter-deposited layer peeled off. The PECVD SiO₂ layer did remain on the Si⁺ implanted to a dose of 1×10^{14} cm⁻² sample, and did seem to protect it from surface erosion. This won't work at higher temperatures, where the Ellingham diagram shows that C-O₂ compounds are more stable than Si-O₂ compounds, but a nitride layer might be a good alternative. Approximately 150 nm of carbon was evaporated onto all samples, for conductivity and protection of the sample surface during focused-ion beam processing. Cross-sectional TEM (XTEM) samples were prepared according to the procedure previously published by the author,¹¹⁷ during which a layer of Platinum was applied to the surface. Both layers, if visible, are noted in all TEM images presented here.

Annealing was performed in both tube and graphite furnaces. Samples annealed at 1050 °C and below were annealed in a Lindberg tube furnace in a high-purity N₂ environment. Anneals at 1250 and 1350 °C used a graphite chamber furnace at diffusion pump vacuum pressures ($\leq 10^{-4}$

Torr)¹⁴² with a residual He environment. Additionally, the samples were placed in tantalum (Ta) foil (folded as envelopes), which is an O₂ getterer, to additionally prevent accidental oxidation of the diamond surface. The Ta envelopes served the additional purpose of separating and marking each sample separately. Transmission electron microscopy analysis was performed on JEOL 200CX and JEOL 2010 microscopes.

Results

As-implanted Comparison: Orientation, Dose, Temperature

Orientation of the diamond crystal, whether (011) or (001), did not affect the implant damage severity or range, as detectable using these TEM methods. Changing the dose did significantly change the damage density in the crystal. As expected, with increasing dose, there was increasing damage, as already shown between the 1×10^{14} and 1×10^{15} cm⁻² dose implants, shown in the SRIM section of Chapter 3, in Figures 3-14(b) and 3-15(b) respectively. Higher Si⁺ doses of 3×10^{15} Si⁺/cm² and 7×10^{15} cm⁻² will be shown in Chapter 7.

The temperatures chosen for this study, 77 K and 303 K, are in the range that ‘freezes in’ point defects in diamond.⁸⁵ However, it is known that even a room temperature implant can, due to dynamic annealing, achieve significantly different results than at liquid nitrogen temperature. As-implanted, the difference between the sample Si⁺ implanted at 1 MeV to a dose of 1×10^{15} cm⁻² at 77 K and 303 K is shown in WBDF-TEM imaging using a g₂₂₀ two-beam condition, as presented in Figure 6-1. The range of damage for the 77 K implant is larger than that of the 303 K implant, as evidenced by Figures 6-1(a) and (b), respectively. Additionally, the 77 K implant seems to have a dark band of damage in the midst of the larger damage band. Upon initial imaging, this was thought to be a continuous amorphous layer of material, but upon high-resolution imaging, was shown to be severely damaged diamond enclosed in a diamond lattice.

Larger differences between these two temperatures appear during the annealing process, as discussed later.

Annealing: Low Dose

As discussed, preliminary annealing experiments were used to determine that even low damage in diamond shows little change when annealed at temperatures below 950 °C, which is 20% of the triple point of diamond-graphite-liquid, or 56% of the stable diamond temperature at vacuum. ¹¹¹ (011)-oriented diamond, Si⁺ implanted at 1 MeV to a dose of $1 \times 10^{14} \text{ cm}^{-2}$ at 303 K, is shown using BF-XTEM imaging in Figure 6-2 (a). After annealing at 950 °C for 10 min, the damaged layer, although slight, is still visible in Figure 6-2 (b). The damage band becomes less noticeable after 40 min as shown in Figure 6-2 (c), but at 120 min of annealing, presented in Figure 6-2, unusual defects extending from the surface, begin to appear. Some defects seem to be oriented at approximately 37° to the surface, though the exact crystal morphology is unclear. As the defects are intermittent, and begin at the surface, it is not believed that these defects are associated with the implant. The defects will be briefly discussed in Appendix A. Another diamond sample, (001)-oriented and similarly implanted, annealed at 1250 °C for 1 hr is shown using WBDF-XTEM imaging in Figure 6-3 and shows that damage is still present at this temperature.

Annealing: High Dose

In the literature, many references were made to the ability of diamond to regain its crystalline form (if the damage threshold was not exceeded beyond amorphization) around 1000 °C. ⁷⁵ Therefore, another annealing sequence was performed just below this threshold to try to capture extended defect formation and evolution. Diamond, (011)-oriented and Si⁺ implanted at 1 MeV to a dose of $1 \times 10^{15} \text{ cm}^{-2}$ (an order of magnitude higher than the previous implant, with $R_D = 540\text{nm}$ and $R_P = 570\text{nm}$) at 303 K, is shown in Figure 6-4 both after implantation, shown in

Figure 6-4(a), and an annealing sequence. No overall repair of the lattice has occurred and the damage band is still quite clear after 10, 40, and 120 min of annealing, shown in Figures 6-4 (b) - (d) respectively. However, significant surface etching occurred during the annealing procedure, as shown in Figure 6-4 (d). Further annealing times would probably completely eliminate the implant damage. Thus, due to the surface etching by residual O₂ in the furnace during annealing, higher-temperature anneals were performed in a graphite chamber under vacuum.

Annealing: Implant Temperature Effect

As noted in an earlier section, there were slight differences in the damage created after the same implant at different implant temperatures. However, after annealing at 1350 °C for 24 hrs, significant differences appear. The specimen implanted at 303 K, shown in Figure 6-5(a), almost completely recrystallized to undamaged diamond, shown in Figure 6-5(b).

In stark contrast, implantation at 77 K leaves pockets of amorphous material near R_p after annealing, as shown in Figures 6-6(a) and (b). These pockets, in WBDF imaging conditions resembled extended defects as presented in Figure 6-6(c). However, tilting to 50° away from the [110] zone axis and performing BF imaging revealed a seemingly ordered and consistently thick layer of defects. However, upon closer review in HRTEM imaging, these were determined to be pockets of amorphous material in a crystalline matrix. As shown in Figure 6-7, HRTEM images taken from the middle of the damaged layer revealed pockets of amorphous material.

Although no extended defects were observed in the damage range after the 1350 °C anneal of samples implanted at both temperatures, unusual and intermittent defects extending from the surface occurred in the sample implanted at 77 K. As in the case of the lower dose ($1 \times 10^{14} \text{ cm}^{-2}$) Si⁺ implant, presented in Figure 4-5(d), these defects are not believed to be associated with the implant because of their intermittent nature and apparent surface orientation. Hence, since these

are defects, though not associated with implantation (the defects were also seen when annealing unimplanted diamonds), these defects will be discussed in Appendix A.

Discussion

As-implanted comparison. As implanted, there is no significant difference between the implant into a (011)-oriented or (111)-oriented diamond, which is not different that what is expected from Si. However, there is considerable difference at higher doses. This is not unexpected, but necessary to comment on because dose will have a large effect upon annealing. Importantly, for the same energy, dose rate, ion species, and implant temperature, Si and Ge amorphized, but diamond did not. In previous chapters, Si⁺ implantation to a dose of 1×10^{15} cm⁻² dose was discussed in the Ge amorphization chapter. For diamond, this dose did not amorphize the diamond upon implant, in implantation at 303 K or 77 K. However, there is some difference seen on implant between the implant temperatures. Both created significant projected range damage, but no immediate defects are seen, nor is a continuous amorphous layer created upon implant. This shows a major difference between Ge, Si and Diamond since small dot-like defects were seen immediately upon non-amorphizing implantation in Ge. No defects are seen upon implant in either Si or Diamond for non-amorphizing implants. This may be related to the mass of the elements (since the lower mass elements show no defects) or the bond energy, since Ge has the lowest bond energy.¹¹¹ Also, the lack of as-implanted defects may be related to the ion-implantation process, since Si⁺ implantation into diamond introduces a more massive particle than the host material, indicating nuclear stopping will begin more rapidly. Si ions into Si are approximately the same mass, and Si ions into Ge are much less massive, and nuclear stopping may not occur for some distance into the crystal.²⁰

Annealing: low dose. The damage created by the lower dose Si⁺ implantation, to a dose of 1×10^{14} cm⁻², seems to be completely eliminated after a 950 °C, 4 hour anneal. However, due to

the presence of the surface initiated defects, this conclusion may be invalid. The defects may have interacted with the damaged diamond to assist in the diffusion of point defects from the damaged area or affected the imaging technique during TEM, making it difficult to view the contrast from damaged material. WBDF TEM images of specimens after high temperature anneal at 1250 °C shows that damage still exists in the crystal. Even for this respectively low dose, higher annealing temperatures (or longer times) are necessary for full repair of the crystalline damage imparted by implantation at 1 MeV. No extended defects were observed at any stage of the annealing process, which is unlike what was seen for non-amorphizing experiments in Ge and Si.

Annealing: high dose. For the higher dose in this study, it is shown that annealing at 1050 °C, even for times up to 2 hours, is not significant to repair the lattice. Annealing at 1350 °C for one hour still reveals residual damage for an implant temperature of 303 K. This is in agreement with recent electrical studies that recommend anneal temperatures around 1500 °C to completely repair the crystalline lattice.⁹² It should be noted that the referenced study was with a B⁺ implantation at 2 MeV and the TEM imaging results from an identical implant will be shown in Appendix B. The results here, and of Vogel,⁹² contradict other studies that recommend temperatures of 600 – 1000 °C^{88 74} are sufficient for lattice repair. Again, no extended defects were observed for the higher dose, non-amorphizing implant.

Annealing: implant temperature effect. At the verge of amorphization, the implant temperature has a profound affect upon annealing. A Si⁺ implantation at 303 K at a dose of $1 \times 10^{15} \text{ cm}^{-2}$, followed by annealing at 1350 °C shows no extended defects forming, and damage is significantly reduced in the crystal from the as-implanted state. However, for implantation at 77 K, the elimination of room-temperature dynamic annealing allowed enough extra damage to

form within the crystal, which upon annealing at 1350 °C, local collapsing of the lattice into amorphous pockets occurred. No extended defects were observed either in the damage range of the specimens implanted at 303 K implant or around the amorphous pockets of material in specimens implanted at 77 K.

The lack of extended defects agrees with molecular dynamics simulations that predict that the stable defect in diamond is the <110> split interstitial, also referred to as a dumbbell structure, which is a point defect, not an extended defect.¹⁴³ However, this structure is not observable in TEM since it is a point defect. The most likely reason that extended defects are not forming in the diamond lattice is the strong covalent bond between the carbon atoms may make other configurations thermodynamically unstable. The diffusion of self-interstitials in carbon may also be faster than in Si or Ge, which may contribute to the lack of extended defect formation. Further computational analysis is necessary to shed definitive light onto the reasoning behind the lack of extended defects in this implantation regime.

Conclusion

This chapter covered ion implantation experiments into single crystal diamonds that did not exceed the crystalline damage level necessary to amorphize the crystal. From these experiments, the following conclusions are drawn. Crystal orientation makes no noticeable difference on ion-implantation damage depth or amount of damage to the diamond. Implantation into (001)-oriented diamonds versus (011) oriented diamonds yields similar implant results, within the limitations of TEM imaging. The verge of diamond amorphization was captured at the 1 MeV, 1×10^{15} Si⁺/cm² implant. Upon implantation, the liquid nitrogen temperature (77 K) and a room temperature implant (303 K), with all other parameters being equal, displayed approximately the same depth and amount of damage. However, the 77K seemed to have a band of defects in WBDF, but upon closer inspection using HRTEM, revealed damaged diamond, and

not an amorphous layer. Upon annealing, the 77 K implant trapped amorphous pockets, while the 303 K implant almost fully recovered the crystal structure. To fully anneal the damage from the crystal, 1 hour at 1250 °C appears almost sufficient for a 1×10^{14} Si/cm² 1 MeV, 303 K implant. However, some damage (though slight) still is apparent for the 1×10^{15} Si/cm² implant after 24 hrs at 1350 °C. Higher annealing temperatures or longer times are necessary to completely anneal out the implant damage. No extended defects were observed to develop in the heavily damaged regions. However, non-uniform defect distribution from the surface did appear in select samples, and is discussed in Appendix A. Since no extended defects were seen in the damaged region, this agrees with molecular dynamics simulations that determined the stable defect in diamond is the <100> split interstitial. The {311} defect does not seem to be the preferred interstitial defect for this diamond-lattice material, as was theorized. The verge of critical damage density to convert crystalline diamond to a buried amorphous layer is at the conditions of an implant equal to an energy, dose, dose rate, and implant temperature of 1 MeV, 1×10^{15} Si⁺/cm², 0.44 μA/cm², 77 K.

In the previous chapters, the defect behavior of Ge was compared to that of Si. In this chapter, it has been shown that for non-amorphizing implants, diamond does not display any defects related to the implant damage. In Ge, non-amorphizing implants at 1 MeV produced dot-like defects, and in Si, {311} defects. Though it seems that diamond fully recrystallizes upon annealing without showing defects, further study is necessary. Higher annealing temperatures could be tried, up to 1700 °C, to see if defects develop. However, it is unlikely that defects will be visible after a higher annealing temperature as past experience in Si shows that a higher annealing temperature would only speed defect dissolution, not formation. Annealing diamonds above 1700 °C destabilizes the crystal, even under the best vacuum, and the C converts to a

graphitic form.^{82, 85} This may be the explanation as to why defects are not seen in this study of diamonds. Defects appear in Si at approximately 750 °C and in Ge at approximately 450 °C and both temperatures are about 50% of the respective melting points, while diamond has no melting point. There is a triple point which occurs at approximately 4492 °C. Thus, 50% of 4492 °C is slightly above 2000 °C, which is above the destabilization temperature of diamond. However, even if the diamond was stable, it is unlikely that {311} defects would form because longer time anneals were used in this study. In Si, defect formation and evolution are related to the time and temperature of the anneal. A {311} defect appears in Si after 5 min at 800 °C, 33 min at 750 °C, or 47 hours and 14 min at 650 °C.²⁷ Therefore, since almost all the damage has annealed out of diamond for 1350 °C 24 hours, without showing extended defects, it is unlikely that longer times or higher temperatures would reveal extended defects.

Thus far, the three Group IV diamond-cubic semiconductors have not created the same defects after identical anneals. For sub-amorphizing implants, C has not shown any extended defects. Si showed none upon implant, but {311} defects were apparent during the annealing process, and were stable to about 65% of the melting point. Ge showed dot-like defects immediately after implant, some of which were stable up to 70% of its melting point. The last condition that will be studied is amorphizing implants into diamond, and that will be discussed in the next chapter.

Table 6-1. Implantation parameters

Parameter Varied from base implant	Orientation	Implant Temperature, T_i (K / °C)	Energy (keV)	Fluence & Ion, ions/cm ²
Base Implant	<100>	303 / 30	1000	1×10^{15} Si
Orientation	<110>	303 / 30	1000	1×10^{15} Si
Dose	<100>	303 / 30	1000	1×10^{14} Si
Dose & Orientation	<110>	303 / 30	1000	1×10^{14} Si
Temperature	<100>	77 / -196	1000	1×10^{15} Si
Temperature & Energy	<100>	77 / -196	2000	1×10^{15} Si

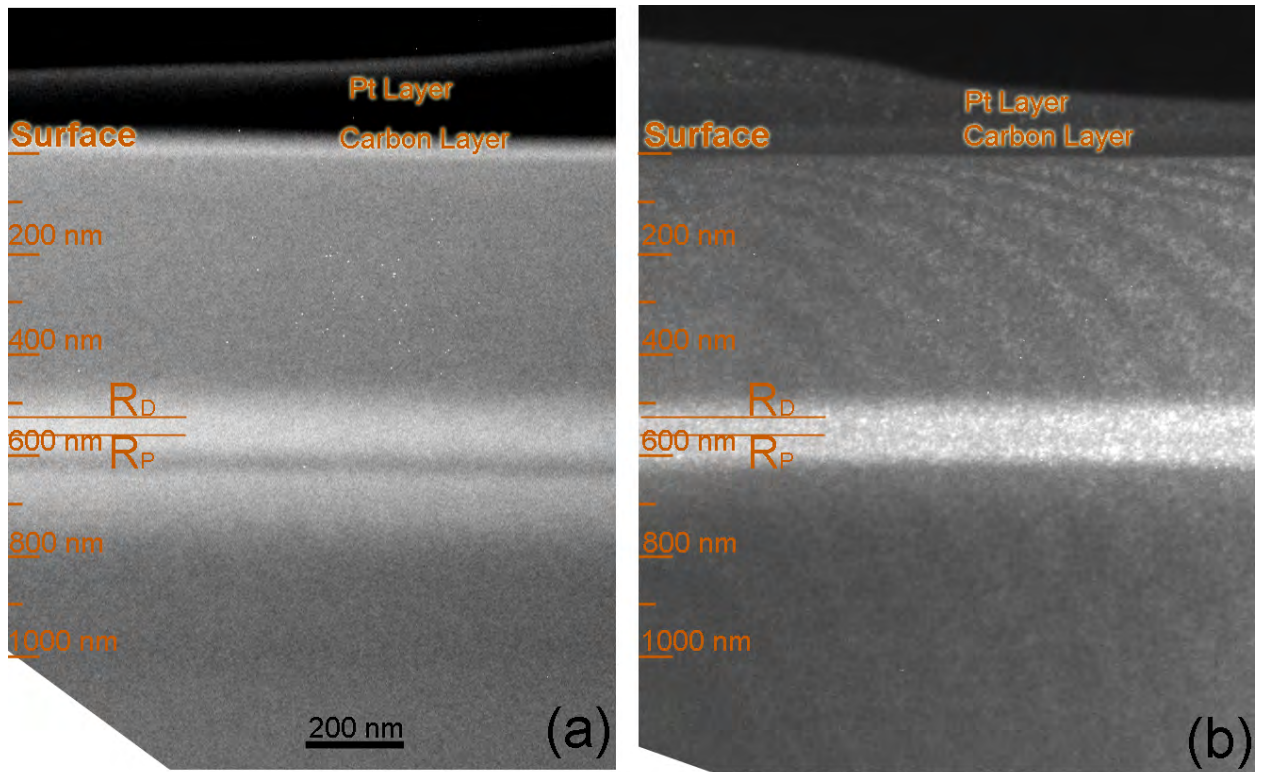


Figure 6-1. WBDX-TEM images of (001)-oriented single-crystal diamond Si^+ implanted at 1 MeV to a dose of $1 \times 10^{15} \text{ cm}^{-2}$ at (a) 77K and (b) 303K.

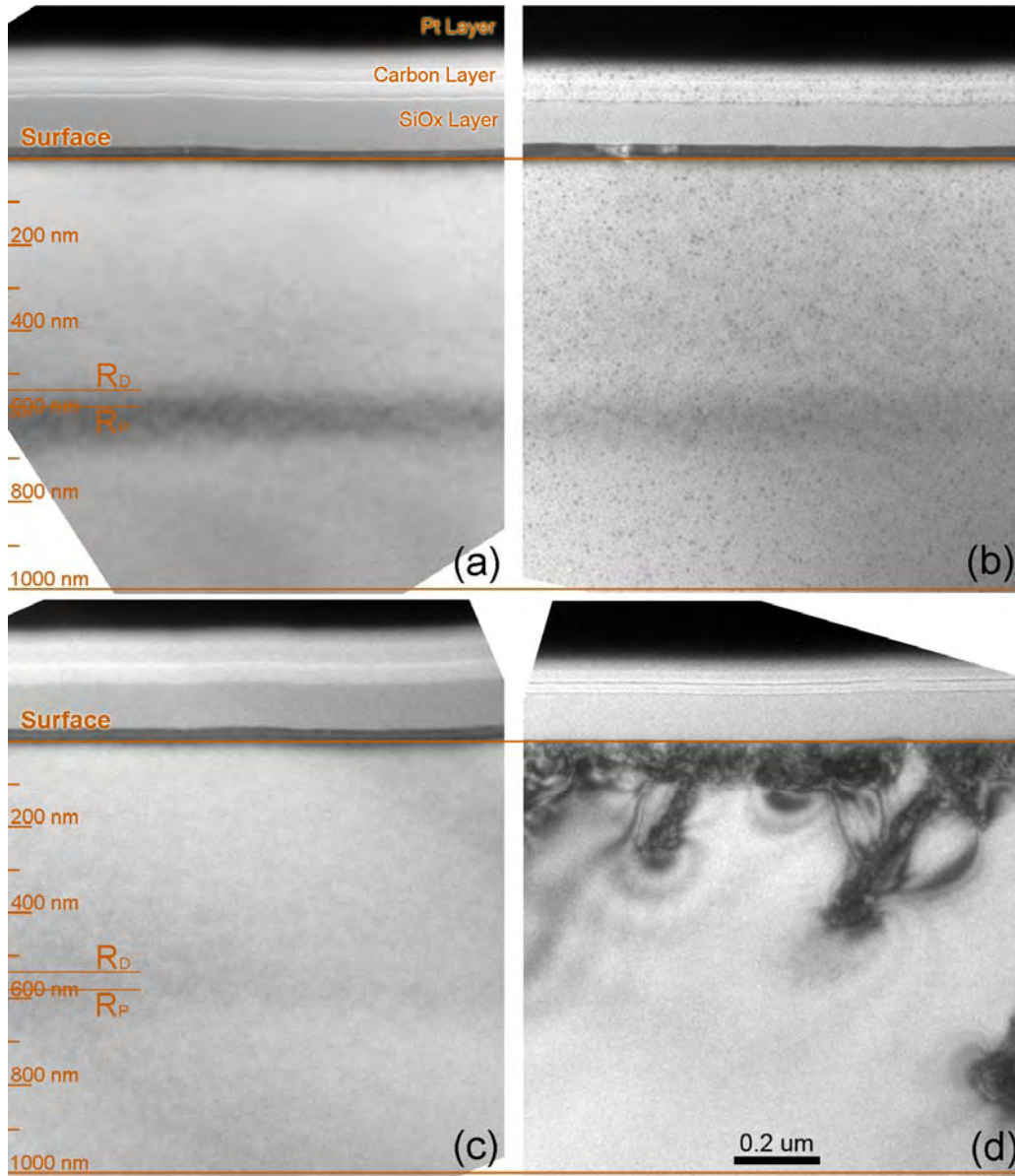


Figure 6-2. BF TEM images of (011)-oriented diamond Si^+ implanted at 1 MeV to a dose of $1 \times 10^{14} \text{ cm}^{-2} \text{ Si}^+$ at 303K (a) as implanted, and annealed at 950 °C for (b) 10 min, (c) 40 min and (d) 120 min.

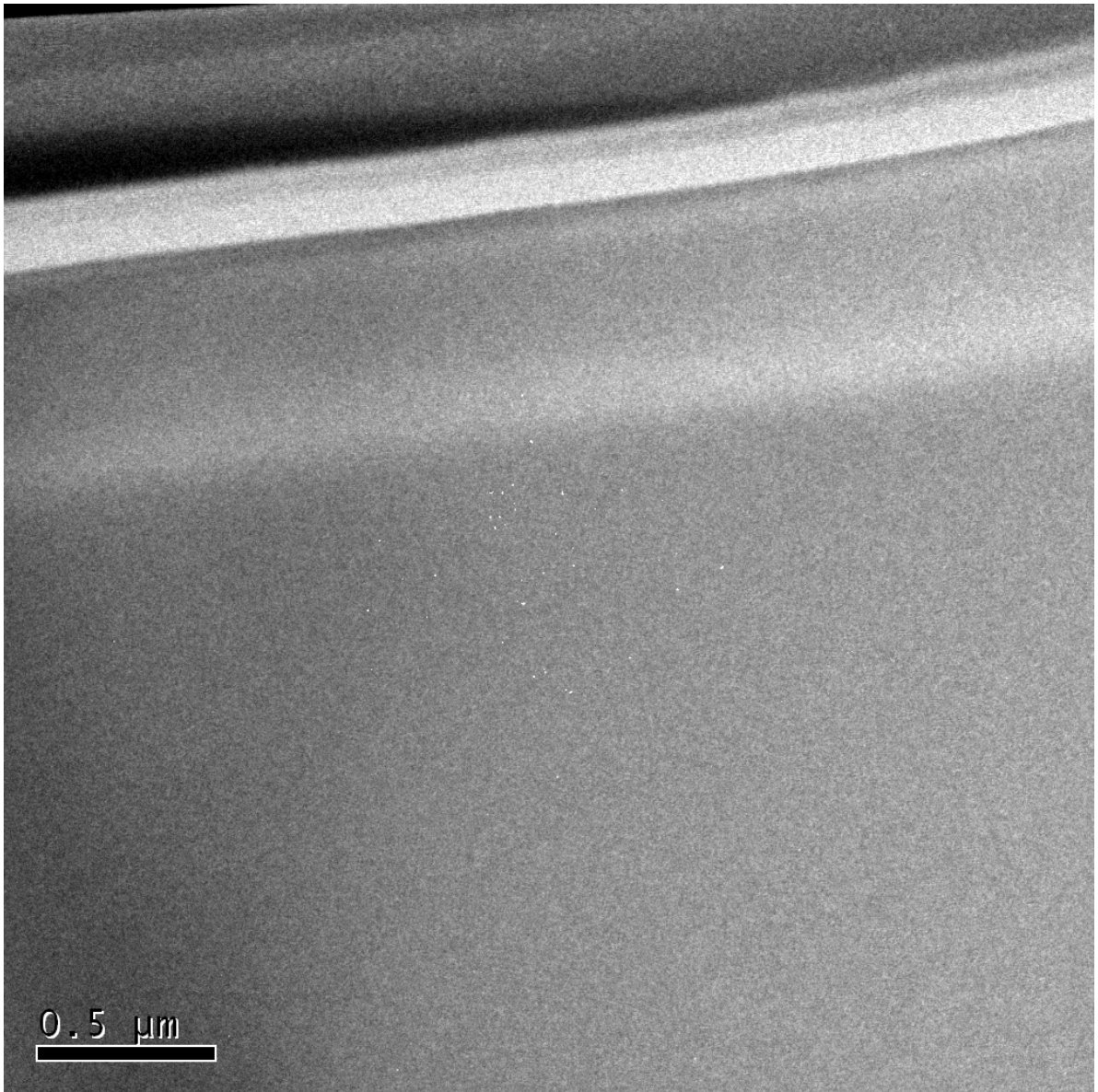


Figure 6-3. WBDF-XTEM image of (001)-oriented diamond Si^+ implanted at 1 MeV to a dose of $1 \times 10^{14} \text{ cm}^{-2}$ at 303K after annealing at 1250 °C for 1 hr.

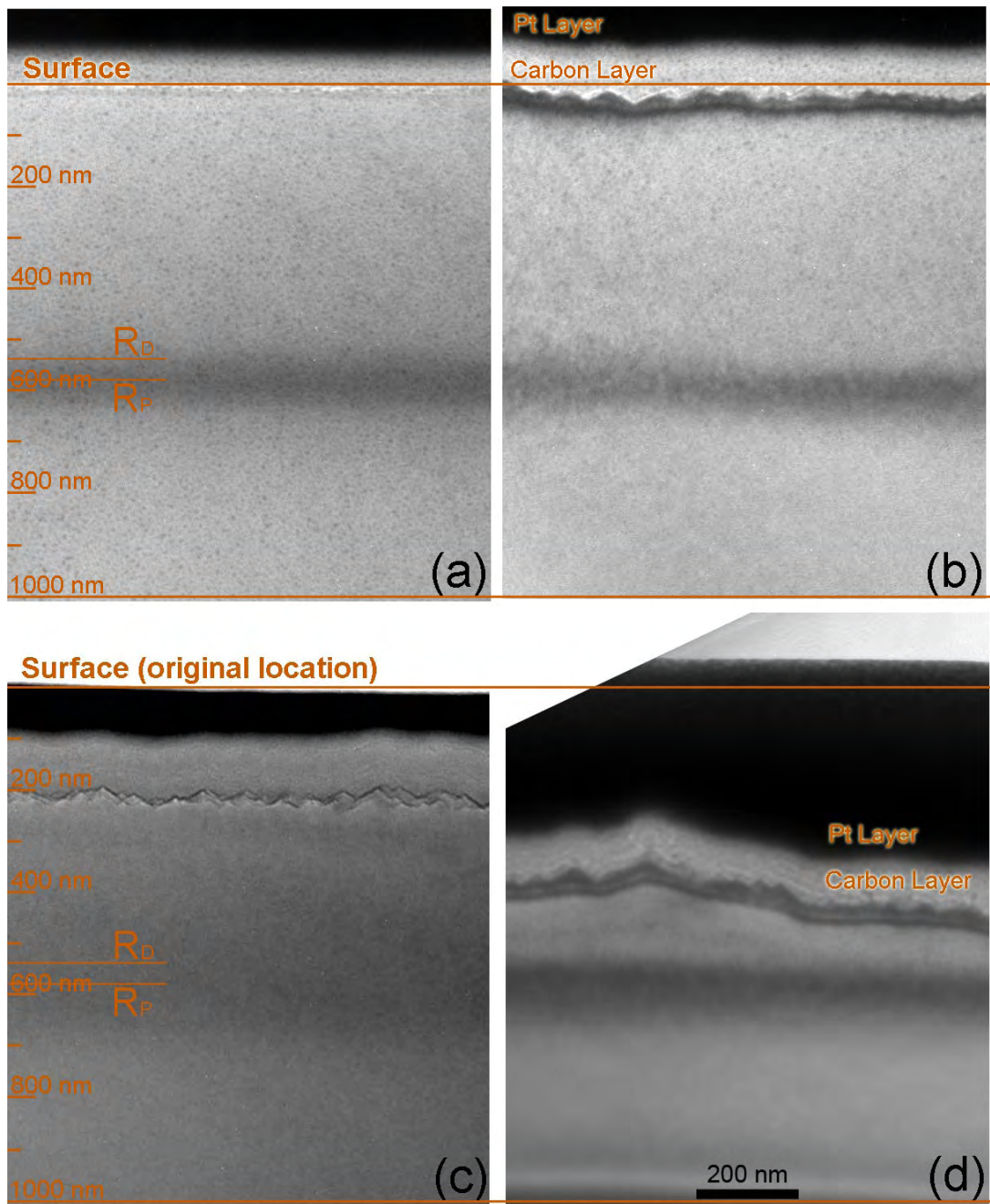


Figure 6-4. BF TEM image of (110)-oriented diamond Si^+ implanted at 1 MeV to a dose of $1 \times 10^{15} \text{ cm}^{-2}$ at 303K (a) as implanted, and after annealing at 950 °C for (b) 10 min, (c) 40 min and (d) 120 min.

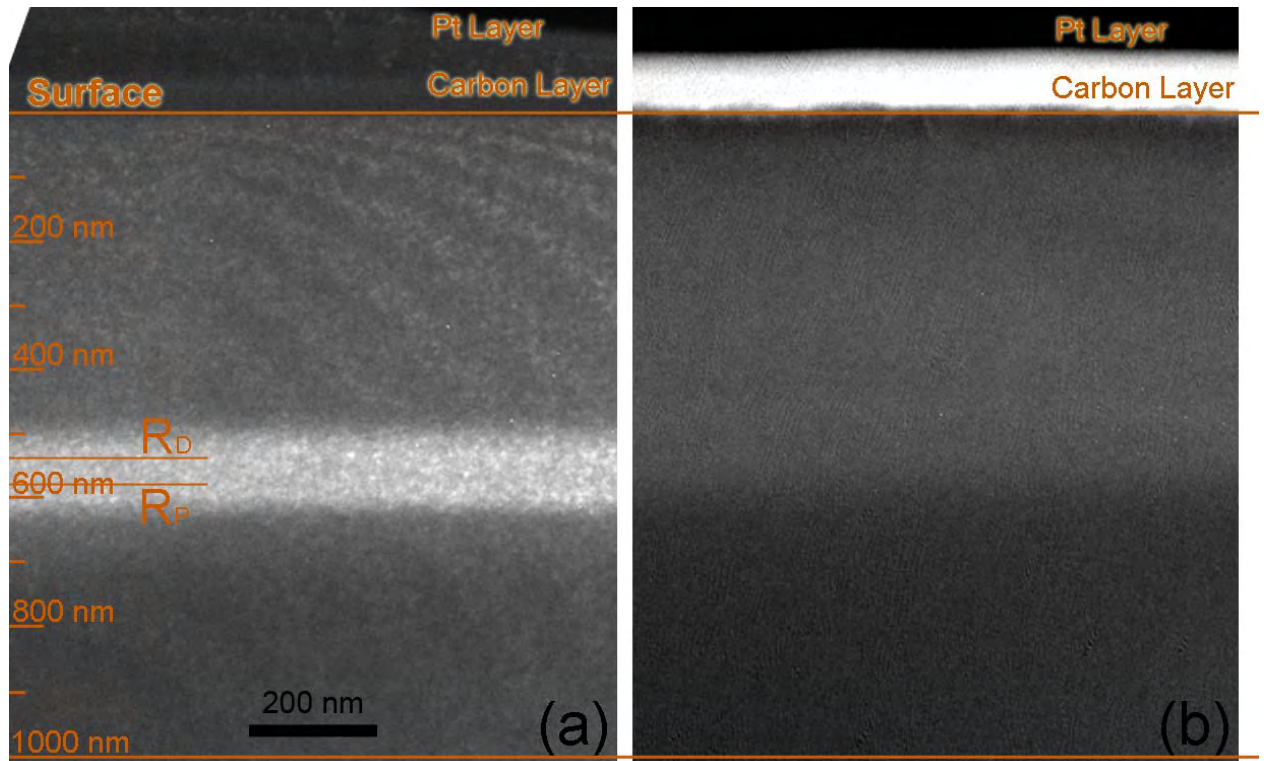


Figure 6-5. WBDF-XTEM images of (001)-oriented diamond Si^+ implanted at 1 MeV to a dose of $1 \times 10^{15} \text{ cm}^{-2}$ at 303K (a) as implanted, (b) and after annealing in vacuum at 1350 °C for 24 hrs.

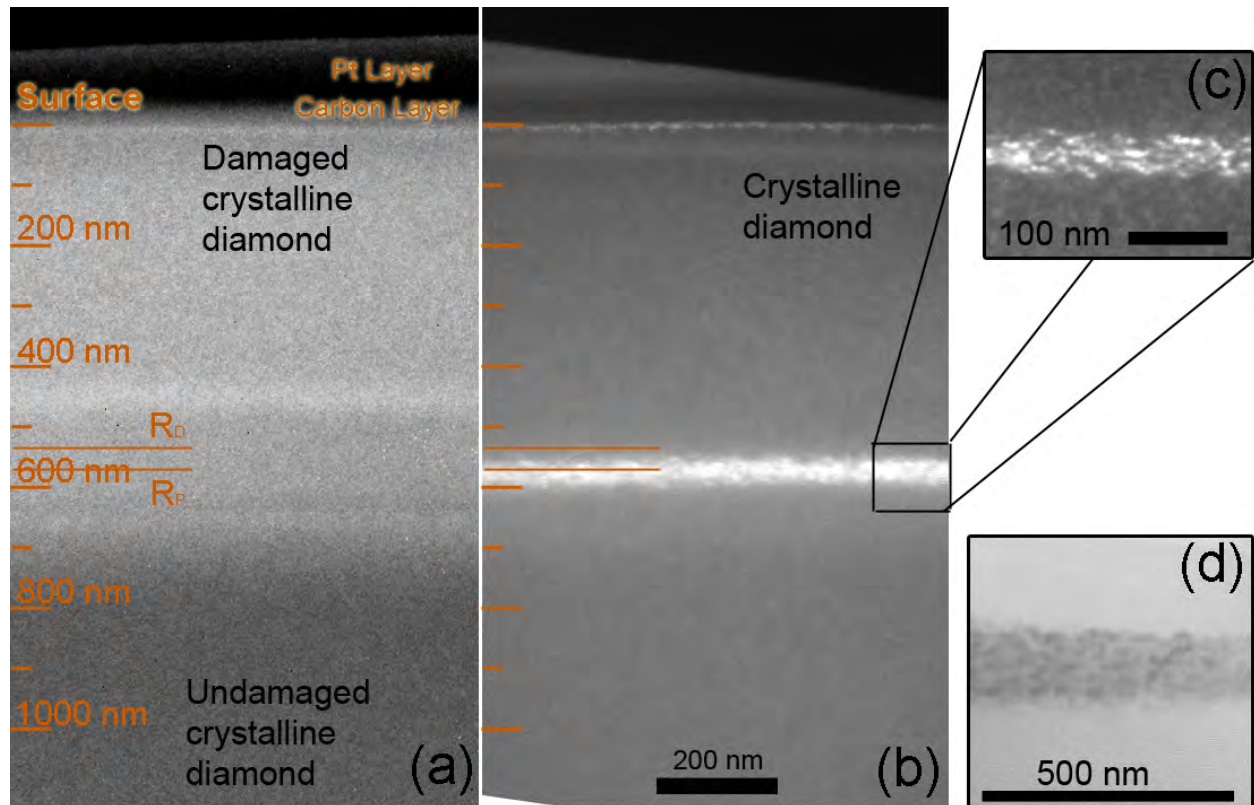


Figure 6-6. WBDF-XTEM images of (001)-oriented diamond Si^+ implanted at 1 MeV to a dose of $1 \times 10^{15} \text{ cm}^{-2}$ at 77K (a) as implanted and (b) annealed in vacuum at 1350 °C for 24 hrs. Detailed views of damage region after annealing imaged using (c) WBDF-XTEM and (d) BF-XTEM (approximately 50° tilt).

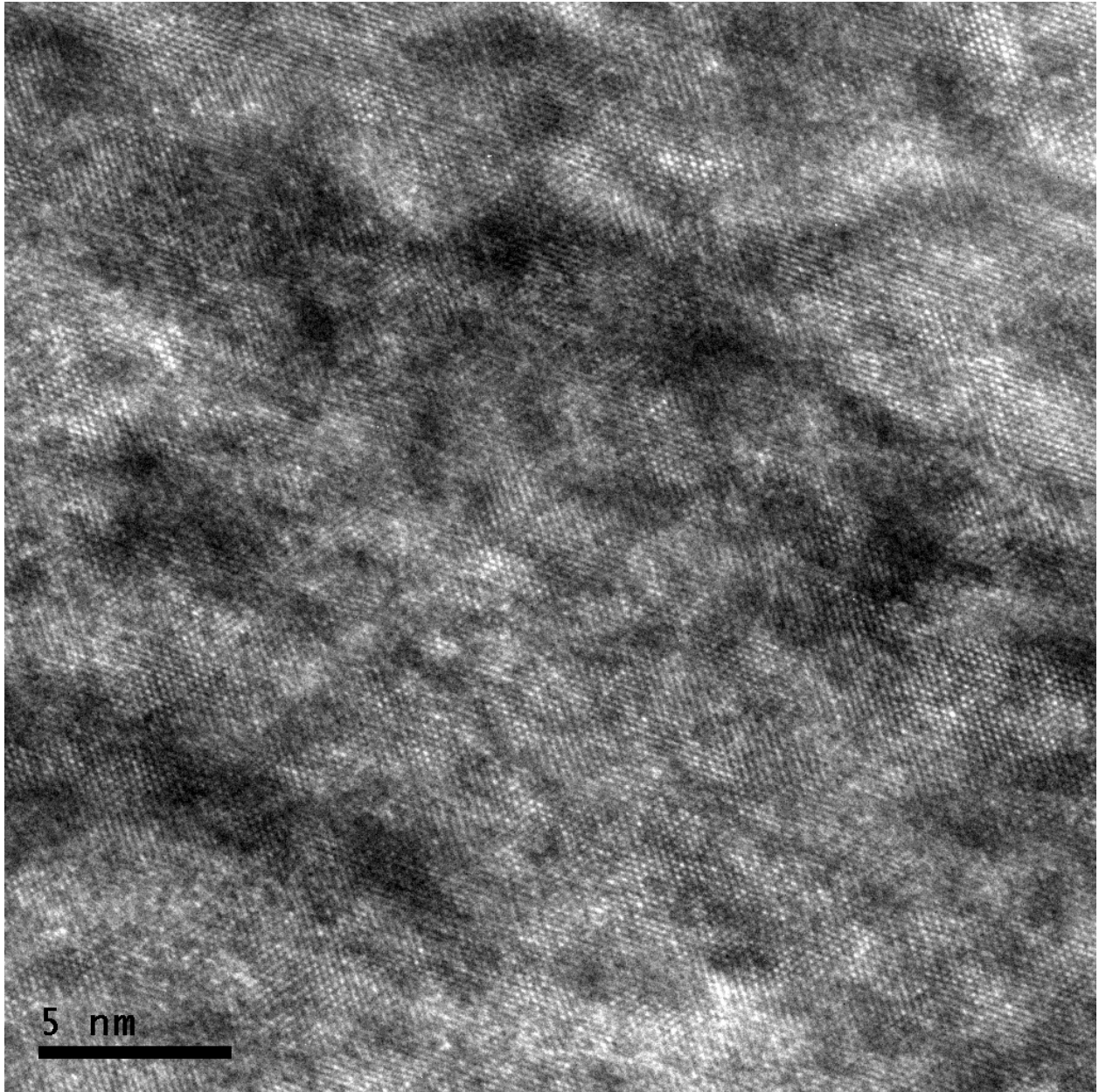


Figure 6-7. HRTEM image of damaged diamond layer in (001)-oriented diamond Si^+ implanted at 1 MeV to a dose of $1 \times 10^{15} \text{ cm}^{-2}$ after annealing at 1350 °C for 24 hrs.

CHAPTER 7 RESULTS FROM AMORPHIZING MEV IMPLANTS INTO DIAMOND

Introduction

The previous chapter described the results of experiments involving implants into diamond that were below the threshold to amorphize the carbon (C), and compared the results to non-amorphizing implants into silicon (Si) and germanium (Ge). This chapter will focus on amorphizing implants into diamond. There is much interest in the amorphization phenomena. For Si, pre-amorphization is used before dopant implants to contain and activate the dopant during solid-phase epitaxial regrowth (SPER),²⁰ and the regrowth process reveals the stable yet detrimental end-of-range extended defects in Si.⁹ Additionally, amorphization in diamond is of interest for creating micro-electrical-mechanical systems (MEMS) devices. Dresselhaus and Kalish noted that there are many outstanding questions about the damage from ion-implantation that could be solved by cross-sectional transmission electron microscope (XTEM) analysis, and one of the outstanding questions was the structure and threshold of ion-amorphized diamond.

However, amorphization is a challenging phenomenon to model, because it is influenced by implant temperature, energy, dose, dose rate and ion species. Implanting diamond adds another complication, since it is not the stable form of elemental C at room temperature and atmospheric pressure. Upon exceeding the amorphization threshold damage, and annealing at sufficient temperatures, diamond will convert to graphite. This transformation has been studied using many techniques,^{19,85} but has not been studied using TEM. For the same reason, no extended defects have been seen in diamond using TEM analysis. It has been theorized that the {311} defect is the stable interstitial defect in all diamond-cubic structures⁷, though molecular dynamics simulations using diamond predict that the split interstitial is the stable defect.¹⁴⁴ Additionally, upon amorphization of the diamond crystal, swelling has been previously observed.

This experiment uses XTEM analysis to document the amorphization and conversion to graphite transition of ion-implanted diamond that has exceeded the threshold for amorphization. The threshold for critical damage is estimated, and compared to previously published results. The density of the amorphous region immediately upon implant, and the density decrease during annealing, is calculated. Finally, data are provided that diamond does not graphitize immediately upon implantation, but instead becomes amorphous and transforms to graphite during annealing.

Experimental Design

Gem-quality high-pressure, high-temperature single-crystal diamonds, with dimensions of approximately $5 \times 5 \times 1 \text{ mm}^3$, were Si^+ implanted in a tandem accelerator implanter at a 7° relative to the incident ions to avoid ion channeling. (001)-oriented diamond was Si^+ implanted at 2 MeV to a dose of $1 \times 10^{15} \text{ cm}^{-2}$ at 77K to create a buried marker layer with point defects frozen-in to avoid migration of the defects to the region of the next implant. This sample was cut into 4 equal pieces, and one additionally Si^+ implanted at 1 MeV to a dose of $7 \times 10^{15} \text{ cm}^{-2}$ at 303K. For a separate experiment, virgin diamond was Si^+ implanted with 1 MeV to a dose of $3 \times 10^{15} \text{ cm}^{-2}$ at 303K. The dose rate for all experiments was $0.44 \mu\text{A}/\text{cm}^2$. Annealing was performed in a graphite chamber furnace at diffusion pump vacuum pressures ($\leq 10^{-4}$ Torr) 142 with a residual helium environment. Cross-sectional transmission electron microscope samples were prepared using the method previously published by the author,¹¹⁷ and outlined in Chapter Three. In that process, layers of carbon and platinum are deposited onto the diamond surface, and (when applicable) are noted on images. Transmission electron microscopy analysis was performed on JEOL 200CX and a JEOL 2010 microscopes. Electron energy loss spectroscopy (EELS) analysis was performed on a FEI Technai TEM. Raman spectroscopy using a He-Ne Laser at 632.81 nm with a spotsizes of approximately $5 \mu\text{m}$ was performed.

Results

TRIM Results

The as-implanted profiles of the samples Si⁺ implanted to doses of 3 and 7 × 10¹⁵ cm⁻² implants are shown in Fig. 7-1(a), and 7-2 (a) respectively. Sections of these samples, as noted on the figures, did undergo the first-order phase transformation to an amorphous structure. As reported in Chapter 3, the TRIM simulated damage profile matched very well with the experimental TEM evidence of damage. Also, TRIM has been used to predict the threshold damage density (TDD) for the amorphization of Si.³⁵ However, when the surface of the as-implanted profiles for these amorphized samples is lined up with the TRIM damage profile, the profile does not match well with the 3 × 10¹⁵ Si⁺ /cm² implant, shown in Figure 7-1(b), and does not match at all to the 7 × 10¹⁵ Si⁺ /cm² implant, shown in Figure 7-2(b). Moreover, if the threshold damage density is attempted to be calculated using this match, the numbers do not make any physical sense since the lower threshold of TRIM-simulated damage is predicted to be in the midst of the amorphous region.

Three plausible explanations were considered. First, the TRIM simulation parameters were incorrect. Second, energy released during the phase change from the diamond crystalline to amorphous carbon phase amorphized surrounding material. Third, significant swelling occurred which is associated with the phase transition. The first explanation was thoroughly explored. The ion species (Si⁺), ion energy (1000 keV) and target species are all set by the experiment. The density of the target was changed from graphite (which is the stable form of carbon at room temperature and pressure) to that of diamond. The displacement energy was set to 50 eV. This parameter has ranged in the literature between 30-55eV; however, the most recent experiments have identified the displacement energy at 50 eV.¹⁰¹ Simulations were run varying the E_d from 10 eV (which is less than the 15 eV used for Si and Ge) to 100 eV, with little change in the depth of

the profile. Damage to the profile was changed, but as energy has the most effect on depth, and energy was kept constant, the depth of the profile did not change significantly (~10-20 nm). Hence, this could not explain the current results. The second explanation of energy release, though plausible, does not seem probable due to the lack of literature evidence to support it. Additionally, it would be difficult to devise an experiment to test the theory. The third explanation, one of swelling of the diamond due to a reduction in the density of the material, seemed a more plausible explanation than the previous two put forth. There is sufficient evidence in the literature to support swelling of other semiconductors like Si and SiGe,^{56,58,61,66} but only a 1-2% swelling. There is also substantial literature on the swelling of SiC^{62,66} and diamond,^{99,102,145} indicating large percent decreases (approximately 12-15% for SiC) in density. To test the swelling theory, a buried marker layer was used.

Swelling of Diamond Experiment

The buried marker layer used was generated via Si⁺ implantation at 2 MeV to a dose of $1 \times 10^{15} \text{ cm}^{-2}$ at 77K. The low temperature ‘froze-in’ point defects,⁸⁵ avoiding defect migration to the area of the future amorphizing implant. The results from the non-amorphizing Si⁺ implant are shown in Figure 7-3(a). A WBDF-XTEM image, using g_{220} imaging conditions, shows the damaged diamond layer approximately 150 - 200 nm thick and centered on the projected range (R_P) at 0.90 μm . A BF-XTEM image inset, shown in Figure 7-3(b) shows the damage more clearly, and although the band of damage is quite distinct, it is not a buried amorphous layer. The non-amorphous nature of the damaged diamond is proven by HR-TEM on-axis [110] lattice imaging, as presented in Figure 7-3(c), which shows a diamond lattice with pockets of damaged diamond throughout. In addition, Raman spectroscopy shows the characteristic diamond peak at approximately 1335 cm^{-1} (FWHM of 5 cm^{-1} indicating a sharp peak) confirms the undamaged, non-amorphous nature of the sample, as displayed in Figure 7-4. However, it should be noted

that the sample volume for this Raman technique is approximately 500 μm into the crystal, while the damaged layer is very small in comparison. Additionally, the cross-section Raman analysis could not be used because the spot size of the laser was as large as the whole sample, including coatings and FIB damage.

The next step to confirm that the buried marker layer would not affect the future amorphizing implant is to compare the TRIM damage profiles. Figure 7-5(a) shows the as-implanted marker layer, next to a TRIM-derived simulation of the ion-implantation induced damage profile, shown in Figure Figure 7-5(b). The grey band designates the area between the damage peak (R_D) and R_P of the marker layer. The total damage of the 2 MeV implant is an order-of-magnitude below the amorphizing implant, and centered almost 400 nm deeper than R_D of the amorphous implant. Therefore, the marker layer implant would have little to no impact on the next amorphizing implant. This is experimentally shown in Figure 7-5(c), in which both implants are visible.

The as-implanted marker layer and the amorphizing Si^+ implant with a dose of $7 \times 10^{15} \text{ cm}^{-2}$ are shown in Figures 7-6 (a) and (b). The swelling that occurred during amorphization is marked on Figure 7-6(b), indicating approximately 150 nm of swelling. The density of the amorphous layer can now be determined.

Density of As-implanted Amorphous (α) C Layer

The amount of crystalline material that underwent amorphization was determined by subtracting the thickness of the swelling at the surface (using the marker layers as guides) from the amorphous thickness [Fig. 7.6]. Note that on-axis [110] BF images were used for the actual measurement, rather than the WBDF images shown, to avoid measuring a tilted image and to obtain a more accurate measurement. This analysis determined the thickness of the crystalline region that converted to the amorphous layer, designated t_{c-a} , being 150 nm \pm 20 nm. A mass

balance of atoms determines the density of the amorphous region, ρ_a , using the known density of diamond, ρ_{diamond} , and the thickness of the amorphous layer, t_a , as shown here:

$$\rho_{\text{diamond}} \times t_{c-a} = \rho_a \times t_a \quad (7-1)$$

$$(1.754 \times 10^{23} \text{ atoms/cm}^3) \times (420 \pm 20 \text{ nm}) = \rho_a \times (570 \pm 20 \text{ nm})$$

$$\rho_a = [(1.754 \times 10^{23} \text{ atoms/cm}^3) \times (420 \pm 20 \text{ nm})] / (570 \pm 20 \text{ nm})$$

$$\rho_a = 1.3 \pm 0.1 \times 10^{23} \text{ atoms/cm}^3$$

For comparison,

$$\rho_{\text{graphit e}} = 1.129 \times 10^{23} \text{ atoms/cm}^3 \quad (\rho_a \text{ is } \sim 15\% \text{ more dense than graphite)}$$

$$\rho_{\text{diamond}} = 1.754 \times 10^{23} \text{ atoms/cm}^3 \quad (\rho_a \text{ is } \sim 25\% \text{ less dense than diamond)}$$

Thus, the density of the as-implanted amorphous carbon (α -C) region seems to be less dense than diamond but slightly more dense than graphite. In terms of thickness, the as-implanted amorphous layer is 35% (+/- 10%) thicker than the crystalline layer that was converted.

Annealing Ion-implantation Induced Amorphous C

For annealing at high temperatures, a 1 MeV, $3 \times 10^{15} \text{ Si}^+ / \text{cm}^2$ at 303K implant into a virgin diamond was used. Fig. 7-7(a) shows a WBDF TEM image, using g_{220} two-beam imaging conditions, of the as-implanted sample. The amorphous layer of the as-implanted sample is approximately 315 +/- 25 nm, again taking the measurement from an untilted, $\langle 110 \rangle$ on-axis BF TEM image [Fig. 7-7(d)]. Assuming that the as-implanted density is approximately the same for this implant as for the previous implant, the thickness of the layer that converted to amorphous material can be determined:

$$\rho_{\text{diamond}} \times t_{c-a} = \rho_a \times t_a \quad (7-2)$$

$$(1.754 \times 10^{23} \text{ atoms/cm}^3) \times t_{c-a} = (1.3 \pm 0.1 \times 10^{23} \text{ atoms/cm}^3) \times (315 \pm 25 \text{ nm})$$

$$t_{c-a} = [1.3 \pm 0.1 \times 10^{23} \text{ atoms/cm}^3 \times (315 \pm 25 \text{ nm})] / (1.754 \times 10^{23} \text{ atoms/cm}^3)$$

$$t_{c-a} = 233 \pm 35 \text{ nm}$$

The thickness of crystalline material that converted to graphite (assuming the as-implanted amorphous density is the same as the previous implant) is approximately 230 nm. This will be an important value to determine the threshold damage density necessary to amorphize diamond.

The Si⁺ implanted at 1 MeV to a dose of $3 \times 10^{15} \text{ cm}^{-2}$ implanted sample was then annealed at 1350 °C for 1 hour and 24 hours in vacuum. The diamond showed additional signs of swelling after the 1 hour and 24 hour anneals, as shown in Figures 7-7(b) and (c), respectively.

Approximately 70 nm of additional swelling occurred during the heat treatments, after the initial implantation and conversion to α -C.

Using the same conservation of atoms mass balance used to determine the density of the as-implanted amorphous layer, the density of the annealed layer can also be determined. For this measurement, on-axis [110] TEM imaging was used to get a detailed view of each interface, both as implanted and annealed for 24 hrs, as presented in Figures 7-6 (d) and (e). The measured thickness of the as-implanted amorphous layer is $325 \pm 15 \text{ nm}$, and the measured thickness after annealing is $390 \pm 15 \text{ nm}$. Therefore, the density of the annealed amorphous layer can be determined, assuming that the as-implanted density is approximately the same as for the previous implant:

$$\rho_{\alpha\text{-as implanted}} \times t_{\alpha\text{-as implanted}} = \rho_{\alpha\text{-annealed}} \times t_{\alpha\text{-annealed}} \quad (7-3)$$

$$\rho_{\alpha\text{-annealed}} = (\rho_{\alpha\text{-as implanted}} \times t_{\alpha\text{-as implanted}}) / t_{\alpha\text{-annealed}}$$

$$\rho_{\alpha\text{-annealed}} = [(1.3 \pm 0.1 \times 10^{23} \text{ atoms/cm}^3) \times (325 \pm 15)] / (390 \pm 15 \text{ nm})$$

$$\rho_{\alpha\text{-annealed}} = 1.1 \pm 0.2 \times 10^{23} \text{ atoms/cm}^3$$

For comparison,

$$\rho_{\text{graphite}} = 1.129 \times 10^{23} \text{ atoms/cm}^3$$

Using the density calculation, the amorphous layer seems to have achieved approximately the same density as graphite. To determine the structural nature of the annealed amorphous layer, diffraction patterns of the samples were obtained.

Determination of the Graphitic Nature of Annealed Diamond

Using the fast Fourier transform (FFT) feature of the Gatan TEM software package, FFT images (which simulate diffraction patterns) were obtained from the on-axis [110] BF images of the diamond sample Si⁺ implanted at 1 MeV to a dose of $3 \times 10^{15} \text{ cm}^{-2}$ at room temperature, as shown in Figure 7-8 (a) with the associated FFT image in Figure 7-8(b), and then annealed for one and 24 hours at 1350 °C, shown in Figures 7-8 (c) and (e) respectively, with the associated FFTs in Figures 7-8 (d) and (f). After the 24 hr, 1350 °C anneal, the HRTEM image shows ordering of the amorphous layer, which is reflected in the FFT as defined bands with a preferred orientation appearing inside the [111] plane diffracted spots. Using the relationship,

$$rd = \lambda l, \quad (7-4)$$

where r is the radius from the center transmitted spot to the area of interest, d being the spacing between planes, λ being the wavelength of the electron used at the particular accelerating energy, and l being the camera length in the microscope, the distance between planes represented by the preferred orientation parentheses-shaped spots can be determined, and compared to graphite. Distances between the diffraction spots were measured, and using the above relationship, knowing that the product of λ and l is the same for both the diamond and the graphite, the d spacing of the preferential non-diamond plane can be determined ($d_{\text{diamond}(111)} = 2.059\text{\AA}$):

$$r_{\text{dia}(111)} d_{\text{dia}(111)} = r_{\text{graphite}} d_{\text{(graphite)}} \quad (7-5)$$

$$1.8 \times 2.059 \text{ \AA} = 1.1 \times d_{(\text{graphite})}$$

$$d_{(\text{graphite})} = \sim 3.37 \text{ \AA}$$

This corresponds well with the reported values of the most intensely diffracted spots in graphite, as reported by JCPDS – International Centre for Diffraction Data 1996, which reports the most intense spots for graphite to be the (002) planar spacing of 3.36 \AA ¹²³ and 3.38 \AA ¹²⁴ for different reported literature values. For the hexagonal crystal four-index scheme, this corresponds to an (0002) graphite plane, since $i = -(h+k)$.

EELS Results of the Amorphous Region

An EELS analysis was conducted on the buried amorphous layer resulting from Si^+ implantation at 1 MeV to a dose of $3 \times 10^{15} \text{ cm}^{-2}$ implanted at 303K. Two EELS spectrums are shown in Fig. 7-9 (a-f): the first shows the as-implanted spectrum in the near surface region [Fig. 7-9 (a)], the mid-amorphous region [Fig. 7-9 (b)], and the bulk crystalline region [Fig. 7-9 (c)], while the second set show the same regions [Fig. 7-9 (d),(e),and (f), respectively] for the sample annealed at 1350 °C for 1 hour. Reference spectrum for diamond, amorphous carbon and graphite can be found in Chapter 3 – Analytical Techniques.

As implanted, the near-surface region and bulk region both show the characteristic three-peak diamond configuration, as shown on Figures 7-9 (a) and (c). Similarly, the same three-peak diamond configuration occurs for the near surface and bulk regions of the annealed sample, shown in Figures 7-9 (d) and (f). The transformed region in between, for the as-implanted sample, lost the three distinct peaks and instead only has a broad peak. This is indicative of amorphous carbon. Upon annealing, the broad peak is preceded by a short peak at approximately half the intensity, quite similar to the graphite standard. This is further indication that the diamond is amorphous upon implantation, and becomes graphite during annealing. Raman results (not shown) additionally agree with this conclusion; broad peaks indicating amorphous

carbon were seen in the as-implanted sample, with defined peaks indicating a crystalline nature seen after annealing. Limitations of the spot size of the Raman technique did not allow for individual cross-sectional location analysis.

Annealed Amorphous-Crystalline Interfaces

The crystalline-amorphous interfaces of the two amorphized samples both have a larger transition region at the surface oriented interface than the bulk-oriented interface. Upon annealing for 1350 °C for 24 hrs, the bulk interface becomes more defined, as shown in Figure 7-7(e). The surface-oriented transition region, while also becoming more defined, has interesting morphological features. Figure 7-10(a) shows the on-axis [110] TEM image of the annealed diamond. The surface interface region, when viewed at higher magnification as shown in Figure 7-10(b), reveals a very rough interface, while the same magnification of the bulk interface is relatively abrupt, as shown in Figure 7-10(c). Using HRTEM imaging, it is clear that trapped pockets of crystalline material are in the first several tens of nanometers of the amorphous region, as shown in Figure 7-10(d). Whether these pockets of crystalline material are stable, or will collapse upon further annealing, is unknown.

Discussion

The results of these amorphization experiments bring some clarification to the amorphization and graphitization of diamond after ion-implantation. Diamond transforms to an amorphous carbon (and not graphitic) state upon surpassing the critical damage threshold, confirmed by TEM, EELS and Raman analysis. The density of the amorphous carbon is approximately $1.3 \pm 0.1 \times 10^{23}$ atoms/cm³, which is 15% more dense than graphite, but approximately 25% less dense than diamond. As implanted, the amorphous layer is 35% ($\pm 10\%$) thicker than its crystalline form before amorphization. And upon annealing for 24 hrs at 1350 °C, the amorphous layer has transformed to graphite, with a density of $1.1 \pm 0.2 \times 10^{23}$ atoms/cm³,

and planar spacings equal to that of graphite. These are the direct results of the experiment. Using these results, the threshold for amorphization can be determined.

Threshold damage density for diamond. To determine the threshold damage density (TDD) while accounting for swelling, the TRIM simulation for the vacancies from 1 MeV, Si⁺ implantation was transformed from vacancies/Å/ion into keV/cm³, using the displacement energy for a diamond atom from its lattice site as 50 eV.¹⁰¹ These results were plotted for four doses: 1×10^{14} and 1×10^{15} Si⁺/cm³ (below the amorphization threshold) and 3 and 7×10^{15} Si⁺/cm² (above the amorphization threshold). Since the conversion to amorphous material creates an increase in the thickness of the amorphous layer, TRIM can no longer be matched up directly to determine the threshold. However, it need not be a direct match. The important interface is the near-surface interface. It is at this point that the crystal has just exceeded the threshold for amorphization. Although this region is typically rougher (wider), which adds error to the calculation, the deeper interface is a poor estimation because atoms that have been implanted past the initial amorphization threshold for the projected range have seen two layers, a crystalline layer and an amorphous layer, before reaching a final depth. Therefore, the damage parameters will be determined from the near-surface α -c interface. Figure 7-11 is a plot of the threshold damage density, in keV/cm³. This is a parameter previously reported in the literature for Si and Ge. For the diamond community, the critical damage (D_C) is normally reported, in vacancies/cm³. The ion-implantation community normally prefers to report amorphization thresholds using a liquid nitrogen implant and reporting parameter displacements per atom (DPA), which is a unitless parameter. The D_C and DPA were determined using the same method as the TDD, using the SRIM simulation of damage and the near-surface α -c interface. Table 7-1 summarizes the calculated values, and repeats the Si and Ge values from earlier experiments.

Initial analysis of the comparison between the diamond-determined thresholds and the Si and Ge thresholds seems confusing. The values for TDD and D_c are higher for diamond than for Si and Ge, indicating that it should be harder to amorphize diamond. However, the value of DPA for diamond (~ 0.14) is significantly less than that of Si and Ge, suggesting that amorphization of diamond is easier than for Si or Ge. The answer to this apparent paradox is in the reporting of the units. DPA is a unitless parameter, and therefore can be compared across elements. However, TDD and D_c are both reported per volume, making density an important factor. Si and Ge have approximately the same atomic density, 5 and 4.42×10^{22} atoms/cm³ respectively. Diamond's atomic density is over three times higher, at 17.63×10^{22} atoms/cm³. Therefore, across the elements, DPA shows the trend that recognizes it is easier to amorphize diamond than Si or Ge on a per-atom basis. When comparing a per volume basis, the number of atoms per volume must be taken into consideration. Thus, D_c can be used to compare the relative number of lattice atoms that must be displaced (in simulation terms) in order for amorphization to take place. For Si and Ge, this is approximately equal to the atomic density. For diamond, however, the D_c value of $\sim 6 \times 10^{22}$ atoms/cm³ is significantly less than half its atomic density of 1.763×10^{23} atoms/cm³. This also indicates that on a per crystal basis, less damage needs to be done to the diamond lattice to allow amorphization to take place, as compared to Si and Ge. The TDD is reported in energy per volume, and as noted, is higher for diamond than for Si and Ge. This, too, can be explained by examining the units of measure. In Si and Ge, the energy to displace an atom from its lattice site is 15 eV, significantly less than the approximately 50 eV to displace diamond atoms.^{21,101} Since there are more atoms per volume in diamond, and more energy is needed to displace an atom, more energy would be needed per volume to amorphize diamond. Furthermore, in Chapter 2, it was noted that simulating the amorphization phenomena is a

challenging task. This supposition is further reinforced in this study, shown by the fact that a single parameter cannot be used to completely describe the amorphization trends among various materials.

Conclusion

Thus far, the results of ion-implantation of both non-amorphizing and amorphizing implants into Ge, Si and C have been presented. In this final analysis, the amorphization threshold of diamond has been surpassed. In comparing the number of displacements per atom necessary in order to amorphize these crystals, diamond has the lowest at approximately 0.4 DPA, as compared to Ge and Si, all at room temperature. This indicates that on a per atom lattice basis, less damage needs to be done to a diamond crystal (per unit cell) than needs to be done to Ge or Si lattice in order to induce amorphization. The measurement of critical damage (D_c) also agrees with this analysis: approximately 6×10^{22} vacancies/cm³ out of 1.7×10^{23} atoms/cm³ in the diamond lattice, approximately 35% of the atoms per unit volume, need to be displaced from the diamond lattice in order to induce amorphization. In Si and Ge, this percentage is on the order of 100% of the atoms in the lattice in order to induce amorphization.

However, on a volumetric basis, more energy must be imparted into the same volume of diamond than Si or Ge to amorphize the same amount of crystal, because of the high energy it takes to displace one carbon atom ($E_D = 50$ eV) versus Si and Ge ($E_D = 15$ eV, for both), in addition to the higher atomic density. Therefore, in order to amorphize all crystals equally, more energy must be imparted into the diamond crystal in order to initiate amorphization.

In discussing the defects apparent after a buried amorphous layer is formed and regrown, both Si and Ge show three kinds of extended defects: regrowth-related, clamshell and end-of-range. No solid phase epitaxial regrowth is observed in diamond, and therefore, no regrowth, end-of-range or clamshell defects. No extended defects were seen to form uniformly in the

projected range of the damaged diamond, either in the crystalline areas or in the graphite region upon annealing. Thus, there seem to be no stable extended defects that reside in diamond after ion-implantation. This agrees with computational simulations that the $\langle 100 \rangle$ split-interstitial (a point defect) is the stable interstitial defect in diamond.

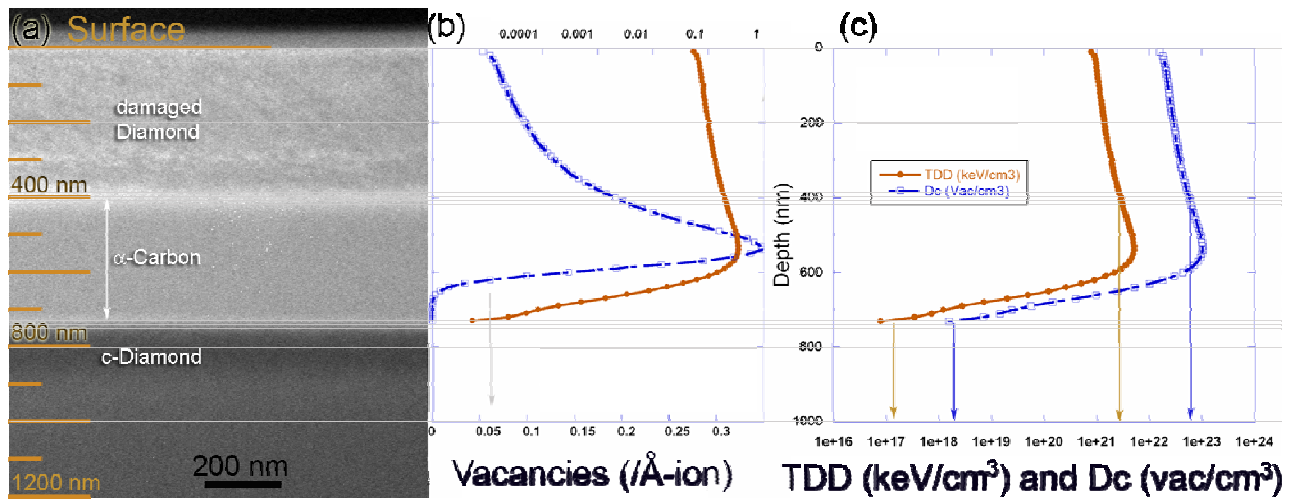


Figure 7-1. (a) WBDF-XTEM image, using g_{220} imaging conditions, of (001)-oriented single-crystal diamond Si^+ implanted at 1 MeV to a dose of $3 \times 10^{15} \text{ cm}^{-2}$ at 303K. (b) The plotted TRIM results of total vacancies created by the implant, in both log and linear axis. (c) The TRIM-derived TDD values, matched with the surface of the amorphized diamond.

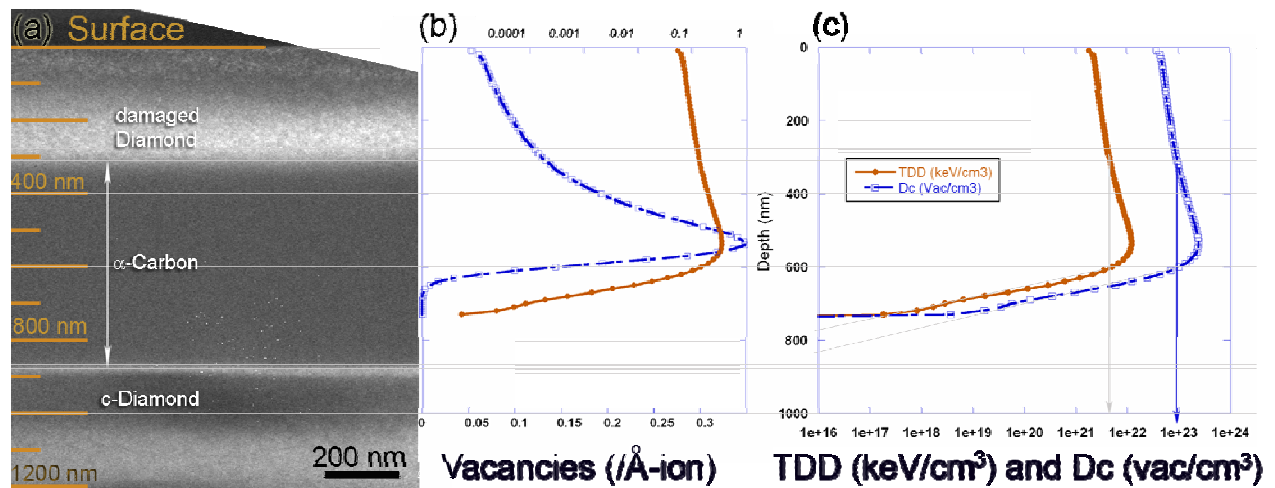


Figure 7-2. (a) WBDF-XTEM image, using g_{220} imaging conditions, of (001)-oriented single-crystal diamond Si^+ implanted at 1 MeV to a dose of $7 \times 10^{15} \text{ cm}^{-2}$ at 303K. (b) The plotted TRIM results of total vacancies created by the implant, in both log and linear axis. (c) The TRIM-derived TDD values, matched with the surface of the amorphized diamond.

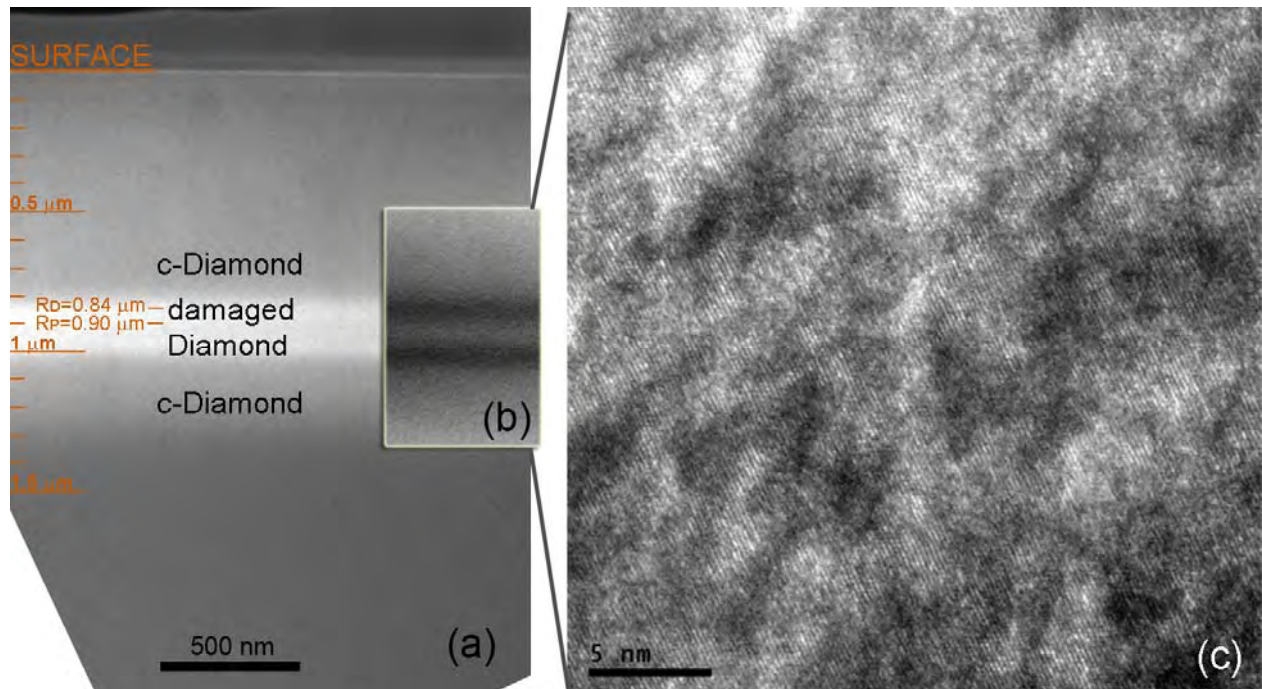


Figure 7-3. (a) WBDF-XTEM image of diamond Si^+ implanted at 2 MeV to a dose of $1 \times 10^{15} \text{ cm}^{-2}$ at 77 K. (b) An inset of an on-axis [110] BF TEM image at the same magnification of the damaged region and (c) an on-axis [110] BF HRTEM image of the center of the damaged region.

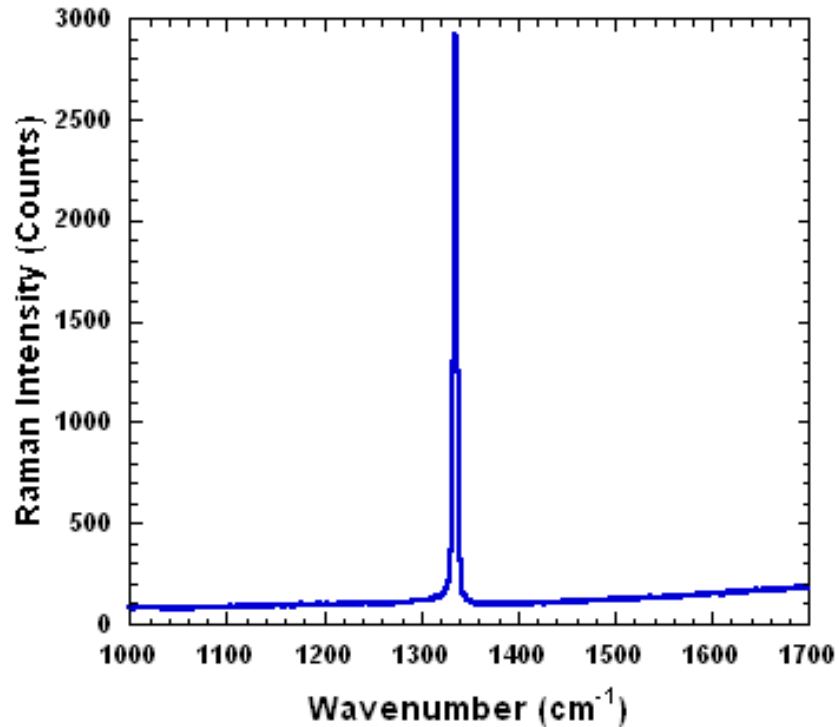


Figure 7-4. Raman spectrum of bulk diamond implanted with 2 MeV, 1×10^{15} Si⁺/cm² at an implant temperature of 77 K, centered at 1400 cm⁻¹. The characteristic sharp diamond peak at approximately 1335 cm⁻¹ is observed. No broad skewed peaks that would indicate radiation damage are seen. Theoretical calculations state that no peaks should occur above 1400 cm⁻¹ for sp³-bonded carbon structures.¹⁴⁶

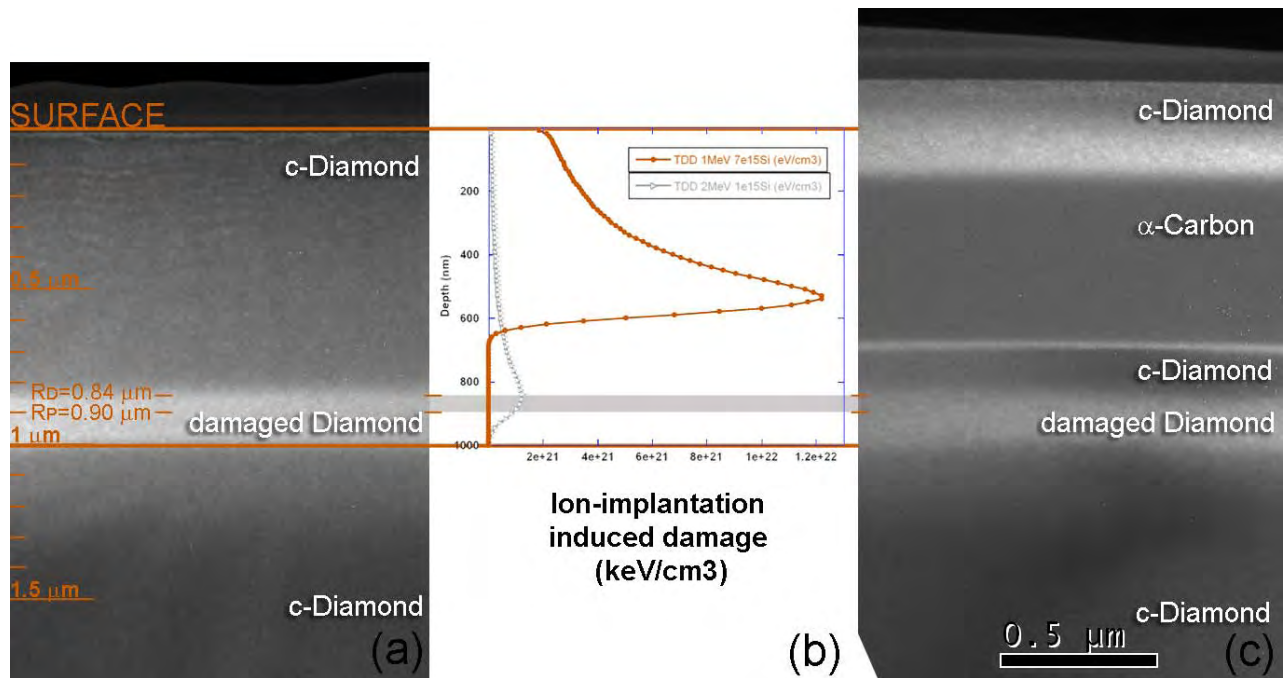


Figure 7-5. (a) WBDF TEM image, using g_{200} imaging conditions, of a (001)-oriented single-crystal diamond implanted with 2 MeV, $1 \times 10^{15} \text{ Si}^+/\text{cm}^2$ at 77 K. (b) The damage density (keV/cm^3) produced by a 2 MeV, $1 \times 10^{15} \text{ Si}^+/\text{cm}^2$ overlaid with a 1 MeV, $7 \times 10^{15} \text{ Si}^+/\text{cm}^2$ implant. (c) WBDF TEM image both implants: 2 MeV, $1 \times 10^{15} \text{ Si}^+/\text{cm}^2$ at 77 K and the 1 MeV, $7 \times 10^{15} \text{ Si}^+/\text{cm}^2$ implant. The 2 MeV implant serves as a buried marker layer.

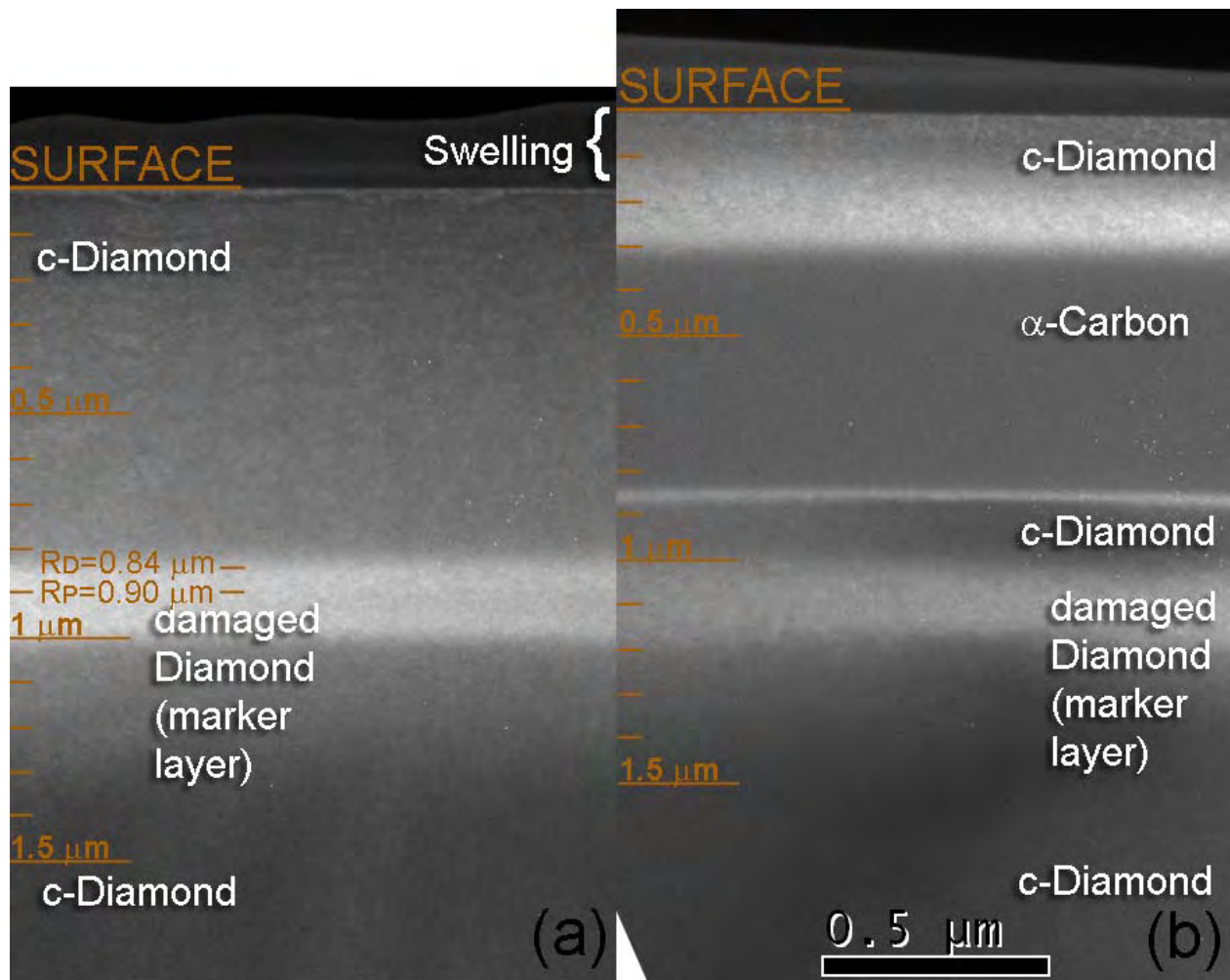


Figure 7-6. WBDF TEM images using g_{220} imaging conditions of (001)-oriented diamond implanted with (a) 2 MeV, $1 \times 10^{15} \text{ Si}^+/\text{cm}^2$ at 77 K showing the crystalline region between the surface and the non-amorphized damage layer. (b) The same sample as with an additional implant of 1 MeV, $7 \times 10^{15} \text{ Si}^+/\text{cm}^2$ at 303K, showing the remaining crystalline regions, separated by an amorphous region.

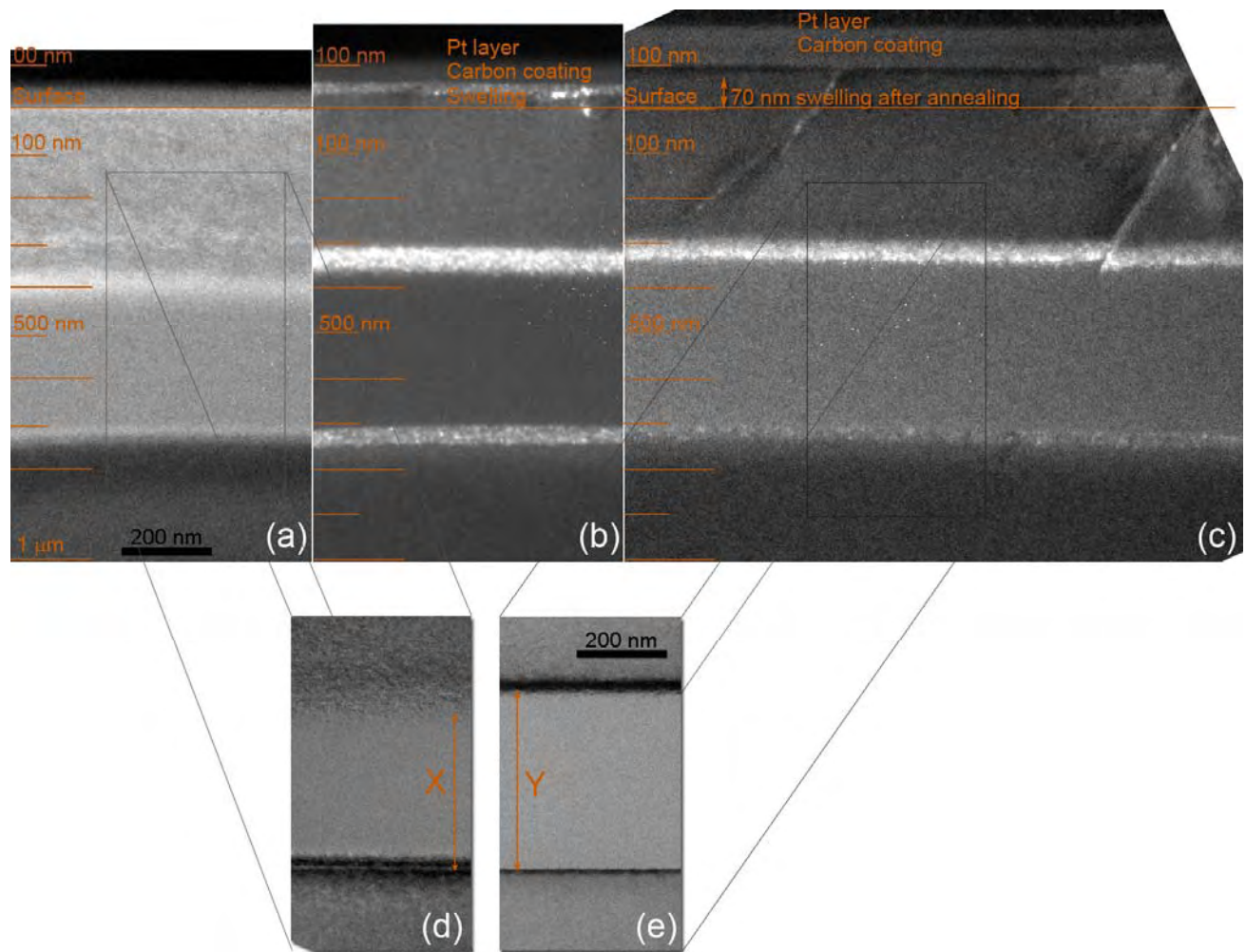


Figure 7-7. WBDF-XTEM images of diamond Si⁺ implanted at 1 MeV to a dose of 3×10^{15} cm⁻² at 303 K (a) as-implanted, annealed at 1350 °C for (b) 1 and (c) 24 hours. On-axis BF-XTEM images of (d) as-implanted and (e) annealed at 1350 °C for 24 hours.

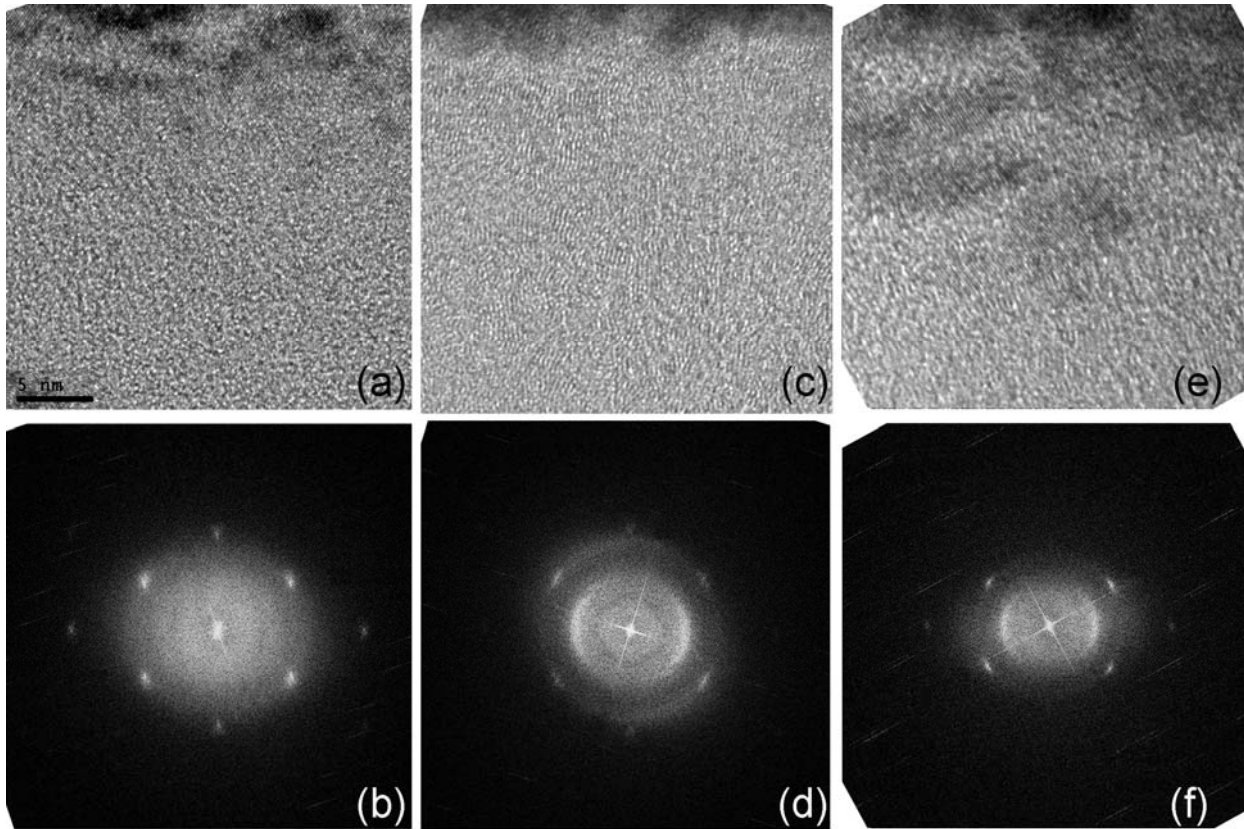


Figure 7-8. HR-XTEM images of diamond Si⁺ implanted at 1 MeV to a dose of $3 \times 10^{15} \text{ cm}^{-2}$ at 303K using on-axis [110] BF imaging conditions, shown with the respective fast Fourier transforms (FFT): (a) as-implanted HRTEM and (b) FFT, and annealed at 1350 °C for 1 hr image (c) and FFT (d) and 24 hrs (e) image and (f) FFT.

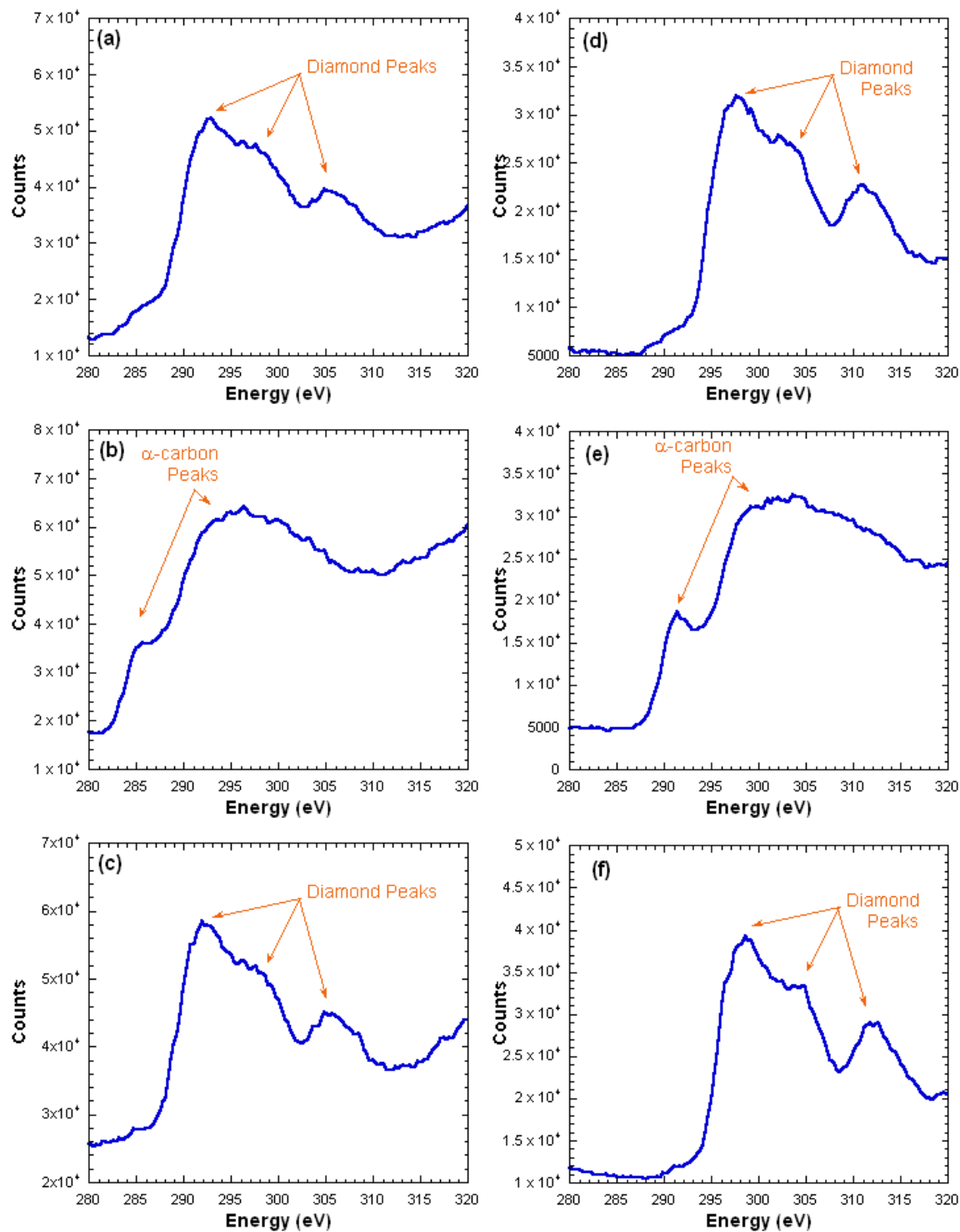


Figure 7-9. EELS spectrum of a (001)-oriented diamond Si⁺ implanted at 1 MeV to a dose of $3 \times 10^{15} \text{ cm}^{-2}$ at 303K, (a) as-implanted in the near-surface crystalline region (b) mid-amorphous layer region and (c) bulk region. After annealing for one hour at 1350 °C in the (d) near-surface, (b) mid-amorphous and (c) bulk regions. Note: the zero loss peak on the annealed sample is skewed to +5 eV.

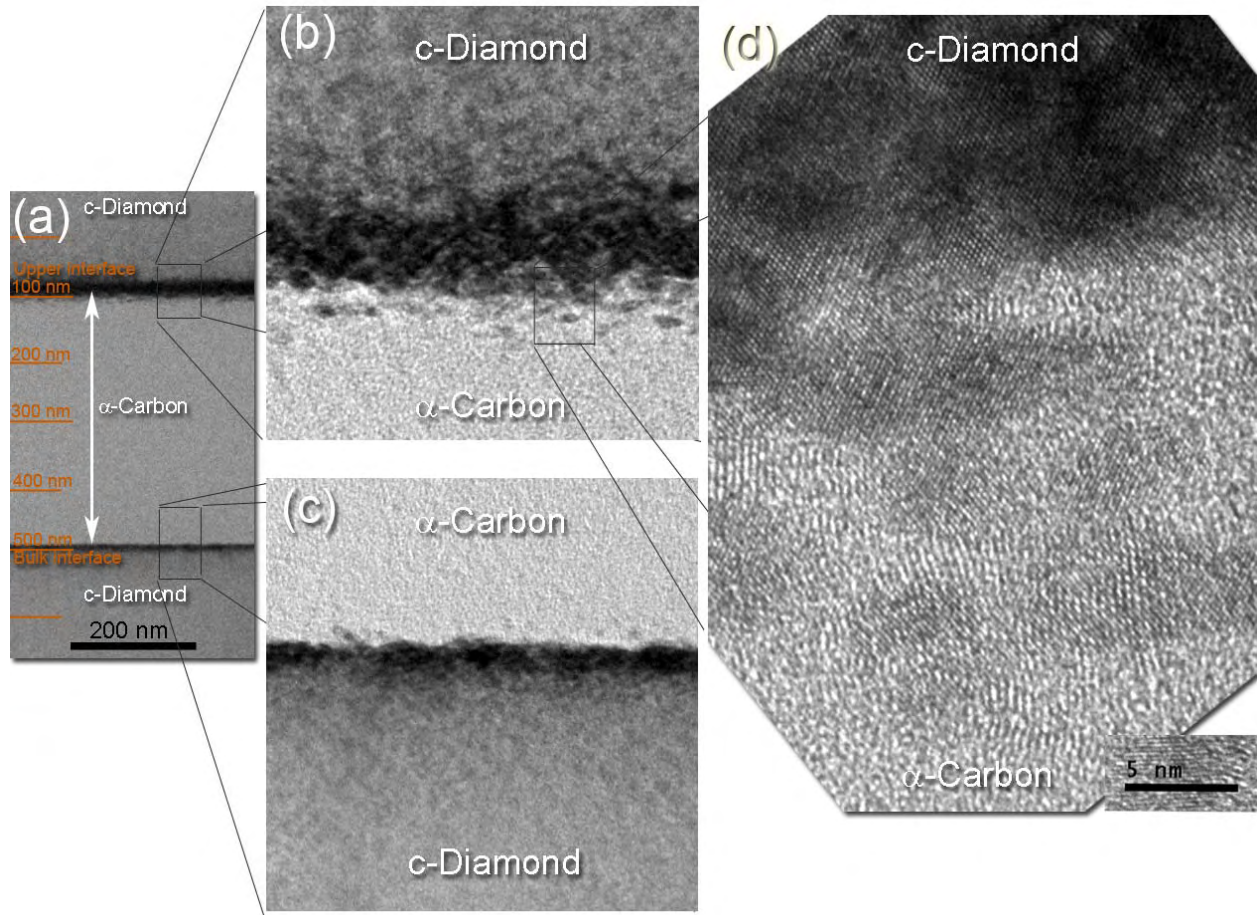


Figure 7-10. HR-XTEM images of (001)-oriented diamond Si^+ implanted at 1 MeV to a dose of $3 \times 10^{15} \text{ cm}^{-2}$ at 303 K and annealed at 1350 °C for 24 hours, using on-axis [110] BF imaging conditions: (a) Whole amorphous-carbon layer, (b) upper layer, (c) lower layer and (d) detailed view of upper region.

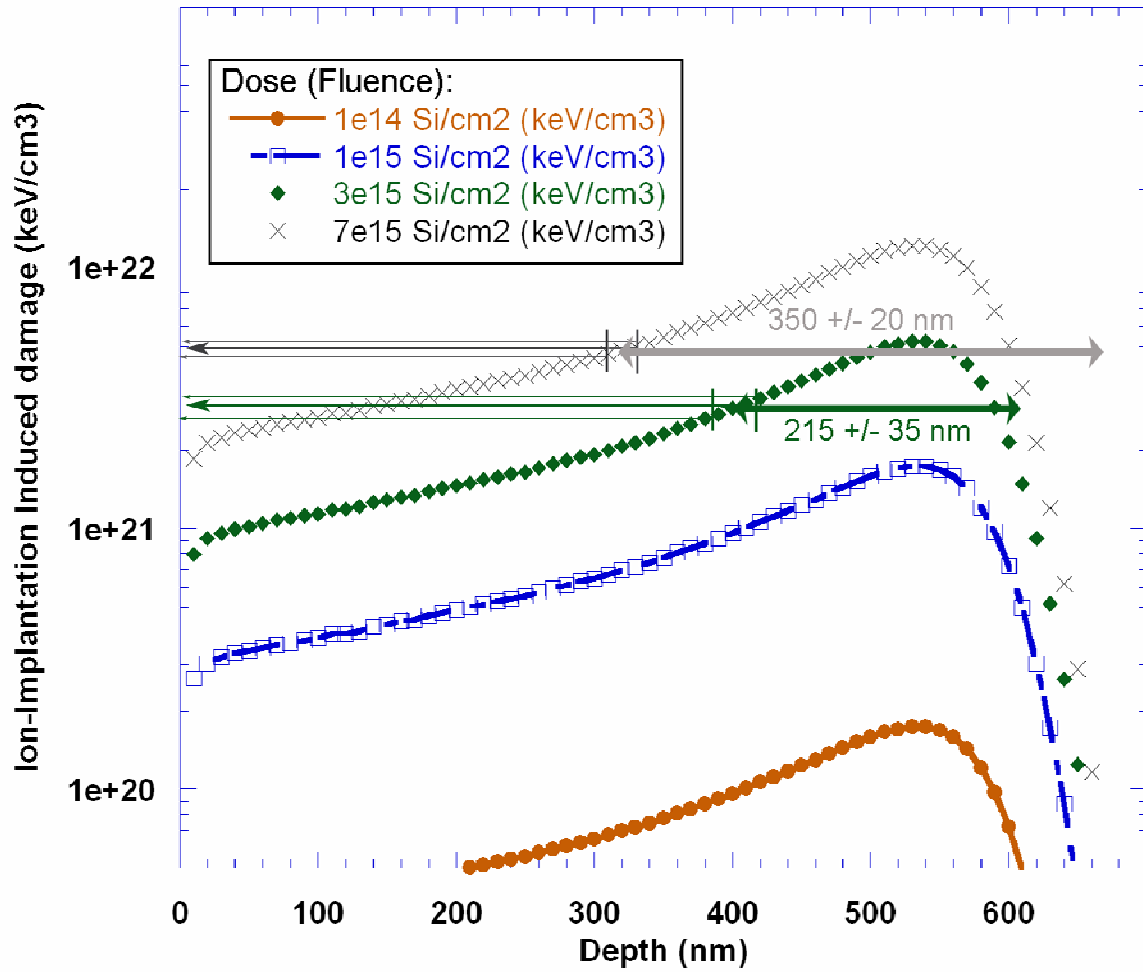


Figure 7-11. SRIM-derived damage density, in keV/cm³, of diamond Si⁺ implanted at 1 MeV to doses of 1×10^{14} (●), 1×10^{15} (□), 3×10^{15} (◆), and 7×10^{15} Si⁺/cm² (×).

Table 7-1. Simulated damage values from current experiments

Material, Implant Energy, Temperature and Dose	Threshold Damage Density (keV/cm ³)	Critical Damage (vac/cm ³)	DPA (unitless)
Diamond 1000 keV, 303 K, 3×10^{15} Si ⁺ cm ⁻²	$5 \pm 1 \times 10^{21}$	$7 \pm 1 \times 10^{22}$	0.3 ± 0.05
Diamond 1000 keV, 303 K, 7×10^{15} Si ⁺ cm ⁻²	$3 \pm 0.5 \times 10^{21}$	$5 \pm 1 \times 10^{22}$	0.5 ± 0.05
Ge 1000 keV, 303 K, 1×10^{15} Si ⁺ cm ⁻²	$7.0 \pm 2 \times 10^{20}$	$4.5 \pm 1.5 \times 10^{22}$	0.8 ± 0.2
Ge 40 keV, 303 K, 1×10^{15} Si ⁺ cm ⁻² <i>Bulk Interface Measurement</i>	$5.5 \pm 1.5 \times 10^{20}$	$3.5 \pm 1 \times 10^{22}$	0.9 ± 0.1
Si 40 keV, 303 K, 1×10^{15} Si ⁺ cm ⁻² <i>Bulk Interface Measurement</i>	$7.5 \pm 1.5 \times 10^{20}$	$5.0 \pm 1 \times 10^{22}$	1.0 ± 0.2

CHAPTER 8 SUMMARY AND FUTURE WORK

Summary

In our study, the behavior of single crystals of diamond-cubic germanium (Ge) and carbon (C) after Si⁺ implantation have been studied, and then compared to the behavior of silicon (Si). The purpose of the ion-implantation was to study the defects that occur after implantation and annealing, and to study the evolution and defect formation after amorphizing implantation and annealing. These are common processes used in silicon device fabrication; therefore, if Ge or C are to be considered as base materials, the effects of these common processes need to become known. The following pages will summarize the results of this study.

Non-amorphizing Si⁺ Implants into Diamond and Ge, as Compared to Si

In Si, the {311} defect and dislocation loop have been well known to impede device performance. The {311} defect has been reported in Ge for light ion and electron implantation. However, no {311} defects in Ge were observed in this study for non-amorphizing implants (1 MeV & 40 keV, 10¹⁴ Si⁺ cm⁻²). Dot-like defects appeared in Ge after implantation, and were stable up to approximately 650 °C. The activation energy of the dissolution of the dot-like defects in Ge was determined to be approximately 0.3 ± 0.1 eV, almost an order of magnitude lower than the {311} defect in Si, which has an activation energy for dissolution of 3.6 eV.¹⁷

In diamond, temperatures exceeding 1350 °C are necessary to completely remove the damage caused by non-amorphizing ion-implantation (1 MeV, < 3 × 10¹⁵ Si⁺ cm⁻²). This result is in agreement with studies that indicate temperatures of 1500 °C are necessary to completely remove damage,⁹² but contradict other studies that report damage repair at temperatures of 500-1000 °C.^{74,80,81,147} Non-amorphizing implants into single-crystal diamond did not result in any consistent defects during the annealing process, over temperatures ranging from 300 to 1350 °C

for 24 hrs. Some defects, originating from the surface, did appear. However, as these defects were not uniform across samples, and also appeared in unimplanted diamonds, these defects are assumed to be unassociated with the implantation process. Appendix A contains XTEM images and brief descriptions of the observed defects.

Amorphizing Si⁺ Implants into Diamond and Ge, as Compared to Si

When the threshold of damage exceeded a certain point, all three diamond-cubic crystal systems converted to amorphous material. Upon annealing, however, the three crystal systems behaved differently. Si and Ge both undergo solid phase epitaxial regrowth and evolution of regrowth-related, clamshell and end-of-range defects after 1 MeV, 10^{15} Si⁺ cm⁻² amorphizing implants. However, the most stable defect in Si is the EOR defect; in Ge, it is the regrowth-related defect. The activation energy for the dissolution of {311} defects in Si is 3.6 eV, while my study determined the activation energy for the dissolution of EOR defects in Ge to be approximately 0.4 ± 0.1 eV. However, the sample size for the determination of this activation energy was low. The number of trapped interstitials in the EOR defects in Ge stayed relatively constant at 10^{14} cm⁻².

Once diamond exceeded the critical value to lose long-range crystal structure (1 MeV, $\geq 3 \times 10^{15}$ Si⁺ cm⁻²), it did not immediately graphitize after implantation (as has been reported in some literature), but instead converted to an amorphous carbon state, with a density of $1.3 \pm 0.1 \times 10^{23}$ atoms cm⁻³, which is approximately 25% less dense than diamond, and 15% more dense than graphite. The amorphous structure was confirmed using selected area diffraction patterns, electron energy loss spectroscopy, and Raman spectroscopy characterization techniques. Upon annealing at sufficiently high temperatures and long times, the amorphous layer converted to graphite. No SPER was observed in diamond, either for reconstruction back to a diamond lattice, or seed growth of the graphitic layer. The critical threshold determined for the amorphization of

diamond is approximately $6 \pm 1 \times 10^{22}$ vacancies cm^{-3} , which is higher than the widely referenced results of 1×10^{22} vacancies cm^{-3} ,¹⁶ but is in the range of recent higher reported thresholds of 2 and 9×10^{22} vacancies cm^{-3} .^{74,101}

Within this study, the amorphization threshold may be compared across all three materials, however the results depend on the parameter used for threshold determination. Using the number of displacements of host atoms per incoming ion atom (DPA), diamond seems to be the easiest material to amorphize due to its low DPA of approximately 0.14. For Si and Ge, this number approached 1.0; all implants were at room temperature. However, more energy is required to displace the C atoms in the diamond lattice, and for that reason, the threshold damage density is largest for diamond, at approximately 4×10^{21} keV cm^{-3} , as compared to approximately 7×10^{20} keV cm^{-3} for Ge and Si, respectively. Interestingly, the number of vacancies cm^{-3} to amorphize the crystal seems to be approximately constant for all three crystal systems, in the range of $4\text{-}7 \times 10^{21}$ vacancies cm^{-3} . Ideally, these results should be compared to the historical literature for amorphization criterion. Using multiple data sources over the past twenty years for the materials of Si, Ge, SiGe, SiC, and C, the author attempted to normalize the data and compare results. This assessment was attempted; however, due to differences in temperature, dose rates, calculation parameters, characterization techniques and parameter definitions, no logical trends in the data were apparent.

Future Work

The current experiments demonstrate that Ge and diamond do not seem to suffer from the same stable defects which occur in Si after ion implantation and annealing. However, as the material behavior differs greatly than Si, the years of Si research cannot be leveraged when engineering these potential new base materials. Although the stable end-of-range defects do not occur at low energies in Ge, and no extended defects seem to occur for non-amorphizing

implants into diamond, other roadblocks may exist for these potential base materials. More research would be necessary to determine whether years of Si technology may be leveraged in order to enable these potential base materials to be viable for electronic devices. The following paragraphs outline further study which could be used to further define and confirm the results of the present research.

Ion choice for implantation. As noted in the literature review, the mass of the incoming ion and the mass of the target material help determine the amount of damage caused during the implantation process. In this study, the ion species, Si^+ , was kept constant across all three target crystal systems (Si, Ge, C) in order to minimize variability in the experiment. However, the result is that three different ion damage patterns occurred within each crystal system – a heavier ion into a lighter base material for Si^+ into C, a lighter ion into a heavier base material for Si^+ into Ge and a self-implant into Si. To reduce the variability in damage, self-implants could be used for another experiment, which could confirm or deny the validity of the defect structures and amorphization thresholds determined in our study.

Affect of dopants and other factors on defect formation. As stated in the previous paragraph, Si^+ was chosen as the implanted species to minimize variability in the experiment. However, for industrial use, it is important to know the effect of electrically-active species on defect formation. In Si, dopants are known to affect defect formation in a number of ways, as presented in Chapter 2. However, it is unknown at this time how dopant species, such as B^+ , P^+ or As^+ , would affect the dot-like defect formation in Ge.

Additionally, other factors have been known to affect defect formation in Si. For example, an oxide layer injects interstitials into the lattice during annealing. This increases the supersaturation of interstitials in the near surface area, which could encourage extended defect

formation. In our study, the 40 keV implants into Ge, upon annealing, created a small GeO_x layer. It is currently unknown whether the GeO_x layer affected the defect formation in this study.

Activation energy of defects in Ge. In our study, an initial estimate of the activation energy for the dissolution of both dot-like defects and end-of-range defects occurring in Ge was determined. However, a small sample size was used to determine the values, and due to the small sample size, the statistical error opportunity is high. In order to confirm the validity of these activation energies, further studies into the formation and dissolution of these defects would be necessary.

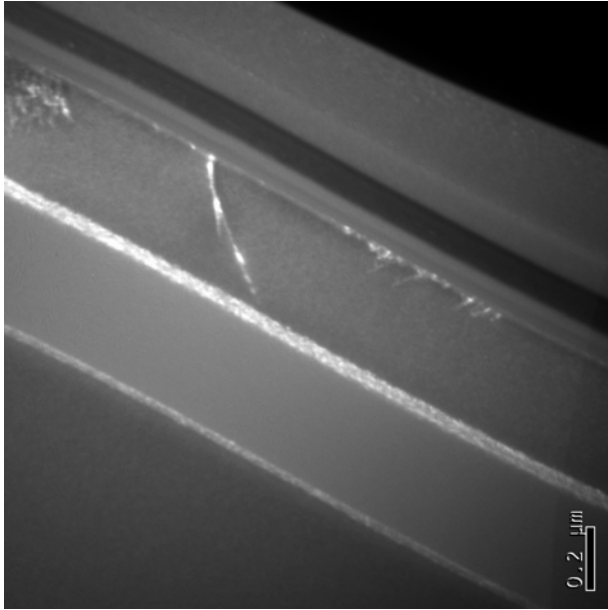
Vacancy clusters in the Ge near surface. Preliminary calculations of the interstitial population in non-amorphizing 1 MeV implants into Ge revealed a substantial increase over the predicted plus-one model used for Si. Additionally, the near-surface dot-like defects dissolved faster than the defects centered near the damage peak. The explanation for why Ge is diverging from the plus-one model may be that both vacancy-clusters (in the near-surface region) and interstitial clusters (in the projected range) are both present after implantation at room temperature for high-energy implants. This theory is supported by recent work revealing vacancy clusters in the near surface region after amorphizing implants into SiGe, which increased for higher concentrations of Ge.¹⁴ This theory could be tested, using the current implanted material, by either positron analysis or copper gettering experiments.

Future work regarding extended defects in Ge should focus on characterizing the dot-like defects and clarifying the formation mechanism. Chronological studies could be used to better quantify the activation energy of the dot-like defects. Positron analysis could be used to confirm a vacancy mechanism at work for potential intrinsic near-surface defects as opposed to extrinsic defects towards and beyond the projected range.

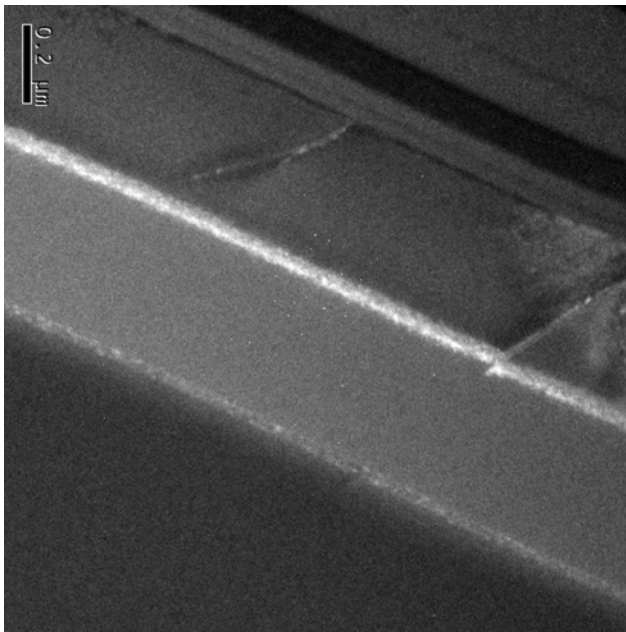
Future work for diamond. The results of our study answered many questions regarding ion implantation into single crystal diamond which have existed in the literature for some time: a more accurate critical damage threshold, the state of amorphous carbon after implantation, and the non-SPER conversion of amorphous carbon to graphite during annealing. Additionally, this study confirmed that anneals higher than 1350 °C for 24 hours are required to completely remove the damage caused by ion implantation, even for relatively low doses. However, this study also revealed the previously unknown phenomena of trapped crystallites in the amorphous region, which were stable up to temperatures of 1350 °C for 24 hrs. Whether these pockets of crystalline material continue to be stable, or will collapse upon further annealing, is unknown.

APPENDIX A SURFACE INITIATED DEFECTS OF ANNEALED DIAMOND

Throughout this study, annealing of the single-crystal diamond samples produced surface-initiated defects. These defects occurred in both implanted and non-implanted specimens. The defects occurred for relatively low anneal temperatures (950 °C) and at high temperatures (1350 °C). As the defects were intermittent, while the implant was uniform, these defects are not thought to be associated with the implantation regimes. However, as they are defects that occurred during the annealing process, and were revealed during XTEM imaging, the images will be presented here. All of the defects seem to originate at the surface, some with a 54° angle between the defect and the surface. That would indicate that the defect is traveling along the (111) plane in the <110> direction. The images presented in the following pages are of defects seen in high dose implants with high temperature and long anneal time; mid-dose implants with high temperatures and short anneal times, low doses with low annealing temperatures and short annealing times, and images of defects seen in an unimplanted annealed diamond.

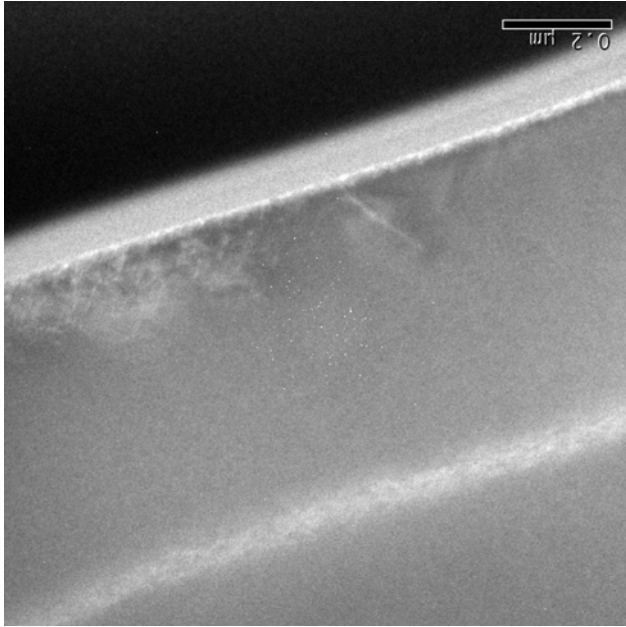


(a)

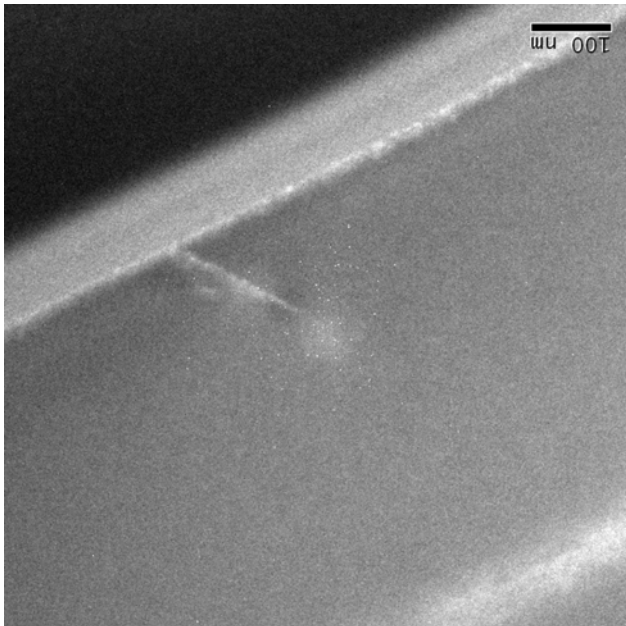


(b)

Figure A-1. WDBF XTEM images of single-crystal diamond Si^+ implanted at 1 MeV to a dose of $3 \times 10^{15} \text{ cm}^{-2}$ at 303 K after annealing for 24 hrs at 1350 °C (a) defects in one section of the sample and (b) same magnification of a different section of the same XTEM sample.

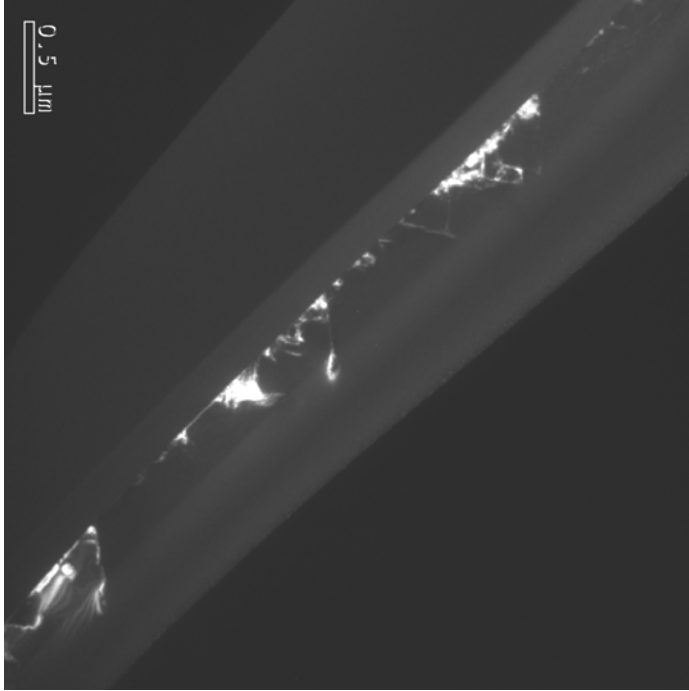


(a)

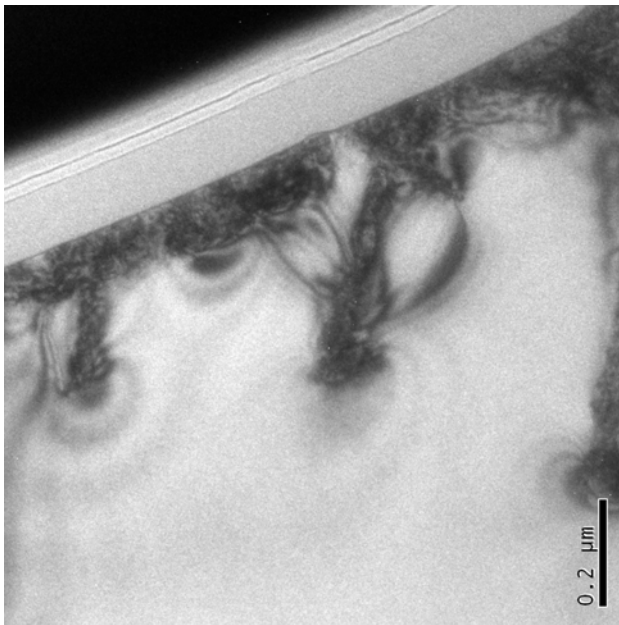


(b)

Figure A-2. WDBF XTEM images of single-crystal diamond Si^+ implanted at 1 MeV to a dose of $1 \times 10^{15} \text{ cm}^{-2}$ at 77 K after annealing for 24 hrs at 1350 °C (a) defects in one section of the sample and (b) higher magnification of a different section of the same XTEM sample.



(a)



(b)

Figure A-3. (a) WBD- and (b) BF-XTEM images of single-crystal diamond Si^+ implanted at 1 MeV to a dose of $1 \times 10^{14} \text{ cm}^{-2}$ at 303 K after annealing for 2 hrs at 950 °C.

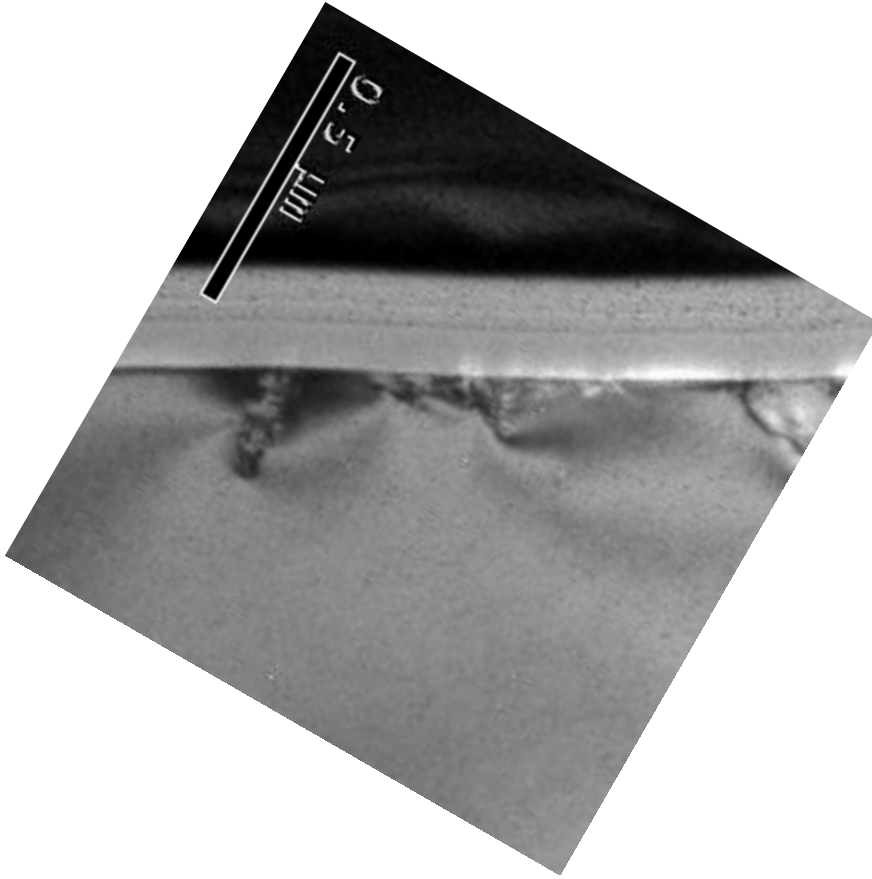


Figure A-4. BF-XTEM images of single-crystal diamond un-implanted, after annealing for 2 hrs at 950 °C.

APPENDIX B BORON IMPLANTATION INTO DIAMOND

Introduction

As noted in the introduction, the implantation of Boron (B^+) is of technological interest for purposes of doping a transistor channel, source or drain region. An electrically well-studied implant in the literature has been repeated here. The B^+ implantation is at 2 MeV to a dose of $1 \times 10^{15} B^+/cm^2$ at an implant temperature of 303 K. Though studied through electrical measurements, the author is unaware of any published XTEM studies. The following summarizes key B^+ doping of diamond papers published in the last 15 years.

In 1993, Zeidler et al. implanted B^+ , C^+ and a combination of the two elements into natural single-crystal diamond at implant temperatures of 77, 300 or 800 K. They concluded that low temperature implantations provided the best carrier concentration and mobility. Using a multiple-step, low-temperature implant, B^+ implantation procedure, this Naval Command group fabricated a single-crystal diamond insulated gate field effect transistor.

In 1996, Fontaine, Uzan-Saguy, Philosoph and Kalish, of Israel, used Prins' suggested cold-implantation rapid-annealing procedure to produce record values of high Hall mobility of B^+ doped diamond. They implanted at -97 C, annealed first at 1050 C and then further annealing at 1450 C for 10 min to achieve a p-type room temperature mobility of $385 cm^2/V s$. In 1998, the same group (plus Prawer from Australia) improved the process to achieve a room temperature Hall mobility of $585 cm^2/V s$, 5% compensation ratio, acceptor concentration of $3.9 \pm 0.3 \times 10^{18} cm^{-2}$ and an activation energy of approximately 0.354 eV. In the same year, Prins studied B^+ doped diamonds by catholuminescence, adding more insight into the resistance behavior of boron doping in both natural and synthetic diamonds.

In 2002, Prins conducted a rigorous study of implanting C^+ , N^+ , B^+ and O^+ into natural single-crystal diamonds, and determined that O^+ and N^+ treated diamond donor states were metastable, and annealed out at temperatures about 600 °C. However, it should be noted that all three dopant atom implanted diamonds had lower electrical resistivities than the C^+ implanted diamonds. The acceptor state in the B^+ treated diamonds was determined to be at ~ 0.37 eV, while the donor states in the N^+ and O^+ implanted diamonds were at ~ 0.28 and ~ 0.32 eV, respectively.

In 2004, Vogel et al. (based out of Germany and the City University in New York) implanted at the same conditions, except the implant temperature was 303 K. Using Hall effect and conductivity measurements, after anneals up to 1650 °C, they showed clear p+ type conduction, with B^+ activation up to 30%, the highest yet reported for ion-implanted diamond. They concluded that the best annealing conditions for removing damage, and achieving the highest conductivity of 230 $cm^2/V s$, was at anneals of 1500 °C for 15 min. Annealing the samples above 1500 °C did not improve, but actually reduced, conductivity measurements.

In 2006, a research group based in Japan, used natural and HPHT diamonds to study B^+ dosage dependencies on structural and electrical properties of doped diamond. A B^+ box profile, 30-380 nm below the surface, was created using doses in the range of $2.1 \times 10^{15} B^+/cm^2 - 1.7 \times 10^{17} B^+/cm^2$. The implant temperature was ~ 400 °C and the anneal treatment was 1450 °C in vacuum for 1 hour. Using the high implant temperature, the group prevented “collapse to graphitization” and allowed the diamond to form a very low resistance p+ diamond layer, with a B concentration of $2.5 \times 10^{21} cm^{-3}$ and resistivity of 2.3 m Ω cm at room temperature. The transport properties were shown to be almost temperature independent and p-type carrier concentration was realized in the range of 80-1000 K.

Experimental Design

Gem-quality HPHT single-crystal diamond samples, approximately $5 \times 5 \times 1 \text{ mm}^3$, were B^+ implanted at 2 MeV to a dose of $1 \times 10^{15} \text{ B}^+/\text{cm}^2$ at an implant temperature of 303 K. This simulates the implant conditions of previous studies. The implantation of B^+ into the diamonds was performed in a tandem accelerator ion implanter, with a dose rate of $0.44 \mu\text{A}/\text{cm}^2$, and the samples were tilted 7° relative to the incident ions to minimize ion channeling. The original nitrogen (N_2) impurity concentration of the diamonds, obvious from the visible light-orange color, is on the order of $10^{18} - 10^{20} \text{ cm}^{-3}$,¹⁴⁰ and was uniform throughout the crystals.

According to simulations,²¹ the damage should peak (R_d) at approximately $1.35 \mu\text{m}$ and the projected range (R_p) of the ions are approximately $1.38 \mu\text{m}$ below the surface of the diamond. After implantation, approximately 150 nm of carbon was evaporated onto all samples, for conductivity and protection of the sample surface during focused-ion beam processing. Cross-sectional TEM (XTEM) samples were prepared according to the procedure previously published,¹¹⁷ during which a layer of Platinum was applied to the surface.

Annealing was performed in both tube and graphite furnaces. Samples annealed at 1050°C and below were annealed in a Lindberg tube furnace in a high-purity N_2 environment. Anneals at 1350°C used a graphite chamber furnace at diffusion pump vacuum pressures ($\leq 10^{-4} \text{ Torr}$)¹⁴² with a residual helium environment. Additionally, the samples were placed in tantalum (Ta) foil (folded as envelopes), which is an oxygen getterer, to additionally prevent accidental oxidation of the diamond surface. The Ta envelopes served the additional purpose of separating and marking each sample. Transmission electron microscopy analysis was performed on JEOL 200CX and JEOL 2010 microscopes.

Results & Discussion

WBDF-XTEM imaging of the B⁺ implant showed that the simulation-predicted R_D = 1.35 μm and R_P = 1.38 μm matched well with the experimental damage band. The damage band is still apparent after a 1000 °C, 10 min anneal in a tube furnace [Fig. B-1(a)], but after a 1350 °C at 24 hour anneal, the crystal structure is almost completely recovered, and the damage band is almost negligible in WBDF imaging. Further annealing, or higher temperature annealing, would likely remove all semblance of damage from the ion implantation process. This agrees well with Vogel's claim that all implant damage, and highest activation of the B⁺ dopant, takes place at 1500 °C for 15 min. Though this experiment was not able to repeat the high anneal temperatures of Vogel's previously reported literature, this study is the first XTEM analysis of the damage and recovery of single-crystal diamond after B⁺ implantation.

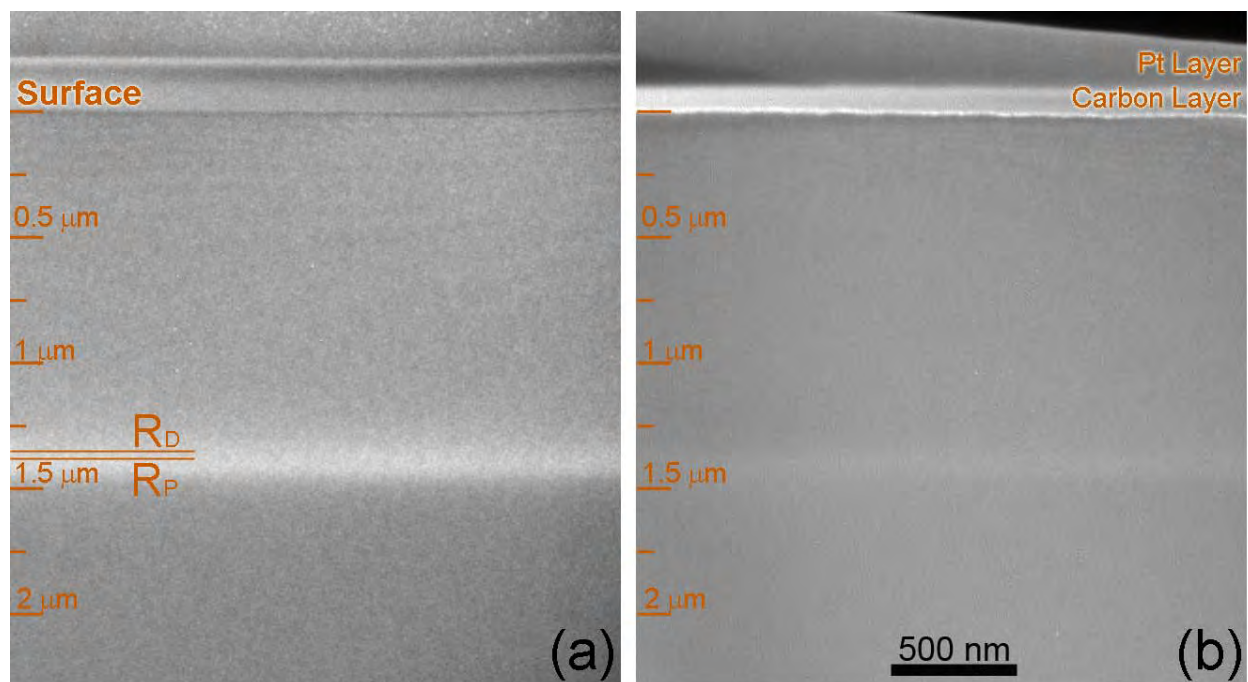


Figure B-1. WBDF-XTEM images of (001)-oriented diamond B^+ implanted at 2 MeV to a dose of $1 \times 10^{15} \text{ cm}^{-2}$ at 303K as implanted, and after annealing (a) in flowing N_2 ambient at 1000 °C for 10 min and (b) in vacuum at 1350 °C for 24 hrs.

LIST OF REFERENCES

- ¹ A.R. Peaker, A. Satta, V. P. Markdevich, E. Simoen, and B. Hamilton, presented at the 16th International Conference on Ion implantation Technology, Marseille, France, 2006 (unpublished).
- ² G. E. Moore, *Electronics* **38**, 114-117 (1965).
- ³ Semiconductor Industry Association, (Sematech, Inc., 2005), Vol. 2005.
- ⁴ Gehan A. J. Amaratunga, *Science* **297**, 1657-1658 (2002).
- ⁵ T. Y. Tan, *Philosophical Magazine A - Physics of Condensed Matter Structure Defects and Mechanical Properties* **44**, 101-125 (1981).
- ⁶ J. H. Li and K. S. Jones, *Appl. Phys. Lett.* **73**, 3748-3750 (1998).
- ⁷ I.G. Salisbury and M. H. Loretto, *Philosophical Magazine A* **39**, 317-323 (1979).
- ⁸ M. Pasemann, D. Hoehl, A. L. Aseev, and O. P. Pchelyakov, *Phys. Status Solidi A-Appl. Res.* **80**, 135-139 (1983).
- ⁹ K. S. Jones, S. Prussin, and E. R. Weber, *Applied Physics A-Materials Science & Processing* **45**, 1-34 (1988).
- ¹⁰ C. A. Ferreira Lima, Howie, A., *Philosophical Magazine* **34**, 1054-1071 (1976).
- ¹¹ T. Akatsu, Bourdelle, K. K., Richtarch, C., Faure, B., and Letertre, F., *Appl. Phys. Lett.* **86**, 181910-181911 (2005).
- ¹² L. Hutchison, A. L. Aseev, and L. I. Fedina, in *Microscopy Of Semiconducting Materials 1993* (1993), pp. 41-46.
- ¹³ R. Crosby, K. S. Jones, M. E. Law, A. N. Larsen, and J. L. Hansen, *Journal Of Vacuum Science & Technology B* **22**, 468-470 (2004).
- ¹⁴ R. Kogler, A. Mucklich, W. Skorupa, A. Peeva, A. Y. Kuznetsov, J. S. Christensen, and B. G. Svensson, *J. Appl. Phys.* **101** (2007).
- ¹⁵ P. A. Stolk, H. J. Gossmann, D. J. Eaglesham, and J. M. Poate, *Mater. Sci. Eng. B-Solid State Mater. Adv. Technol.* **36**, 275-281 (1996).
- ¹⁶ C. Uzan-Saguy, Cytermann, C., Brener, R., Richter, V., Shaanan, M., and Kalish, R., *Applied Physics Letters* **67**, 1194-1196 (1995).
- ¹⁷ D. J. Eaglesham, Stolk, P. A., Gossmann, H.-J. and Poate, J. M., *Applied Physics Letters* **65**, 2305-2307 (1994).

- 18 E. Chason, S. T. Picraux, J. M. Poate, J. O. Borland, M. I. Current, T. D. delaRubia, D. J. Eaglesham, O. W. Holland, M. E. Law, C. W. Magee, J. W. Mayer, J. Melngailis, and A. F. Tasch, *J. Appl. Phys.* **81**, 6513-6561 (1997).
- 19 M.S. Dresselhaus and R. Kalish, *Ion Implantation in Diamond, Graphite and Related Materials*. (Springer-Verlag, Berlin Heidelberg New York, 1992), p.202.
- 20 J. F. Ziegler, *Ion Implantation Technology, 6th Edition*, 752 pages, (Ion Implantation Technology Co., Yorktown, 1996).
- 21 J. F. Ziegler, *Nucl. Instrum. Methods Phys. Res. Sect. B-Beam Interact. Mater. Atoms* **219-20**, 1027-1036 (2004).
- 22 S. Libertino, in *17TH International Conference on the Application of Accelerators in Research and Industry*, edited by AIP Conference Proceedings (AIP, Catania, Italy, 2003), Vol. 680, pp. 750-754.
- 23 A. Claverie, B. Colombeau, B. De Mauduit, C. Bonafos, X. Hebras, G. Ben Assayag, and F. Cristiano, *Applied Physics A-Materials Science & Processing* **76**, 1025-1033 (2003).
- 24 G. Z. Pan, K. N. Tu, and S. Prussin, *Appl. Phys. Lett.* **71**, 659-661 (1997).
- 25 J. L. Benton, S. Libertino, P. Kringhoj, D. J. Eaglesham, J. M. Poate, and S. Coffa, *J. Appl. Phys.* **82**, 120-125 (1997).
- 26 S. Coffa, S. Libertino, and C. Spinella, *Appl. Phys. Lett.* **76**, 321-323 (2000).
- 27 P. Keys, *Phosphorus-Defect Interactions During Thermal Annealing of Ion Implanted Silicon*. Dissertation, University of Florida, Gainesville, FL (2001), p.137.
- 28 J. Wong-Leung, S. Fatima, C. Jagadish, J. D. Fitz Gerald, C. T. Chou, J. Zou, and D. J. H. Cockayne, *J. Appl. Phys.* **88**, 1312-1318 (2000).
- 29 H. Bartsch, D. Hoehl, and G. Kastner, *Phys. Status Solidi A-Appl. Res.* **83**, 543-551 (1984).
- 30 I. G. Salisbury and M. H. Loretto, *Radiat. Eff. Defects Solids* **59**, 59-68 (1981).
- 31 L. S. Robertson, K. S. Jones, L. M. Rubin, and J. Jackson, *J. Appl. Phys.* **87**, 2910-2913 (2000).
- 32 R. Brindos, P. Keys, K. S. Jones, and M. E. Law, *Appl. Phys. Lett.* **75**, 229-231 (1999).
- 33 F. F. Morehead, B. L. Crowder, and R. S. Title, *J. Appl. Phys.* **43**, 1112-& (1972).

- 34 M. K. Elghor, O. W. Holland, C. W. White, and S. J. Pennycook, *Journal Of Materials Research* **5**, 352-359 (1990).
- 35 S. Prussin, D. I. Margolese, and R. N. Tauber, *J. Appl. Phys.* **57**, 180-185 (1985).
- 36 L. Pelaz, L. A. Marques, and J. Barbolla, *J. Appl. Phys.* **96**, 5947-5976 (2004).
- 37 L. A. Christel, J. F. Gibbons, and T. W. Sigmon, *J. Appl. Phys.* **52**, 7143-7146 (1981).
- 38 G. Z. Pan, K. N. Tu, and S. Prussin, *Appl. Phys. Lett.* **68**, 1654-1656 (1996); B. Demauduit, L. Laanab, C. Bergaud, M. M. Faye, A. Martinez, and A. Claverie, *Nucl. Instrum. Methods Phys. Res. Sect. B-Beam Interact. Mater. Atoms* **84**, 190-194 (1994).
- 39 M. E. Law and S. M. Cea, *Comput. Mater. Sci.* **12**, 289-308 (1998).
- 40 L. Pelaz, L. A. Marques, M. Aboy, P. Lopez, and J. Barbolla, *Comput. Mater. Sci.* **33**, 92-105 (2005).
- 41 C. S. Rafferty, G. H. Gilmer, M. Jaraiz, D. Eaglesham, and H. J. Gossmann, *Appl. Phys. Lett.* **68**, 2395-2397 (1996).
- 42 C. Rafferty and R. K. Smith, *Cmes-Computer Modeling In Engineering & Sciences* **1**, 151-159 (2000).
- 43 I. Avci, M. E. Law, E. Kuryliw, A. F. Saavedra, and K. S. Jones, *J. Appl. Phys.* **95**, 2452-2460 (2004).
- 44 C. Zechner, N. Zographos, D. Matveev, and A. Erlebach, *Mater. Sci. Eng. B-Solid State Mater. Adv. Technol.* **124**, 401-403 (2005).
- 45 J. Kim, F. Kirchhoff, J. W. Wilkins, and F. S. Khan, *Phys. Rev. Lett.* **84**, 503-506 (2000).
- 46 M. Kohyama and S. Takeda, *Phys. Rev. B* **51**, 13111-13116 (1995).
- 47 L. A. Marques, L. Pelaz, P. Castrillo, and J. Barbolla, *Phys. Rev. B* **71** (2005).
- 48 P. Kebabian, D. Wolf, S. R. Phillpot, and H. Gleiter, *Journal Of Materials Research* **13**, 2077-2099 (1998).
- 49 A. L. Aseev, Ivakhnishin, V. M., Stas', V. F., Smirnov, L.S., *Soviet Physics Solid State (Translation of Fiz. Tverd. Tela)* **25**, 1786-1789 (1983).
- 50 A. L. Aseev, V. M. Ivakhnishin, V. F. Stas, and L. S. Smirnov, *Fiz. Tverd. Tela* **25**, 3097-3103 (1983).

- 51 K. Zellama, Morhange, J. F., Germain, P., Bourgoïn, J.C., *Physica Status Solidi (a)* **56**, 717-723 (1979).
- 52 Y. L. Chao, S. Prussin, J. C. S. Woo, and R. Scholz, *Appl. Phys. Lett.* **87**, 142102 (2005).
- 53 A. Satta, T. Janssens, T. Clarysse, E. Simoen, M. Meuris, A. Benedetti, I. Hoflijk, B. De Jaeger, C. Demeurisse, and W. Vandervorst, *Journal Of Vacuum Science & Technology B* **24**, 494-498 (2006).
- 54 A. Satta, E. Simoen, T. Clarysse, T. Janssens, A. Benedetti, B. De Jaeger, M. Meuris, and W. Vandervorst, *Appl. Phys. Lett.* **87**, 172109 (2005).
- 55 A. Satta, E. Simoen, R. Duffy, T. Janssens, T. Clarysse, A. Benedetti, M. Meuris, and W. Vandervorst, *Appl. Phys. Lett.* **88**, 162118 (2006); A. Satta, E. Simoen, T. Janssens, T. Clarysse, B. De Jaeger, A. Benedetti, I. Hoflijk, B. Brijs, M. Meuris, and W. Vandervorst, *J. Electrochem. Soc.* **153**, G229-G233 (2006).
- 56 B. Stritzker, R. G. Elliman, and J. Zou, *Nucl. Instrum. Methods Phys. Res. Sect. B-Beam Interact. Mater. Atoms* **175**, 193-196 (2001).
- 57 I. Jencic, I. M. Robertson, and J. Skvarc, *Nucl. Instrum. Methods Phys. Res. Sect. B-Beam Interact. Mater. Atoms* **148**, 345-349 (1999).
- 58 H. Huber, W. Assmann, S. A. Karamian, A. Mucklich, W. Prusseit, E. Gazis, R. Grotzschel, M. Kokkoris, E. Kossionidis, H. D. Mieskes, and R. Vlastou, *Nucl. Instrum. Methods Phys. Res. Sect. B-Beam Interact. Mater. Atoms* **122**, 542-546 (1997).
- 59 S. Solmi, L. Mancini, S. Milita, M. Servidori, G. Mannino, and M. Bersani, *Appl. Phys. Lett.* **79**, 1103-1105 (2001); P. Alippi and L. Colombo, *Phys. Rev. B* **62**, 1815-1820 (2000).
- 60 J. P. Dismukes, R. J. Paff, and L. Ekstrom, *Journal Of Physical Chemistry* **68**, 3021-& (1964); C. Tzoumanekas and P. C. Kelires, *Phys. Rev. B* **66** (2002).
- 61 K. Laaziri, S. Roorda, and J. M. Baribeau, *J. Non-Cryst. Solids* **191**, 193-199 (1995).
- 62 R. Devanathan, F. Gao, and W. J. Weber, *Appl. Phys. Lett.* **84**, 3909 (2004).
- 63 B. Pecz, A. Barna, V. Heera, F. Fontaine, and W. Skorupa, in *Silicon Carbide And Related Materials, Ecscrm2000* (Trans Tech Publications Ltd, Zurich-Uetikon, 2000), Vol. 353-3, pp. 199-202.
- 64 H. Weishart, F. Eichhorn, V. Heera, B. Pecz, A. Barna, and W. Skorupa, *J. Appl. Phys.* **98** (2005).

- 65 M. Ishimaru, Nucl. Instrum. Methods Phys. Res. Sect. B-Beam Interact. Mater. Atoms **250**, 309-314 (2006).
- 66 M. Ishimaru, I. T. Bae, A. Hirata, Y. Hirotsu, J. A. Valdez, and K. E. Sickafus, Phys. Rev. B **72** (2005).
- 67 J. Isberg, a, J. Hammersberg a, D. J. Twitchen b and A. J. Whitehead b, Diamond and Related Materials **13**, 320-324 (2004); E. Ebert Kohn, W. Aleksov, A. Denisenko, A. Adamschik, M. Schmid, P., Microelectronics, 2002. MIEL 2002. 23rd International Conference on **1**, 59 - 66 (2002).
- 68 M. Kubovic Aleksov A., M. Kasu b, P. Schmid, D. Grobe, S. Ertl, M. Schreck, B. Stritzker and E. Kohn, Diamond and Related Materials **13**, 233-240 (2004).
- 69 F. P. Bundy, W. A. Bassett, M. S. Weathers, R. J. Hemley, H. K. Mao, and A. F. Goncharov, Carbon **34**, 141-153 (1996).
- 70 F. P. Bundy, H. T. Hall, H. M. Strong, and R. H. Wentorf, Nature **176**, 51-55 (1955).
- 71 M. Kubovic, M. Kasua, I. Kallfassa, M. Neuburgera, A. Aleksova, G. Koleyc, M. G. Spencerc and E. Kohna, Diamond and Related Materials **13**, 802-807 (2003).
- 72 J. Isberg, J. Hammersberg, E. Johansson, T. Wikström, D.J. Twitchen, A.J. Whitehead, S.E. Coe, and G.A. Scarsbrook, Science **297**, 1670-1672 (2002).
- 73 D. L. Dreifus, A. Collins, T. Humphreys, K. Das, and P.E. Phersson, *Diamond for Electronic Applications*. (Materials Research Society, Pittsburg, Pennsylvania, 1995); Y. Bando, M. Akaishi, H. Kanda, Y. Matsui, T. Kobayashi, K. Watanabe, and N. Yamashita, *New Semiconducting Materials: Diamond and Related Materials: Proceedings of the 6th NIRIM International Symposium on Advanced Materials (ISAM '99)*. (National Institute for Research in Inorganic Materials, Tsukuba, Japan, 1999).
- 74 P. Olivero, S. Rubanov, P. Reichart, B. C. Gibson, S. T. Huntington, J. Rabeau, A. D. Greentree, J. Salzman, D. Moore, D. N. Jamieson, and S. Praver, Adv. Mater. **17**, 2427-+ (2005).
- 75 P. Olivero, S. Rubanov, P. Reichart, B. C. Gibson, S. T. Huntington, J. R. Rabeau, A. D. Greentree, J. Salzman, D. Moore, D. N. Jamieson, and S. Praver, Diamond And Related Materials **15**, 1614-1621 (2006).
- 76 A. Olbrich, Ebersberger, B., Boit, C., Niedermann, Ph., Hanni, W., Vancea, J., and Hoffman, H., Journal of Vacuum Science & Technology B **17**, 1570-1574 (1999).
- 77 K. Ueda, M Kasu, Y. Yamauchi, T. Makimoto, M. Schwitters, D.J. Twitchen, G.A. Scarsbrook, and S.E. Coe, IEEE Electron Device Letters **27**, 570-572 (2006); M.

- Kubovic, K. Janischowsky, and E. Kohn, *Diamond and Related Materials* **14**, 514-517 (2005).
- 78 S. Koizumi, K. Watanabe, F. Hasegawa, and H. Kanda, *Science* **292**, 1899-1901 (2001).
- 79 M. Werner, *Semiconductor Science And Technology* **18**, S41-S46 (2003); M. Werner, R. Job, A. Denisenko, A. Zaitsev, W. R. Fahrner, C. Johnston, P. R. Chalker, and I. M. BuckleyGolder, *Diamond And Related Materials* **5**, 723-727 (1996); M. Yokoba, Koide, Y., Otsuki, A., Ako, F., Oku, T., Murakami, M., *J. Appl. Phys.* **81**, 6815-6821 (1997); P.E. Viljoen, E.S. Lambers, and P.H. Holloway, *Journal of Vacuum Science and Technology B* **12**, 2997-3005 (1994).
- 80 J. R. Zeidler, Hewett, C. A., Wilson, R. G., *Phys. Rev. B* **47**, 2065–2071 (1993).
- 81 R. Kalish, Reznik, A., Prawer, S., Saada, D., Adler, J., *Phys. Status Solidi A-Appl. Res.* **174**, 83-89 (1999).
- 82 J. F. Prins, *Semicond. Sci. Technol.* **18**, S27-S33 (2003).
- 83 J. F. Prins, *Diamond And Related Materials* **10**, 1756-1764 (2001).
- 84 J.F. Prins, *Mater. Sci. Rep. (Netherlands)* **7** (Feb. 1992) 271-364 (1992).
- 85 R. Kalish and S. Prawer, in *Handbook of Industrial Diamonds and Diamond Films*, edited by M.A. Prelas, F. Popovici, and L.K. Bigelow (New York, 1997), pp. 945-982.
- 86 G. Davies, B. Campbell, A. Mainwood, M. Newton, M. Watkins, H. Kanda, and T. R. Anthony, *Phys. Status Solidi A-Appl. Res.* **186**, 187-198 (2001); H. E. Smith, G. Davies, M. E. Newton, and H. Kanda, *Phys. Rev. B* **69** (2004).
- 87 J.F. Prins, *Appl. Phys. Lett.* **73**, 2308-2310 (1998).
- 88 J. F. Prins, *Diamond And Related Materials* **11**, 612-617 (2002).
- 89 C. Uzan-Saguy, R. Kalish, R. Walker, D. N. Jamieson, and S. Prawer, *Diamond And Related Materials* **7**, 1429-1432 (1998).
- 90 F. Fontaine, C. UzanSaguy, B. Philosoph, and R. Kalish, *Appl. Phys. Lett.* **68**, 2264-2266 (1996).
- 91 R. Walker, Prawer,S., Jamieson,D. N., Nugent, K. W. and Kalish, R., *Appl. Phys. Lett.* **71**, 1492-1494 (1997).
- 92 T. Vogel, J. Meijer, and A. Zaitsev, *Diamond And Related Materials* **13**, 1822-1825 (2004).

- 93 H. Weishart, V. Heera, and W. Skorupa, *J. Appl. Phys.* **97** (2005).
- 94 B. Fizgeer, C. Uzan-Saguy, C. Cytermann, V. Richter, I. Avigal, M. Shaanan, R. Brener, and R. Kalish, *Phys. Status Solidi A-Appl. Res.* **186**, 281-289 (2001).
- 95 C. Saguy, A. Reznik, E. Baskin, Z. Remes, and R. Kalish, *Diamond And Related Materials* **13**, 722-726 (2004); H. Kato, S. Yamasaki, and H. Okushi, *Appl. Phys. Lett.* **86** (2005).
- 96 L.W. Yin, Zou, Z.D., Li, M.S. Geng, G.L., Sun, D. S., Hao, Z. Y. Yao, Z.Y., *Cryst. Res. Technol.* **35**, 1289-1294 (2000).
- 97 J. F. Prins, *Diamond And Related Materials* **9**, 1835-1839 (2000).
- 98 J. F. Prins, T. E. Derry, and J. P. F. Sellschop, *Phys. Rev. B* **34**, 8870-8874 (1986).
- 99 Johan F. and Trevor E. Derry Prins, *Nuclear Instruments and Methods in Physics Research Section B: Beam Interactions with Materials and Atoms* **166-167**, 364-373 (2000).
- 100 R. Kalish, A. Reznik, K. W. Nugent, and S. Prawer, *Nucl. Instrum. Methods Phys. Res. Sect. B-Beam Interact. Mater. Atoms* **148**, 626-633 (1999).
- 101 R. Brunetto, Giuseppe A Baratta and Giovanni Strazzulla, *Journal of Physics: Conference Series* **6**, 120-125 (2005).
- 102 S. Prawer, Kalish, R., *Phys. Rev. B* **51**, 15711-15722 (1995).
- 103 R. Walker, S. Prawer, D. N. Jamieson, K. W. Nugent, and R. Kalish, *Appl. Phys. Lett.* **71**, 1492-1494 (1997); S. Prawer, D. N. Jamieson, K. W. Nugent, R. Walker, C. Uzan-Saguy, and R. Kalish, *Diam. Films Technol.* **8**, 195-210 (1998).
- 104 P.F. Lai, S. Prawer, and L.A. Bursill, *Diamond and Related Materials* **10**, 82-86 (2001).
- 105 L. W. Yin, M. S. Li, D. S. Sun, and J. J. Cui, *Materials Letters* **48**, 21-25 (2001).
- 106 L. W. Yin, M. S. Li, D. S. Sun, F. Z. Li, and Z. Y. Hao, *Materials Letters* **55**, 397-402 (2002).
- 107 Y. Nishibayashi, Y. Ando, H. Furuta, K. Kobashi, H. Furuta, K. Meguro, T. Imai, T. Hirao, and K. Oura, *Molecular Crystals And Liquid Crystals* **386**, 183-188 (2002).
- 108 F. Langenhorst, J. P. Poirier, and D. J. Frost, *Journal Of Materials Science* **39**, 1865-1867 (2004).

- 109 R. Erni, B Freitag, P Hartel, H. Muller, P. Tiemeijer, M. Van der Stam, M. Stekelenburg,
D. Hubert, P. Specht, and V. Garibay-Febles, *Microscopy and Microanalysis* **12**, 492-
497 (2006).
- 110 D. P. Adams, M. J. Vasile, T. M. Mayer, and V. C. Hodges, *Journal Of Vacuum Science
& Technology B* **21**, 2334-2343 (2003).
- 111 in *CRC Handbook of Chemistry and Physics*, edited by David R. Lide (Taylor & Francis
Group, 2005-2006), pp. 4-125.
- 112 J. W. Edington, *Practical Electron Microscopy*. (1977).
- 113 J.I. Gersten and F.W. Smith, *The Physics and Chemistry of Materials*. (John Wiley &
Sons, Inc., 2001), p.826.
- 114 Yu-Ran Luo and J. Alistair Kerr, in *CRC Handbook of Chemistry and Physics*, edited by
David R. Lide (Taylor & Francis Group, 2005-2006), pp. 9 - 54-62.
- 115 L.L. Berger, in *CRC Handbook of Chemistry and Physics*, edited by David R. Lide
(Taylor & Francis Group, 2005-2006), pp. 12-82.
- 116 D. Saada, J. Adler, and R. Kalish, *Int. J. Mod. Phys. C* **9**, 61-69 (1998).
- 117 D. P. Hickey, E. Kuryliw, K. Siebein, K. S. Jones, R. Chodelka, and R. Elliman, *Journal
Of Vacuum Science & Technology A* **24**, 1302-1307 (2006).
- 118 L. A. Giannuzzi and F. A. Stevie, *Micron* **30**, 197-204 (1999).
- 119 T. Evans, in *Physical Properties of Diamond*, edited by R. Berman (Clarendon Press,
Oxford, 1965), pp. 116-134.
- 120 W. Zhu, in *Diamond Electronic Properties and Applications*, edited by Lawrence S. Pan
and Don R. Kania (Kluwer Academic Publishers, Boston, 1995), pp. 175-240.
- 121 Kurt E. Sickafus, in *Encyclopedia of Materials Characterization*, edited by C. Richard
Brundle, Charles A. Evans Jr., and Shaun Wilson (Butterworth-Heinemann, Boston,
1992), pp. 99-119.
- 122 R. Brydson, *Electron Energy Loss Spectroscopy*. (BIOS Scientific Publishers Limited,
Oxford, 2001).
- 123 Ferguson, Berry, and Thompson, *Mem. Geo. Soc. Am.* **85** (1962).
- 124 Sanc and Plychna, *Foreing Trade Corporation* (1990).

- 125 Roy H. Geiss, in *Encyclopedia of Materials Characterization*, edited by C. Richard Brundle, Charles A. Evans Jr., and Shaun Wilson (Butterworth-Heinemann, Boston, 1992), pp. 120-134.
- 126 R.F. Egerton, *Electron energy-loss pectroscopy in the electron microscope*. (Plenum Press, New York, 1986).
- 127 J. Robertson, *Materials Science & Engineering R-Reports* **37**, 129-281 (2002).
- 128 D. S. Knight and W. B. White, *Journal Of Materials Research* **4**, 385-393 (1989).
- 129 William B. White, in *Encyclopedia of Materials Characterization*, edited by C. Richard Brundle, Charles A. Evans Jr., and Shaun Wilson (Butterworth-Heinemann, Boston, 1992), pp. 428-441.
- 130 S. E. Thompson, M. Armstrong, C. Auth, M. Alavi, M. Buehler, R. Chau, S. Cea, T. Ghani, G. Glass, T. Hoffman, C. H. Jan, C. Kenyon, J. Klaus, K. Kuhn, Z. Y. Ma, B. McIntyre, K. Mistry, A. Murthy, B. Obradovic, R. Nagisetty, P. Nguyen, S. Sivakumar, R. Shaheed, L. Shiften, B. Tufts, S. Tyagi, M. Bohr, and Y. El-Mansy, *IEEE Transactions On Electron Devices* **51**, 1790-1797 (2004).
- 131 P. R. Chidambaram, C. Bowen, S. Chakravarthi, C. Machala, and R. Wise, *IEEE Transactions On Electron Devices* **53**, 944-964 (2006).
- 132 L. Csepregi, R. P. Kullen, J. W. Mayer, and T. W. Sigmon, *Solid State Commun.* **21**, 1019-1021 (1977).
- 133 K.C. Thompson-Russell and J. W. Edington, in *Monographs in Practical Electron Microscopy in Materials Science*, edited by J. W. Edington (Philips Technical Library, Holland, 1977), Vol. 5, p. 62.
- 134 V. C. Venezia, T. E. Haynes, A. Agarwal, L. Pelaz, H. J. Gossmann, D. C. Jacobson, and D. J. Eaglesham, *Appl. Phys. Lett.* **74**, 1299-1301 (1999).
- 135 E. Simoen, A. Satta, M. Meuris, T. Janssens, T. Clarysse, A. Benedetti, C. Demeurisse, B. Brijs, I. Hoflijk, W. Vandervorst, and C. Claeys, in *Gettering And Defect Engineering In Semiconductor Technology Xi* (Trans Tech Publications Ltd, Zurich-Uetikon, 2005), Vol. 108-109, pp. 691-696.
- 136 K. S. Jones and D. Venables, *J. Appl. Phys.* **69**, 2931-2937 (1991).
- 137 T. Sands, J. Washburn, R. Gronsky, W. Maszara, D.K. Sadana, and G.A. Rozgonyi, 13th Intl. Conf. on Defects in Semiconductors, Coronado, 531-537 (1984).
- 138 V.S. Vavilov, *Phys. Status Solidi A (East Germany)* **31** (16 Sept. 1975) 11-26 (1975); V.S. Vavilov, *Radiat. Eff. (UK)* **37** (1978) 229-36 (1978).

- 139 K. S. Jones, M. E. Law, R. Brindos, and P. Keys, in *Microscopy Of Semiconducting Materials 2001* (Iop Publishing Ltd, Bristol, 2001), pp. 349-356.
- 140 P.J. Glielisse, in *Handbook of Industrial Diamonds and Diamond Films*, edited by M.A. Prelas, F. Popovici, and L.K. Bigelow (Marcel Dekker, Inc., New York, 1997), pp. 49-88.
- 141 R. T. DeHoff, *Thermodynamics in Materials Science*. (McGraw-Hill), p.326.
- 142 J.F. O'Hanlon, *A User's Guide to Vacuum Technology*, Third ed. (John Wiley & Sons, Hoboken, 2003).
- 143 S. Praver, I. Rosenblum, J. O. Orwa, and J. Adler, *Chemical Physics Letters* **390**, 458-461 (2004).
- 144 D. C. Hunt, D. J. Twitchen, M. E. Newton, and J. M. Baker, T. R. Anthony, W. F. Banholzer, W. F. Banholzer, S. S. Vagarali, *Phys. Rev. B* **61**, 3863–3876 (2000).
- 145 E. W. Maby, C. W. Magee, and J. H. Morewood, *Appl. Phys. Lett.* **39**, 157-158 (1981); C. Uzansaguy, V. Richter, S. Praver, Y. Lifshitz, E. Grossman, and R. Kalish, *Diamond And Related Materials* **4**, 569-574 (1995).
- 146 J. O. Orwa, K. W. Nugent, D. N. Jamieson, and S. Praver, *Phys. Rev. B* **62**, 5461-5472 (2000).
- 147 J. D. Hunn, S. P. Withrow, C. W. White, R. E. Clausing, L. Heatherly, C. P. Christensen, and N. R. Parikh, *Nucl. Instrum. Methods Phys. Res. Sect. B-Beam Interact. Mater. Atoms* **99**, 602-605 (1995).

BIOGRAPHICAL SKETCH

Diane Patricia Hickey was born in Summit, New Jersey and moved to Mobile, Alabama at a young age. A graduate of McGill-Toolen High School, she attended Auburn University where she was selected into the Cater Society, recognizing her as one of the top fifteen female leaders on campus. She was a technical editor of The Auburn Plainsman, a Camp War Eagle counselor, a founder of the engineering ambassadors' Cupola Engineering Society, and member of several honor societies including Mortar Board before graduating with a B. S. in chemical engineering in 1996. During that time, she also volunteered for the 1996 Atlanta Summer Olympics. From 1997-2003, Diane worked for Accenture, C-Bridge and the non-profit Cassiopeia Science Foundation., with volunteer work with Hands-On Atlanta, the Nexus Art Center, the United Way and the 2000 Sydney Summer Olympics. In 2003, she started graduate studies at the University of Florida, receiving her Master of Science in Materials Science and Engineering in 2004. She also pursued graduate work in science communication in the College of Journalism. Through journalism and the Materials Research Society, she became involved in science outreach and was selected to attend outreach training sponsored by the National Science Foundation as a part of the Nanoscale Informal Science Education Network. She has written and presented her science communication research at several conferences, was awarded best paper at the 2005 AMHCR conference, and recorded a podcast essay for the San Francisco Exploratorium's SmallTalk series. Diane's materials science and engineering research focus involves using germanium and single-crystal diamond for electronic devices, and will receive her doctoral degree in materials science and engineering in August of 2007.